The State of the Art Time-Domain Wavefield Imaging using a Discontinuous Galerkin Forward-Backward Time-Stepping Method

Forouz Mahdinezhad Saraskanroud

PhD thesis
Submitted in Partial Fulfillment
of the Requirements for the Degree of
Doctor of Philosophy

Department of Electrical and Computer Engineering
University of Manitoba
Winnipeg, Manitoba, Canada

Examining Committee Membership

The following served on the Examining Committee for this thesis. The decision of the Examining Committee is by majority vote.

Supervisor:	Ian Jeffrey Associate Professor, Dept. of ECE, University of Manitoba
External Examiner:	Milica Popovic Associate Professor, Dept. of Engineering, McGill University
Internal Member:	Joe LoVetri Professor, Dept. of ECE, University of Manitoba
Internal-External Member:	Scott Ormiston Professor, Dept. of Mechanical Engineering, University of Manitoba

Author's Declaration

I hereby declare that I am the sole author of this thesis. This is a true copy of the thesis, including any required final revisions, as accepted by my examiners.

I understand that my thesis may be made electronically available to the public.

Abstract

In this thesis, an efficient wavefield imaging technique of Forward/Backward Time-Stepping (FBTS) in the Time Domain (TD) is developed, employing the Discontinuous Galerkin Method (DGM) as the spatial-discretization technique. The FBTS method is based on calculating gradients of a TD cost functional with respect to the constitutive parameters of the target, and updating the modeled target using Conjugate Gradient (CG) method. The DGM and Runge-Kutta method are used to solve the mentioned problem, respectively, in space and time. We call this TD - Microwave Imaging (MWI) technique DGM-FBTS and present it, for the first time, for dispersive media.

The electromagnetic (EM) two-dimensional non-dispersive Transverse Magnetic (TM) DGM-FBTS is compared to Frequency Domain (FD) imaging algorithms for synthetic and experimental imaging targets in terms of computational cost, the quality of results, and robustness. For the first time, a direct comparison of TD and single-frequency FD MWI, DGM-Contrast Source Inversion (CSI) and DGM-Gauss Newton Inversion (GNI) schemes are used as the FD counterparts, all implemented in Matlab. For experimental data, the DGM-FBTS algorithm shows a robust noise performance, generating higher-resolution results than the two FD methods.

The DGM-FBTS formulation is also modified for quantitative ultrasound imaging with preliminary results presented, as a foundation for future experimental work in this area. This ultrasound imaging technique is validated briefly in this work, and it shows to be promising in quantitative wavefield imaging.

Finally, a novel development and investigation of quantitative hybrid time- and frequency-domain techniques is presented, focusing on enhancing the performance of both FD and TD schemes by improving the inversion speed and image resolution, respectively. These hybrid schemes are tested/validated on experimental data to study their accuracy in the presence of

measurement noise and system modeling error. These results show improvement of image resolution compared to stand-alone FD algorithms (especially for complicated targets) and improvement in computational time by an average of 44% compared to stand-alone TD algorithm.

Contributions

The specific contributions of this work are:

- The development of 2D transverse-magnetic time-domain discontinuous Galerkin method (DGM) forward solver in Matlab[1], including:
  - The electromagnetic version of this forward solver for non-dispersive media,
  - The electromagnetic version of this forward solver for dispersive media,
  - The ultrasound version of this forward solver for non-dispersive media.
- The development of 2D time-domain DGM- Forward-Backward Time-Stepping (FBTS) inversion algorithm in Matlab, including:
  - The electromagnetic version of this inversion algorithm for non-dispersive media,
  - The electromagnetic version of this inversion algorithm for dispersive media,
  - The ultrasound version of this inversion algorithm for non-dispersive media.
- The validation of these inversion algorithms using synthetic and experimental data.
- The first-time comparison of the electromagnetic version of 2D DGM-FBTS with two FD inversion algorithms[2]; DGM-CSI and DGM-GNI, with synthetic and experimental data.
- Presenting and developing hybridization methods using quantitative inversion algorithms of TD DGM-FBTS, FD DGM-CSI and FD DGM-GNI, and showing their significant benefits by testing/evaluating them using synthetic and experimental data.

[1] A Matlab code of the frequency-domain DGM forward solver developed by the previous members of the Electromagnetic Imaging Laboratory (EIL) at University of Manitoba (UofM) was available before this thesis. We benefited from these implementations for the TD implementation of the forward solvers in this thesis.

[2] Implementing the inversion algorithms of DGM-CSI and DGM-GNI is not the subject of this thesis. We use these pre-implemented (by UofM-EIL) inversion algorithms in this thesis for the comparison reason.

Provided below is a list of the outcomes (presentation and published and submitted) works resulting from this research.

1- Forouz M. Saraskanroud, and Ian Jeffrey, "TD Microwave Imaging using a DG Method Forward Solver," *PhotonIcs & Electromagnetics Research Symposium (PIERS)*, June, 2019, Rome, Italy.

2- Forouz M. Saraskanroud, and Ian Jeffrey, "A Comparison of Time-Domain and Frequency-Domain Microwave Imaging of Experimental Targets," in *IEEE Transactions on Computational Imaging,* vol. 7, pp. 611-623, 2021, doi: 10.1109/TCI.2021.3089464.

3- Forouz M. Saraskanroud, and Ian Jeffrey, "Hybrid Approaches in Microwave Imaging using Quantitative TD and FD Algorithms," in *IEEE Transactions on Computational Imaging,* vol. 8, pp. 121-132, 2022, doi: 10.1109/TCI.2022.3146815.

Acknowledgements

I would like to thank my academic advisor, Dr. Ian Jeffrey, for giving me the opportunity to undertake this research.

I extend my gratitude to Natural Sciences and Engineering Research Council of Canada (NSERC), the University of Manitoba GETS program, the Canadian Foundation for Innovation Johns Evans Leader Fund for the Computing infrastructure support. I also thank the Mitacs and 151 Research Inc. for the internship program.

I would also like to express my appreciation for the time taken for reviewing my work by my examining committee members; Dr. Joe LoVetri, Dr. Scott Ormiston, and my external examiner Dr. Milica Popovic.

Finally, to my family and friends, thank you for your continued support and encouragement during this PhD career.

Dedication

I dedicate this thesis to my lovely beautiful mom, Farah, and my dear husband, Behrouz.

Table of Contents

List of Figures

List of Tables

List of Abbreviations

Abbreviations	Description
2D	two-dimensional
3D	Three-dimensional
ABC	Absorbing Boundary Condition
ADE	Auxiliary Differential Equation
CG	Conjugate-Gradient
CO	Calibration Object
CSI	Contrast Source Inversion
DGM	Discontinuous Galerkin Method
EIL	Electromagnetic Imaging Laboratory
EM	electromagnetic
FBTS	Forward-Backward time-stepping
FD	Frequency Domain
FEM	Finite-Element Method
GNI	Gauss Newton Inversion
GSS	Golden Section Search
MC	Metallic Cylinder
MRI	Magnetic Resonance Imaging
MWI	Microwave Imaging
NF	Normalization Factor
ODE	Ordinary Differential Equation
OI	Object of Interest
PDE	Partial Differential Equations
PEC	Perfect Electric Conductor
RMSD	Root Mean Square Deviation

Abbreviations	Description
SD	Steepest Descent
SPI	Successive Parabolic Interpolation
TD	Time Domain
TM	Transverse Magnetic
UofM	University of Manitoba
US	Ultrasound

List of Symbols and Discrete Matrix Operators and Vectors

The following notation is used in this thesis:

- Calligraphic notation is used to denoted time-variant version of fields, e.g. $\vec{\mathcal{E}}(t,\vec{r})$. The time-harmonic version (of fields) are shown with capital letters (non-calligraphic), e.g. $\vec{E}(\vec{r})$,
- Matrix operators defined in this thesis are shown with bold notation, e.g. $\boldsymbol{\mathcal{K}}$,
- Vector-valued parameters in space are denoted using an arrow over uppercase or lowercase non-bold letters, e.g. $\vec{\mathcal{E}}$ and $\vec{r}$,
- All vectors are denoted by underlines, e.g. $\underline{\mathrm{p}}$, while all matrices are shown with two underline signs, e.g. $\underline{\underline{\epsilon_{\infty}}}$,
- The stacked vector form of the vector-valued parameters in space are shown with an underline. For instance the stacked vector form of the electric field $\vec{\mathcal{E}}(t,\vec{r}) = \mathcal{E}_x(t,\vec{r})\ \hat{a}_x + \mathcal{E}_y(t,\vec{r})\ \hat{a}_y + \mathcal{E}_z(t,\vec{r})\ \hat{a}_z$ in three-dimensional space is denoted by $\underline{\mathcal{E}}(t,\vec{r}) = \begin{bmatrix} \mathcal{E}_x(t,\vec{r}) \\ \mathcal{E}_y(t,\vec{r}) \\ \mathcal{E}_z(t,\vec{r}) \end{bmatrix}$,
- ∂_i is the partial derivative operator with respect to parameter i.

Symbols	Description
Ω	Entire computational domain
D	Imaging domain
S	Measurement domain
M	Total number of transmitters
N	Total number of receivers
t	Time
Δt	Time step
T	Final measurement time
$\vec{r}$	Cartesian position vector
j	Imaginary unit: $j = \sqrt{-1}$
$\vec{\mathcal{B}}$	Magnetic flux density
$\vec{\mathcal{D}}$	Electric flux density
$\vec{D}$	Time-harmonic electric flux density
$\vec{\mathcal{E}}$, $\vec{\mathcal{E}}^{inc}$, $\vec{\mathcal{E}}^{sct}$	Total, incident and scattered electric fields
$\vec{E}$, $\vec{E}^{inc}$, $\vec{E}^{sct}$	Time-harmonic total, incident and scattered electric fields
$\vec{\mathcal{H}}$, $\vec{\mathcal{H}}^{inc}$, $\vec{\mathcal{H}}^{sct}$	Total, incident and scattered magnetic fields
$\vec{H}$, $\vec{H}^{inc}$, $\vec{H}^{sct}$	Time-harmonic total, incident and scattered magnetic fields
$\vec{\mathcal{P}}$	Polarization
ε	Permittivity
ε_r	Relative permittivity
$\varepsilon_{r,eff}$	Effective relative permittivity in frequency-domain
ε', ε''	Real and imaginary part of frequency-domain permittivity
ε_0	Free space permittivity
ε_s	Static permittivity
ε_∞	Optical permittivity
μ	Permeability
μ_r	Relative permeability
μ_0	Free space permeability
σ_s	Static conductivity
σ_e	Dispersive media's effective conductivity
σ_a	Alternative polarization-dependant conductivity
τ_r	Debye model relaxation time
τ_{rr}	Relative relaxation time in Debye model
τ_{r0}	Free space relaxation time in Debye model

Symbols	Description
ω	Angular frequency
c^{em}	Speed of electromagnetic wave
c_0	Speed of light in free space
Z^{em}	Impedance of electromagnetic wave
η_0	Electromagnetic intrinsic impedance of free space
$\vec{\mathcal{J}}_c$, $\vec{\mathcal{J}}_E$, $\vec{\mathcal{J}}_M$	Conduction, electric, and magnetic current densities
$\vec{\mathcal{J}}_{c,S}$, $\vec{\mathcal{J}}_{E,S}$, $\vec{\mathcal{J}}_{M,S}$	Surface conduction, surface electric, and surface magnetic current densities
ρ	Electric charge density
ρ_S	Surface charge density
$\mathcal{F}$	Cost functional
$\mathcal{F}'$	Cost functional's Fréchet derivative
$\underline{\eta}_{NF}$	Normalization factor vector
$\underline{p}$	Constitutive parameter vector
$\mathcal{W}$	Weight function (envelope function)
$\underline{\mathcal{R}}$	Weighted data error vector
$\delta(.)$	Dirac delta function
$\underline{\mathcal{G}}$	Gradient vector
N_E	Total number of finite volumes (or elements) in Ω
V_n	nth finite volume in Ω such that $\bigcup_n V_n \approx \Omega$
ℓ	Lagrange interpolating polynomial function
$\underline{\ell}^n$	Lagrange interpolating polynomial for the nth element
ψ	Test function
$\underline{\underline{\mathcal{M}}}$	Element-wise mass (matrix) operator
$\underline{\underline{\mathcal{S}}}$	Element-wise stiffness (matrix) operator
$\underline{\underline{I}}$	Identity matrix
P	Order of nodal coefficients for fields
R	Order of nodal coefficients for constitutive parameters
$\underline{u}$	Field vector
$\underline{v}$	Normalized field vector
$\underline{w}$	Solution to the adjoint operator $\tilde{\mathcal{K}}^*$
$\underline{u}_m^{model}$	Model field vector
$\underline{u}_m^{meas}$	Measured field vector
$\underline{s}$	Source vector
$\underline{\tilde{s}}$	Normalized source vector

Symbols	Description
$\underline{\hat{s}}$	Adjoint (backward-in-time) solver source vector
$h^{\mathcal{X}}$	Search direction for the parameter $\mathcal{X}$
$\gamma^{\mathcal{X}}$	Search direction for the parameter $\mathcal{X}$
Γ	Search distance or search step
V	Volume
ϱ	Fluid mass density
ρ	Average amount of a volume density
ρ_0	Background's average density
ρ_r	Relative average density
ρ_1	Density fluctuations
$\vec{U}$	Ultrasound volume velocity
$\vec{U}_0$	Average amount of a volume velocity
$\vec{u}$	Velocity fluctuations
$P(.)$	Pressure
P_0	Average amount of pressure over a volume
$\mathbb{p}$	Pressure fluctuations
κ'	Compressibility
κ'_0	Background compressibility
κ'_r	Relative compressibility
F^{src}	Ultrasound source force
c^{us}	Speed of ultrasound wave
Z^{us}	impedance of ultrasound wave
$\underline{v}^{us}$	Ultrasound's normalized field vector
$\underline{s}^{us}$	Ultrasound's normalized source vector
$\underline{w}^{us}$	Solution to the Ultrasound's adjoint operator
$S^{tot}(.)$, $S^{sct}(.)$, $S^{inc}(.)$	Total, scattered and incident S-parameters
ζ	Root Mean Square Deviation (RMSD) metric

Matrix Operators	**Description**
∂	Differential operator
$\nabla\times$	Curl operator
$\nabla\cdot$	Divergence operator
∇	Gradient operator
$*$	Convolution operator
$\odot$	Element-wise product of two vectors
$\| \, . \, \|$	Euclidean norm or 2-norm
$\langle ., \, . \rangle$	Inner product operator
T	Transpose operator
$\boldsymbol{\mathcal{K}}$	Forward solver differential operator
$\tilde{\boldsymbol{\mathcal{K}}}$	Normalized forward solver differential operator
$\tilde{\boldsymbol{\mathcal{K}}}^*$	Adjoint operator of $\tilde{\boldsymbol{\mathcal{K}}}$
BlockDiag	Block diagonal operator
$\boldsymbol{\mathcal{V}}^{RP}$	Interpolation operator from order P to order R
$\boldsymbol{\mathcal{K}}^{us}$	Ultrasound's forward solver differential operator
$\boldsymbol{\mathcal{K}}^{*,us}$	Adjoint operator of $\boldsymbol{\mathcal{K}}^{us}$

Chapter 1

Introduction

This thesis presents the development and implementation of a time domain (TD) wavefield imaging algorithm with the primary focus on Microwave Imaging (MWI) while providing an overview of an analogous ultrasound TD algorithm. MWI involves solving microwave electromagnetic (EM) inverse scattering problems, and has been used as an imaging technique in many applications starting with astronomy [4, 5], and biomedical application of cancer detection [6, 7]. Other MWI applications include through-wall imaging [8, 9], medical imaging like stroke and breast cancer detection/classification [10, 11, 12], industrial non-destructive testing [13, 14], and aircraft radars [15].

Generally speaking, MWI techniques are classified to: TD and Frequency Domain (FD) techniques by the reconstruction algorithm's domain/formulation, into quantitative and qualitative techniques by the format of the reconstructed image, and into linear and non-linear methods by the type of mathematical formulation of the inverse problem. Herein we are concerned with non-linear TD quantitative imaging. Specifically, we develop an algorithm referred to as the Discontinuous Galerkin Method - Forward-Backward Time-Stepping algorithm (DGM-FBTS) for the application of near-field imaging, steering toward a specific biomedical application of breast cancer detection.

In this chapter, we briefly review the concepts of MWI and inverse problems. This thesis's motivation and goals are described, and the outline of the thesis is presented afterward.

1.1 MWI

MWI for medical applications has been of particular interest in the last two decades because of its non-invasive diagnostic capabilities, low cost, and safety compared to Magnetic Resonance Imaging (MRI) and X-ray CT [16, 17, 18, 19, 20, 21, 22, 23]. Despite the benefits of MWI compared to today's care standards like MRI and X-ray CTs in medical diagnosis, it has one main drawback. These standards still generate higher resolution images, so that recovering higher resolution images in MWI has been the main goal over the last decades.

MWI techniques usually start with illuminating the object of interest or the unknown object with either monochromatic (FD-MWI) [24, 25, 26, 27, 28, 29] or wide-band EM radiation, e.g. TD-MWI [28, 29, 30, 31], wide-band simultaneous frequency domain imaging or wide-band frequency hopping. A reconstruction algorithm, based on the collected data, is then applied to map the measured scattered signal from the target to an image of the spatial distribution of the object's electrical properties such as permittivity and conductivity. Whether in TD or FD, this mapping procedure minimizes a cost functional, which includes the discrepancy between the measured fields and those produced by a system model with estimated spatial distribution of the object's electrical properties. This cost functional is minimized by either stochastic [32] or deterministic [33] optimization algorithms.

Machine/deep learning techniques in artificial intelligence, simulated annealing, neural networks, and genetic algorithms are some examples of useful stochastic optimization algorithms in MWI with very slow convergence or training session. On the other hand, gradient search methods like Steepest Descent (SD) or Conjugate-Gradient (CG) schemes are examples of deterministic techniques, which usually converge more rapidly to local solutions [34]. All of these techniques can be employed to either FD or TD -based algorithms in MWI. Herein we are concerned with

deterministic gradient-based methods.

1.2 Motivation, Goals and Contributions

1.2.1 The Choice of Conjugate-Gradient based TD Inversion over FD algorithms

The general problem of determining a target's constitutive parameters using measured microwave data is referred to as the microwave inverse scattering problem. One solves the inverse problem using an inverse solver formulated according to one of the possible strategies mentioned in Section 1.1.

Conventional methods of FD monochromatic image reconstruction have occupied the majority of literature in MWI. For these FD methods, both the forward scattering problem (computing electric/magnetic fields by having full knowledge of target's parameter) and inverse scattering problem (estimating target's electric/magnetic parameters from partial knowledge of electric/-magnetic fields outside of the target) are formulated and solved in the FD. The common drawback of all of these techniques is low image resolution due to a lack of information about the target. Lack of information in imaging algorithms usually happens due to using insufficient collected informative data during the measurement process, which is highly effected by the type of imaging algorithm. An insufficient number of transmitter/receiver pairs or measurement frequencies (or poor frequency selection) in the measurement process can result in a lack of information in the measurement data. Imaging at higher frequencies has the potential to produce higher resolution images, but the ill-posedness and non-linearity, which are two obstacles of inverse problems in MWI, are more pronounced at higher frequencies [35, 30]. Obtaining a high-resolution image from a single monochromatic measurement is unlikely.

FD strategies like frequency hopping or simultaneously frequency inversions have been applied in the last two decades to provide higher-resolution images [36]. In these strategies, lower

frequency reconstructions are used as *prior information*[1] for better resolution reconstructions at higher frequencies. In this manner we can avoid having the algorithm get trapped in local minima at higher frequencies. However, using either more frequencies or independent frequency-domain forward models incurs a significant increase in computational cost.

There are a few TD inversion strategies proposed in the literature for inverse scattering problems [35, 30, 31, 37, 38, 39]. TD inversion techniques require TD data which, in general, means that TD methods use more information about the target than FD inversion techniques [31, 1]. As a result, the image resolution and the target's image accuracy are generally higher in TD imaging, which would make one expect that past research has paid significant attention to these MWI techniques. However, the lower per-iteration speed of 2D TD methods (compared to monochromatic 2D FD algorithms) appears to have suppressed interest in TD imaging. This rationale should no longer prevail due to available High-Performance Computing (HPC). Besides, we suspect that TD techniques may be more efficient than FD methods - including simultaneous frequency inversion or frequency hopping techniques - for three-dimensional problems.

Further comparing TD and FD MWI algorithms, monochromatic FD imaging is unable to image *dispersive loss*[2] as TD and multi-frequency FD inversion algorithms do. Almost all dielectrics are dispersive and a dispersive media's constitutive parameters are frequency-dependent. That makes it impossible for a single-frequency FD inversion to distinguish dispersive materials from lossy non-dispersive materials [40]. This frequency dependency may be crucial to model using simultaneous frequency inversion FD imaging technique as the number of unknowns will double (at least) by introducing dispersive models in FD algorithms. Although, it seems that the ill-posedness of FD algorithms is more pronounced when modeling the dispersivity of materials as the dispersive models usually add an auxiliary equation and so more unknowns (fields in forward solver and constitutive parameters in inversion algorithm) to the system, it has been shown that

[1] Any information about the target, e.g., shape, location, or dielectric parameters' initial values, that allows us to initialize the inverse solver with something other than a "blind" image is referred to as *prior information*.

[2] For a detailed description of *dispersive loss*, please refer to Section 2.1.2.

it brings the advantage of providing robust multi-frequency FD inversion techniques [41, 42, 36]. This increases computational costs, and also requires lots of information about target(s) coming from measured data by adding frequencies. Despite the benefits of imaging the dispersivity of materials, and considering that it does not increase the computational costs of TD algorithms, there is a lack of work on TD algorithms in this area.

So, inverse EM scattering using monochromatic data has three significant shortcomings. First, it is almost impossible to have a high-resolution image using just single-frequency data due to the non-linearity and ill-posedness of the MWI optimization problem, unless the number of transmitters/receivers and the non-linearity of the scattering problem (contrast value) were in favor of the used inversion technique (high number of transceivers with low contrast target). Second, choosing a "good" frequency to perform the experiments is tough. According to the literature [43, 44, 45], one can improve resolution using techniques like simultaneous frequency inversions or frequency hopping methods. Still, in FD-MWI, we may struggle to pick proper frequencies, whether in a single- or multi-frequency imaging algorithm [1]. Third, TD and multi-frequency FD algorithms can distinguish dispersive loss from conductive loss. As almost all dielectrics are dispersive to some degree, this gives a distinct advantage to these algorithms, because detecting dispesive loss (as opposed to conductive loss) helps to better distinguish target(s).

So far we argued FD and TD inversion techniques software-wise. Hardware-wise, different data acquisition processes are required for experiments by FD and TD inversion techniques. As FD imaging algorithms typically operate on complex-valued data, the energy interrogation and data collecting part usually use sinusoidal energy, e.g., by a Vector Network Analyzer (VNA). On the other hand, TD imaging algorithms operate on real-valued signals coming directly from a time-domain measurement system, or a broadband VNA-measured data after applying signal processing. Although real-valued signal compared to broadband complex-valued VNA-measured data suffer from low signal-to-noise ratio (SNR) degrading image resolution, there have been lots of strategies in this area studying/boosting the SNR [46, 47, 48, 49, 50].

This thesis focuses on a novel TD-MWI technique, hoping to provide more accurate results than FD-MWI with the ability to image dispersive materials as a frequency-dependency parameter, such that MWI has its rightful place in the medical space in the future. Of course, this accuracy comes with computational costs that can certainly be compensated to some extent by parallelism strategies and HPC. Besides, because of availability, we use broadband VNA-measured data acquisition for all of the experiments in this thesis.

The TD-MWI technique used in this thesis, is formulated using Partial Differential Equation (PDE) conjugate gradient minimization of a cost functional. Comparing TD deterministic optimization algorithms, the iterative PDE-based methods are less time-consuming in comparison with time convolution integral-based algorithms [31]. To this end, the PDE gradient-based method of CG is chosen over the other types in this thesis as the inverse solver.

1.2.2 The Choice of DGM Forward Solver

The general problem of determining the total/scattered EM fields over the measurement domain from knowledge of the target's constitutive parameters is the forward/direct scattering problem. One solves the forward problem numerically using a forward solver by simulating the system model.

Generally speaking, forward solvers are critical components to any imaging problem because, in the majority of imaging technique types, we repeatedly solve the forward problem. Therefore, improving the modeling capabilities of a forward solver implies enhanced imaging capabilities. The DGM forward solver has some significant features. The DGM solver's major benefit is its high flexibility in solving inverse scattering problems due to supporting high-order locally varying polynomial expansions of both the fields and constitutive parameters in each mesh element. The DG model can support any imaging system geometry, boundary condition, and even inhomogeneous background media [51]. Using inhomogeneous backgrounds to represent prior target information can be crucial in the sense of preventing the inversion algorithm from getting stuck

in local minima for high contrast scatterers.

Herein, the DGM forward solver has been chosen to benefit from its significant features along with the advantages of the designated TD inverse algorithm. We have the first time-domain imaging algorithm that uses the time-domain DGM as a forward solver.

1.2.3 Ultrasound Imaging

In addition to solving the TD inverse problem for EM, we can use the same imaging strategy to establish a new way of image detecting in Ultrasound (US). As ultrasounds exhibit similar wave behaviour as in EM, it is straightforward to modify the TD-EM formulation to produce a TD-US inversion method capable of reconstructing the ultrasound properties of a target.

An US equivalent of the EM DGM-FBTS algorithm is included in this work. US is not a focus of this work, but is included to provide a foundation for future studies.

1.2.4 General Contributions

The contributions of this work are:

1) The development of the first high-order time-domain quantitative non-linear algorithm, namely the DGM-FBTS algorithm with CG minimization.

The DGM-FBTS formulation supports dispersive media through the addition of a Debye model included as an auxiliary differential equation.

2) An evaluation of the dispersive DGM-FBTS imaging algorithm compared to its FD counterpart, by using it to reconstruct the spatial distribution of optical and static permittivities as well as the relaxation time of Debye targets.

3) A framework for applying time-domain imaging to broadband measurement data first collected in the frequency domain, i.e., to calibrate experimental data collected from the 2D imaging

hardware in the UofM EIL so that it can be used for time-domain imaging.

4) A comparison between TD and FD methods for intricate synthetical/experimental targets demonstrating the benefits of TD imaging for practical problems by alleviating the needs for frequency selection and in some cases overcoming the need for prior information.

No comparisons of TD and FD imaging algorithms existed in the literature before of publishing [1], as a contribution of this thesis.

5) An equivalent formulation of the solvers for ultrasound, laying a framework for multimodal imaging in the future. Ultrasound imaging and/or multimodal imaging are not the focus of this thesis.

6) The development of two hybrid schemes combining quantitative time- and frequency-domain algorithms for, to the best of my knowledge, the first time. These hybrid formulations improve the performance of standalone time- and frequency-domain algorithms as demonstrated for both synthetic and experimental target data.

1.3 Preview/Scope

This thesis aims to develop theories in three-dimensional (3D) space while all implementations are applied to the two-dimensional (2D) space with a Transverse Magnetic (TM) wave configuration. Improving the TD-FBTS algorithm itself, beyond adopting the DGM forward solver, is not the scope of this work. The thesis lays a foundation for making future contributions to time-domain imaging algorithms.

Two previously implemented frequency domain inverse algorithms, namely DGM-Contrast Source Inversion (CSI) and DGM-Gauss Newton Inversion (GNI) have been employed in this

work. Previous UofM-EIL members have developed these solvers, and they are great tools used for comparing the TD tools developed herein. The details of the mentioned FD methods have been omitted from this report because their developments were not part of this work. Interested readers are referred to the EIL literature for more details about these two algorithms [52, 51].

The remainder of the thesis is presented as follows:

- The fundamentals of the inverse problem are presented in Chapter 2. This Chapter also goes through Maxwell's equations and gives a general perspective about MWI.
- Chapter 3 reviews the continuous form of the FBTS imaging algorithm for both dispersive and non-dispersive media.
- We follow the method-of-lines approach in this work, and take care of the space- and time-discretizations separately. Chapter 4 presents the DGM spatial-discretization of the MWI problem followed by applying general boundary conditions to the problem, highlighting the DGM discretization scheme's benefits.
- Next, focusing on the time-dependence of the differential equations, time-integrating for the forward solver fields is discussed in Chapter 5. The chapter leads to solving the forward problem using a few implicit/explicit time-stepping strategies.
- Chapter 6 goes into the details of the inverse solver implementation used in this work. We briefly talk about the CG algorithm and the details necessary to implement it. The chapter includes details of how the DGM discretization is used to discretize the continuous FBTS formulation.
- Chapter 7 formulates DGM-FBTS to ultrasound problems.
- Chapter 8 discusses the hardware setup(s) and data calibration followed by the implementations' results when applied to both synthetic targets and experimental targets.

- Finally, Chapter 9 introduces the first quantitative hybrid schemes by TD DGM-FBTS and FD DGM-CSI/GNI algorithms.

- The thesis concludes in Chapter 10, where the work is summarized, conclusions are drawn, and some thoughts for prospective future achievements are proposed.

Chapter 2

Electromagnetic Fundamentals and Maxwell's Equations

This chapter presents Maxwell's equations and formulates the electromagnetic scattering problem.

2.1 Maxwell's Equations

In this section, we first review the basic Maxwell's equations for non-dispersive media and then augment these Partial Differential Equations (PDEs) for the general case of dispersive media.

2.1.1 Non-dispersive media

The general form of Maxwell's curl equations for macroscopic electromagnetic field behavior in the TD are given by the following coupled PDEs as a function of location $\vec{r}$ in 3D space and time t:

$$\partial_t \vec{\mathcal{D}}(t,\vec{r}) - \nabla \times \vec{\mathcal{H}}(t,\vec{r}) + \vec{\mathcal{J}}_c(t,\vec{r}) = -\vec{\mathcal{J}}_E(t,\vec{r}) \tag{2.1a}$$

$$\partial_t \vec{\mathcal{B}}(t,\vec{r}) + \nabla \times \vec{\mathcal{E}}(t,\vec{r}) = -\vec{\mathcal{J}}_M(t,\vec{r}) \tag{2.1b}$$

where $\vec{\mathcal{D}}$ [C/m^2] and $\vec{\mathcal{B}}$ [Wb/m^2] are the electric and magnetic flux densities and $\vec{\mathcal{J}}_E$ [A/m^2] and $\vec{\mathcal{J}}_M$ [V/m^2] are the electric and magnetic current densities, respectively. $\vec{\mathcal{E}}$ [V/m] and $\vec{\mathcal{H}}$ [A/m] are the electric field (intensity) and magnetic field (intensity). $\vec{\mathcal{J}}_c$ [A/m^2] is the conduction current density. The physical medium is characterized by the constitutive parameters of permittivity ε [F/m], permeability μ [H/m] and (static) conductivity σ_s [S/m]. Equations (2.1a) and (2.1b) are commonly called Ampére's and Faraday's laws, respectively.

Microwave imaging is commonly performed at low field strengths and applied to simple isotropic materials (or to materials that can be well-approximated as such). Consequently, if we restrict consideration to a linear constitutive relationship for a stationary, isotropic, non-dispersive medium, then:

$$\vec{\mathcal{J}}_c(t,\vec{r}) = \sigma_s(\vec{r})\vec{\mathcal{E}}(t,\vec{r}) \tag{2.2a}$$

$$\vec{\mathcal{D}}(t,\vec{r}) = \varepsilon(\vec{r})\vec{\mathcal{E}}(t,\vec{r}) \tag{2.2b}$$

$$\vec{\mathcal{B}}(t,\vec{r}) = \mu(\vec{r})\vec{\mathcal{H}}(t,\vec{r}) \tag{2.2c}$$

where $\varepsilon(\vec{r}) = \varepsilon_0\varepsilon_r(\vec{r})$ and $\mu(\vec{r}) = \mu_0\mu_r(\vec{r})$, or $\varepsilon(\vec{r}) = \varepsilon_0(1+\chi(\vec{r}))$ and $\mu(\vec{r}) = \mu_0(1+\chi_m(\vec{r}))$. ε_r and μ_r are the relative permittivity and permeability and $\varepsilon_0 = 8.85\times10^{-12}$ [F/m] and $\mu_0 = 4\pi\times10^7$ [H/m] are the permittivity and permeability of free space (vacuum). χ and χ_m are the electric and magnetic susceptibilities, which are the measures of electric and magnetic polarization properties of materials, respectively. For instance, the quantity $\vec{\mathcal{P}}(t,\vec{r}) = \varepsilon_0\chi(\vec{r})\vec{\mathcal{E}}(t,\vec{r})$ represents the average electric dipole moment per unit volume and $\vec{\mathcal{P}}$ [C/m^2] is called dielectric polarization density or simply polarization. Similarly, $\vec{\mathcal{M}}(t,\vec{r}) = \chi_m(\vec{r})\vec{\mathcal{H}}(t,\vec{r})$ represents the average quantity of magnetic moment per unit volume and $\vec{\mathcal{M}}$ [A/m] is called magnetization.

Using the auxiliary equations (2.2), Maxwells' curl equations reduce to 6 equations in 6 unknowns in 3D space, assuming the constitutive parameters are known. Specifically, Maxwell's

curl equations in non-dispersive media are:

$$\varepsilon_0\varepsilon_r(\vec{r})\partial_t\vec{\mathcal{E}}(t,\vec{r}) - \nabla\times\vec{\mathcal{H}}(t,\vec{r}) + \sigma_s(\vec{r})\vec{E}(t,\vec{r}) = -\vec{\mathcal{J}}_E(t,\vec{r}) \tag{2.3a}$$

$$\mu_0\mu_r(\vec{r})\partial_t\vec{\mathcal{H}}(t,\vec{r}) + \nabla\times\vec{\mathcal{E}}(t,\vec{r}) = -\vec{\mathcal{J}}_M(t,\vec{r}) \tag{2.3b}$$

For simplicity, we introduce the differential operator $\boldsymbol{\mathcal{K}}$, field vector $\underline{u}$ and source[1] vector $\underline{s}$:

$$\boldsymbol{\mathcal{K}} = \begin{bmatrix} \varepsilon\partial_t + \sigma_s & -\nabla\times \\ \nabla\times & \mu\partial_t \end{bmatrix}, \qquad \underline{u} = \begin{bmatrix} \vec{\mathcal{E}} \\ \vec{\mathcal{H}} \end{bmatrix}, \qquad \underline{s} = \begin{bmatrix} \vec{\mathcal{J}}_E \\ \vec{\mathcal{J}}_M \end{bmatrix}. \tag{2.4}$$

Then Maxwell's equations can be succinctly written as

$$\boldsymbol{\mathcal{K}}\underline{u} = -\underline{s}. \tag{2.5}$$

In the following section we rewrite (2.5) for the linear, isotropic, temporally dispersive dielectric materials, with neither time-varying magnetic susceptibility and nor magnetoelectric coupling.

2.1.2 Dispersive media

At the presence of time-varying electric field, the polarization response of materials can not be instantaneous and this dynamic response is described by the convolutional constitutive relationship:

$$\vec{\mathcal{D}}(t,\vec{r}) = \int_{-\infty}^{t} \varepsilon_0\varepsilon_r(t-t',\vec{r})\ \vec{\mathcal{E}}(t',\vec{r})\ dt', \tag{2.6}$$

or by using the convolution operator $*$, $\vec{\mathcal{D}}(t,\vec{r}) = \varepsilon(t,\vec{r}) * \vec{\mathcal{E}}(t,\vec{r})$. These materials with this dielectric mamory are called dispersive [53, 54]. The relative permittivity in (2.6) contains of two optical and dispersive parts:

$$\varepsilon_r(t,\vec{r}) = \varepsilon_\infty(\vec{r}) + \chi(t,\vec{r}), \tag{2.7}$$

[1]The charge and current densities ρ, $\mathcal{J}$ are usually taken (thought of) as the *sources* of the electromagnetic fields, and they are localized in space for wave propagation problems, e. g., flowing these densities on an antenna.

where $\varepsilon_\infty \geq 1$ is the instantaneous or optical permittivity and χ here is the time-dependant susceptibility kernel, describing the dispersive part.

In the frequency domain, the convolutional constitutive relation (2.6) appears as a simple multiplication, and at a single radial frequency ω becomes:

$$\vec{D}(\omega, \vec{r}) = \varepsilon_0 \varepsilon_r(\omega, \vec{r}) \vec{E}(\omega, \vec{r}), \tag{2.8}$$

where $\vec{D}$ [C/m^2] and $\vec{E}$ [V/m] are the time-harmonic forms of the electric flux density and electric field. So the dispersive materials are usually distinguished by their frequency dependent (i.e., dispersion) constitutive parameters[2] [55].

All materials are in fact electromagnetically dispersive. Although, in some cases, e.g. metals, the loss is dominantly the result of the static conductivity, called conduction loss. We neglect the dipole motions, which are the cause of dispersivity, in these materials when dealing with the electromagnetic equations. On the other hand, in dielectrics (non-metallic materials), e.g. human body tissues, the polarization-dependant term usually dominates the static conductivity [56]. This fact is usually neglected in FD microwave imaging modalities, as this dispersivity is frequency-dependent and the resulting loss is hard to distinguish from conduction loss. In these FD modalities, we image both types of loss by the complex permittivity $\varepsilon(\omega, \vec{r}) = \varepsilon'(\omega, \vec{r}) + j\varepsilon''(\omega, \vec{r})$. Note that in all of the time-harmonic equations in this thesis, a dependence of $e^{j\omega t}$ is suppressed, where $j = \sqrt{-1}$.

Therefore, the dispersive media's effective conductivity σ_e [S/m] in a general microwave imaging scenario comes from both the electron collisions, which introduces the static conductivity σ_s [S/m] and the dipole motions, making the polarization-dependant conductivity σ_a [S/m] due

[2]Note that the primary mechanism that determines the medium's frequency despersion is its time domain response.

to an alternating field:

$$\sigma_e = \sigma_s + \sigma_a. \tag{2.9}$$

There are many methods in the literature modeling the material dispersion by either convolution integral or differential equation, including Debye, Cole-Cole and Lorentz models [57, 58, 59, 60, 61, 62, 54, 63, 64].

According to Lazebnik et al. in [65], the single-pole Debye model provides an accurate representation of the frequency-dependent behavior of the constitutive parameters in the biomedical application of breast cancer detection at microwave frequencies. So, we use the Debye model in this work and in the following we show that it is a reasonable model for the targets considered here, too. The relation to model the dispersive behaviour of the time-harmonic (complex) relative permittivity, ε_r, of the materials is[3]:

$$\varepsilon_r(\omega, \vec{r}) = \varepsilon_\infty(\vec{r}) + \frac{\Delta\varepsilon_r(\vec{r})}{1 + j\omega\tau_r(\vec{r})} \tag{2.10}$$

where $\Delta\varepsilon_r(\vec{r}) = \varepsilon_s(\vec{r}) - \varepsilon_\infty(\vec{r})$ is a positive quantity, ε_∞, ε_s and τ_r [s] are the relative optical permittivity, relative static permittivity and the relaxation time, respectively.

By substituting (2.10) in (2.8), we obtain:

$$\vec{D}(\omega, \vec{r})\ (1 + j\omega\tau_r(\vec{r})) = \varepsilon_0\varepsilon_\infty(\vec{r})\vec{E}(\omega, \vec{r})\ (1 + j\omega\tau_r(\vec{r})) + \varepsilon_0\Delta\varepsilon_r(\vec{r})\ \vec{E}(\omega, \vec{r}). \tag{2.11}$$

By transforming (2.11) from the phasor domain to the TD, we obtain:

$$\vec{\mathcal{D}}(t, \vec{r}) + \tau_r(\vec{r})\ \partial_t\vec{\mathcal{D}}(t, \vec{r}) = \varepsilon_0\varepsilon_\infty(\vec{r})\tau_r(\vec{r})\ \partial_t\vec{\mathcal{E}}(t, \vec{r}) + \varepsilon_0\varepsilon_s(\vec{r})\ \vec{\mathcal{E}}(t, \vec{r}). \tag{2.12}$$

Equation (2.12) is called the TD Auxiliary Differential Equation (ADE) [54] for the electric flux

[3] In the case of using other models, the formulation would differ from this point onwards. For instance, in the case of using Cole-Cole model, $\varepsilon_r(\omega, \vec{r}) = \varepsilon_\infty(\vec{r}) + \frac{\Delta\varepsilon_r(\vec{r})}{1+(j\omega\tau_r(\vec{r}))^\alpha}$, where $0 < \alpha < 1$ [66].

density in dispesive media, as it relates the electric flux to the electric field, to solve the Maxwell's curl equation.

An alternative form of the ADE due to the polarization $\vec{\mathcal{P}}$ using:

$$\vec{\mathcal{D}}(t,\vec{r}) = \varepsilon_0\varepsilon_\infty(\vec{r})\vec{\mathcal{E}}(t,\vec{r}) + \vec{\mathcal{P}}(t,\vec{r}), \tag{2.13}$$

after rewriting it based on polarization and electric fields, is[4] [54]:

$$\vec{\mathcal{P}}(t,\vec{r}) + \tau_r(\vec{r})\ \partial_t\vec{\mathcal{P}}(t,\vec{r}) = \varepsilon_0\ \Delta\varepsilon_r(\vec{r})\ \vec{\mathcal{E}}(t,\vec{r}). \tag{2.14}$$

From (2.1), (2.13), and the ADE (2.14), the augmented Maxwell's equations for the dispersive media in TD are given by the PDEs:

$$\varepsilon_0\varepsilon_\infty(\vec{r})\ \partial_t\vec{\mathcal{E}}(t,\vec{r}) - \nabla\times\vec{\mathcal{H}}(t,\vec{r}) + \sigma_s(\vec{r})\ \vec{\mathcal{E}}(t,\vec{r}) + \partial_t\vec{\mathcal{P}}(t,\vec{r}) = -\vec{\mathcal{J}}_E(t,\vec{r}) \tag{2.15a}$$

$$\mu_0\mu_r(\vec{r})\ \partial_t\vec{\mathcal{H}}(t,\vec{r}) + \nabla\times\vec{\mathcal{E}}(t,\vec{r}) = -\vec{\mathcal{J}}_M(t,\vec{r}) \tag{2.15b}$$

$$\partial_t\vec{\mathcal{P}}(t,\vec{r}) - \frac{\varepsilon_0\Delta\varepsilon(\vec{r})}{\tau_r(\vec{r})}\ \vec{\mathcal{E}}(t,\vec{r}) + \frac{1}{\tau_r(\vec{r})}\ \vec{\mathcal{P}}(t,\vec{r}) = 0. \tag{2.15c}$$

With the goal of removing the time-derivative of $\vec{\mathcal{P}}$ from equation (2.15a), we substitute the equation (2.15c) into (2.15a). Adopting the notation used in [54], we introduce the quantities α,

[4] In the case of using Cole-Cole model, this formulation would be replaced by $\vec{\mathcal{P}}(t,\vec{r}) + (\tau_r(\vec{r}))^\alpha\ \frac{\partial^\alpha\vec{\mathcal{P}}(t,\vec{r})}{\partial t^\alpha} = \varepsilon_0\ \Delta\varepsilon_r(\vec{r})\ \vec{\mathcal{E}}(t,\vec{r})$. Here $\frac{\partial^\alpha\vec{\mathcal{P}}(t,\vec{r})}{\partial t^\alpha}$ is the Letnikov fractional derivative represented by $\frac{\partial^\alpha\vec{\mathcal{P}}(t,\vec{r})}{\partial t^\alpha} = \frac{1}{\Gamma(1-\alpha)}\frac{d}{dt}\int_0^t(t-s)^{-\alpha}\vec{\mathcal{P}}(s,\vec{r})\ ds$, [66].

β and f_r as follows for simplicity:

$$\beta(\vec{r}) \triangleq \frac{\varepsilon_0 \Delta\varepsilon_r(\vec{r})}{\tau_r(\vec{r})} \tag{2.16a}$$

$$\alpha(\vec{r}) \triangleq \beta(\vec{r}) + \sigma_s(\vec{r}) \tag{2.16b}$$

$$f_r(\vec{r}) \triangleq \frac{1}{\tau_r(\vec{r})}. \tag{2.16c}$$

Then, the augmented Maxwell's equations can be simplified to

$$\varepsilon_0\varepsilon_\infty(\vec{r})\ \partial_t\vec{\mathcal{E}}(t,\vec{r}) - \nabla\times\vec{\mathcal{H}}(t,\vec{r}) + \alpha(\vec{r})\ \vec{\mathcal{E}}(t,\vec{r}) - f_r(\vec{r})\vec{\mathcal{P}}(t,\vec{r}) = -\vec{\mathcal{J}}_E(t,\vec{r}) \tag{2.17a}$$

$$\mu_0\mu_r(\vec{r})\ \partial_t\vec{\mathcal{H}}(t,\vec{r}) + \nabla\times\vec{\mathcal{E}}(t,\vec{r}) = -\vec{\mathcal{J}}_M(t,\vec{r}) \tag{2.17b}$$

$$\partial_t\vec{\mathcal{P}}(t,\vec{r}) - \beta(\vec{r})\ \vec{\mathcal{E}}(t,\vec{r}) + f_r(\vec{r})\ \vec{\mathcal{P}}(t,\vec{r}) = 0. \tag{2.17c}$$

Like the previous section, we rewrite the augmented Maxwell's equations by the defined differential operator $\boldsymbol{\mathcal{K}}^d$ and field vectors $\underline{u}^d$ as

$$\boldsymbol{\mathcal{K}}^d\underline{u}^d = -\underline{s}^d \tag{2.18}$$

for simplicity, where the superscript d indicates the dispersive case:

$$\boldsymbol{\mathcal{K}}^d = \begin{bmatrix} \varepsilon_0\varepsilon_\infty\partial_t + \alpha & -\nabla\times & -f_r \\ \nabla\times & \mu_0\mu_r\partial_t & \emptyset \\ -\beta & \emptyset & \partial_t + f_r \end{bmatrix}, \qquad \underline{u}^d = \begin{bmatrix} \vec{\mathcal{E}} \\ \vec{\mathcal{H}} \\ \vec{\mathcal{P}} \end{bmatrix}, \qquad \underline{s}^d = \begin{bmatrix} \vec{\mathcal{J}}_E \\ \vec{\mathcal{J}}_M \\ \emptyset \end{bmatrix}. \tag{2.19}$$

It is important to note that the non-dispersive equations (2.5) are a special case of (2.18) when $\Delta\varepsilon_r \to 0$ or $\beta \to 0$ and so the response of $\vec{\mathcal{P}}$ from the auxiliary equation (2.17c) goes to zero. Both sets of equations of (2.5) for non-dispersive media and (2.18) for dispersive media are essential in illustrating the required formulations to solve the forward electromagnetic problem.

The forward problem approximates the fields resulting from known sources in a known media (with known constitutive parameters). We use forward solvers to compute field approximation(s) associated with estimates of the target's constitutive parameters when solving inverse problems.

2.1.3 2D TM Problems

The focus of this thesis has been on implementing two-dimensional transverse magnetic (2D-TM) codes. In this and subsequent chapters, theory is developed for 3D physics. At the end of each chapter we explicitly talk about the restriction to the 2D-TM case.

If we assume that all targets and sources are invariant in one direction, we can benefit from two-dimensional (2D) imaging. In this case, rates of change along the length of the targets (which we assume is the z-direction) are assumed to be 0; $\vec{\mathcal{E}}(x,y,z) = \vec{\mathcal{E}}(x,y)$, $\vec{\mathcal{H}}(x,y,z) = \vec{\mathcal{H}}(x,y)$, and $\vec{\mathcal{P}}(x,y,z) = \vec{\mathcal{P}}(x,y)$. Consequently, the curl equations (2.17) decouple into two sets of equations: one involves $\mathcal{E}_z$, $\mathcal{H}_x$, $\mathcal{H}_y$, $\mathcal{P}_z$ and $\mathcal{J}_{Ez}$, and the other involves $\mathcal{E}_x$, $\mathcal{E}_y$, $\mathcal{H}_z$, $\mathcal{P}_x$, $\mathcal{P}_y$ and $\mathcal{J}_{Ex}$, $\mathcal{J}_{Ey}$. The first set of PDEs represents the Transverse Magnetic or TM polarization involving a single electric field component in the z-direction ($\mathcal{E}_x = \mathcal{E}_y = 0$ & $\mathcal{H}_z = 0$) and the second set of PDEs represents the Transverse Electric or TE polarization which contains a single magnetic field component in the z-direction ($\mathcal{H}_x = \mathcal{H}_y = 0$ & $\mathcal{E}_z = 0$). Therefore, if we only electrically source $\mathcal{J}_{Ez}$ then the TM polarization waves are provoked and if we only electrically source $\mathcal{J}_{Ex}$ or $\mathcal{J}_{Ey}$ then the TE polarization waves are produced.

For the specific case of 2D TM electromagnetic scattering problem, when the electric field and electric current density are in the z-direction in the rectangular coordinate system, the propagation of the TM wave would be in the $x-y$ plane, so $\mathcal{E}_x = \mathcal{E}_y = \mathcal{H}_z = 0$ and consequently $\mathcal{P}_x = \mathcal{P}_y = 0$. The original PDE system of (2.18), which contains nine equations, reduces to a

system of PDEs with just four equations:

$$\boldsymbol{\mathcal{K}}^d = \begin{bmatrix} \varepsilon_0\varepsilon_\infty\partial_t + \alpha & \partial_y & -\partial_x & -f_r \\ \partial_y & \mu_0\mu_r\partial_t & 0 & 0 \\ -\partial_x & 0 & \mu_0\mu_r\partial_t & 0 \\ -\beta & 0 & 0 & \partial_t - f_r \end{bmatrix}, \qquad \underline{u}^d = \begin{bmatrix} \mathcal{E}_z \\ \mathcal{H}_x \\ \mathcal{H}_y \\ \mathcal{P}_z \end{bmatrix}, \qquad \underline{s}^d = \begin{bmatrix} \mathcal{J}_{Ez} \\ \mathcal{J}_{Mx} \\ \mathcal{J}_{My} \\ 0 \end{bmatrix}. \quad (2.20)$$

For synthetic and experimental problems we limit problem configurations to be TM configurations.

2.2 Physical Boundary Conditions

Generally speaking, what makes an electromagnetic forward problem presented by Maxwell's equations uniquely solvable, like any system of PDEs, is the problem's boundary conditions. At a material interface (material discontinuity), certain rules about the behaviour of the fields, crossing the interface, exist. We use those rules, called boundary conditions, in addition to initial conditions discussed in the next chapter, to solve the forward problem uniquely.

Here in this section, we first present the most typical case of dielectric interface boundary condition, and then we discuss the particular case of a perfect electric conductor [67].

2.2.1 Dielectric Interfaces

Consider the shared interface of two mediums 1 and 2. We show the characteristic parameters of mediums with subindices 1 and 2. The tangential and normal fields at the interface must satisfy boundary conditions as a result of Poisson's equation:

$$\nabla \cdot \vec{\mathcal{D}}(t, \vec{r}) = \rho(t, \vec{r}) \quad (2.21)$$

and the condition of solenoidal magnetic flux density:

$$\nabla \cdot \vec{\mathcal{B}}(t, \vec{r}) = 0. \tag{2.22}$$

where ρ [C/m^3] is the electric charge density.

Gauss's Theorem

Suppose volume V enclosed by surface ∂V. If $\vec{F}$ is a continuously differentiable vector field defined on V, then according to the Gauss's theorem:

$$\iiint_V \nabla \cdot \vec{F} \; dv = \oiint_{\partial V} \vec{F} \cdot \vec{n} \; ds \tag{2.23}$$

where $\vec{n}$ is the outward pointing unit normal vector at surface ∂V.

Applying Gauss's theorem to the Poisson's equation (2.21) and the condition of solenoidal magnetic flux density (2.22), two boundary conditions are:

$$\vec{n} \cdot [\vec{\mathcal{B}}_2(t, \vec{r}) - \vec{\mathcal{B}}_1(t, \vec{r})] = 0, \tag{2.24a}$$

$$\vec{n} \cdot [\vec{\mathcal{D}}_2(t, \vec{r}) - \vec{\mathcal{D}}_1(t, \vec{r})] = \rho_S(t, \vec{r}), \tag{2.24b}$$

where ρ_S is the surface charge density on the shared interface.

Stokes's Theorem

Suppose S is a surface enclosed by the curve ∂S. If the vector field $\vec{F}$ over the surface S has continuous first order partial derivatives in this region, then according to the Stokes's theorem:

$$\iint_S (\nabla \times \vec{F}) \cdot ds = \oint_{\partial S} \vec{F} \cdot dl. \tag{2.25}$$

Using the same analogy and applying the Stokes's theorem to the integrals of the Ampere's law (2.1a) and Faraday's law (2.1b), we can find two more constraints for the fields as boundary conditions:

$$\vec{n} \times [\vec{\mathcal{H}}_2(t, \vec{r}) - \vec{\mathcal{H}}_1(t, \vec{r})] = \vec{\mathcal{J}}_{E,S}(t, \vec{r}) + \vec{\mathcal{J}}_{c,S}(t, \vec{r}), \tag{2.26a}$$

$$\vec{n} \times [\vec{\mathcal{E}}_2(t, \vec{r}) - \vec{\mathcal{E}}_1(t, \vec{r})] = -\vec{\mathcal{J}}_{M,S}(t, \vec{r}). \tag{2.26b}$$

where $\vec{\mathcal{J}}_{E,S}$, $\vec{\mathcal{J}}_{M,S}$ and $\vec{\mathcal{J}}_{c,S}$ are electric, magnetic and conduction surface current densities, respectively on the surface S. Continuity of the tangential electric field and magnetic field at the shared interface between the two medium in the absence of the current densities can be interpreted from these results.

In summary, the dielectric boundary conditions are given by (2.24) and (2.26) which specify the change in normal and tangential field components across dielectric interfaces. Note that these boundary conditions hold for both non-dispersive and dispersive media.

2.2.2 Perfect Electric Conductors (PEC)

There is no electric field and consequently, no electric displacement penetrating inside a perfect electric conductor. If we take the first medium as the PEC media, then:

$$\vec{n} \cdot \vec{\mathcal{D}}_2(t, \vec{r}) = \rho_S(t, \vec{r}) \tag{2.27a}$$

$$\vec{n} \times \vec{\mathcal{E}}_2(t, \vec{r}) = -\vec{\mathcal{J}}_{M,S}(t, \vec{r}). \tag{2.27b}$$

Also, according to Faraday's law, magnetic flux density (and consequently magnetic field) inside a PEC is zero:

$$\vec{n} \cdot \vec{\mathcal{B}}_2(t, \vec{r}) = 0, \tag{2.28a}$$

$$\vec{n} \times \vec{\mathcal{H}}_2(t, \vec{r}) = \vec{\mathcal{J}}_{E,S}(t, \vec{r}) + \vec{\mathcal{J}}_{c,S}(t, \vec{r}). \tag{2.28b}$$

2.3 General Perspective of TD-MWI

This section reviews the general concept of a simple MWI system's hardware/software in a general form with dispersive media. Here, we use the same set of antennas as both transmitters and receivers i.e., collocated transceivers.

A general imaging system is shown in Figure 2.1. An unknown target or Object of Interest (OI) located inside the imaging domain D is successively illuminated by M transmitters surrounding the object, outside of D. For each illumination, measurements of the electric ($\vec{\mathcal{E}}$) or magnetic ($\vec{\mathcal{H}}$) field(s) (or both) are collected by N receivers[5] defining the measurement domain or measurement surface S. Measuring the polarization vector $\vec{\mathcal{P}}$ is not required/practical because it is numerically calculated from the measured electric field and the known constitutive parameters on S external to D by the auxiliary equation of (2.17c). Although it is not measured, we still refer to it as $\vec{\mathcal{P}}^{meas}$ in this thesis.

[5] In a co-resident system, N is at most M.

We consider the entire system, either the physical system or computational model, to reside inside a bounded region Ω, which usually determines the boundary conditions (e.g. metallic boundary or an absorbing condition).

Consider that in practice there is a need to install different types of antennas for measuring various fields (electric or magnetic) with different polarizations. Using transceivers, the measurement error due to the antennas' coupling effect reduces because of fewer and more distant antennas.

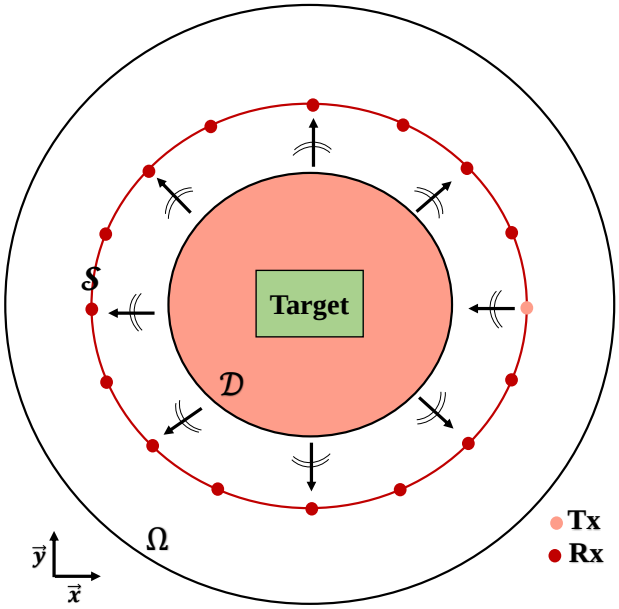

Figure 2.1: A general imaging system. Ω, D and S are the entire computational domain, the imaging and the measurements domains, respectively.

To reproduce the properties of the target from field measurements, we first construct an objective function that relates the measured fields to fields produced by a model estimate of the target parameters. The cost functional $\mathcal{F}(\underline{p})$ considered here, following the notation used in [31], is:

$$\mathcal{F}(\underline{p}) = \int_0^T \sum_{m=1}^{M} \sum_{n=1}^{N} \mathcal{W}_m(t) \ \| \ \underline{\eta}_{NF}(\vec{r}_n) \ \odot \ \left[\underline{u}_m^{model}(\underline{p}, t, \vec{r}_n) - \underline{u}_m^{meas}(t, \vec{r}_n) \right] \|^2 \, dt, \tag{2.29}$$

where T is the final time ($t = 0...T$) of the measurements. $\underline{\eta}_{NF}$ is the stacked Normalization Factor (NF), and $\underline{u}_m^{model}$ and $\underline{u}_m^{meas}$ are the model field vector and the measured field vector, respectively. The target properties are represented by $\underline{p}$, the constitutive parameter vector. The symbol $\odot$ denotes the element-wise product of two vectors and $\| \ . \ \|$ is the Euclidean norm or 2-norm. Here, $\mathcal{W}_m(t)$ is a user-defined non-negative weight function (envelope function) applying zero initial conditions (a requirement that is needed by the algorithm as discussed in Appendix A). We can rewrite the cost functional definition in (2.29) using the weighted data error vector $\underline{\mathcal{R}}_m(\underline{p}, t, \vec{r}_n)$ described by:

$$\underline{\mathcal{R}}_m(\underline{p}, t, \vec{r}_n) = \mathcal{W}_m(t) \ \underline{\eta}_{NF}(\vec{r}_n) \ \odot \ \left[\underline{u}_m^{model}(\underline{p}, t, \vec{r}_n) - \underline{u}_m^{meas}(t, \vec{r}_n) \right], \tag{2.30}$$

as:

$$\mathcal{F}(\underline{p}) = \int_0^T \sum_{m=1}^{M} \sum_{n=1}^{N} \frac{1}{\mathcal{W}_m(t)} \ \| \ \underline{\mathcal{R}}_m(\underline{p}, t, \vec{r}_n) \right] \|^2 \, dt. \tag{2.31}$$

In brief, the equation (2.31) quantifies the error in the measured and modelled fields for a given estimate of the target properties $\underline{p}$.

The goal of an imaging algorithm is to reconstruct accurate estimates of $\underline{p}$ by minimizing (2.31) given knowledge of the measured fields.

What follows provides the remaining details of the cost-functional.

The spatial-dependant NF vector $\underline{\eta}_{NF}$ is required to ensure that each differential equation

contributes more-or-less equally to the cost functional:

$$\underline{\eta}_{NF}(\vec{r}) = \begin{bmatrix} \underline{\eta}_E(\vec{r}) \\ \underline{\eta}_H(\vec{r}) \\ \underline{\eta}_P(\vec{r}) \end{bmatrix}. \tag{2.32}$$

The modelled fields vector $\underline{u}_m^{model}(\underline{p}, t, \vec{r}_n)$, which is a function of the estimated target constitutive parameters vector $\underline{p}$, and the measured fields vector $\underline{u}_m^{meas}(t, \vec{r}_n)$ due to the source m at the receiver location $\vec{r}_n$, for dispersive media are:

$$\underline{u}_m^{d,model}(\underline{p}, t, \vec{r}) = \begin{bmatrix} \underline{\mathcal{E}}_m^{model}(\underline{p}, t, \vec{r}) \\ \underline{\mathcal{H}}_m^{model}(\underline{p}, t, \vec{r}) \\ \underline{\mathcal{P}}_m^{model}(\underline{p}, t, \vec{r}) \end{bmatrix}, \qquad \underline{u}_m^{d,meas}(t, \vec{r}_n) = \begin{bmatrix} \underline{\mathcal{E}}_m^{meas}(t, \vec{r}_n) \\ \underline{\mathcal{H}}_m^{meas}(t, \vec{r}_n) \\ \underline{\mathcal{P}}_m^{meas}(t, \vec{r}_n) \end{bmatrix}, \tag{2.33}$$

where the constitutive parameters vector $\underline{p}$ is:

$$\underline{p} = \begin{bmatrix} \varepsilon_\infty(\vec{r}) \\ \Delta\varepsilon_r(\vec{r}) \\ \mu_r(\vec{r}) \\ \sigma_s(\vec{r}) \\ \tau_{rr}(\vec{r}) \end{bmatrix}. \tag{2.34}$$

We, again in the case of dispersive imaging, assume that the relaxation time is the product of the free space relaxation time τ_{r0}, which is a constant, and the relative relaxation time $\tau_{rr}(\vec{r})$:

$$\tau_r(\vec{r}) \triangleq \tau_{r0}\ \tau_{rr}(\vec{r}) \qquad \text{or} \qquad f_r(\vec{r}) = f_{r0}\ f_{rr}(\vec{r}). \tag{2.35}$$

This kind of definition is similar to the permittivity and permeability definitions of $\varepsilon = \varepsilon_0\varepsilon_r$ and $\mu = \mu_0\mu_r$ and it is necessary for the purpose of balancing/normalizing the functions comprising $\underline{p}$.

Note that as mentioned in the list of symbols, all of the vector functions like the electric field $\vec{\mathcal{E}}(t,\vec{r}) = \mathcal{E}_x(t,\vec{r})\ \hat{a}_x + \mathcal{E}_y(t,\vec{r})\ \hat{a}_y + \mathcal{E}_z(t,\vec{r})\ \hat{a}_z$ are shown in the form of a stacked vector $\underline{\mathcal{E}}(t,\vec{r})$ by the following definition:

$$\underline{\mathcal{E}}(t,\vec{r}) = \begin{bmatrix} \mathcal{E}_x(t,\vec{r}) \\ \mathcal{E}_y(t,\vec{r}) \\ \mathcal{E}_z(t,\vec{r}) \end{bmatrix}. \tag{2.36}$$

As a part of MWI with the DGM-FBTS method, we are required to solve the forward problem for estimated constitutive parameters at each iteration. This requires us to computationally model the system of study using a target estimation. In this computational model, the equation (2.18) introduces a system of three Ordinary Differential Equation (ODE)s in the 3D space for each of the receivers. The overall ODE system can be evolved over time by explicit/implicit time-marching methods like Runge-Kutta, resulting in $\underline{u}_m^{d,model}(\underline{p},t,\vec{r}_n)$.

Depending on the target's characteristics and the application of the MWI problem, the number of unknown elements in the vector $\underline{p}$ decreases, as some of its parameters may be known (or approximately known). For instance, in non-magnetic materials, the relative permeability is about $\mu_r = 1$. Sometimes, the dielectrics' static conductivity is negligible ($\sigma_s = 0$) because of the dominant loss due to the $\Delta\varepsilon_r$ parameter. In other cases, according to literature, the relaxation time is constant and equal to $\tau_r = \frac{1}{f_r} = 17.5\ ps$ over the body tissues at some frequencies of the microwave band [59]. We chose the free space relaxation time τ_{r0} to be 17.5 ps in this work.
In MWI it is common to use regularization techniques along with the standard cost functional of (2.29) in different inverse solvers in order to obtaining meaningful solutions to the ill-posed inverse scattering problem. This is especially true in FD imaging due to the limited frequency-domain data used during the inversion process. For the TD algorithm developed in this thesis, no regu-

larization is used. The time-domain measurement data contains sufficient information that, when combined with the highly robust FBTS method (which generates very smooth gradients), and the robust technique of step size seeker, can produce meaningful solutions without any additional regularization.

2.3.1 2D TM Considerations

Consider a 2D TM electromagnetic scattering problem (depicted as a literal interpretation of Figure 2.1) where the physics are governed by the dispersive equations (2.20). With no magnetic current density, the only non-zero element of the source is the electric current density in z-direction. These point sources, or the transmitters for this system, are located at $\vec{r}_m \,; m = 1 : M$, such as

$$(\underline{s}_m^d(t,\vec{r}))^{2DTM} = \begin{bmatrix} \vec{\mathcal{J}}_{E,m}(t,\vec{r}) \\ \emptyset \\ \emptyset \end{bmatrix}, \tag{2.37}$$

or

$$(\underline{s}_m^d(t,\vec{r}))^{2DTM} = \begin{bmatrix} \mathcal{I}_{z,m}(t)\delta(\vec{r}-\vec{r}_m) \\ 0 \\ 0 \\ 0 \end{bmatrix}. \tag{2.38}$$

For the 2D model, the fields $\underline{u}_m^{d,model}(\underline{p},t,\vec{r})$ and $\underline{u}_m^{d,meas}(t,\vec{r})$, due to the current source m, $\mathcal{I}_{z,m}(t)$, at the receiver location n, reduce to the components:

$$(\underline{u}_m^{d,model}(\underline{p},t,\vec{r}_n))^{2DTM} = \begin{bmatrix} \mathcal{E}_{z,m}^{model}(\underline{p},t,\vec{r}_n) \\ \mathcal{H}_{x,m}^{model}(\underline{p},t,\vec{r}_n) \\ \mathcal{H}_{y,m}^{model}(\underline{p},t,\vec{r}_n) \\ \mathcal{P}_{z,m}^{model}(\underline{p},t,\vec{r}_n) \end{bmatrix}, \qquad (\underline{u}_m^{d,meas}(t,\vec{r}_n))^{2DTM} = \begin{bmatrix} \mathcal{E}_{z,m}^{meas}(t,\vec{r}_n) \\ \mathcal{H}_{x,m}^{meas}(t,\vec{r}_n) \\ \mathcal{H}_{y,m}^{meas}(t,\vec{r}_n) \\ \mathcal{P}_{z,m}^{meas}(t,\vec{r}_n) \end{bmatrix}. \tag{2.39}$$

2.3.2 A Step-by-Step Overview of the DGM-FBTS Algorithm

In this chapter we have presented Maxwell's curl equations, the augmented form of Maxwell's equations for dispersive media, the general perspective of TD microwave imaging, and the specific case of 2D-TM imaging.

The following section lists the steps required to execute the TD DGM forward solver and the inverse solver used in the DGM-FBTS algorithm developed in this thesis to provide the readers a general overview. The algorithmic steps illustrated here are described later in detail.

Algorithm 1 illustrates the steps for the implemented time domain forward solver using the discontinuous Galerkin method. The first four lines of this algorithm initializes the geometry, source, and parameters of the forward solver. Next, the algorithm solves for the fields due to each of the sources and collects the required fields either at the location of receivers or inside the domain D depending on the requirements. Note that here $\partial_t \underline{v} = \underline{\underline{A}}\ \underline{v} + \underline{B}$ is the normalized rewritten form of formulation (2.18), and will be explained thoroughly in the next chapter.

The continuous form of the forward solver along with its required initial conditions for the fields are presented in Chapter 3. The discretized form of the forward solver is discussed in Chapter 5 after introducing the DG method. The chapter is allocated to solving the discretized forward problem in time using some explicit/implicit iterative methods.

Algorithm 2 provides the steps of the implemented time domain inverse solver scheme using the FBTS method. The first four lines initialize the problem. Afterward, the cost-functional minimization is iteratively performed. Lines 6-16 show the FBTS method steps described in Chapter 3 in continuous form. Chapter 6 discusses the FBTS discretization and the rest of the steps shown in Algorithm 2.

Algorithm 1 TD DGM Forward Solver

1: Specify the desired constitutive parameters model,
2: Specify the number of the transmitters M and receivers N,
3: Set the problem boundary conditions,
4: Specify the locations of the transmitter/receivers on domain S,
5: Compute the discretized matrix $\underline{\underline{A}}$ (and its LUPQ decomposition) in the DGM form of Maxwell's; $\partial_t \underline{v} = \underline{\underline{A}}\ \underline{v} + \underline{B}$,
6: **for** $m = 1, 2, \ldots, M$ **do**
7: Apply a wide band point source (We use Gaussian point source in this work. Other options of source signals are not tested in this work.)
8: Compute the discretized matrix $\underline{B}$ in the DGM form of Maxwell's for each transmitter; $\partial_t \underline{v} = \underline{\underline{A}}\ \underline{v} + \underline{B}$,
9: Apply initial conditions of the fields to the problem,
10: Solve for the vector of coefficients $\underline{v}$ by an iterative implicit/explicit Runge-Kutta methods,
11: Collect the fields at the receiver locations (or inside the domain D to calculate the required gradients for the inverse solver),
12: **end for**.

Algorithm 2 TD DGM-FBTS Inverse Solver

1: Specify an initial guess for the constitutive parameters model in domain D,
2: Specify the number of the transmitters M and receivers N,
3: Set the problem boundary conditions,
4: Specify the locations of the transmitter/receivers on domain S,
5: **while** the algorithm is converging **do**
6: **for** $m = 1, 2, \ldots, M$ **do**
7: Apply the same source (Gaussian) as the original forward solver's,
8: Run forward-in-time forward solver,
9: collect the fields at domain D.
10: **end for**,
11: **for** $m = 1, 2, \ldots, M$ **do**
12: Apply the windowed data error quantities as the point source amplitude in time,
13: Run backward-in-time forward solver,
14: Collect the fields at domain D.
15: **end for**,
16: Calculate the gradients,
17: Calculate search (conjugate gradient) direction h for each parameter,
18: Find the search step,
19: Update the parameter model,
20: Run the forward solver and collect the receiver's data,
21: Compute the cost functional $\mathcal{F}$,
22: Get back to line 6.

Chapter 3

The Continuous Form of FBTS

In this chapter, the forward-backward time-stepping algorithm is developed for electromagnetic inverse scattering in dispersive media. In the FBTS method, the forward/backward time-stepping name comes from this fact that it involves running things backwards in time.

As the dispersive media is a more general type of media, we derive the dispersive FBTS formulation using Maxwell's equations and the ADE introduced in Section 2.1.2 for dispersive media in this chapter. Spatial and temporal discretization of Maxwell's equations and the FBTS formulation are discussed in Chapters 4 and 5, respectively. We restrict the FBTS formulation to 2D-TM problems and non-dispersive media in the final sections of this chapter.

Note: The non-dispersive FBTS gradients derivation in this chapter follows the methodology introduced in [31] for the 2D TM case, and is augmented by the specific spatial discretization method, time-marching methods, and the local minimum seeker repetitive algorithm used in this work. The extended FBTS to dispersive media is introduced for the first time in this work.

3.1 The Optimization Process

In Section 2.3 we introduced the cost functional of (2.29), repeated here for convenience,

$$\mathcal{F}(\underline{p}) = \int_0^T \sum_{m=1}^{M} \sum_{n=1}^{N} \mathcal{W}_m(t) \;\; \| \; \underline{\eta}_{NF}(\vec{r}_n) \;\odot\; \left[\underline{u}_m^{model}(\underline{p}, t, \vec{r}_n) - \underline{u}_m^{meas}(t, \vec{r}_n) \right] \; \|^2 \; dt, \tag{3.1}$$

and addressed minimizing this functional through optimization tactics as an inverse problem. Solving this optimization problem requires solving a highly nonlinear and mathematically ill-posed[1] problem. This section enumerates all of the steps during this optimization process.

- The first step to minimize the cost functional is to pick an optimization method. Note that there are many different kinds of methods that could be applied (as discussed in Chapter 1). The CG method has been selected in this work because the gradients can be computed in closed-form, and a gradient-based local optimization method benefits from improved convergence over other techniques (see Section 1.2.1).

- Having settled on CG, the next step becomes about how to calculate the gradient of the cost functional with respect to the functions stored in $\underline{p}$.

- Once the gradient is known, the next step is to update the value of $\underline{p}$ by searching along the conjugate gradient direction, i.e., we must determine the search distance (step-size) for the gradients' directions to minimize the cost functional.

- After updating the model, the optimization process iterates the process of computing the gradients and determining the step size.

[1] In this problem, ill-posedness is due to instability and non-uniqueness of the response.

3.2 The Cost Functional's Fréchet Derivative

In this section we seek to evaluate the (Fréchet) gradient of the cost functional (3.1) with respect to the constitutive functions ε_∞, $\Delta\varepsilon_r$, μ_r, σ and τ_{rr} represented by $\underline{p}$.

The designated cost functional $\mathcal{F}$, mapping functions in space D to the one-dimensional space $\mathbb{R}$, is a function of discrepancies of electromagnetic fields over the measurement domain S. These discrepancies are non-linear functions mapping the modeled parameters of the spatial area D to vector fields on S. Consequently, the Fréchet Derivatives of functional $\mathcal{F}$ mathematically quantifies changes in $\mathcal{F}$ (the differentials) relative to the changes in each of vectors of the modeled parameters $\underline{p}$ in space.

Let a variation in the constituitve parameters be denoted by

$$\underline{\delta p} = \begin{bmatrix} \delta\varepsilon_\infty(\vec{r}) \\ \delta\Delta\varepsilon_r(\vec{r}) \\ \delta\mu_r(\vec{r}) \\ \delta\sigma_s(\vec{r}) \\ \delta\tau_{rr}(\vec{r}) \end{bmatrix}, \tag{3.2}$$

following the method in [31], the cost functional's Fréchet derivative ${\mathcal{F}'}_p$ in the $\underline{\delta p}$ direction is

$${\mathcal{F}'}_p\underline{\delta p} = 2\int_0^T \sum_{m=1}^{M}\sum_{n=1}^{N} (\underline{\mathcal{R}}_m(\underline{p},t,\vec{r}_n))^\intercal \ \underline{\delta v}_m(\underline{p},t,\vec{r}_n)\ dt, \tag{3.3}$$

where superscript $\intercal$ stands for transpose operator and $\underline{\delta v}(\underline{p},t,\vec{r}_n)$ is the Fréchet differential of the vector of functions

$$\underline{v}(\underline{p},t,\vec{r}) = \underline{\eta}_{NF}(\vec{r}) \ \odot \ \underline{u}^{model}(\underline{p},t,\vec{r}) \tag{3.4}$$

at the receiver positions. Here, $\underline{v}(\underline{p},t,\vec{r}_n)$ and $\underline{\mathcal{R}}(\underline{p},t,\vec{r}_n)$ are vectors of nonlinear operators that

map the constitutive parameter vector $\underline{p}$ to the normalized field vector $\underline{v}$ and the data error vector $\underline{\mathcal{R}}$ at the receiver locations.

As the Fréchet derivative ${\mathcal{F}'}_p$ is a linear operator/functional, the Fréchet differential ${\mathcal{F}'}_p\underline{\delta p}$ can be represented as an inner product according to Riesz representation theorem [68]. In what follows, we will focus on rewriting the right-hand side of (3.3) as an inner product of $\underline{\mathcal{G}}$ and $\underline{\delta p}$:

$$ {\mathcal{F}'}_p\underline{\delta p} = \langle \underline{\mathcal{G}}, \underline{\delta p} \rangle, \tag{3.5} $$

to identify the gradients $\underline{\mathcal{G}}$ from the Fréchet derivative ${\mathcal{F}'}_p$. For the vectors of time-domain functions presented in the cost functional, the inner product definition involves integrals in space and time.

Inner product definition

We use the $\langle .,\ . \rangle$ to represent the inner product of two functions of space and time, defined as:

$$ \langle \underline{f}(t,\vec{r}),\ \underline{g}(t,\vec{r}) \rangle = \int_0^T \iiint_\infty (\underline{f}(t,\vec{r}))^\intercal\ \underline{g}(t,\vec{r})\ dV, \tag{3.6} $$

if the two arbitrary functions of $\underline{f}$ and $\underline{g}$ are functions of time and location, and

$$ \langle \underline{f}(\vec{r}),\ \underline{g}(\vec{r}) \rangle = \iiint_\infty (\underline{f}(\vec{r}))^\intercal\ \underline{g}(\vec{r})\ dV, \tag{3.7} $$

if the functions $\underline{f}$ and $\underline{g}$ are just functions of position. The superscript $^\intercal$ in these definitions stands for transpose operator.

3.3 The Forward-in-Time Operator

The purpose of this section is normalizing (2.18) and describing proper initial conditions to solve the forward problem, or what we call here the forward-in-time solver. The choice of the vector of normalized factors $\underline{\eta}_{NF}$ must be considered when deriving the adjoint operator, and any changes in these parameters can change the adjoint operator and consequently the derived gradients. Therefore, we need to be careful when choosing how to normalize the equations. Good choices of NFs not only serve to normalize the fields, but they also help simplify the gradients.

The vector $\underline{\eta}_{NF}$ adopted in this work is chosen as equation (3.8), where $\underline{1}_{3,1}$ is the all-one vector with size of 3-by-1 and η_0 is the intrinsic impedance of free space.

$$\underline{\eta}_{NF}(\vec{r}) = \begin{bmatrix} \underline{1}_{3,1} \\ \eta_0 \ \underline{1}_{3,1} \\ \frac{1}{\varepsilon_0 \Delta\varepsilon_r(\vec{r})} \ \underline{1}_{3,1} \end{bmatrix} \tag{3.8}$$

This choice of NF does not change the electric field's amplitude, and adjusts the amplitudes of other fields to be commensurate with the electric field. The choice of $\eta_0 \ \underline{1}_{3,1}$ in the second row of $\underline{\eta}_{NF}$ means that we multiply the amplitudes of the magnetic fields by η_0. Finally, $\frac{1}{\varepsilon_0 \Delta\varepsilon_r(\vec{r})} \ \underline{1}_{3,1}$ at the last row means that we multiply the polarization parameters by the factor of $\frac{1}{\varepsilon_0 \Delta\varepsilon_r(\vec{r})}$ to normalize their amplitude with respect to the other fields.

Rewriting the expanded system of equations (2.18) in terms of the normalized field vector $\underline{v}(\underline{p}, t, \vec{r}) = \begin{bmatrix} \underline{1}_{3,1} \\ \eta_0 \ \underline{1}_{3,1} \\ \frac{1}{\varepsilon_0 \Delta\varepsilon_r(\vec{r})} \ \underline{1}_{3,1} \end{bmatrix} \odot \underline{u}^d(\underline{p}, t, \vec{r})$, produces the normalized dispersive system:

$$\tilde{\boldsymbol{\mathcal{K}}} \underline{v} = -\underline{\tilde{s}} \tag{3.9}$$

where the tilde indicates the normalized dispersive formulations and

$$\tilde{\mathcal{K}} = \begin{bmatrix} \varepsilon_\infty \partial_{c_0 t} + \eta_0 \alpha & -\nabla\times & -\eta_0 \beta \\ \nabla\times & \mu_r \partial_{c_0 t} & \emptyset \\ -\eta_0 \beta & \emptyset & \Delta\varepsilon_r \partial_{c_0 t} + \eta_0 \beta \end{bmatrix}, \qquad \underline{v} = \begin{bmatrix} \vec{\mathcal{E}} \\ \eta_0 \vec{\mathcal{H}} \\ \frac{\vec{\mathcal{P}}}{\varepsilon_0 \Delta\varepsilon_r} \end{bmatrix}, \qquad \underline{\tilde{s}} = \begin{bmatrix} \eta_0 \vec{\mathcal{J}}_E \\ \vec{\mathcal{J}}_M \\ \emptyset \end{bmatrix}, \tag{3.10}$$

where c_0 is the speed of light in free space and the time derivations replaced by $\partial_{c_0 t}$ during the normalization process.

Solving (3.9) (with appropriate boundary conditions) for a given estimate of the constitutive parameters produces the fields at each iteration of the FBTS algorithm. The initial condition for this problem is $\underline{\tilde{s}}(t=0,\vec{r}) = \underline{0}$ and so $\underline{v}(t=0,\vec{r}) = \underline{0}$ or

$$\begin{aligned} &\mathcal{E}_x(t=0,\vec{r}) = \mathcal{E}_y(t=0,\vec{r}) = \mathcal{E}_z(t=0,\vec{r}) = 0, \\ &\mathcal{H}_x(t=0,\vec{r}) = \mathcal{H}_y(t=0,\vec{r}) = \mathcal{H}_z(t=0,\vec{r}) = 0, \\ &\mathcal{P}_x(t=0,\vec{r}) = \mathcal{P}_y(t=0,\vec{r}) = \mathcal{P}_z(t=0,\vec{r}) = 0. \end{aligned} \tag{3.11}$$

In addition to ensuring causality, these initial conditions are necessary for the FBTS inversion algorithm; details can be found in Appendix A. This problem is called the forward-in-time problem in the FBTS method; having a known initial condition at time zero means it can be solved by time-marching forwards in time.

3.3.1 2D TM Forward Operator in Time

The forward in time solver for the 2D-TM case has the following system of equations

$$\partial_z(.) = 0, \qquad \mathcal{E}_x = \mathcal{E}_y = 0, \qquad \mathcal{H}_z = 0, \qquad \mathcal{P}_x = \mathcal{P}_y = 0 \tag{3.12}$$

$$\begin{cases} \varepsilon_\infty(\vec{r})\partial_{c_0 t}\mathcal{E}_z(t,\vec{r}) - \partial_x[\eta_0\ \mathcal{H}_y(t,\vec{r})] + \partial_y[\eta_0\ \mathcal{H}_x(t,\vec{r})] + \eta_0\alpha(\vec{r})\mathcal{E}_z(t,\vec{r}) - \ \cdots \\ \qquad\qquad \eta_0\beta(\vec{r})\ [\frac{1}{\varepsilon_0\Delta\varepsilon_r}\ \mathcal{P}_z(t,\vec{r})] = \eta_0\mathcal{J}_{Ez}(t,\vec{r}) \\ \mu_r(\vec{r})\partial_{c_0 t}[\eta_0\ \mathcal{H}_x(t,\vec{r})] + \partial_y\mathcal{E}_z(t,\vec{r}) = \mathcal{J}_{Mx}(t,\vec{r}) \\ \mu_r(\vec{r})\partial_{c_0 t}[\eta_0\ \mathcal{H}_y(t,\vec{r})] - \partial_x\mathcal{E}_z(t,\vec{r}) = \mathcal{J}_{My}(t,\vec{r}) \\ \Delta\varepsilon_r(\vec{r})\partial_{c_0 t}[\frac{1}{\varepsilon_0\Delta\varepsilon_r}\ \mathcal{P}_z(t,\vec{r})] - \eta_0\beta(\vec{r})\mathcal{E}_z(t,\vec{r}) + \eta_0\beta(\vec{r})\ [\frac{1}{\varepsilon_0\Delta\varepsilon_r}\ \mathcal{P}_z(t,\vec{r})] = 0 \end{cases} \tag{3.13}$$

where the initial conditions for this system are:

$$\begin{cases} \mathcal{E}_z(t=0,\vec{r}) = 0 \\ \mathcal{H}_x(t=0,\vec{r}) = 0 \\ \mathcal{H}_y(t=0,\vec{r}) = 0 \\ \mathcal{P}_z(t=0,\vec{r}) = 0 \end{cases} . \tag{3.14}$$

Non-Dispersive Non-Magnetic Media

In some cases, approximating the region of interest as non-dispersive non-magnetic media in order to reduce the computational cost and potentially improve convergence speed is beneficial. Also, some targets just have no magnetic part and have little to no dispersive properties. In this subsection (followed by similar subsections studying non-dispersive 2D TM) we modify/simplify the 2D TM forward-in-time system to non-dispersive and non-magnetic media.

While solving the inverse problem, if the media can be approximated as non-dispersive non-magnetic, the number of unknowns reduces to two. In this case the variation of the constitutive

parameters become:

$$\delta \underline{p} = \begin{bmatrix} \delta\varepsilon_r \\ \delta\sigma_s \end{bmatrix}. \tag{3.15}$$

Correspondingly, the size of the cost functional's Fréchet derivative $\mathcal{F}'_p$ in (3.3) is reduced.

The forward solver system of equations of (3.13) for the non-dispersive 2D-TM becomes:

$$\partial_z(.) = 0, \qquad \mathcal{E}_x = \mathcal{E}_y = 0, \qquad \mathcal{H}_z = 0, \qquad \mathcal{P}_x = \mathcal{P}_y = \mathcal{P}_z = 0 \tag{3.16}$$

$$\begin{cases} \varepsilon_r(\vec{r})\partial_{c_0 t}\mathcal{E}_z(t,\vec{r}) - \partial_x[\eta_0\ \mathcal{H}_y(t,\vec{r})] + \partial_y[\eta_0\ \mathcal{H}_x(t,\vec{r})] + \eta_0\sigma_s(\vec{r})\mathcal{E}_z(t,\vec{r}) = \eta_0\mathcal{J}_{Ez}(t,\vec{r}) \\ \mu_0\partial_{c_0 t}[\eta_0\ \mathcal{H}_x(t,\vec{r})] + \partial_y\mathcal{E}_z(t,\vec{r}) = \mathcal{J}_{Mx}(t,\vec{r}) \\ \mu_0\partial_{c_0 t}[\eta_0\ \mathcal{H}_y(t,\vec{r})] - \partial_x\mathcal{E}_z(t,\vec{r}) = \mathcal{J}_{My}(t,\vec{r}) \end{cases} \tag{3.17}$$

where ε_r is the relative permittivity. The equations (3.17) are obtained from (3.13) by setting $\Delta\varepsilon_r = 0$ and $\mu_r(\vec{r}) = \mu_0$ everywhere.

The initial conditions for this system are:

$$\begin{cases} \mathcal{E}_z(t=0,\vec{r}) = 0 \\ \mathcal{H}_x(t=0,\vec{r}) = 0 \\ \mathcal{H}_y(t=0,\vec{r}) = 0 \end{cases}. \tag{3.18}$$

3.4 The Fréchet Differential $\underline{\delta v}(\underline{p}, t, \vec{r})$

The goal of this section is to derive an expression or a differential equation for the Fréchet Differential of the normalized field vector $\underline{v}(\underline{\delta p}, t, \vec{r})$ at $\underline{p}$ in the direction $\underline{\delta p}$, shown by $\underline{\delta v}(\underline{p}; \underline{\delta p}, t, \vec{r})$ or $\underline{\delta v}(\underline{p}, t, \vec{r})$, based on the fact that $\underline{v}$ is the solution of equation (3.9).

We start with expanding $\underline{v}(\underline{p} + \underline{\delta p}, t, \vec{r})$ by Taylor series to its first order:

$$\underline{v}(\underline{p} + \underline{\delta p}, t, \vec{r}) = \underline{v}(\underline{p}, t, \vec{r}) + \underline{\delta v}(\underline{p} + \underline{\delta p}, t, \vec{r}) + o(\underline{\delta p}) \tag{3.19}$$

where $o(\underline{\delta p})$ stands for a vector function such that: $\lim_{\underline{\delta p} \to 0} \frac{\| o(\underline{\delta p}) \|}{\| \underline{\delta p} \|} \to 0$.
On the other hand, as the right-hand side of Equation (3.9) is independent from $\underline{p}$, we have:

$$\tilde{\boldsymbol{\mathcal{K}}}_{\underline{p}+\underline{\delta p}} \; \underline{v}(\underline{p} + \underline{\delta p}, t, \vec{r}) - \tilde{\boldsymbol{\mathcal{K}}}_{\underline{p}} \; \underline{v}(\underline{p}, t, \vec{r}) = 0 \tag{3.20}$$

where

$$\tilde{\boldsymbol{\mathcal{K}}}_{\underline{p}+\underline{\delta p}} = \tilde{\boldsymbol{\mathcal{K}}}_{\underline{p}} + \begin{bmatrix} \delta\varepsilon_\infty \partial_{c_0 t} + \eta_0 \delta\alpha & \emptyset & -\eta_0 \delta\beta \\ \emptyset & \delta\mu_r \partial_{c_0 t} & \emptyset \\ -\eta_0 \delta\beta & \emptyset & \delta\Delta\varepsilon_r \partial_{c_0 t} + \eta_0 \delta\beta \end{bmatrix}. \tag{3.21}$$

After substituting (3.19) in (3.20), the differential $\underline{\delta v}(\underline{p}; \underline{\delta p}, t, \vec{r})$ is estimated as the solution of the following equation:

$$\tilde{\boldsymbol{\mathcal{K}}} \; \underline{\delta v}(\underline{p}, t, \vec{r}) = - \begin{bmatrix} \delta\varepsilon_\infty \partial_{c_0 t} + \eta_0 \delta\alpha & \emptyset & -\eta_0 \delta\beta \\ \emptyset & \delta\mu_r \partial_{c_0 t} & \emptyset \\ -\eta_0 \delta\beta & \emptyset & \delta\Delta\varepsilon_r \partial_{c_0 t} + \eta_0 \delta\beta \end{bmatrix} \underline{v}(\underline{p}, t, \vec{r}). \tag{3.22}$$

Since the initial conditions of the Equation (3.9) is independent of $\underline{p}$, the following initial condition apply to (3.22):

$$\underline{\delta v}(t = 0, \vec{r}) = \underline{0}. \tag{3.23}$$

If we change the transmitter, the fields $\underline{v}$ will change. So for each transmitter m, the Fréchet differential of the fields $\underline{v}_m$ with respect to $\underline{p}$ in the $\underline{\delta p}$ direction is the solution of (3.22) which illustrates the sensitivity of operator $\tilde{\boldsymbol{\mathcal{K}}}$ due to the change in $\underline{p}$.

Equation (3.22) provides a way to compute $\underline{\delta v}$, and now we are able to evaluate the Fréchet

derivative of the cost functional (3.3). In the following, we are going to isolate $\underline{\delta p}$'s effect on the cost functional in order to maximize the rate of change of the cost functional with respect to the direction $\underline{\delta p}$, i.e., we are going to determine an expression for the gradient of the cost functional.

3.5 The Adjoint Operator

This section contains a brief introduction to the adjoint operator and how defining an appropriate adjoint operator helps facilitate calculating the gradients.

We start this section with a notationally useful definition:

A Collection of Dirac Delta functions

$\underline{\tilde{\delta}}(\vec{r},\ \vec{r}_n = \vec{r}_1 \dots \vec{r}_N) = \underline{\delta}(\vec{r},\vec{r}_1) + \underline{\delta}(\vec{r},\vec{r}_2) + ... + \underline{\delta}(\vec{r},\vec{r}_N)$ represents a sum of Dirac Delta functions with the non-zero quantity at $\vec{r}_n$ locations where $n = 1 \dots N$.

For now we suppress transmitter indexing for the sake of less complications. One convenient way of calculating the required Fréchet derivative $\mathcal{F}'$ is through introducing an adjoint operator $\tilde{\boldsymbol{\mathcal{K}}}^*$:

$$\tilde{\boldsymbol{\mathcal{K}}}^* \underline{w}(\underline{p}, t, \vec{r}) = \underline{\mathcal{R}}(\underline{p}, t, \vec{r})\ \underline{\tilde{\delta}}(\vec{r}, \vec{r}_n) \tag{3.24}$$

where $\vec{r}_n$ is the location of receivers. Remember that $\underline{\mathcal{R}}(\underline{p}, t, \vec{r})$ is the data error (Equation (2.30)). The vector $\underline{w}(\underline{p}, t, \vec{r})$ is interpreted as the solution to the adjoint operator equation (3.24) when sources are cost-functional discrepancies at the observation points. Consider that by choosing this particular right-hand-side for solving the adjoint fields in (3.24), we related the quantities to the cost functional.

According to the adjoint operator definition:

$$\langle \tilde{\boldsymbol{\mathcal{K}}}^{*}\underline{g},\ \underline{f}\rangle = \langle \underline{g},\ \tilde{\boldsymbol{\mathcal{K}}}\underline{f}\rangle, \tag{3.25}$$

and defining $\underline{g}$ and $\underline{f}$ as $\underline{g} = \underline{w}(\underline{p}, t, \vec{r})$ and $\underline{f} = \underline{\delta v}(\underline{p}, t, \vec{r})$, we obtain the following equality:

$$\langle \tilde{\boldsymbol{\mathcal{K}}}^{*}(\underline{w}(\underline{p}, t, \vec{r})),\ \underline{\delta v}(\underline{p}, t, \vec{r})\rangle = \langle \underline{w}(\underline{p}, t, \vec{r}),\ \tilde{\boldsymbol{\mathcal{K}}}(\underline{\delta v}(\underline{p}, t, \vec{r}))\rangle. \tag{3.26}$$

Expanding both sides of equation (3.26) using the inner product definition (3.6) gives:

$$\int_0^T \iiint_\infty (\tilde{\boldsymbol{\mathcal{K}}}^{*}(\underline{w}(\underline{p}, t, \vec{r})))^{\intercal}\ \underline{\delta v}(\underline{p}, t, \vec{r})\ dV dt = \int_0^T \iiint_\infty (\underline{w}(\underline{p}, t, \vec{r}))^{\intercal}\ \tilde{\boldsymbol{\mathcal{K}}}(\underline{\delta v}(\underline{p}, t, \vec{r}))\ dV dt, \tag{3.27}$$

and substituting the term $\tilde{\boldsymbol{\mathcal{K}}}^{*}(\underline{w}(\underline{p}, t, \vec{r}))$ into the right hand side of equation (3.24), we have:

$$\int_0^T \iiint_\infty (\underline{\mathcal{R}}(\underline{p}, t, \vec{r})\ \tilde{\delta}(\vec{r}, \vec{r}_r))^{\intercal}\ \underline{\delta v}(\underline{p}, t, \vec{r})\ dV dt = \int_0^T \iiint_\infty (\underline{w}(\underline{p}, t, \vec{r}))^{\intercal}\ \tilde{\boldsymbol{\mathcal{K}}}(\underline{\delta v}(\underline{p}, t, \vec{r}))\ dV dt. \tag{3.28}$$

The spatial integral on the left side of (3.28) is easily evaluated due to the presence of the delta functions. After re-writing (3.28) for a sum of transmitters and evaluating the left-hand spatial integral we arrive at:

$$\sum_{m=1}^{M} \int_0^T \sum_{n=1}^{N} (\underline{\mathcal{R}}_m(\underline{p}, t, \vec{r}_n))^{\intercal}\ \underline{\delta v}_m(\underline{p}, t, \vec{r}_n)\ dt = \sum_{m=1}^{M} \int_0^T \iiint_\infty (\underline{w}_m(\underline{p}, t, \vec{r}))^{\intercal}\ \tilde{\boldsymbol{\mathcal{K}}}(\underline{\delta v}_m(\underline{p}, t, \vec{r}))\ dV dt. \tag{3.29}$$

Comparing to the Fréchet derivative of the cost functional in equation (3.3), the left side of the above expression is equal to $\frac{1}{2}\mathcal{F}'_p \underline{\delta p}$ and so:

$$\mathcal{F}'_p \underline{\delta p} = 2 \sum_{m=1}^{M} \int_0^T \iiint_\infty (\underline{w}_m(\underline{p}, t, \vec{r}))^{\intercal}\ \tilde{\boldsymbol{\mathcal{K}}}(\underline{\delta v}_m(\underline{p}, t, \vec{r}))\ dV dt. \tag{3.30}$$

This last expression relates the cost functional derivatives to the field adjoint vectors $\underline{w}_m(\underline{p}, t, \vec{r})$ and the differentials of the functional $\tilde{\boldsymbol{\mathcal{K}}}(\underline{\delta v}_m(\underline{p}, t, \vec{r}))$ relative to the change of $\underline{p}$. The term $\tilde{\boldsymbol{\mathcal{K}}}(\underline{\delta v}(\underline{p}, t, \vec{r}))$ has been calculated in Section 3.4 and can easily be replaced here.

As the last two steps to derive the required gradients in this work, we need to solve the (3.24) for the field adjoint vector $\underline{w}_m(\underline{p}, t, \vec{r})$. In order to do so we need to know the adjoint operator.

3.6 The Backwards-in-Time Operator

This section presents the adjoint operator $\tilde{\boldsymbol{\mathcal{K}}}^*$, referred to herein as the backward-in-time operator. The goal of this section is finding the field adjoint $\underline{w}(t, \vec{r})$.

A detailed derivation of the adjoint $\tilde{\boldsymbol{\mathcal{K}}}^*$ for the operator $\tilde{\boldsymbol{\mathcal{K}}}$ can be found in Appendix A. This adjoint operator is:

$$\tilde{\boldsymbol{\mathcal{K}}}^* = \begin{bmatrix} -\varepsilon_\infty(\vec{r})\partial_{c_0 t} + \eta_0\alpha(\vec{r}) & \nabla\times & -\eta_0\beta(\vec{r}) \\ -\nabla\times & -\mu_r(\vec{r})\partial_{c_0 t} & \emptyset \\ -\eta_0\beta(\vec{r}) & \emptyset & -\Delta\varepsilon_r(\vec{r})\partial_{c_0 t} + \eta_0\beta(\vec{r}) \end{bmatrix}. \tag{3.31}$$

As mentioned in Appendix A, this adjoint operator relates the field adjoints:

$$\underline{w} = \begin{bmatrix} \vec{w}_1 \\ \vec{w}_2 \\ \vec{w}_3 \end{bmatrix} \tag{3.32}$$

to the adjoint sources:

$$\underline{\hat{s}} = \begin{bmatrix} \vec{\hat{s}}_1 \\ \vec{\hat{s}}_2 \\ \vec{\hat{s}}_3 \end{bmatrix} \tag{3.33}$$

by the equation

$$\tilde{\boldsymbol{\mathcal{K}}}^{*}\underline{w} = -\underline{\hat{s}}, \tag{3.34}$$

with zero conditions on the field adjoints at time T. Thus it is crucial to ensure that the following conditions are met when using FBTS when using the adjoint (Appendix A.10).

$$\underline{\vec{v}}\ (t=0,\ \vec{r}) = \underline{0} \tag{3.35a}$$

$$\underline{\vec{w}}\ (t=T,\ \vec{r}) = \underline{0} \tag{3.35b}$$

Substituting (3.31) and (2.30) into (3.34) and using the (3.8) for the normalization vector $\underline{\eta}_{NF}$, we have

$$\begin{bmatrix} -\varepsilon_{\infty}(\vec{r})\partial_{c_0 t} + \eta_0\alpha(\vec{r}) & \nabla\times & -\eta_0\beta(\vec{r}) \\ -\nabla\times & -\mu_r(\vec{r})\partial_{c_0 t} & \emptyset \\ -\eta_0\beta(\vec{r}) & \emptyset & -\Delta\varepsilon_r(\vec{r})\partial_{c_0 t} + \eta_0\beta(\vec{r}) \end{bmatrix} \begin{bmatrix} \vec{w}_1(\underline{p},t,\vec{r}) \\ \vec{w}_2(\underline{p},t,\vec{r}) \\ \vec{w}_3(\underline{p},t,\vec{r}) \end{bmatrix} = \cdots$$

$$\mathcal{W}_m(t)\underline{\delta}(\vec{r},\vec{r}_r) \begin{bmatrix} \vec{\mathcal{E}}(\underline{p},t,\vec{r}_n) - \vec{\mathcal{E}}^{meas}(t,\vec{r}_n) \\ \eta_0\ [\vec{\mathcal{H}}(\underline{p},t,\vec{r}_n) - \vec{\mathcal{H}}^{meas}(t,\vec{r}_n)] \\ \frac{1}{\varepsilon_0\Delta\varepsilon_r(\vec{r})}[\vec{\mathcal{P}}(\underline{p},t,\vec{r}_n) - \vec{\mathcal{P}}^{meas}(t,\vec{r}_n)] \end{bmatrix}. \tag{3.36}$$

Solving equations (3.36) in the time range $[0:T]$, is referred to as a backward-in-time solution in the FBTS method because the known (zero) initial (or final) condition at time T suggests that one solves it by starting at time $t = T$, or the final measurement time. In other words, (3.36) provides the time-reversed fields $\vec{w}$ generated by the measurement error as the sources at the receiver locations at time $t = T$.

3.6.1 2D TM Backwards-in-Time Operator

The backward-in-time system has the following equations:

$$\partial_z = 0, \qquad w_{1x} = w_{1y} = 0, \qquad w_{2z} = 0, \qquad w_{3x} = w_{3y} = 0, \tag{3.37}$$

$$\begin{cases} \varepsilon_\infty(\vec{r})\partial_{c_0 t} w_{1z}(t,\vec{r}) - \partial_x w_{2y}(t,\vec{r}) + \partial_y w_{2x}(t,\vec{r}) - \eta_0\alpha(\vec{r}) w_{1z}(t,\vec{r}) + \eta_0\beta(\vec{r}) w_{3z}(t,\vec{r}) = -\hat{s}_{1z}(t,\vec{r}) \\ \mu_r(\vec{r})\partial_{c_0 t} w_{2x}(t,\vec{r}) + \partial_y w_{1z}(t,\vec{r}) = -\hat{s}_{2x}(t,\vec{r}) \\ \mu_r(\vec{r})\partial_{c_0 t} w_{2y}(t,\vec{r}) - \partial_x w_{1z}(t,\vec{r}) = -\hat{s}_{2y}(t,\vec{r}) \\ \Delta\varepsilon_r(\vec{r})\partial_{c_0 t} w_{3z}(t,\vec{r}) + \eta_0\beta(\vec{r}) w_{1z}(t,\vec{r}) - \eta_0\beta(\vec{r}) w_{3z}(t,\vec{r}) = -\hat{s}_{3z}(t,\vec{r}) \end{cases}, \tag{3.38}$$

where the sources $\hat{s}_{1z}(t,\vec{r})$, $\hat{s}_{2x}(t,\vec{r})$, $\hat{s}_{2y}(t,\vec{r})$, $\hat{s}_{3z}(t,\vec{r})$ are:

$$\begin{cases} \hat{s}_{1z}(t,\vec{r}) = \mathcal{W}_m(t)\underline{\delta}(\vec{r},\vec{r}_r)\ [\mathcal{E}_z(t,\vec{r}_n) - \mathcal{E}_z^{meas}(t,\vec{r}_n)] \\ \hat{s}_{2x}(t,\vec{r}) = \eta_0\ \mathcal{W}_m(t)\underline{\delta}(\vec{r},\vec{r}_r)\ [\mathcal{H}_x(t,\vec{r}_n) - \mathcal{H}_x^{meas}(t,\vec{r}_n)] \\ \hat{s}_{2y}(t,\vec{r}) = \eta_0\ \mathcal{W}_m(t)\underline{\delta}(\vec{r},\vec{r}_r)\ [\mathcal{H}_y(t,\vec{r}_n) - \mathcal{H}_y^{meas}(t,\vec{r}_n)] \\ \hat{s}_{3z}(t,\vec{r}) = \frac{1}{\varepsilon_0\Delta\varepsilon_r(\vec{r})}\ \mathcal{W}_m(t)\underline{\delta}(\vec{r},\vec{r}_r)\ [\mathcal{P}_z(t,\vec{r}_n) - \mathcal{P}_z^{meas}(t,\vec{r}_n)] \end{cases}. \tag{3.39}$$

The initial conditions for this solver are:

$$\begin{cases} w_{1z}(t=T,\vec{r}) = 0 \\ w_{2x}(t=T,\vec{r}) = 0 \\ w_{2y}(t=T,\vec{r}) = 0 \\ w_{3z}(t=T,\vec{r}) = 0 \end{cases}. \tag{3.40}$$

Non-Dispersive Non-Magnetic Media

The backward-in-time solver has the following system of equations for a non-dispersive non-magnetic 2D TM case:

$$\partial_z(.) = 0, \qquad w_{1x} = w_{1y} = 0, \qquad w_{2z} = 0, \qquad w_{3x} = w_{3y} = w_{3z} = 0, \tag{3.41}$$

$$\begin{cases} \varepsilon_r(\vec{r})\ \partial_{c_0 t} w_{1z}(t,\vec{r}) - \partial_x w_{2y}(t,\vec{r}) + \partial_y w_{2x}(t,\vec{r}) - \eta_0 \sigma_s(\vec{r})\ w_{1z}(t,\vec{r}) = -\hat{s}_{1z}(t,\vec{r}) \\ \mu_0\ \partial_{c_0 t} w_{2x}(t,\vec{r}) + \partial_y w_{1z}(t,\vec{r}) = -\hat{s}_{2x}(t,\vec{r}) \\ \mu_0\ \partial_{c_0 t} w_{2y}(t,\vec{r}) - \partial_x w_{1z}(t,\vec{r}) = -\hat{s}_{2y}(t,\vec{r}) \end{cases}, \tag{3.42}$$

where the sources $\hat{s}_{1z}(t,\vec{r})$, $\hat{s}_{2x}(t,\vec{r})$ and $\hat{s}_{2y}(t,\vec{r})$ are:

$$\begin{cases} \hat{s}_{1z}(t,\vec{r}) = \mathcal{W}_m(t) \underline{\delta}(\vec{r},\vec{r}_r)\ [\mathcal{E}_z(t,\vec{r}_n) - \mathcal{E}_z^{meas}(t,\vec{r}_n)] \\ \hat{s}_{2x}(t,\vec{r}) = \eta_0\ \mathcal{W}_m(t) \underline{\delta}(\vec{r},\vec{r}_r)\ [\mathcal{H}_x(t,\vec{r}_n) - \mathcal{H}_x^{meas}(t,\vec{r}_n)] \\ \hat{s}_{2y}(t,\vec{r}) = \eta_0\ \mathcal{W}_m(t) \underline{\delta}(\vec{r},\vec{r}_r)\ [\mathcal{H}_y(t,\vec{r}_n) - \mathcal{H}_y^{meas}(t,\vec{r}_n)] \end{cases}. \tag{3.43}$$

The initial conditions for this solver becomes:

$$\begin{cases} w_{1z}(t=T,\vec{r}) = 0 \\ w_{2x}(t=T,\vec{r}) = 0 \\ w_{2y}(t=T,\vec{r}) = 0 \end{cases}. \tag{3.44}$$

3.7 Deriving the Gradients

Now that we have determined the adjoint operator, we can proceed to evaluate the gradient of the designated cost functional ((3.3)) for each of the unknown parameters in $\underline{p}$.

Getting back to the equation (3.30) and substituting $\tilde{\boldsymbol{\mathcal{K}}}(\underline{\delta v}(\underline{p},t,\vec{r}))$ by the right hand side of (3.22), gives

$$\mathcal{F'}_p(\underline{p},\vec{r})\underline{\delta p}(\underline{p},\vec{r}) = -2\sum_{m=1}^{M}\int_0^T \iiint_\infty (\underline{w}_m(\underline{p},t,\vec{r}))^t \cdots \left(\begin{bmatrix} \delta\varepsilon_\infty(\underline{p},\vec{r})\partial_{c_0 t}+\eta_0\delta\alpha(\underline{p},\vec{r}) & \emptyset & -\eta_0\delta\beta(\underline{p},\vec{r}) \\ \emptyset & \delta\mu_r(\underline{p},\vec{r})\partial_{c_0 t} & \emptyset \\ -\eta_0\delta\beta(\underline{p},\vec{r}) & \emptyset & \delta\Delta\varepsilon_r(\underline{p},\vec{r})\partial_{c_0 t}+\eta_0\delta\beta(\underline{p},\vec{r}) \end{bmatrix} \underline{v}_m(\underline{p},t,\vec{r})\right) dVdt. \tag{3.45}$$

By taking equations (3.5), (3.2) and (3.7) into account and defining $\underline{\mathcal{G}} = \begin{bmatrix} \underline{\mathcal{G}}_{\delta\varepsilon_\infty}(\underline{p},\vec{r}) \\ \underline{\mathcal{G}}_{\delta\Delta\varepsilon_r}(\underline{p},\vec{r}) \\ \underline{\mathcal{G}}_{\delta\mu_r}(\underline{p},\vec{r}) \\ \underline{\mathcal{G}}_{\delta\sigma_s}(\underline{p},\vec{r}) \\ \underline{\mathcal{G}}_{\delta f_r}(\underline{p},\vec{r}) \end{bmatrix}$, the expanded matrix version of (3.45) becomes:

$$\iiint_{\infty} \begin{bmatrix} \underline{\mathcal{G}}_{\delta\varepsilon_\infty}(\underline{p},\vec{r}) \\ \underline{\mathcal{G}}_{\delta\Delta\varepsilon_r}(\underline{p},\vec{r}) \\ \underline{\mathcal{G}}_{\delta\mu_r}(\underline{p},\vec{r}) \\ \underline{\mathcal{G}}_{\delta\sigma_s}(\underline{p},\vec{r}) \\ \underline{\mathcal{G}}_{\delta f_r}(\underline{p},\vec{r}) \end{bmatrix}^t \begin{bmatrix} \delta\varepsilon_\infty(\underline{p},\vec{r}) \\ \delta\Delta\varepsilon_r(\underline{p},\vec{r}) \\ \delta\mu_r(\underline{p},\vec{r}) \\ \delta\sigma_s(\underline{p},\vec{r}) \\ \delta f_r(\underline{p},\vec{r}) \end{bmatrix} dV = -2 \sum_{m=1}^{M} \int_0^T \iiint_{\infty} \begin{bmatrix} \vec{w}_{1m}(\underline{p},t,\vec{r}) \\ \vec{w}_{2m}(\underline{p},t,\vec{r}) \\ \vec{w}_{3m}(\underline{p},t,\vec{r}) \end{bmatrix}^t \cdots$$

$$\left(\begin{bmatrix} \delta\varepsilon_\infty(\underline{p},\vec{r})\partial_{c_0 t} + \eta_0\delta\alpha(\underline{p},\vec{r}) & \emptyset & -\eta_0\delta\beta(\underline{p},\vec{r}) \\ \emptyset & \delta\mu_r(\underline{p},\vec{r})\partial_{c_0 t} & \emptyset \\ -\eta_0\delta\beta(\underline{p},\vec{r}) & \emptyset & \delta\Delta\varepsilon_r(\underline{p},\vec{r})\partial_{c_0 t} + \eta_0\delta\beta(\underline{p},\vec{r}) \end{bmatrix} \begin{bmatrix} \vec{v}_{1m}(\underline{p},t,\vec{r}) \\ \vec{v}_{2m}(\underline{p},t,\vec{r}) \\ \vec{v}_{3m}(\underline{p},t,\vec{r}) \end{bmatrix} \right) dV\,dt. \tag{3.46}$$

To enforce equality of the integrals in (3.46), we can enforce equality of the integrands and remove the integrals. As the differentials of α and β are:

$$\delta\alpha(\underline{p},\vec{r}) = \delta\sigma_s(\underline{p},\vec{r}) + \delta\beta(\underline{p},\vec{r}) \tag{3.47a}$$

$$\delta\beta(\underline{p},\vec{r}) = \varepsilon_0\ f_r(\underline{p},\vec{r})\ \delta\Delta\varepsilon_r(\underline{p},\vec{r}) + \varepsilon_0\ \Delta\varepsilon_r(\underline{p},\vec{r})\ \delta f_r(\underline{p},\vec{r}), \tag{3.47b}$$

it follows that expanding the integrands of (3.46) and separating the terms with the same consti-

tutive parameter variations, the gradients with respect to the constitutives functions are revealed:

$$\begin{cases} \underline{\mathcal{G}}_{\varepsilon_\infty}(\underline{p},\vec{r}) = & -2\sum\limits_{m=1}^{M}\int_0^T \vec{w}_{1m}(\underline{p},t,\vec{r})\odot\partial_{c_0t}\vec{v}_{1m}(\underline{p},t,\vec{r})\ dt \\ \underline{\mathcal{G}}_{\Delta\varepsilon_r}(\underline{p},\vec{r}) = & -2\sum\limits_{m=1}^{M}\int_0^T \vec{w}_{3m}(\underline{p},t,\vec{r})\odot\partial_{c_0t}\vec{v}_{1m}(\underline{p},t,\vec{r})\ dt+\cdots \\ & -2\eta_0\varepsilon_0 f_r(\underline{p},\vec{r})\sum\limits_{m=1}^{M}\int_0^T \left[\vec{w}_{1m}(\underline{p},t,\vec{r})-\vec{w}_{3m}(\underline{p},t,\vec{r})\right]\odot\left[\vec{v}_{1m}(\underline{p},t,\vec{r})-\vec{v}_{3m}(\underline{p},t,\vec{r})\right]\ dt \\ \underline{\mathcal{G}}_{\mu_r}(\underline{p},\vec{r}) = & -2\sum\limits_{m=1}^{M}\int_0^T \vec{w}_{2m}(\underline{p},t,\vec{r})\odot\partial_{c_0t}\vec{v}_{2m}(\underline{p},t,\vec{r})\ dt \\ \underline{\mathcal{G}}_{\sigma_s}(\underline{p},\vec{r}) = & -2\eta_0\sum\limits_{m=1}^{M}\int_0^T \vec{w}_{1m}(\underline{p},t,\vec{r})\odot\vec{v}_{1m}(\underline{p},t,\vec{r})\ dt \\ \underline{\mathcal{G}}_{f_r}(\underline{p},\vec{r}) = & -2\eta_0\varepsilon_0 f_r(\underline{p},\vec{r})\sum\limits_{m=1}^{M}\int_0^T \left[\vec{w}_{1m}(\underline{p},t,\vec{r})-\vec{w}_{3m}(\underline{p},t,\vec{r})\right]\odot\left[\vec{v}_{1m}(\underline{p},t,\vec{r})-\vec{v}_{3m}(\underline{p},t,\vec{r})\right]\ dt \end{cases} \tag{3.48}$$

Finally, (3.48) provides the primary result of this chapter; the gradients for all of the unknown constitutive parameters in the imaging domain D. Of course, we need to discretize these formulations, both spatially and temporally, and those steps are the subjects of the following two chapters.

At a given iteration, the gradient calculations require a summation of the dot products between fields and adjoint fields over the transmitters and an integral over the measurement time.The fields are the results of solving the forward-in-time system described in Section 3.3, and the adjoint fields are the results of solving the backward-in-time system discussed in Section 3.6.

If some of the constitutive parameters of a target are known, we can easily replace the related gradient with a zero vector/matrix of the same size. These cases happen a lot in practice, as is explained in Section 2.3.

3.7.1 Gradients for the 2D TM Case

Reducing (3.48) to the 2D-TM case is straightforward, resulting in:

$$\begin{cases} \underline{\mathcal{G}}_{\varepsilon_\infty}(\underline{p},\vec{r}) = & -2\sum\limits_{m=1}^{M}\int_0^T w_{1z,m}(\underline{p},t,\vec{r})\odot\partial_{c_0t}\mathcal{E}_{z,m}(\underline{p},t,\vec{r})\ dt \\ \underline{\mathcal{G}}_{\Delta\varepsilon_r}(\underline{p},\vec{r}) = & -2\sum\limits_{m=1}^{M}\int_0^T w_{3z,m}(\underline{p},t,\vec{r})\odot\partial_{c_0t}\mathcal{E}_{z,m}(\underline{p},t,\vec{r})\ dt+\cdots \\ & -2\eta_0\varepsilon_0 f_r(\underline{p},\vec{r})\sum\limits_{m=1}^{M}\int_0^T\left[w_{1z,m}(\underline{p},t,\vec{r})-w_{3z,m}(\underline{p},t,\vec{r})\right]\odot\left[\mathcal{E}_{z,m}(\underline{p},t,\vec{r})-\cdots\right. \\ & \left.\frac{1}{\varepsilon_0\Delta\varepsilon_r}\ \mathcal{P}_{z,m}(\underline{p},t,\vec{r})\right]\ dt \\ \underline{\mathcal{G}}_{\mu_r}(\underline{p},\vec{r}) = & -2\eta_0\sum\limits_{m=1}^{M}\int_0^T w_{2x,m}(\underline{p},t,\vec{r})\odot\partial_{c_0t}\ \mathcal{H}_{x,m}(\underline{p},t,\vec{r})+w_{2y,m}(\underline{p},t,\vec{r})\odot\partial_{c_0t}\ \mathcal{H}_{y,m}(\underline{p},t,\vec{r})\ dt \\ \underline{\mathcal{G}}_{\sigma_s}(\underline{p},\vec{r}) = & -2\eta_0\sum\limits_{m=1}^{M}\int_0^T w_{1z,m}(\underline{p},t,\vec{r})\odot\mathcal{E}_{z,m}(\underline{p},t,\vec{r})\ dt \\ \underline{\mathcal{G}}_{\tau_{rr}}(\underline{p},\vec{r}) = & 2\eta_0\frac{\tau_0\varepsilon_0\Delta\varepsilon_r(\underline{p},\vec{r})}{\tau_r^2(\underline{p},\vec{r})}\sum\limits_{m=1}^{M}\int_0^T\left[w_{1z,m}(\underline{p},t,\vec{r})-w_{3z,m}(\underline{p},t,\vec{r})\right]\odot\left[\mathcal{E}_{z,m}(\underline{p},t,\vec{r})-\cdots\right. \\ & \left.\frac{1}{\varepsilon_0\Delta\varepsilon_r}\ \mathcal{P}_{z,m}(\underline{p},t,\vec{r})\right]\ dt \end{cases} \tag{3.49}$$

Non-Dispersive Non-Magnetic Media

The gradients for the non-dispersive non-magnetic 2D-TM case are:

$$\begin{cases} \underline{\mathcal{G}}_{\varepsilon_r}(\underline{p},\vec{r}) & = -2\sum\limits_{m=1}^{M}\int_0^T w_{1z,m}(\underline{p},t,\vec{r})\odot\partial_{c_0t}\mathcal{E}_{z,m}(\underline{p},t,\vec{r})\ dt \\ \underline{\mathcal{G}}_{\sigma_s}(\underline{p},\vec{r}) & = -2\eta_0\sum\limits_{m=1}^{M}\int_0^T w_{1z,m}(\underline{p},t,\vec{r})\odot\mathcal{E}_{z,m}(\underline{p},t,\vec{r})\ dt \end{cases}. \tag{3.50}$$

In this chapter we have derived the continuous domain gradients required for the CG solution to the TD-FBTS microwave imaging algorithm. The next two chapters discuss the spatial and temporal discretizations of the TD-FBTS scheme.

Chapter 4

The Discontinuous Galerkin Method

In microwave imaging, the inversion algorithm that seeks to reconstruct a model of the unknown target is commonly implemented as an iterative optimization method. Each iteration of an iterative inverse solver simulates the fields within the measurement domain corresponding to an updated target model. This process demands an efficient and accurate forward solver. Additional solves are required to produce the gradients (i.e., computing the adjoint fields).

The Discontinuous Galerkin Method (DGM) is a robust forward solver that has high flexibility to introduce versatile inhomogeneous backgrounds and imaging enclosures (boundaries). The EIL has been using a frequency-domain DGM forward solver for different imaging applications for a number of years [51, 69, 52]. This forward solver has been developed to the dispersive and non-dispersive time-domain versions as a part of this work.

The main objective of this chapter is to present details of the time-domain DGM. For the time-harmonic version of this forward solver, readers are referred to [52].

This chapter is focused on spatially discretizing the normalized Maxwell's equations for dis-

persive media.

4.1 Discretizing the computational domain

Assume a partition of the 3D computational domain Ω into N_E finite volumes (or elements), V_n, $n = 1, 2, \ldots N_E$ such that $\bigcup_n V_n \approx \Omega$. Depending on the type of elements, these elements have faces (facets) common with the adjacent elements. These faces are surfaces in 3D, lines in 2D and points in 1D scenarios. In each element, both fields and constitutives are expressed in terms of a basis of Lagrange polynomials of order $p(n)$, where this order can vary between elements. By construction, such a basis expansion is generally discontinuous across element interfaces.

The interpolating Lagrange polynomial with the $\ell_k(\vec{r}_j) = \delta_{kj}$ property, where δ is Kronecker delta function, is:

$$\ell_k(\vec{r}) = \prod_{j=1,\ j\neq k}^{N_p} \frac{\vec{r} - \vec{r}_j}{\vec{r}_k - \vec{r}_j}, \tag{4.1}$$

where $\ell_k(\vec{r})$ uniquely exists, as long as $\vec{r}_j$ points or nodes are distinct [3].

The number of nodes and consequently the number of required basis functions required to represent an pth order polynomial in different dimensional spaces are:

$$N_p = \begin{cases} (p+1) \quad \text{in 1D}, \\ \frac{1}{2}(p+1)(p+2) \quad \text{in 2D}, \\ \frac{1}{6}(p+1)(p+2)(p+3) \quad \text{in 3D}. \end{cases} \tag{4.2}$$

Introducing the local time-dependent coefficients $v_x(t, \vec{r}_k^{\,n})$, $v_y(t, \vec{r}_k^{\,n})$ and $v_z(t, \vec{r}_k^{\,n})$ at a fixed time t - where $k = 1 : N_p$ - defined as the value of the function at the kth node in V_n, the electric field can be expanded in the Lagrange basis $\{\ell_k^n\}$ as:

$$\vec{v}^n(t,\vec{r}) \approx \sum_{k=1}^{N_p} v_x(t,\vec{r}_k^{\,n})\ell_k^n(\vec{r})\ \hat{a}_x + \sum_{k=1}^{N_p} v_y(t,\vec{r}_k^{\,n})\ell_k^n(\vec{r})\ \hat{a}_y + \sum_{k=1}^{N_p} v_z(t,\vec{r}_k^{\,n})\ell_k^n(\vec{r})\ \hat{a}_z, \tag{4.3}$$

where $\vec{v}^n(t,\vec{r})$ is a field over the element n at time t. $\hat{a}_x$, $\hat{a}_y$ and $\hat{a}_z$ are the unit vectors of the rectangular coordinate system, respectively in the x, y and z direction. Note that the all of the fields expansions follow the same structure.

Utilizing the vector of the Lagrange interpolation polynomials of $\underline{\ell}^n$ for the nth element with N_p nodal points:

$$\underline{\ell^n(\vec{r})} = \begin{bmatrix} \ell_1^n(\vec{r}) \\ \ell_2^n(\vec{r}) \\ \ell_3^n(\vec{r}) \\ \vdots \\ \ell_{N_p}^n(\vec{r}) \end{bmatrix}, \tag{4.4}$$

and an analogous definition for $\underline{v_x^n(t)}$, $\underline{v_y^n(t)}$ and $\underline{v_z^n(t)}$, the equation (4.3) is rewritten as:

$$\vec{v}^n(t,\vec{r}) \approx (\underline{\ell^n(\vec{r})})^\intercal\ \underline{\vec{v}^n(t)}, \tag{4.5}$$

where:

$$\underline{\vec{v}^n(t)} = \underline{v_x^n(t)}\ \hat{a}_x + \underline{v_y^n(t)}\ \hat{a}_y + \underline{v_z^n(t)}\ \hat{a}_z. \tag{4.6}$$

4.2 Local DGM Volumetric Matrices

This section is allocated to the DGM local expansions of parameters in the Maxwell's PDEs (3.9). In this section we restrict consideration to an arbitrary nth mesh element, and for simplicity superscript n is omitted throughout. Theory is developed for the discrete forward operator; the

discrete adjoint operator can be derived analogously.

Remember (3.9) and (3.10) from the previous chapter, repeated here for convenience:

$$\tilde{\boldsymbol{\mathcal{K}}}\underline{v} = -\underline{\tilde{s}}; \tag{4.7}$$

$$\tilde{\boldsymbol{\mathcal{K}}} = \begin{bmatrix} \varepsilon_\infty \partial_{c_0 t} + \eta_0 \alpha & -\nabla\times & -\eta_0\beta \\ \nabla\times & \mu_r \partial_{c_0 t} & \emptyset \\ -\eta_0\beta & \emptyset & \Delta\varepsilon_r \partial_{c_0 t} + \eta_0\beta \end{bmatrix}, \tag{4.8}$$

$$\underline{v} = \begin{bmatrix} \vec{v}_1 \\ \vec{v}_2 \\ \vec{v}_3 \end{bmatrix} = \begin{bmatrix} \vec{\mathcal{E}} \\ \eta_0\ \vec{\mathcal{H}} \\ \frac{\vec{\mathcal{P}}}{\varepsilon_0 \Delta\varepsilon_r} \end{bmatrix}, \qquad \underline{\tilde{s}} = \begin{bmatrix} \vec{s}_1 \\ \vec{s}_2 \\ \vec{s}_3 \end{bmatrix} = \begin{bmatrix} \eta_0 \vec{\mathcal{J}}_E \\ \vec{\mathcal{J}}_M \\ \emptyset \end{bmatrix}. \tag{4.9}$$

Consider testing Maxwell's equations at a fixed time t by the scalar test function $\psi(\vec{r})$, where we consider a "strong form" by applying integration by parts twice (as opposed to the "weak form" in which the testing function must be differentiable [3]) leading to:

$$\int_{V_n} \psi(\vec{r})\ \varepsilon_\infty(\vec{r})\ \partial_{c_0 t}\vec{v}_1(t,\vec{r})\ \vec{dr} - \int_{V_n} \psi(\vec{r})\ \nabla\times\vec{v}_2(t,\vec{r})\ \vec{dr} + \eta_0 \int_{V_n} \psi(\vec{r})\ \alpha(\vec{r})\ \vec{v}_1(t,\vec{r})\ \vec{dr}\ldots$$
$$- \eta_0 \int_{V_n} \psi(\vec{r})\ \beta(\vec{r})\vec{v}_3(t,\vec{r})\ \vec{dr} + \oiint_{\partial V_n} \psi(\vec{r})\ \hat{n}(\vec{r})\times\left(\vec{v}_2(t,\vec{r}) - \vec{v}_2^{\wedge}(t,\vec{r})\right)\vec{dr} = \ldots$$
$$- \int_{V_n} \psi(\vec{r})\vec{s}_1(t,\vec{r})\ \vec{dr}, \tag{4.10a}$$

$$\int_{V_n} \psi(\vec{r})\ \mu_r(\vec{r})\ \partial_{c_0 t}\vec{v}_2(t,\vec{r})\ \vec{dr} + \int_{V_n} \psi(\vec{r})\ \nabla\times\vec{v}_1(t,\vec{r})\ \vec{dr} - \ldots$$
$$\oiint_{\partial V_n} \psi(\vec{r})\ \hat{n}(\vec{r})\times\left(\vec{v}_1(t,\vec{r}) - \vec{v}_1^{\wedge}(t,\vec{r})\right)\vec{dr} = -\int_{V_n} \psi(\vec{r})\ \vec{s}_2(t,\vec{r})\ \vec{dr}, \tag{4.10b}$$

$$\int_{V_n} \psi(\vec{r})\ \Delta\varepsilon_r(\vec{r})\partial_{c_0 t}\vec{v}_3(t,\vec{r})\ \vec{dr} - \eta_0 \int_{V_n} \psi(\vec{r})\ \beta(\vec{r})\ \vec{v}_1(t,\vec{r})\ \vec{dr} + \eta_0 \int_{V_n} \psi(\vec{r})\ \beta(\vec{r})\ \vec{v}_3(t,\vec{r})\ \vec{dr} = 0, \tag{4.10c}$$

where ∂V_n is the boundary surface of V_n and $\hat{n}(\vec{r})$ is the outward unit normal vector to the surface ∂V_n. The sign $^\wedge$ represents a quantity that is used to enforce the appropriate boundary conditions at the interface between elements by considering the solution from both sides of the interface [3]. The surface integrals in (4.10a) and (4.10b) introduces a surface flux or the dynamics of the problem that accounts for the flow of information in the underlying PDE by coupling adjacent elements.

The next step is discretizing the tested equations by expanding the fields in the basis (4.5). By adopting the same basis function set as test functions, we arrive at the discontinuous Galerkin

method discretization [3].

$$\int_{V_n} \underline{\ell(\vec{r})}\ (\underline{\ell(\vec{r})})^{\intercal}\ \partial_{c_0 t}[\underline{\underline{\varepsilon_\infty}}\ \underline{\vec{v}_1(t)}]\ \vec{dr} - \int_{V_n} \underline{\ell(\vec{r})}\ \nabla \times [(\underline{\ell(\vec{r})})^{\intercal}\ \underline{\vec{v}_2(t)}]\ \vec{dr} + \eta_0 \int_{V_n} \underline{\ell(\vec{r})}\ (\underline{\ell(\vec{r})})^{\intercal} \ldots$$
$$[\underline{\underline{\alpha}}\ \underline{\vec{v}_1(t)}]\ \vec{dr} - \eta_0 \int_{V_n} \underline{\ell(\vec{r})}\ (\underline{\ell(\vec{r})})^{\intercal}\ [\underline{\underline{\beta}}\ \underline{\vec{v}_3(t)}]\ \vec{dr} + \underline{\vec{\mathcal{F}}^{v1}(t)} = -\int_{V_n} \underline{\ell(\vec{r})}\ (\underline{\ell(\vec{r})})^{\intercal} \underline{\vec{s}_1(t)}\ \vec{dr}, \tag{4.11a}$$

$$\int_{V_n} \underline{\ell(\vec{r})}\ (\underline{\ell(\vec{r})})^{\intercal}\ \partial_{c_0 t}[\underline{\underline{\mu_r}}\ \underline{\vec{v}_2(t)}]\ \vec{dr} + \int_{V_n} \underline{\ell(\vec{r})}\ \nabla \times [(\underline{\ell(\vec{r})})^{\intercal}\ \underline{\vec{v}_1(t)}]\ \vec{dr} + \underline{\vec{\mathcal{F}}^{v2}(t)} = -\int_{V_n} \underline{\ell(\vec{r})} \ldots$$
$$(\underline{\ell(\vec{r})})^{\intercal}\ \underline{\vec{s}_2(t)}\ \vec{dr}, \tag{4.11b}$$

$$\int_{V_n} \underline{\ell(\vec{r})}\ (\underline{\ell(\vec{r})})^{\intercal}\ \partial_{c_0 t}[\underline{\underline{\Delta\varepsilon_r}}\ \underline{\vec{v}_3(t)}]\ \vec{dr} - \eta_0 \int_{V_n} \underline{\ell(\vec{r})}\ (\underline{\ell(\vec{r})})^{\intercal}\ [\underline{\underline{\beta}}\ \underline{\vec{v}_1(t)}]\ \vec{dr} + \eta_0 \int_{V_n} \underline{\ell(\vec{r})}\ (\underline{\ell(\vec{r})})^{\intercal} \ldots$$
$$[\underline{\underline{\beta}}\ \underline{\vec{v}_3(t)}]\ \vec{dr} = 0. \tag{4.11c}$$

where

$$\vec{\mathcal{F}}^{v1}(t,\vec{r}) = \oiint_{\partial V_n} \ell(\vec{r})\ \hat{n}(\vec{r}) \times \left(\vec{v}_2(t,\vec{r}) - \vec{v}_2^{\wedge}(t,\vec{r})\right)\ \vec{dr}, \tag{4.12a}$$

$$\vec{\mathcal{F}}^{v2}(t,\vec{r}) = -\oiint_{\partial V_n} \ell(\vec{r})\ \hat{n}(\vec{r}) \times \left(\vec{v}_1(t,\vec{r}) - \vec{v}_1^{\wedge}(t,\vec{r})\right)\vec{dr}. \tag{4.12b}$$

and the $\underline{\vec{\mathcal{F}}^{v1}(t)}$ and $\underline{\vec{\mathcal{F}}^{v2}(t)}$ are the discretized vectors of $\vec{\mathcal{F}}^{v1}(t,\vec{r})$ and $\vec{\mathcal{F}}^{v2}(t,\vec{r})$ over the N_p nodes in element n, respectively. Note that $\underline{\ell(\vec{r})}$, $\underline{\vec{v}_i(t)}$, $\underline{\vec{s}_i(t)}$ and $\underline{\vec{\mathcal{F}}^{vi}(t)}$, where $i = 1,2,3$ and $vi = v1, v2, v3$, are N_p-by-1 vectors and $\underline{\underline{\varepsilon_\infty}}$, $\underline{\underline{\alpha}}$, $\underline{\underline{\beta}}$, $\underline{\underline{\mu_r}}$ are N_p-by-N_p diagonal matrices and the terms related to these parameters in the equations (4.11) are discretized along with the multiplications of parameters, for instance:

$$\varepsilon_\infty(\vec{r})\vec{v}_1(t,\vec{r}) \approx (\underline{\ell(\vec{r})})^{\intercal}\ [\underline{\underline{\varepsilon_\infty}}\ \underline{\vec{v}_1(t)}]. \tag{4.13}$$

The element-wise mass and stiffness matrices are used to simplify the local discretization

notation of Maxwell's within an element:

$$\underline{\underline{\mathcal{M}}} \triangleq \int_{V_n} \underline{\ell(\vec{r})}\ (\underline{\ell(\vec{r})})^{\intercal}\ \vec{dr}, \qquad \underline{\underline{\mathcal{S}}}_i \triangleq \int_{V_n} \underline{\ell(\vec{r})}\ (\partial_i \underline{\ell(\vec{r})})^{\intercal}\ \vec{dr}. \tag{4.14}$$

After substituting the mass and stiffness matrices and simplifying the nine scalar Maxwell's equations, (4.11) become:

$$\partial_{c_0 t}[\underline{v_{1x}(t)}] + \underline{\underline{\varepsilon_\infty}}^{-1}\underline{\underline{\mathcal{D}}}_z \underline{v_{2y}(t)} - \underline{\underline{\varepsilon_\infty}}^{-1}\underline{\underline{\mathcal{D}}}_y \underline{v_{2z}(t)} + \eta_0 \underline{\underline{\varepsilon_\infty}}^{-1}\ \underline{\underline{\alpha}}\ \underline{v_{1x}(t)} - \eta_0 \underline{\underline{\varepsilon_\infty}}^{-1}\ \underline{\underline{\beta}}\ \underline{v_{3x}(t)} + \underline{\underline{\varepsilon_\infty}}^{-1} \ldots$$
$$\underline{\underline{\mathcal{M}}}^{-1} \underline{\mathcal{F}_x^{v1}(t)} = -\underline{\underline{\varepsilon_\infty}}^{-1} \underline{s_{1x}(t)}\ , \tag{4.15a}$$

$$\partial_{c_0 t}[\underline{v_{1y}(t)}] - \underline{\underline{\varepsilon_\infty}}^{-1}\underline{\underline{\mathcal{D}}}_z \underline{v_{2x}(t)} + \underline{\underline{\varepsilon_\infty}}^{-1}\underline{\underline{\mathcal{D}}}_x \underline{v_{2z}(t)} + \eta_0 \underline{\underline{\varepsilon_\infty}}^{-1}\ \underline{\underline{\alpha}}\ \underline{v_{1y}(t)} - \eta_0 \underline{\underline{\varepsilon_\infty}}^{-1}\ \underline{\underline{\beta}}\ \underline{v_{3y}(t)} + \underline{\underline{\varepsilon_\infty}}^{-1} \ldots$$
$$\underline{\underline{\mathcal{M}}}^{-1} \underline{\mathcal{F}_y^{v1}(t)} = -\underline{\underline{\varepsilon_\infty}}^{-1}\ \underline{s_{1y}(t)}\ , \tag{4.15b}$$

$$\partial_{c_0 t}[\underline{v_{1z}(t)}] + \underline{\underline{\varepsilon_\infty}}^{-1}\ \underline{\underline{\mathcal{D}}}_y \underline{v_{2x}(t)} - \underline{\underline{\varepsilon_\infty}}^{-1}\ \underline{\underline{\mathcal{D}}}_x \underline{v_{2y}(t)} + \eta_0 \underline{\underline{\varepsilon_\infty}}^{-1}\ \underline{\underline{\alpha}}\ \underline{v_{1z}(t)} - \eta_0 \underline{\underline{\varepsilon_\infty}}^{-1}\ \underline{\underline{\beta}}\ \underline{v_{3z}(t)} + \underline{\underline{\varepsilon_\infty}}^{-1} \ldots$$
$$\underline{\underline{\mathcal{M}}}^{-1}\ \underline{\mathcal{F}_z^{v1}(t)} = -\underline{\underline{\varepsilon_\infty}}^{-1}\ \underline{s_{1z}(t)}\ , \tag{4.15c}$$

$$\partial_{c_0 t}[\underline{v_{2x}(t)}] - \underline{\underline{\mu_r}}^{-1}\ \underline{\underline{\mathcal{D}}}_z \underline{v_{1y}(t)} + \underline{\underline{\mu_r}}^{-1}\ \underline{\underline{\mathcal{D}}}_y \underline{v_{1z}(t)} + \underline{\underline{\mu_r}}^{-1}\ \underline{\underline{\mathcal{M}}}^{-1}\ \underline{\mathcal{F}_x^{v2}(t)} = -\underline{\underline{\mu_r}}^{-1}\ \underline{s_{2x}(t)}\ , \tag{4.15d}$$

$$\partial_{c_0 t}[\underline{v_{2y}(t)}] + \underline{\underline{\mu_r}}^{-1}\ \underline{\underline{\mathcal{D}}}_z \underline{v_{1x}(t)} - \underline{\underline{\mu_r}}^{-1}\ \underline{\underline{\mathcal{D}}}_x \underline{v_{1z}(t)} + \underline{\underline{\mu_r}}^{-1}\ \underline{\underline{\mathcal{M}}}^{-1}\ \underline{\mathcal{F}_y^{v2}(t)} = -\underline{\underline{\mu_r}}^{-1}\ \underline{s_{2y}(t)}\ , \tag{4.15e}$$

$$\partial_{c_0 t}[\underline{v_{2z}(t)}] - \underline{\underline{\mu_r}}^{-1}\ \underline{\underline{\mathcal{D}}}_y \underline{v_{1x}(t)} + \underline{\underline{\mu_r}}^{-1}\ \underline{\underline{\mathcal{D}}}_x \underline{v_{1y}(t)} + \underline{\underline{\mu_r}}^{-1}\ \underline{\underline{\mathcal{M}}}^{-1}\ \underline{\mathcal{F}_z^{v2}(t)} = -\underline{\underline{\mu_r}}^{-1}\ \underline{s_{2z}(t)}\ , \tag{4.15f}$$

$$\partial_{c_0 t}[\underline{v_{3x}(t)}] - \eta_0 \underline{\underline{\Delta\varepsilon_r}}^{-1}\ \underline{\underline{\beta}}\ \underline{v_{1x}(t)} + \eta_0\ \underline{\underline{\Delta\varepsilon_r}}^{-1}\ \underline{\underline{\beta}}\ \underline{v_{3x}(t)} = 0\ , \tag{4.15g}$$

$$\partial_{c_0 t}[\underline{v_{3y}(t)}] - \eta_0 \underline{\underline{\Delta\varepsilon_r}}^{-1}\ \underline{\underline{\beta}}\ \underline{v_{1y}(t)} + \eta_0 \underline{\underline{\Delta\varepsilon_r}}^{-1}\ \underline{\underline{\beta}}\ \underline{v_{3y}(t)} = 0\ , \tag{4.15h}$$

$$\partial_{c_0 t}[\underline{v_{3z}(t)}] - \eta_0 \underline{\underline{\Delta\varepsilon_r}}^{-1}\ \underline{\underline{\beta}}\ \underline{v_{1z}(t)} + \eta_0 \underline{\underline{\Delta\varepsilon_r}}^{-1}\ \underline{\underline{\beta}}\ \underline{v_{3z}(t)} = 0\ , \tag{4.15i}$$

where $\underline{\underline{\mathcal{D}}}_i = \underline{\underline{\mathcal{M}}}^{-1}\underline{\underline{\mathcal{S}}}_i$.

The simplified version of (4.15) set of equations, which contains the local matrices are:

$$\partial_{c_0 t}\ \underline{v(t)}^n = -\underline{\underline{A}}^n\ \underline{v(t)}^n - \underline{\underline{B}}^n\ \underline{\underline{\mathcal{F}^n(t)}}\ \underline{v(t)}^n - \underline{C(t)}^n\ , \tag{4.16}$$

where $\underline{\underline{\mathcal{F}^n(t)}}$ is the sparse flux matrix with non-zero entries arising from interactions to each of the adjacent elements, and:

$$\underline{\underline{A}}^n = \underline{\underline{A_1}} + \underline{\underline{A_2}} \,, \tag{4.17}$$

$$\underline{\underline{A_1}} = \begin{bmatrix}
\eta_0 \underline{\underline{\varepsilon_\infty}}^{-1} \underline{\underline{\alpha}} & \underline{0} & \underline{0} & \underline{0} & \underline{0} & \underline{0} & -\eta_0 \underline{\underline{\varepsilon_\infty}}^{-1} \underline{\underline{\beta}} & \underline{0} & \underline{0} \\
\underline{0} & \eta_0 \underline{\underline{\varepsilon_\infty}}^{-1} \underline{\underline{\alpha}} & \underline{0} & \underline{0} & \underline{0} & \underline{0} & \underline{0} & -\eta_0 \underline{\underline{\varepsilon_\infty}}^{-1} \underline{\underline{\beta}} & \underline{0} \\
\underline{0} & \underline{0} & \eta_0 \underline{\underline{\varepsilon_\infty}}^{-1} \underline{\underline{\alpha}} & \underline{0} & \underline{0} & \underline{0} & \underline{0} & \underline{0} & -\eta_0 \underline{\underline{\varepsilon_\infty}}^{-1} \underline{\underline{\beta}} \\
\underline{0} & -\underline{\underline{\mu_r}}^{-1} \underline{\underline{\mathcal{D}}}_z & \underline{\underline{\mu_r}}^{-1} \underline{\underline{\mathcal{D}}}_y & \underline{0} & \underline{0} & \underline{0} & \underline{0} & \underline{0} & \underline{0} \\
\underline{0} & \underline{0} & \underline{0} & \underline{0} & \underline{0} & \underline{0} & \underline{0} & \underline{0} & \underline{0} \\
\underline{0} & \underline{0} & \underline{0} & \underline{0} & \underline{0} & \underline{0} & \underline{0} & \underline{0} & \underline{0} \\
-\eta_0 \underline{\underline{\Delta \varepsilon_r}}^{-1} \underline{\underline{\beta}} & \underline{0} & \underline{0} & \underline{0} & \underline{0} & \underline{0} & \eta_0 \underline{\underline{\Delta \varepsilon_r}}^{-1} \underline{\underline{\beta}} & \underline{0} & \underline{0} \\
\underline{0} & -\eta_0 \underline{\underline{\Delta \varepsilon_r}}^{-1} \underline{\underline{\beta}} & \underline{0} & \underline{0} & \underline{0} & \underline{0} & \underline{0} & \eta_0 \underline{\underline{\Delta \varepsilon_r}}^{-1} \underline{\underline{\beta}} & \underline{0} \\
\underline{0} & \underline{0} & -\eta_0 \underline{\underline{\Delta \varepsilon_r}}^{-1} \underline{\underline{\beta}} & \underline{0} & \underline{0} & \underline{0} & \underline{0} & \underline{0} & \eta_0 \underline{\underline{\Delta \varepsilon_r}}^{-1} \underline{\underline{\beta}}
\end{bmatrix}, \tag{4.18}$$

$$\underline{\underline{A_2}} = \begin{bmatrix}
\underline{0} & \underline{0} & \underline{0} & \underline{0} & \underline{\underline{\varepsilon_\infty}}^{-1} \underline{\underline{\mathcal{D}}}_z & \underline{\underline{\varepsilon_\infty}}^{-1} \underline{\underline{\mathcal{D}}}_y & \underline{0} & \underline{0} & \underline{0} \\
\underline{0} & \underline{0} & \underline{0} & -\underline{\underline{\varepsilon_\infty}}^{-1} \underline{\underline{\mathcal{D}}}_z & \underline{0} & \underline{\underline{\varepsilon_\infty}}^{-1} \underline{\underline{\mathcal{D}}}_x & \underline{0} & \underline{0} & \underline{0} \\
\underline{0} & \underline{0} & \underline{0} & \underline{\underline{\varepsilon_\infty}}^{-1} \underline{\underline{\mathcal{D}}}_y & \underline{\underline{\varepsilon_\infty}}^{-1} \underline{\underline{\mathcal{D}}}_x & \underline{0} & \underline{0} & \underline{0} & \underline{0} \\
\underline{0} & -\underline{\underline{\mu_r}}^{-1} \underline{\underline{\mathcal{D}}}_z & \underline{\underline{\mu_r}}^{-1} \underline{\underline{\mathcal{D}}}_y & \underline{0} & \underline{0} & \underline{0} & \underline{0} & \underline{0} & \underline{0} \\
\underline{\underline{\mu_r}}^{-1} \underline{\underline{\mathcal{D}}}_z & \underline{0} & -\underline{\underline{\mu_r}}^{-1} \underline{\underline{\mathcal{D}}}_x & \underline{0} & \underline{0} & \underline{0} & \underline{0} & \underline{0} & \underline{0} \\
-\underline{\underline{\mu_r}}^{-1} \underline{\underline{\mathcal{D}}}_y & -\underline{\underline{\mu_r}}^{-1} \underline{\underline{\mathcal{D}}}_x & \underline{0} & \underline{0} & \underline{0} & \underline{0} & \underline{0} & \underline{0} & \underline{0} \\
\underline{0} & \underline{0} & \underline{0} & \underline{0} & \underline{0} & \underline{0} & \underline{0} & \underline{0} & \underline{0} \\
\underline{0} & \underline{0} & \underline{0} & \underline{0} & \underline{0} & \underline{0} & \underline{0} & \underline{0} & \underline{0} \\
\underline{0} & \underline{0} & \underline{0} & \underline{0} & \underline{0} & \underline{0} & \underline{0} & \underline{0} & \underline{0}
\end{bmatrix}, \tag{4.19}$$

$$\underline{\underline{B}} = \mathbf{BlockDiag}\left(\begin{bmatrix} \underline{\underline{\varepsilon_\infty}}^{-1}\underline{\underline{\mathcal{M}}}^{-1} \\ \underline{\underline{\varepsilon_\infty}}^{-1}\underline{\underline{\mathcal{M}}}^{-1} \\ \underline{\underline{\varepsilon_\infty}}^{-1}\underline{\underline{\mathcal{M}}}^{-1} \\ \underline{\underline{\mu_r}}^{-1}\ \underline{\underline{\mathcal{M}}}^{-1} \\ \underline{\underline{\mu_r}}^{-1}\ \underline{\underline{\mathcal{M}}}^{-1} \\ \underline{\underline{\mu_r}}^{-1}\ \underline{\underline{\mathcal{M}}}^{-1} \\ \underline{0} \\ \underline{0} \\ \underline{0} \end{bmatrix}\right), \qquad \underline{C(t)}^n = \begin{bmatrix} \underline{\underline{\varepsilon_\infty}}^{-1}\underline{s_{1x}(t)} \\ \underline{\underline{\varepsilon_\infty}}^{-1}\underline{s_{1y}(t)} \\ \underline{\underline{\varepsilon_\infty}}^{-1}\underline{s_{1z}(t)} \\ \underline{\underline{\mu_r}}^{-1}\ \underline{s_{2x}(t)} \\ \underline{\underline{\mu_r}}^{-1}\ \underline{s_{2y}(t)} \\ \underline{\underline{\mu_r}}^{-1}\ \underline{s_{2z}(t)} \\ \underline{0} \\ \underline{0} \\ \underline{0} \end{bmatrix}, \qquad \underline{v(t)}^n = \begin{bmatrix} \underline{v_{1x}(t)} \\ \underline{v_{1y}(t)} \\ \underline{v_{1z}(t)} \\ \underline{v_{2x}(t)} \\ \underline{v_{2y}(t)} \\ \underline{v_{2z}(t)} \\ \underline{v_{3x}(t)} \\ \underline{v_{3y}(t)} \\ \underline{v_{3z}(t)} \end{bmatrix}. \quad (4.20)$$

So far in this section, the local matrices for a specific element n have been generated using the Mass and Stiffness matrices and local interpolation coefficients. The resulted matrices' sizes are $9N_p$-by-1 for the field and source coefficient vectors $\underline{v(t)}^n$ and $\underline{C(t)}^n$ and $9N_p$-by-$9N_p$ for the other matrices $\underline{\underline{A}}^n$, $\underline{\underline{B}}^n$ and $\underline{\underline{\mathcal{F}^n(t)}}$.

4.3 Evaluating Fluxes on Interfaces

This section provides some details about the local flux term, which is the heart of the formulations (4.10) and couples an element to its neighbours.

The goal here is to evaluate the surface integrals of equations (4.12) by summing the contributions over each of the element faces. Hence, we use the expansion polynomials $\underline{\ell^{n,f}(\vec{r})}$ which are defined on the face (facet) f; substituting it into equation (4.12) gives:

$$\begin{aligned} \underline{\vec{\mathcal{F}}^{vi,n}(t)} &= \sum_{f=1}^{N_f} \iint_{\partial V_n, f} \underline{\ell^{n,f}(\vec{r})}\ \vec{\Phi}^{vi,n,f}(t,\vec{r})\ d\vec{r} \\ &= \sum_{f=1}^{N_f} \underline{\underline{\mathcal{M}^{n,f}}}\ \underline{\vec{\Phi}^{vi,n,f}(t)} \qquad ; \qquad vi = v1, v2 \end{aligned} \quad (4.21)$$

where $\underline{\underline{\mathcal{M}^{n,f}}}$ is the mass matrix corresponding to the the fth face of element n. N_f is the total number of faces regarding element n, which means that this element has common boundaries with N_f other elements; $f = 1 : N_f$.

Appropriate choices of flux conditions can be found in [3]. According to [3], a natural choice for the flux in wave equations is:

$$\vec{\Phi}^{v1}(t,\vec{r}^{n,f}) \triangleq \frac{Z^+(\vec{r}^{n,f})}{Z^-(\vec{r}^{n,f})+Z^+(\vec{r}^{n,f})}\ \hat{n}(\vec{r}^{n,f}) \times \left[\vec{v_2}^-(t,\vec{r}^{n,f}) - \vec{v_2}^+(t,\vec{r}^{n,f})\right] - \dots$$
$$\frac{\alpha}{Z^-(\vec{r}^{n,f})+Z^+(\vec{r}^{n,f})}\ \hat{n}(\vec{r}^{n,f}) \times \hat{n}(\vec{r}^{n,f}) \times \left[\vec{v_1}^-(t,\vec{r}^{n,f}) - \vec{v_1}^+(t,\vec{r}^{n,f})\right], \tag{4.22a}$$

$$\vec{\Phi}^{v2}(t,\vec{r}^{n,f}) \triangleq \frac{-Y^+(\vec{r}^{n,f})}{Y^-(\vec{r}^{n,f})+Y^+(\vec{r}^{n,f})}\ \hat{n}(\vec{r}^{n,f}) \times \left[\vec{v_1}^-(t,\vec{r}^{n,f}) - \vec{v_1}^+(t,\vec{r}^{n,f})\right] - \dots$$
$$\frac{\alpha}{Y^-(\vec{r}^{n,f})+Y^+(\vec{r}^{n,f})}\ \hat{n}(\vec{r}^{n,f}) \times \hat{n}(\vec{r}^{n,f}) \times \left[\vec{v_2}^-(t,\vec{r}^{n,f}) - \vec{v_2}^+(t,\vec{r}^{n,f})\right], \tag{4.22b}$$

where α is a numerical parameter and $\hat{n}$ is the unit normal outward vector from the element n on the surface of fth face. The minus superscripts represent quantities associated with nth element and the positive superscripts represent the quantities in the neighbour across the fth facet. $Z(\vec{r})$ is the impedance defined by $\sqrt{\frac{\mu_0\mu_r(\vec{r})}{\varepsilon_0\varepsilon_\infty(\vec{r})}}$ at the location $\vec{r}$ and $Y(\vec{r})$ is the admittance defined by $Y(\vec{r}) = Z(\vec{r})^{-1}$ at the location $\vec{r}$.

If parameter $\alpha \in [0,\ 1]$ is chosen 0, called "central flux" [3], an equal contribution from the internal and external boundaries is used to calculate the flux term. The choice of $\alpha = 1$ refers to classic "upwind flux" [3]. Here in this work, we use $\alpha = 1$, as it offers visually smoother solution [3].

Properly evaluating the flux integrals requires care in accounting for the potential of having different solution orders in adjacent elements. In such cases, interpolation is required, and details can be found in [52].

4.4 Boundary Conditions

In this section two boundary conditions are presented using the "strong form" representation of flux terms.

4.4.1 Absorbing Boundary Condition

The characteristics of an absorbing boundary imposes zero incoming waves of electric and magnetic from the absorbing layer, means that the flux terms arising from $\vec{v}_1^+$ and $\vec{v}_2^+$ are zero. Assuming zero incoming flux from the neighbouring elements leads to a simple Silver-Müller absorbing boundary condition:

$$\vec{\Phi}^{v1}_{ABC}(t,\vec{r}^{n,f}) = \frac{1}{2}\,\hat{n}(\vec{r}^{n,f})\;\vec{v_1}^-(t,\vec{r}^{n,f}) - \frac{\alpha}{2Z^-(\vec{r}^{n,f})}\;\hat{n}(\vec{r}^{n,f})\times\hat{n}(\vec{r}^{n,f})\times\vec{v_1}^-(t,\vec{r}^{n,f}),$$
$$\vec{\Phi}^{v2}_{ABC}(t,\vec{r}^{n,f}) = \frac{-1}{2}\,\hat{n}(\vec{r}^{n,f})\;\vec{v_1}^-(t,\vec{r}^{n,f}) - \frac{\alpha}{2Y^-(\vec{r}^{n,f})}\;\hat{n}(\vec{r}^{n,f})\times\hat{n}(\vec{r}^{n,f})\quad\times\vec{v_2}^-(t,\vec{r}^{n,f}).$$

4.4.2 Perfect Electric Conductor (PEC) Boundary Condition

In the case of a Perfect Electric Conductor (PEC) surface f adjacent to the element n, the following conditions hold for the PEC neighbour:

$$\begin{cases} Z^+(\vec{r}^{n,f}) = 0, \\ \vec{v_1}^+(t,\vec{r}^{n,f}) = \vec{v_2}^+(t,\vec{r}^{n,f}) = \vec{0} \end{cases}. \tag{4.24}$$

These conditions simplify the the flux terms of (7.21) to:

$$\vec{\Phi}^{v1}_{PEC}(t,\vec{r}^{n,f}) = -\frac{\alpha}{Z^-(\vec{r}^{n,f})}\;\hat{n}(\vec{r}^{n,f})\times\hat{n}(\vec{r}^{n,f})\times\;\vec{v_1}^-(t,\vec{r}^{n,f}),$$
$$\vec{\Phi}^{v2}_{PEC}(t,\vec{r}^{n,f}) = -\;\hat{n}(\vec{r}^{n,f})\times\;\vec{v_1}^-(t,\vec{r}^{n,f}).$$

4.5 Constructing the Global System

So far, the previous sections of this chapter have focused on discretizing Maxwelle's PDEs in a local volume of V_n. The last step of this discretization is to collect the local equations into a sparse block global system of equations:

$$\partial_{c_0 t}\ \underline{v(t)} = -\underline{\underline{E}}\ \underline{v(t)} - \underline{\underline{Q}}\ \underline{\underline{\mathcal{F}(t)}}\ \underline{v(t)} - \underline{R(t)}, \tag{4.26}$$

where the matrices $\underline{\underline{E}}$ and $\underline{\underline{Q}}$ are the result of a block-diagonal concatenation of matrices $\underline{\underline{A}}^n$ and $\underline{\underline{B}}^n$, respectively. $\underline{R(t)}$ is the concatenation of $\underline{C(t)}^n$s, and $\underline{\underline{\mathcal{F}(t)}}$ is the general flux matrix $\underline{\underline{\mathcal{F}(t)}} = \sum_{n=1}^{N_E} \underline{\underline{\mathcal{F}^n(t)}}$.

The end result, (4.26) is a system of ODEs. Solving this system of ODEs is the subject of the next chapter.

Chapter 5

Integration in the Temporal Dimension

We have emphasized so far the discrete spatial representation of the DGM formulation. This chapter concentrates on different time-integration methods employed to solve the semidiscrete system of ODEs (4.26), which is simplified here for conciseness as:

$$\partial_t \, \underline{v}(t) = \mathfrak{F}(\underline{v}, t). \tag{5.1}$$

Here, $\underline{v}$ is the vector of unknowns or the field coefficients as a function of time corresponding to the DGM spatial discretization in Ω.

The next sections focus on time integration, first explaining the general difference between implicit and explicit methods, and then presenting four different implicit and explicit strategies. Then we study the implementation features of each of these four methods. The techniques presented in this chapter have been selected from [3, 70, 71, 72, 73, 74, 75].

5.1 Explicit versus Implicit Time Integration Methods

Two German mathematicians, Carl Runge and Wilhelm Kutta, developed a family of implicit and explicit iterative methods used for temporal discretization and solving ODEs, around 1900. This family of iterative methods are called Runge-Kutta in numerical analysis [76].

To illustrate the differences of implicit and explicit methods, we initiate with rewriting the equation (5.1) and separating $\mathfrak{F}(\underline{v}, t)$ into the source term $\underline{\mathfrak{s}}(t)$ which is a function of time, and the term $\underline{A}\ \underline{v}(t)$, which is a linear function of the fields:

$$\partial_t\ \underline{v}(t) = \underline{A}\ \underline{v}(t) + \underline{\mathfrak{s}}(t). \tag{5.2}$$

The simplest explicit routine, from the Runge–Kutta (RK) family, is the Forward Euler method, which approximates the time derivative as a forward difference. Let $v^n = v(n\Delta t)$ where Δt is a time step and n is the time step index. To launch from $\underline{v}^n$ to $\underline{v}^{n+1}$ separated by time step Δt by Forward Euler method, we have:

$$\frac{\underline{v}^{n+1} - \underline{v}^n}{\Delta t} = \underline{A}\ \underline{v}^n + \mathfrak{s}^n. \tag{5.3}$$

The simplest implicit routine, from Runge–Kutta family, is the Backward Euler method, where the time derivative is approximated by a backward difference:

$$\frac{\underline{v}^{n+1} - \underline{v}^n}{\Delta t} = \underline{A}\ \underline{v}^{n+1} + \mathfrak{s}^{n+1}. \tag{5.4}$$

Solving for the updated solution $\underline{v}^{n+1}$ gives:

$$\underline{v}^{n+1} = (\underline{I} + \Delta t\ \underline{A})\ \underline{v}^n + \Delta t\ \mathfrak{s}^n \qquad \text{Explicit,} \tag{5.5}$$

$$\underline{v}^{n+1} = (\underline{I} - \Delta t\ \underline{A})^{-1}\ [\underline{v}^n + \Delta t\ \mathfrak{s}^{n+1}] \qquad \text{Implicit,} \tag{5.6}$$

where the inverse operator is symbolic of solving a system of equations (but does not mean computing the inverse). There are two important differences between these two strategies: First, the forward Euler method, like all explicit methods, suffers from numerical instability if the time step is chosen too large [77]. Second, while the backward Euler method, like all implicit methods, does not suffer the instability of its explicit counterpart, it requires solving a system of linear equations at each time step by multiplying $(\underline{I} - \Delta t\ \underline{A})^{-1}$ by some other term (right hand side). Note that we generally assume that the media is stationary so A is constant and this inverse can be computed once and stored.

The electromagnetic wave propagation by a point source is categorized as a stiff-problem[1]. It is well-known that implicit methods are the most efficient methods to solve these kinds of ODEs [77]. However, one requires an associated method for solving the implicit equation. In this project, an LUPQ decomposition [78] step is utilized for solving the sparse matrix equations arising from implicit time-marching schemes.

5.2 Low-Storage Explicit Runge-Kutta (LSERK)

The explicit Runge-Kutta method described in this section has been picked from [3], and is a low-storage fourth-order explicit RK whose pseudo-code is described in Algorithm 3. The low-storage version requires three fewer intermediate storage vectors than the standard fourth-order RK method, at the price of one additional stage of computation. The cost of the additional stage is offset by the low-storage method (less computational cost) allowing larger stable time steps Δt [3].

The related coefficients for this LSERK (Algorithm 3) are given in table 5.1.

[1]The differential equations that feature an exponential dynamical decaying solution are called stiff-problems.

Algorithm 3 Low-Storage Fourth-Order Explicit Runge-Kutta

Compute the DGM constant matrices,
Set zero (temporal) initial values for fields; $\underline{v}^0 = \underline{0}$,
Set the a_i, b_i and c_i coefficients for $i = 1, \ldots, 5$ according to table 5.1
for $n = 1, 2, \ldots, N$ **do**
    $\underline{u}^{(0)} = \underline{v}^n$,
    for $i = 1, \ldots, 5$ **do**
        $\underline{k}^{(i)} = a_i \; \underline{k}^{(i-1)} + \Delta t \; \mathfrak{F}(\underline{u}^{(i-1)}, t^n + c_i \; \Delta t)$
        $\underline{u}^{(i)} = \underline{u}^{(i-1)} + b_i \; k^{(i)}$
    end for
    $\underline{v}^{n+1} = \underline{u}^{(5)}$
end for
Return the $\underline{v}^n$ values for the time indices $n = 1, 2, \ldots, N$.
$=0$

i	a_i	b_i	c_i
1	0	$\frac{1432997174477}{9575080441755}$	0
2	$-\frac{567301805773}{1357537059087}$	$\frac{5161836677717}{13612068292357}$	$\frac{1432997174477}{9575080441755}$
3	$-\frac{2404267990393}{2016746695238}$	$\frac{17201146321549}{2090206949498}$	$\frac{2526269341429}{6820363962896}$
4	$-\frac{3550918686646}{2091501179385}$	$\frac{3134564353537}{4481467310338}$	$\frac{2006345519317}{3224310063776}$
5	$-\frac{1275806237668}{842570457699}$	$\frac{2277821191437}{14882151754819}$	$\frac{2802321613138}{2924317926251}$

Table 5.1: Table of LSERK's coefficients reproduced from [3]

5.3 Diagonally Implicit Runge-Kutta (DIRK) Method

This section describes another Runge-Kutta method that has been evaluated for solving the DGM system of equations as part of this work. This scheme is a fourth-order four-stage diagonally implicit Runge-Kutta method, presented for the first time by Jawias et al. [71], designed explicitly for the Linear Ordinary Differential Equations (LODEs) governing wave and heat phenomena.

The DIRK algorithm is described step-by-step in Algorithm 4.

Algorithm 4 4th Order DIRK

1: **Compute** the DGM constant matrices,
2: **Set** zero (temporal) initial values for fields; $\underline{v}^0 = \underline{0}$,
3: **Set** the a_i, b_i and c_i coefficients for $i = 1, \ldots, 5$ according to Butcher Tableau,
4: **for** $i = 1, 2, \ldots, 4$ **do** decomposition

$$[\underline{L}_i, \underline{U}_i, \underline{P}_i, \underline{Q}_i] = (\underline{I} - a_{ii}\Delta t \ \underline{A})$$

5: **end for**
6: **for** $n = 1, 2, \ldots, N$ **do**
7: **Compute** $\underline{V}_1$ using the LUPQ-decompositions:

$$\underline{Y}_1 = \underline{A} \ \underline{v}^n,$$
$$\underline{V}_1 = (\underline{I} - a_{11}\Delta t \ \underline{A})^{-1} \left[\underline{Y}_1 + \underline{\mathfrak{s}}(t^n + c_1\Delta t)\right].$$

8: **for** $i = 2, \ldots, 4$ **do Compute** $\underline{V}_i$; $i = 1, 2, \ldots$, using the LUPQ-decompositions:

$$\underline{Y}_i = \underline{A} \ \underline{V}_{i-1},$$
$$\underline{V}_i = (\underline{I} - a_{ii}\Delta t \ \underline{A})^{-1}[\underline{Y}_1 + \Delta t \ \sum_{j=2}^{i} a_{i(j-1)} \ \underline{Y}_j \ + \underline{\mathfrak{s}}(t^n + c_i\Delta t)].$$

9: **end for**
10: **Compute** $\underline{v}^{n+1}$:

$$\underline{v}^{n+1} = \underline{v}^n + \Delta t \ \sum_{i=1}^{4} b_i \ \underline{V}_i$$

11: **end for**
12: **Return** the $\underline{v}^n$ values for the time indices $n = 1, 2, \ldots, N$.

The coefficients required for this algorithm are written in the Butcher's array as follows:

$$\begin{array}{c|c} c & a \\ \hline & b^{\intercal} \end{array} =$$

0.20	0.20			
0.05	−0.15	0.20		
0.40	−0.78518518518519	0.98518518518519	0.20	
0.80	0.70671936758894	−0.19819311123659	0.091473743647652	0.20
	0.40740740740741	0.016931216931217	0.10714285714286	0.46851851851852

5.4 2nd Order Rosenbrock Implicit Method

According to [72], the TD MWI's OD equations, like other wave equations, may not demand highly accurate calculations, and decreasing the time integration solution order seems feasible. Therefore, providing the required restrained accuracy, second-order Runge-Kutta methods could be more efficient, and sufficiently accurate, than higher-order methods. There is only one LU (LUPQ) decomposition required in this method as opposed to simple implicit Runge-Kutta methods, like DIRK.

In the following, a second-order two-stage implicit Runge-Kutta method known as Rosenbrock is represented. Algorithm 5 describes the steps of this method in detail [72].

Algorithm 5 2nd-order Rosenbrock

1: **Compute** the DGM constant matrices,
2: **Set** zero (temporal) initial values for fields; $\underline{v}^0 = \underline{0}$,
3: **Set** $\gamma = 0.5$,
4: **Do** decomposition $[\underline{L}, \underline{U}, \underline{P}, \underline{Q}] = (\underline{I} - \gamma \Delta t \ \underline{A})$,
5: **for** $n = 1, 2, \ldots, N$ **do**
6: **Compute** $\underline{K}$ using the LUPQ-decomposition:

$$\underline{K} = (\underline{I} - \gamma \Delta t \ \underline{A})^{-1} \left[\underline{v}^n + \gamma \Delta t \ \underline{\mathfrak{s}}(t^n + \gamma \Delta t) \right]$$

7:

$$\underline{F} = \underline{A} \ \underline{K} + \underline{\mathfrak{s}}(t^n + \gamma \Delta t)$$

8: **Compute** $\underline{v}^{n+1}$ using the LUPQ-decomposition:

$$\underline{v}^{n+1} = (\underline{I} - \gamma \Delta t \ \underline{A})^{-1} \left[\underline{v}^n + \Delta t \ (1 - \gamma) \ \underline{F} + \gamma \Delta t \ \underline{\mathfrak{s}}(t^n + \Delta t) \right]$$

9: **end for**
10: **Return** the $\underline{v}^n$ values for the time indices $n = 1, 2, \ldots, N$.

5.5 Trapezoidal Rule - 2nd Order Backward Differentiation Formula (TR-BDF2)

This section represents another efficient implicit method, which is introduced as one of the top methods to solve a Cauchy problem by [72]. The method is referred to as TR-BDF2, which stands for Trapezoidal Rule - 2nd Order Backward Differentiation Formula. This stiffly accurate L-stable diagonally implicit method has been presented by Skvortsov's [72]. This method, like the Rosenbrock implicit method, needs just one LU (LUPQ) decomposition as opposed to simple implicit Runge-Kutta methods, like DIRK.

Algorithm 6 presents the TR-BDF2 method.

Algorithm 6 TR-BDF2

1: **Compute** the DGM constant matrices,
2: **Set** zero (temporal) initial values for fields; $\underline{v}^0 = \underline{0}$,
3: **Set** $\gamma = 1 - \frac{\sqrt{2}}{2}$, $c = 2\gamma$ and $a = \frac{1-\gamma}{2}$,
4: **Do** decomposition $[\underline{L}, \underline{U}, \underline{P}, \underline{Q}] = (\underline{I} - \gamma\Delta t\ \underline{A})$,
5: **for** $n = 1, 2, \ldots, N$ **do**
6: **Compute** $\underline{V}$ using the LUPQ-decomposition:

$$\underline{Y} = \underline{A}\underline{v}^n$$
$$\underline{V} = (\underline{I} - \gamma\Delta t\ \underline{A})^{-1}\left[\underline{v}^n + \gamma\Delta t\ \underline{Y} + \gamma\Delta t\ \underline{\mathfrak{s}}(t^n) + \gamma\Delta t\ \underline{\mathfrak{s}}(t^n + c\Delta t)\right]$$

7: **Compute** $\underline{v}^{n+1}$ using the LUPQ-decomposition:

$$\underline{v}^{n+1} = (\underline{I} - \gamma\Delta t\ \underline{A})^{-1}\left[\underline{v}^n + a\Delta t\ \underline{Y} + a\Delta t\ \underline{A}\ \underline{V} + a\Delta t\ \underline{\mathfrak{s}}(t^n) + a\Delta t\ \underline{\mathfrak{s}}(t^n + c\Delta t) + \gamma\Delta t\ \underline{\mathfrak{s}}(t^n + \Delta t)\right]$$

8: **end for**
9: **Return** the $\underline{v}^n$ values for the time indices $n = 1, 2, \ldots, N$.

5.6 Implicit and Explicit Methods' Evaluation

One can examine the implicit and explicit methods through their two features: memory requirement and execution time. Although memory requirement for the microwave imaging problem performed by TD DGM-BFTS is not the biggest issue, the execution time plays the most crucial role in deciding the optimum approach due to the high computational cost. However the following discussion focuses on speeding up TD inversion solver by choosing the fastest available time-marching method, we should be careful about the accuracy presented by these methods. As the FBTS method is a robust scheme, we present the cases with the same final reconstructed images to have a fair comparison of the implicit and explicit methods.

This section presents a homogeneous non-dispersive 2D TM imaging scenario by which the four time marching methods previously discussed, are evaluated by comparing their execution time and accuracy.

The synthetic imaging example considered here has a simple geometry illustrated in Figure

5.1. Note that all of the meshes in this work are triangular and unstructured, generated by Gmsh [79].

In this example, there are two cylindrical targets tagged as T1 and T2 located asymmetrically inside the cylindrical domain D. Both targets have diameters of 0.028 m, and the imaging domain D has a diameter of 0.07 m. The four transceivers are located at a radius of 0.055 m and angles of $0, \pi/2, \pi, \frac{3}{4}\pi$ with fixed meshes enforced by cylinders of S1, S2, S3, and S4, with a diameter of 0.004 m. This problem is simulated with an absorbing boundary condition at radius 0.066 m.

Note that the transmitters (and receivers) are simulated as point sources in 2D (or line sources in 3D assuming no variation along the third dimension), and the S_is centered on the source locations ensure having a fixed mesh around the sources. These sources' amplitudes, follow equation (5.4) in time with $A_m = 1$ A/m^2 and $\tau = 0.125$ ns. Figure 5.2 shows the frequency response of sources' amplitude.

$$\mathcal{I}_{z,m}(t) = A_m(\frac{t}{\tau})^3(4 - \frac{t}{\tau})e^{-\frac{t}{\tau}} \tag{5.4}$$

The constitutive parameters in this problem are as follows. The whole space of Ω has constitutive of free space or $\varepsilon_r = 1$ and $\mu_r = 1$, while lossless T1 and T2 targets have relative permittivities of 2.5 and 3.0, respectively. Both targets have a relative permeability of $\mu_r = 1$.

We run the implemented forward solver with the 1st order DGM, for the time interval $[0,\ T = 3.3$ ns] with the possible maximum or optimum time step Δt for each of the implicit and explicit methods discussed earlier. Table 5.2 gives these optimum time steps for the specific scenario 1 and the average execution time for each strategy and, for each source, by the same system with the same number of cores on Matlab. These time steps are the maximum amounts of time steps by

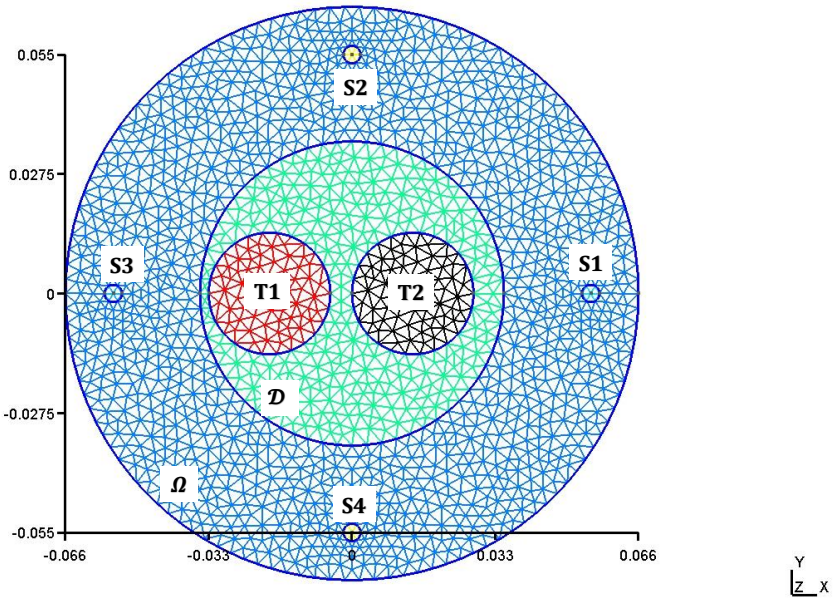

Figure 5.1: Scenario 1: time-marching methods evaluation: two cylindrical shaped scatterers, four sources. ($\#Nodes_{(\Omega)} = 1676$, $\#Elements_{(\Omega)} = 3236$, $\#Elements_{(D)} = 732$)

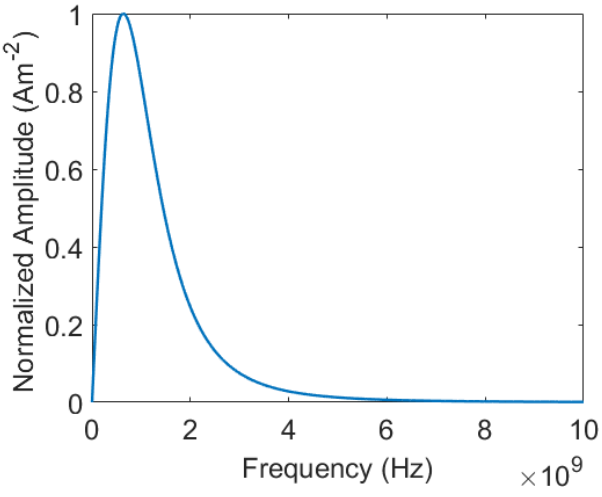

Figure 5.2: Frequency response of the time-domain source signal.

which each time-marching methods can solve the PDEs without messing/deforming the measured fields at the receiver points. Consider that the point of finding the maximum/optimum time step

	Average Execution Time (s)	Optimum Time Step Δt (ps)
LSERK	9.70	2
DIRK	6.73	30
Rosenbrock	7.00	10
TR-BDF2	3.31	30

Table 5.2: Comparison of Some Implicit and Explicit RK methods, when the $\underline{A}$ sparse matrix has the size of 29124×29124.

is lowering the execution and computational time and also lowering the required memory.

The optimum time step for an explicit method is the maximum possible time step before the response becomes unstable. The optimum time step for any of the implicit methods is the maximum amount of this parameter before the fields reshape and lose their smooth form. This reshaping can be observed by comparing the fields in time resulted from the designated implicit method with the resulted fields of an explicit one. Although, replacing an explicit by an implicit, if one increases the time step by, for example, a factor of ten in the implicit scheme, a slight time-shifting has been observed. This time-shifting does not cause any difficulty for the final results because a right calibration process can fix these small discrepancies.

Table 5.2 gives a worthy evaluation perspective about the LSERK, DIRK, Rosenbrock, and TR-BDF2 schemes. According to this table, the TR-BDF2 method outperforms the other three. In this case, the general Forward problem takes about 41 s, which means that the rest of the code including the DGM discretization takes about 7 s in average for each transmitter. In the rest of this thesis, TR-BDF2 will be used as the time-marching method, unless it is noted otherwise.

Figure 5.3 captures the the normalized electric field calculated by the four schemes, measured by receiver 2, when transmitter 1 is active. We can see a small shifting in time in the implicit method with Δt of 30 ps, as expected.

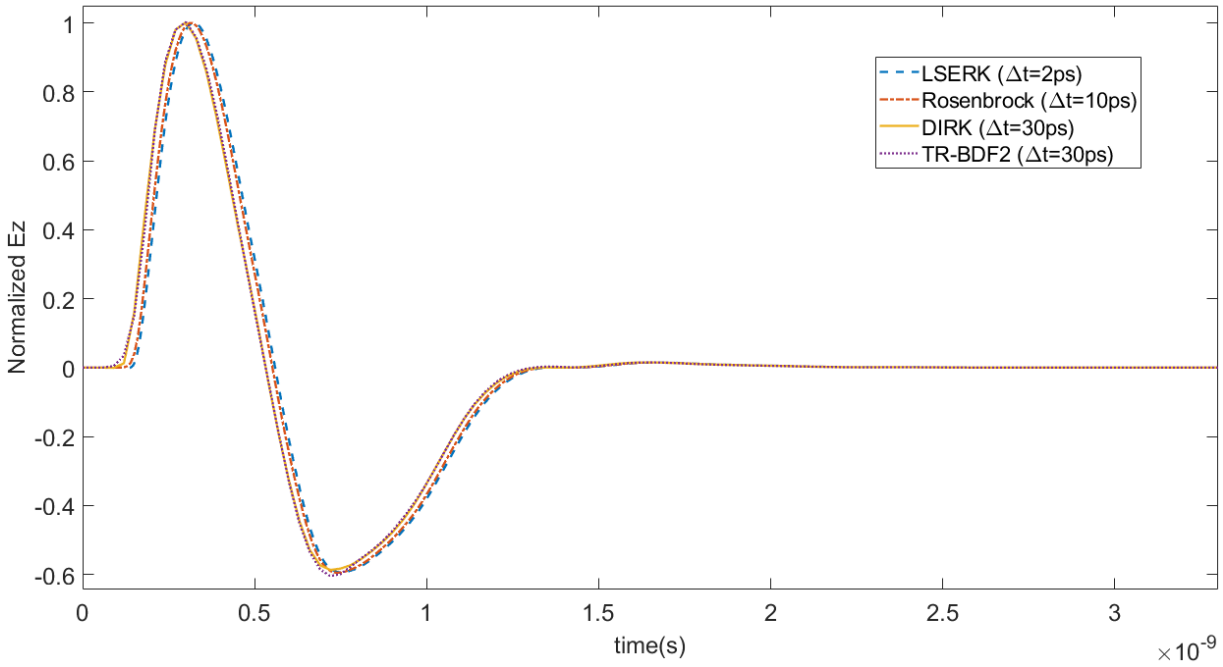

Figure 5.3: The normalized electric field captured by receiver 2 when the transmitter 1 is propagating.

5.7 General Evaluation of the TD DGM Forward Solver

Having presented the DGM formulation we can now validate the implemented forward solver.

Two techniques are used in this section to validate the implemented forward solver. First, we compare the results of the solver to the fields obtained by a FD DGM solver. This FD forward solver has been previously implemented and evaluated by the UofM EIL members [51].

Second, the TD DGM solver is applied to a PEC cylinder enabling a comparison to the available analytic solution for that problem. The frequency response of a known metallic cylinder is analytically available in literature, e.g., [80]. Note that any other known target can be used instead, but the metallic target is chosen in this work because it has a convenient analytic response.

5.7.1 Comparing TD-DGM fields to FD-DGM fields

In this section, we compare the well-proven frequency domain discontinuous Galerkin forward solver with the time domain discontinuous Galerkin forward solver. This comparison is performed by converting the time domain fields to frequency domain fields at discrete frequencies using a discrete Fourier transform. The scattered and incident fields over the domain D - a square with the side of 24.2486 cm - will be compared.

We use a box-like target that we refer to as the BoxTarget. The constitutive parameters of this target are shown in Figure 5.4. The BoxTarget contains a square-shaped shell with 24 cm outer sides and three cylinders enclosed. The permittivity of the lossless square shell is 2.0. The relative permittivities of the three cylinders are $\varepsilon_r = (2.5,\ 3.0,\ 0.0)$ with conductivities of $\sigma_s = (0.0559,\ 0.0,\ 0.0559)$ S/m, respectively. The background is free space and the problem's absorbing boundary is a circle of 34.6 cm radius.

We assume a transmitter located at $(x,\ y,\ z) = (25,\ 0,\ 0)$ cm. The same mesh, shown in Figure 5.5, and the 3rd order basis function for the fields/constitutives are used for the both TD and FD solvers.

The frequency of 2 GHz is chosen for this geometry so that the free space wavelength is about 15 cm. For this reason, the dominant frequency of the source signal in the TD forward solver is chosen to be 2 GHz by selecting τ in equation (5.4) equal to 0.04 ns.

We calculate $E_z^{inc}(\omega, \vec{r})$ using the straightforward summation of equation (5.5). The time step dt, and the final time T for the BoxTarget are chosen to be 30 ps (using the TR-BDF2) and 3 ns, respectively.

$$E_z^{inc}(\omega, \vec{r}) = \sum_{t=0:dt:T} \mathcal{E}_z^{inc}(t, \vec{r}) e^{-j\omega t}\, dt \tag{5.5}$$

The scattered fields (the TD-DGM's responses) are being transformed in the same way from the time domain to the frequency domain.

Note that the FBTS method is implemented based on total fields as discussed in previous

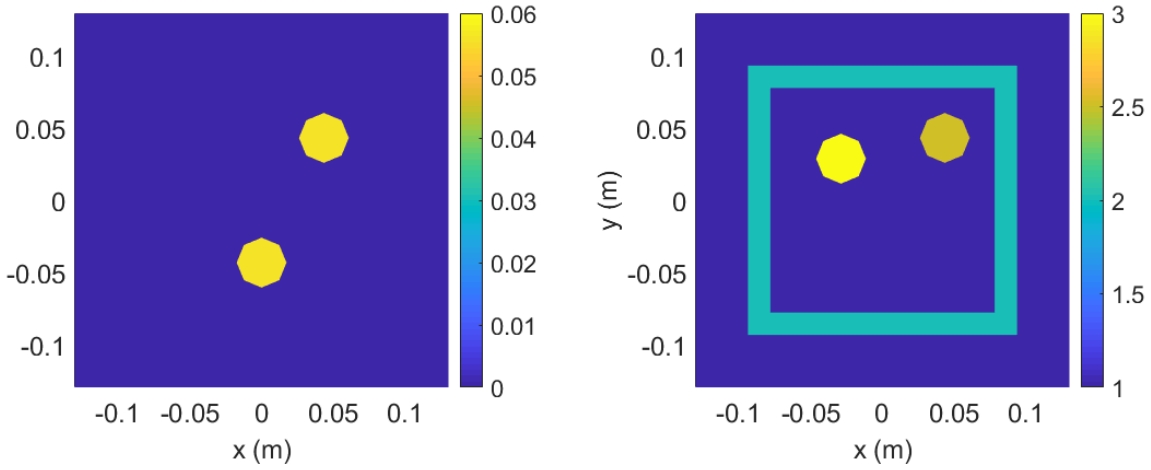

Figure 5.4: (Scenario 2) BoxTarget Properties. (left) conductivity, and (right) permittivity.

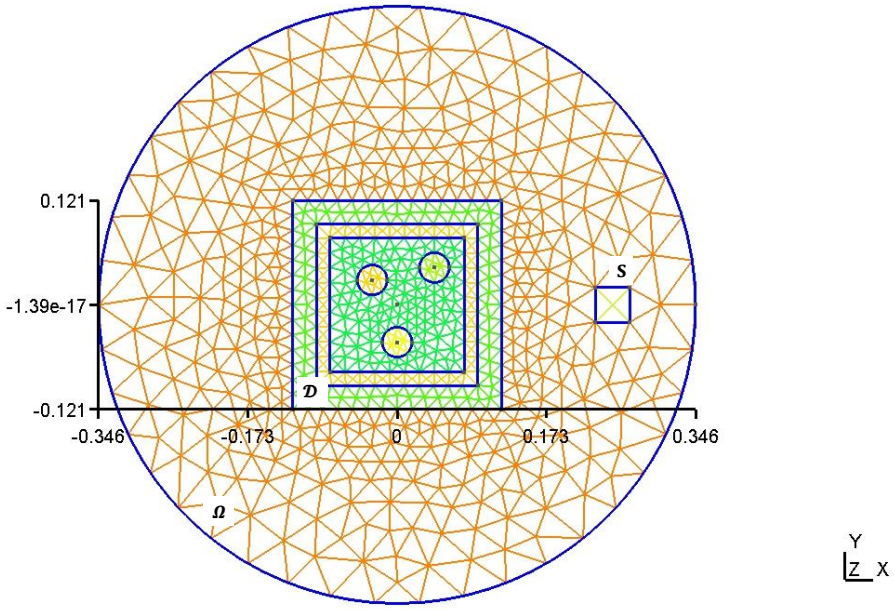

Figure 5.5: (Scenario 2) The forward solvers' mesh for the BoxTarget.

chapters. The TD method's scattered fields are being calculated by subtracting the total fields with (total fields) and without (incident fields) the presence of the BoxTarget. The reason we illustrate incident and scattered fields separately here, is to better compare this modality (FBTS)

with the FD method.

In all of the related figures, the right column shows the results of the TD DGM while the FD results are in the left column. The first, second, and third rows show E_z, H_x, and H_y. The figures demonstrate that the general shape of the TD and FD results are the same. Differences in the results are attributed to the following:

Consider that the FD-DG method's incident fields are being calculated analytically using the Green's function in free space, which gives us an ideal response in the domain D. However, the incident field by FBTS is actually the total field computed without the presence of any target, so the (incident) field has interactions with the boundary. Besides, equation (5.5) is an estimation of the Fourier transform. For the ideal case, the summation has to be an integral, and the limits of this integral have to be infinity.

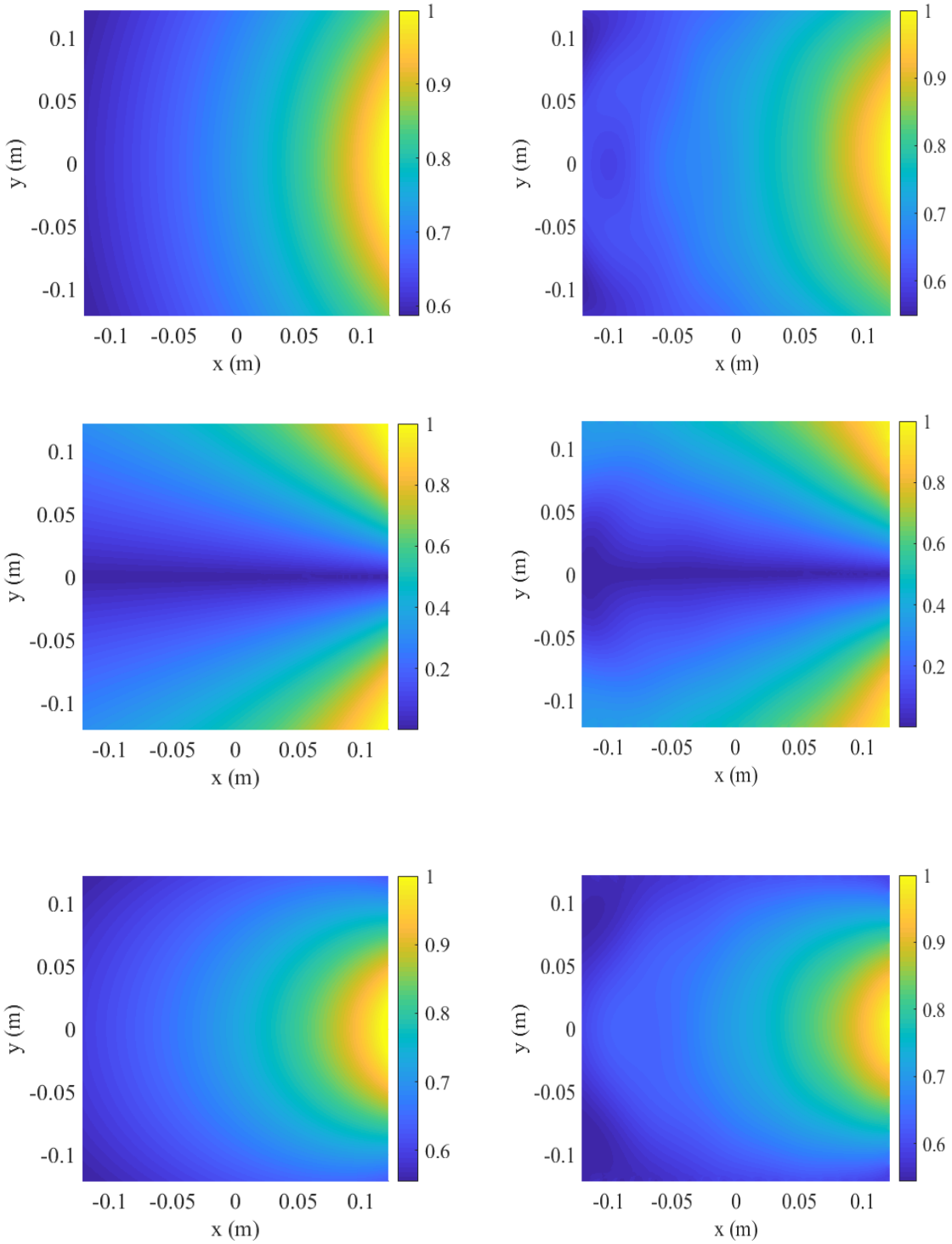

Figure 5.6: The normalized amplitude of the incident E_z (first row), H_x (second row) and H_y (third row) by the FD-DGM (left) and the TD-DGM (right) at 2 GHz.

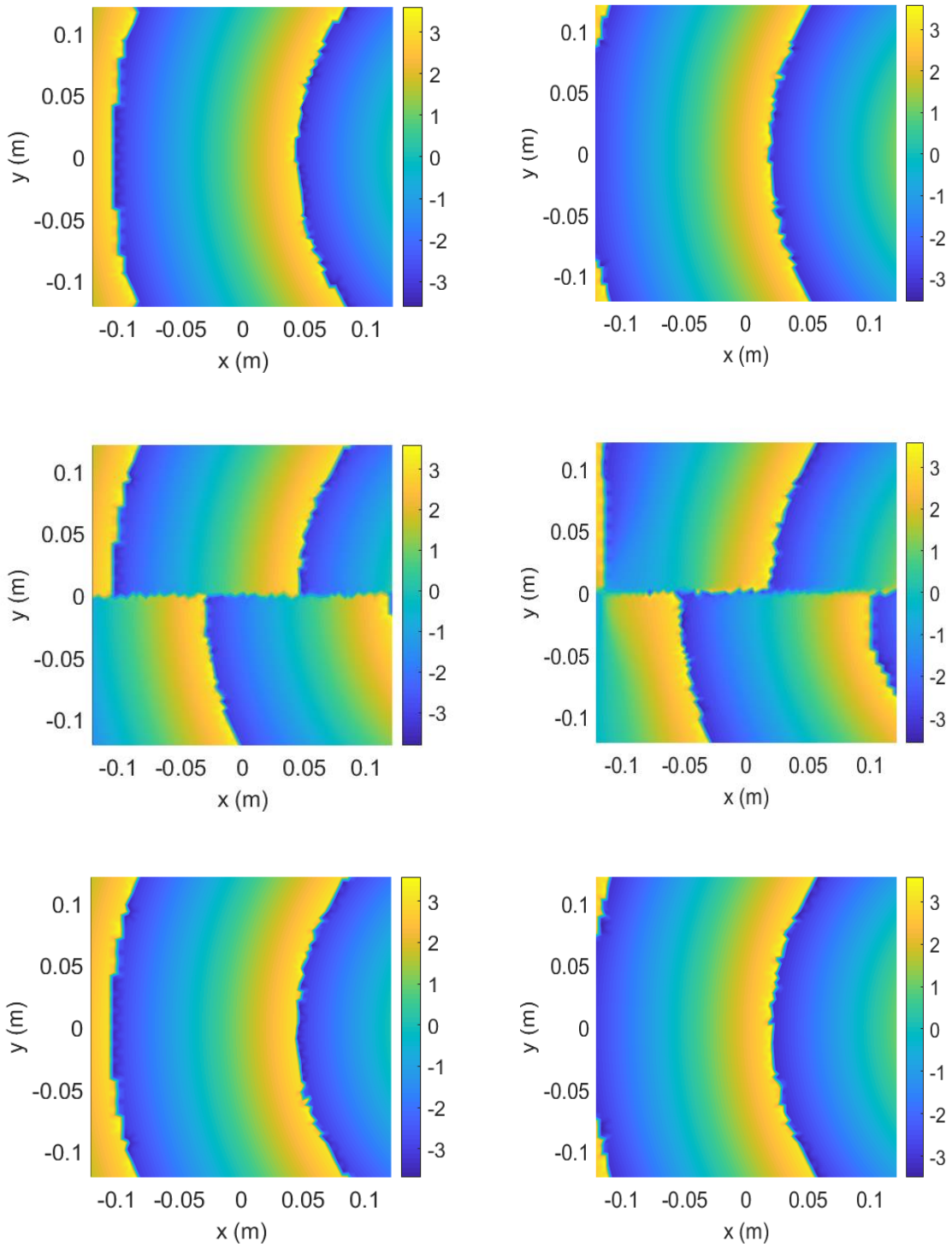

Figure 5.7: The phase of the incident E_z (first row), H_x (second row) and H_y (third row) by the FD-DGM (left) and the TD-DGM (right) at 2 GHz.

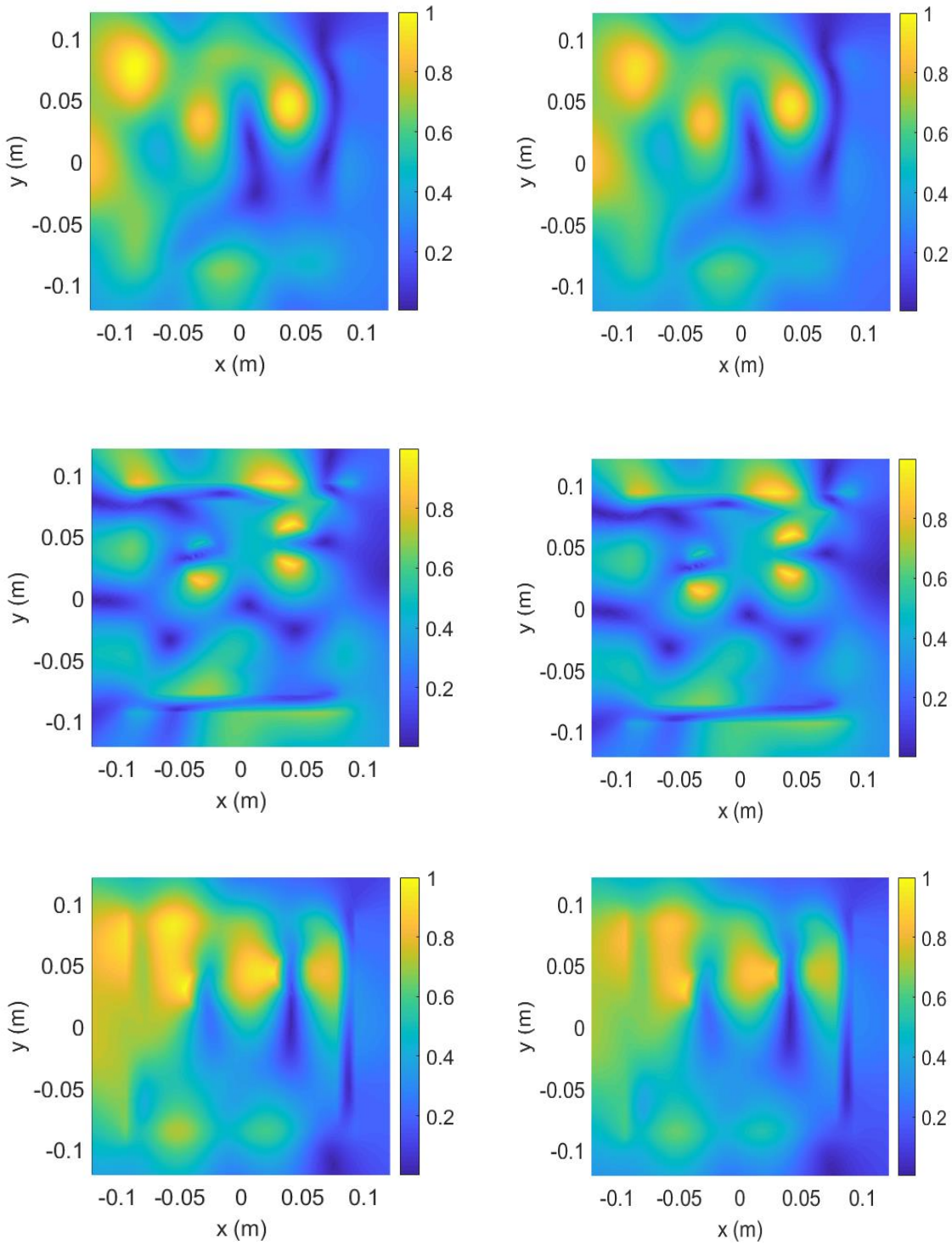

Figure 5.8: The normalized amplitude of the scattered E_z (first row), H_x (second row) and H_y (third row) by the FD-DGM (left) and the TD-DGM (right) at 2 GHz.

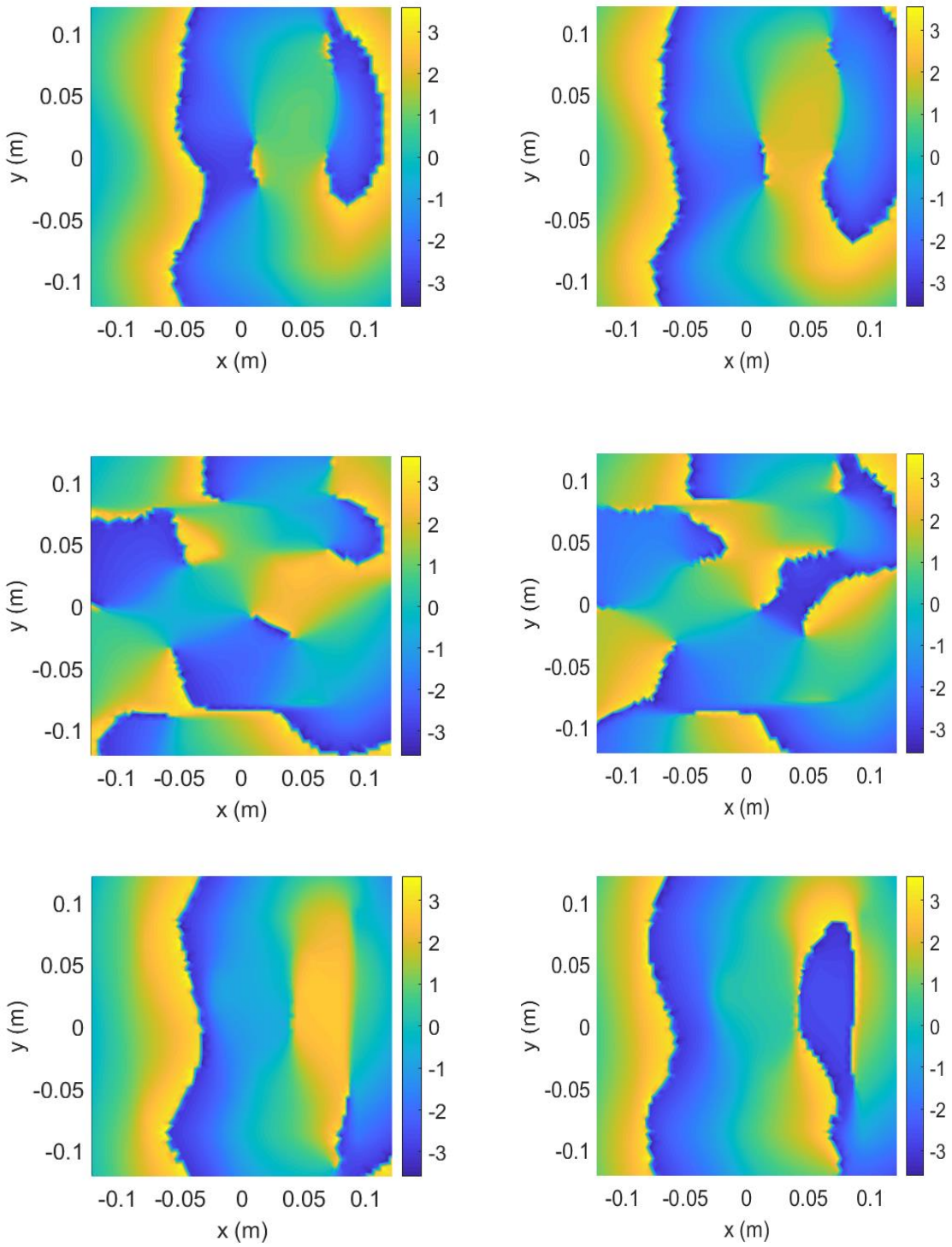

Figure 5.9: The phase of the scattered E_z (first row), H_x (second row) and H_y (third row) by the FD-DGM (left) and the TD-DGM (right) at 2 GHz.

5.7.2 Analytic PEC Cylinder Comparison

This section compares the TD-DGM code to the analytic solution for a PEC cylinder. This target will be used again in forthcoming chapters as a calibration object for experimental examples. This scenario's geometry is shown in Figure 5.10, consists of a circular PEC cylinder in free space. The metallic cylinder (MC) target is located at the center of the imaging domain D. The target has an external diameter of 0.0889 m, and the imaging domain's diameter is 0.15 m. Eight transceivers are located equidistantly on the measuring domain (circle) with a radius of 0.1525 m. This problem is simulated with an absorbing cylindrical boundary at radius 0.44 m. The source amplitudes follow the equation (5.4) in time with $A_m = 1$ A/m^2 and $\tau = 0.04$ ns (with dominant frequency of 2 GHz).

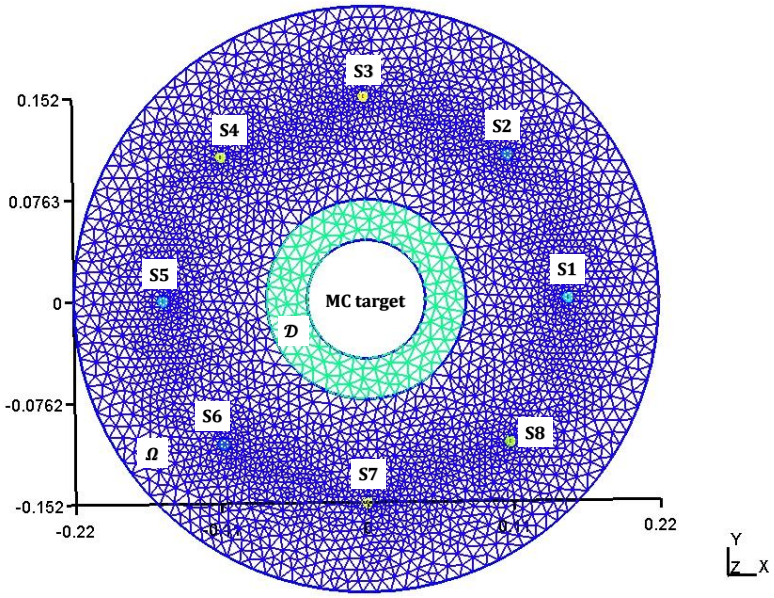

Figure 5.10: Imaging Scenario 3: a metallic cylinder target, eight sources

The figure 5.11 illustrates the analytic answer (blue graph) of scenario 3 versus the simulated

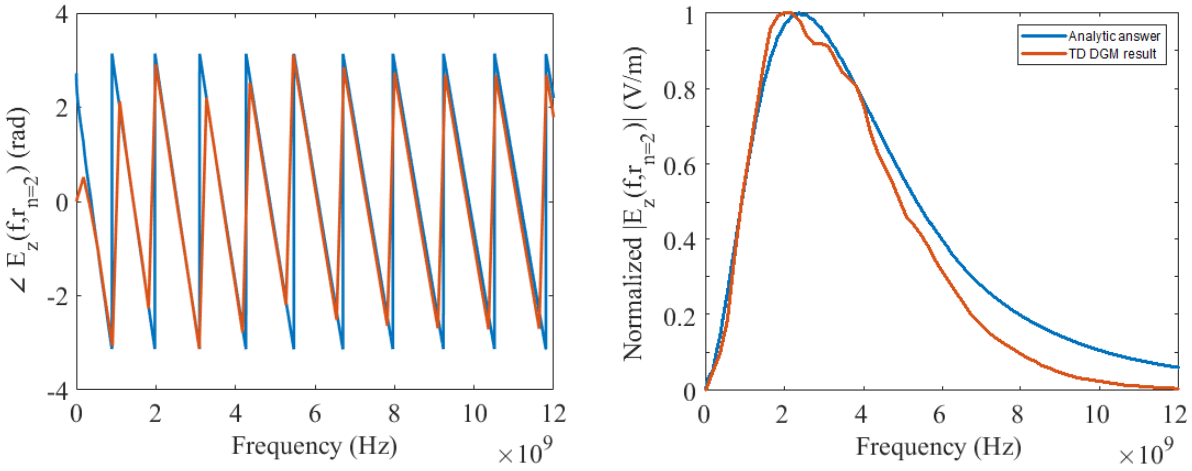

Figure 5.11: Analytic answer vs. TD DGM result. Amplitude (right) and phase (left) of the scattered electric field by transmitter 1 at receiver 2 from the metallic cylinder target.

results of the TD DG method (red graph) in frequency domain. We picked the first transmitter and second receiver pair of scattered electric field to show here, but other pairs have similar behaviour.

Although the phases in 5.11-a are nicely aligned, the amplitudes in Figure 5.11-b do not completely aligned. This slight mismatch is again due to total fields interacting with the boundary in the TD DGM forward solver. This discrepancy can be calibrated, and as will be shown in Chapter 8, the forward model works sufficiently well for high-quality experimental inversion.

Chapter 6

DGM-FBTS

The previous chapter time-integrated the DGM system of linear ODEs, resulting in the DGM time-domain forward solver. This chapter combines DGM with FBTS leading to the DGM-FBTS inversion algorithm.

After initializing the inverse problem and operating the forward- and backward-in-time solvers, we compute the discretized gradients based on equation (3.48) and features of the DGM basis discussed in Chapter 4. Once the gradients are computed, the conjugate gradient method can be applied.

6.1 Discrete Gradients in Ω

To apply the Conjugate Gradient algorithm we must first calculate the gradients of the cost functional with respect to the unknown (constitutive) parameters. Specifically, we compute them using the DGM discretization.

Using the DGM basis functions, the continuous form of the fields $\vec{w}_{1m}(\underline{p}, t, \vec{r})$ and $\vec{v}_{1m}(\underline{p}, t, \vec{r})$

related to transmitter m, in element n are approximated as:

$$\begin{aligned}\vec{w}_{1m}^{n}(\underline{p},t,\vec{r}) &\approx \sum_{k=1}^{N_p} \vec{w}_{1m}(\underline{p},t,\vec{r}_k^{\,n})\ \ell_k^n(\vec{r}) \\ &\approx (\underline{\ell^n(\vec{r})})^{\intercal}\ \underline{\vec{w}_{1m}^{n}(\underline{p},t)}, \qquad (6.1)\\ \vec{v}_{1m}^{n}(\underline{p},t,\vec{r}) &\approx \sum_{k=1}^{N_p} \vec{v}_{1m}(\underline{p},t,\vec{r}_k^{\,n})\ \ell_k^n(\vec{r}) \\ &\approx (\underline{\ell^n(\vec{r})})^{\intercal}\ \underline{\vec{v}_{1m}^{n}(\underline{p},t)} \qquad (6.2)\end{aligned}$$

where $\ell_k^n(\vec{r})$ is the kth Lagrange polynomial of order p on V_n

Recall that the gradient with respect to the optical permittivity is:

$$\underline{\mathcal{G}}_{\underline{\varepsilon}_\infty}(\underline{p},\vec{r}) = 2\sum_{m=1}^{M}\int_0^T \vec{w}_{1m}(\underline{p},t,\vec{r})\ \partial_{c_0 t}\vec{v}_{1m}(\underline{p},t,\vec{r})\ dt.$$

In the following, we discretize this gradient; the remaining gradients can be discretized analogously. By substituting equations (6.1)-(6.2) into this gradient, an approximation for the continuous form of this gradient is:

$$\underline{\mathcal{G}}_{\underline{\varepsilon}_\infty}^{n}(\underline{p},\vec{r}) \approx 2\sum_{m=1}^{M}\int_0^T \left((\underline{\ell^n(\vec{r})})^{\intercal}\ \underline{\vec{w}_{1m}^{n}(\underline{p},t)}\right)\ \partial_{c_0 t}\left((\underline{\ell^n(\vec{r})})^{\intercal}\ \underline{\vec{v}_{1m}^{n}(\underline{p},t)}\right)\ dt.$$

However, the continuous form of this approximate gradient can be recovered by the value of the gradient at the location of nodal basis points in the element n, so it suffices to calculate:

$$\underline{\mathcal{G}}_{\underline{\varepsilon}_\infty}(\underline{p},\vec{r}_k^{\,n}) = 2\sum_{m=1}^{M}\int_0^T \vec{w}_{1m}(\underline{p},t,\vec{r}_k^{\,n})\ \partial_{c_0 t}\vec{v}_{1m}(\underline{p},t,\vec{r}_k^{\,n})\ dt,$$

for $k = 1 : N_p$. Having expanded the fields to order P and the constitutive parameters to order

R, the interpolation matrix $\boldsymbol{\mathcal{V}}^{RP}$ [1] projects Pth order nodal coefficients of the gradients to Rth order nodal coefficients.

$$\underline{\mathcal{G}_{\varepsilon_\infty}(\underline{p})} = \boldsymbol{\mathcal{V}}^{RP}\left(2\sum_{m=1}^{M}\int_0^T \underline{\vec{w}_{1m}(\underline{p},t)}\ \partial_{c_0 t}\underline{\vec{v}_{1m}(\underline{p},t)}\ dt\right) \tag{6.3}$$

Equation (6.3) is the discrete form of the TD cost functional gradient due to the optical permittivity. The rest of the gradients are likewise easily determined.

6.2 The DGM Discrete Conjugate Gradient Solution

Having calculated the necessary discrete gradients using the DGM field coefficients, this section fills in the rest of the steps used to reconstruct a target image.

6.2.1 Search Direction

After computing the gradients, we update the search direction $\underline{h_{i+1}}^{\mathcal{X}}$ for each of the unknown parameters $\mathcal{X} = \varepsilon_\infty,\ \Delta\varepsilon_r,\ \mu_r,\ \sigma_s,\ \tau_{rr}$, using the following relation. Here, i denotes the iteration index.

$$\underline{h_{i+1}}^{\mathcal{X}} = \underline{g_{i+1}}^{\mathcal{X}} + \gamma_i^{\mathcal{X}}\ \underline{h_i}^{\mathcal{X}} \tag{6.4}$$

Fletcher-Reeves [81] or Polak-Ribiere-Polyak [82] schemes are commonly used to update the parameter γ_i, as the final results. We witnessed no benefit of one of these techniques over the other in the examples tested in this thesis. Note that we need different search directions for different parameters of $\mathcal{X}$, and the line-search is in the negative direction of the gradients, so $\underline{g} = -\underline{\mathcal{G}}$ for each of the parameters $\mathcal{X}$.

[1] For the cases that $P < R$, we have to be careful about finding the right interpolation matrix $\boldsymbol{\mathcal{V}}^{RP}$, otherwise it leads to losing data. The process of calculating this operator is described in [1].

Fletcher-Reeves

γ_{i+1}^{FR} is the Fletcher-Reeves search direction for the current iteration of the inverse solver, where $(\underline{\cdot}, \underline{\cdot})_{\mathcal{D}}$ is the inner product of two vectors over the imaging domain $\mathcal{D}$.

$$\gamma_{i+1}^{FR} = \frac{(\underline{g_{i+1}},\ \underline{g_{i+1}})_{\mathcal{D}}}{(\underline{g_i},\ \underline{g_i})_{\mathcal{D}}}. \tag{6.5}$$

Polak-Ribiere-Polyak

The Polak-Ribiere-Polyak search direction γ_{i+1}^{PRP} for the current iteration of the inverse solver is:

$$\gamma_{i+1}^{PRP} = \frac{(\underline{g_{i+1}},\ \underline{g_{i+1}} - \underline{g_i})_{\mathcal{D}}}{(\underline{g_i},\ \underline{g_i})_{\mathcal{D}}}. \tag{6.6}$$

6.2.2 Search Distance/Step

The next step of the Conjugate Gradient optimization technique is finding a proper search distance (or search step) $\Gamma > 0$ such that:

$$f(\underline{p}_i + \Gamma_i\ \underline{H}_i) = \arg\min_{\Gamma} \{f(\underline{p}_i + \Gamma\ \underline{H}_i) \mid \Gamma \geq 0\}. \tag{6.7}$$

Here, f is our cost functional, $\underline{p}_i$ is the (reconstructed) constitutive parameters vector of Equation (2.34) at iteration i and the vector $\underline{H}_i$ is the concatenation of the search directions at the current iteration:

$$\underline{H} = \begin{bmatrix} \underline{h}^{\varepsilon_\infty} \\ \underline{h}^{\Delta\varepsilon_r} \\ \underline{h}^{\mu_r} \\ \underline{h}^{\sigma_s} \\ \underline{h}^{\tau_{rr}} \end{bmatrix}. \tag{6.8}$$

Here we need an algorithm to find an approximate minimum of a function, f, of one real variable, Γ, by limited-precision arithmetic. The derivative $f'(\Gamma)$ is challenging to compute, so

a method that does not need the function derivative is desirable. Since the evaluation of f is computationally expensive for this specific problem, a technique should be used to guarantee convergence to the correct answer within some prescribed tolerance, using just a small number of cost functional evaluations.

To this end, we are after an algorithm that is guaranteed to succeed in finding the local minimum of the one variable function f, over the interval $[a_{lm},\ b_{lm}]$, in the presence of rounding error, in a reasonable time [83] (same things as small number of points). An algorithm providing all of these requirements, which uses the combination of Golden Section Search (GSS) - similar to Bisection zero finding algorithm - and Successive Parabolic Interpolation (SPI) - similar to zero finding algorithm of Successive Linear Interpolation - [83], is used in this work. SPI method has a super-linear convergence, but there is no convergence guarantee when it is used alone. GSS, on the other hand, has a linear convergence (slower) with the guarantee of convergence. Mixing GSS and SPI methods, we have a fast enough minimum finding algorithm that sure converges (to either local or global minimum) [83].

Consider that, like most of the minimization methods, it is impossible to be sure that the global minimum has been found by the combination of GSS and SPI. The reader may wonder why we did not use another method as a remedy in this case. The answer is: those methods usually need upper bound derivatives (first and second) as prior information, and that brings more computational cost to the problem, which we wish to avoid [83].

The GSS-SPI algorithm will find the unique minimum if f is unimodal[2] in the absence of rounding errors. A computed approximation to a unimodal function (e.g., this study's case) is δ-unimodal for some positive δ, where the size of δ depends on the function and the precision of computation. Giving an upper bound on the error to this algorithm, we can justify it in the presence of rounding error [83].

[2]Please find the definitions related to unimodality in Appendix B.

GSS-SPI - Local Minimum Seeking

This section briefly reviews the iterative algorithm of the hybrid golden section search and successive parabolic interpolation. For more details, the readers are referred to [83].

The input parameters of this algorithm are the domain limits $a_{lm},\ b_{lm}$, the positive absolute tolerance tl, the relative tolerance ϵ, an initial value for the extreme point x, and of-course the function f (the matrices $\underline{p}_i$, $\underline{H}_i$, and the forward solver).

The function f is defined on the interval $[a_{lm},\ b_{lm}]$ at each iteration of the CG method. The tl and ϵ define the tolerance $Tol = |x|\ \epsilon + tl$, which is the minimum distance between the evaluated points of f. In this algorithm, the function f is assumed to be δ-unimodal with the constraint of $\delta < Tol$ and the x is the approximation of the global minimum of function f with the maximum error of $3 \times Tol$[3]. When the function f is not δ-unimodal on the designated interval, the algorithm gives the local minimum instead of the global minimum.

Suppose we represent the relative machine precision[4] ($\beta^{(1-\tau)}$ for τ-digit truncated floating-point arithmetic with base β) with parameter ϵ_{mach}. In that case, the parameter ϵ has to be smaller than $2\ \epsilon_{mach}$, and it should not be significantly smaller than $\sqrt{\epsilon_{mach}}$. For the details and the reasons of these selection, the readers are referred to [83].

According to [83], if ignoring the rounding error and f function has a continuous second derivative, the hybrid GSS-SPI's convergence is expected to be super-linear with the least(minimum) order of about 1.3247.

The GSS-SPI algorithm's pseudocode is illustrated in detail in Algorithm 7. At each iteration of this algorithm, there are six points, namely a_{lm}, b_{lm}, u, v, w and x. A local minimum lies in the interval $[a_{lm}, b_{lm}]$, and this interval changes for each GSS-SPI iteration. The point x is the updated location of the local minimum at each iteration. The next lowest value of f is shown by $f(w)$. v reserves the previous amount of the parameter w, and the last point where we calculate

[3]Please refer to [83] for the details.

[4]Machine precision is the smallest number ϵ_{mach} such that the difference between 1 and $1 + \epsilon_{mach}$ is nonzero.

Algorithm 7 GSS-SPI for ith iteration of the inverse solver Adapted from [83]

Initialize $c = \frac{3-\sqrt{5}}{2}$, $v = w = x = a_{lm} + c\ (b_{lm} - a_{lm})$ and $d = e = 0$,
Compute the cost functional due to the constitutive parameter vector of $(\underline{p}_i + x\ \underline{H}_i)$ or $f(x)$,
Initialize $fv = fw = fx = f(x), Iteration_{lm} = 1$,

while (1) **do**
  Set $m = \frac{a_{lm}+b_{lm}}{2}$, $Tol = \epsilon\ |x| + tl$, $t2 = 2\ Tol$,
  if $|x - m| > (t2 - \frac{b_{lm}-a_{lm}}{2})$ **then**
    Set $p = q = r = 0$
    if $|e| > Tol$ **then**
      % Parabola Fitting:
      $r = (x - w)(fx - fv)$, $q = (x - v)(fx - fw)$
      $p = q(x - v) - r(x - w)$, $q = 2(q - r)$
      if $q > 0$ **then** $p = -p$ **else** $q = -q$
      $r = e,\ e = d$
    end if
    if $(|p| < |\frac{qr}{2}|) \wedge (p > q(a_{lm} - x)) \wedge (p < q(b_{lm} - x))$ **then**
      % Parabolic Interpolation:
      $d = \frac{p}{q},\ u = x + d$
      % $f(.)$ needs to be far enough from a_{lm} and b_{lm}:
      if $(u - a_{lm} < t2) \vee (b_{lm} - u < t2)$ **then** $d =$ **if** $x < m$ **then** Tol **else** $-Tol$
    else
      % Golden Section Search:
      $e =$ (**if** $x < m$ **then** b_{lm} **else** a_{lm}) $- x,\ d = c\ e$
    end if
    % $f(.)$ needs to be far enough from x:
    $u = x +$ (**if** $|d| \geqslant Tol$ **then** d **else if** $d > 0$ **then** Tol **else** $-Tol$)
    Compute the cost functional due to the constitutive parameter vector of $(\underline{p}_i + u\ \underline{H}_i)$ or $f(u)$, $fu = f(u)$
    % Updating the five points a_{lm}, b_{lm}, v, w and x:
    if $fu \leqslant fx$ **then**
      if $u < x$ **then** $b = x$ **else** $a = x,\ \ v = w, fv = fw, w = x, fw = fx, x = u, fx = fu$
    else
      if $u < x$ **then** $a = u$ **else** $b = u$,
      if $fu \leqslant fw \vee w = x$ **then** $v = w, fv = fw, w = u, fw = fu$
      else if $fu \leqslant fv \vee v = x \vee v = w$ **then** $v = u, fv = fu$,
      end if
    end if
  else
    Break!
  end if
  $Iteration_{lm} = Iteration_{lm} + 1$
end while
Return $\Gamma_i = x$ and $Iteration_{lm}$.

the function f is stored in u (Figure 6.1).

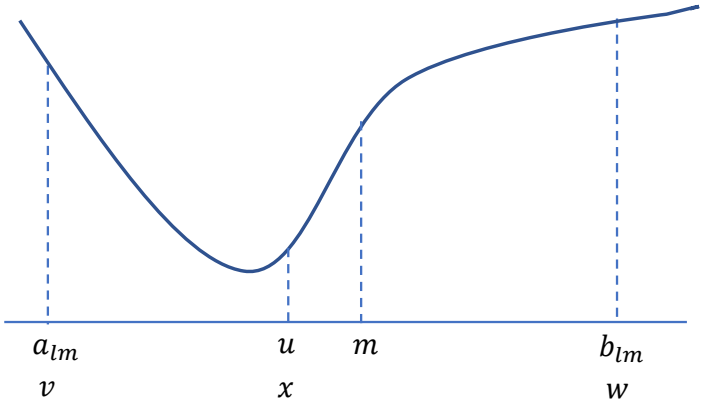

Figure 6.1: A possible configuration of the points in GSS-SPI.

On line 6, m gives the midpoint of the interval. If $max(x-a,\ b-x)$ is less (or equal) than 2 Tol (criteria in line 7), the point x would be our local minimum point and the algorithm terminates. Otherwise, the next step is fitting a parabola to the $(v, f(v))$, $(w, f(w))$, $(x, f(x))$ points such that $x + \frac{p}{q}$ is its turning point. The points p and q are calculated as:

$$p = \pm[(x-v)^2(f(x)-f(w)) - (x-w)^2(f(x)-f(v))], \tag{6.9a}$$

$$q = \mp 2[(x-v)(f(x)-f(w)) - (x-w)(f(x)-f(v))]. \tag{6.9b}$$

If x is close to the local minimum, the $\frac{p}{q}$ correction would be small. In line 14, after fitting the parabola, we put $e = \frac{p}{q}$ for the next cycle. If $x + \frac{p}{q} \notin (a_{lm}, b_{lm})$, or $|\frac{p}{q}| \geqslant \frac{|e|}{2}$, the golden section search starts, so that the parameter u updates as:

$$u = \begin{cases} \frac{\sqrt{5}-1}{2}x + \frac{3-\sqrt{5}}{2}a_{lm}, & x \geqslant m \\ \frac{\sqrt{5}-1}{2}x + \frac{3-\sqrt{5}}{2}b_{lm}, & x < m \end{cases}. \tag{6.10}$$

Otherwise, a parabolic interpolation starts by taking u as $x + \frac{p}{q}$, except that making the distances $|u-x|$, $u - a_{lm}$, and $b-u$ have to be greater (or equal) than Tol. Next, the other parameters

get updated accordingly and the cycle is repeated.

Note that this algorithm never calculates the function f at two points closer than Tol. Therefor, the δ-unimodality condition of f for some $\delta < Tol$ is enough to have the minimum accuracy of $2\ Tol + \delta$ by the algorithm [83].

6.2.3 Finalizing the Inverse Algorithm and Stopping Condition

The last step of the conjugate gradient iterative method is to update the constitutive parameters for iteration $i+1$ based on the computed/calculated search distance Γ:

$$\underline{p}_{i+1} = \underline{p}_i + \Gamma\ \underline{H}_i \tag{6.11}$$

After updating these parameters, the CG algorithm continues to minimize the cost functional iteratively.

There exist many stopping conditions for iterative algorithms in the literature, e.g., relative error change [1, 2, 84, 41], and KS test [85]. However, it is still common in MWI to just run some iterations and stop the algorithm manually while monitoring inversion algorithm convergence. This thesis, also, does not have a robust stopping condition except stopping the algorithm when the cost functional minimization process slows down drastically, in conjunction with experience developed running this algorithm.

Chapter 7

Ultrasound Inverse Problems

The inversion algorithm developed here was motivated by electromagnetic imaging problems in microwave range of frequency (300 MHz to 300 GHz). Further still, the mechanical wave propagation of ultrasound (frequency above human hearing (20 KHz)) energy can be represented in a similar fashion, making the formulation capable of ultrasound imaging. Here, an ultrasound TD solver (US-TD-FBTS), is presented which results in an inverse solver capable of reconstructing, the ultrasound parameters of unknown objects.

In this chapter, we provide the details for converting the time-domain forward and inverse solvers to ultrasound, with the goal of reconstructing some images for its preliminary performance evaluation. Here in this thesis, we use the non-dispersive assumption for the ultrasound waves.

7.1 Basics of Ultrasound Wave Propagation

In this section, we start with the basics of lossless ultrasound wave propagation to derive the required formulations in the time domain, using an approach similar to that of previous works by UofM-EIL members, e.g., [86, 87].

The two primary laws of ultrasound waves, which lead us to the final equations of ultrasound

wave propagation, are conservation of mass and conservation of linear momentum.

According to the mass conservation law (Equation (7.1a)), the mass inside an isolated volume $V(t)$ always remains constant during the volume's reshaping and movements by time. Here $\varrho(t,\vec{r})$ [kg/m^3] is the fluid mass density.

Also the linear momentum conservation law, shown in Equation (7.1b), states the continuum generalization of Newton's second law by parameters of the volume velocity $\vec{U}(t,\vec{r})$ [m/s], fluid mass density $\varrho(t,\vec{r})$ [kg/m^3], and the fluid pressure $P(t,\vec{r})$ [N/m^2]. The assumption is that the only source/form of force comes from the pressure gradients of the fluid volume[1], and the viscosity and external forces are zero.

$$\frac{d}{dt}\int_{V(t)} \varrho(t,\vec{r})\; dv = 0, \tag{7.1a}$$

$$\frac{d}{dt}\int_{V(t)} \varrho(t,\vec{r})\; \vec{U}(t,\vec{r})\; dv = -\int_{V(t)} \nabla P(t,\vec{r})\; dv. \tag{7.1b}$$

Before going forward, we separate the variational and the average parts of the ultrasound parameters according to the following definitions:

$$\begin{cases} P(t,\vec{r}) = P_0 + \mathbb{p}(t,\vec{r}), \\ \vec{U}(t,\vec{r}) = \vec{U}_0 + \vec{u}(t,\vec{r}), \\ \varrho(t,\vec{r}) = \rho(\vec{r}) + \rho_1(t,\vec{r}), \end{cases} \tag{7.2}$$

where P_0, $\vec{U}_0$, and $\rho(\vec{r})$ are the average quantities over the volume $V(t)$. P_0 is constant and $\vec{U}_0 = 0$ as the fluid is assumed to be at rest. Note that by these definitions, the parameters $\mathbb{p}(t,\vec{r})$, $\vec{u}(t,\vec{r})$, and $\rho_1(t,\vec{r})$ are assumed to be small fluctuations such that $|\mathbb{p}(t,\vec{r})| \ll |P_0|$ and $|\rho_1(t,\vec{r})| \ll |\rho(\vec{r})|$.

[1] According to [88, 89, 86], piezoelectric transducers, which are usually used as ultrasound transducers, insonificate target object(s) by generating ultrasonic pressure waves. The transducer's structure deforms and generates local pressure changes in the propagating medium (water), When it is driven with a voltage signal. Then, transducers in receiving mode detect these pressure changes after passing through the medium and target(s). The received pressure changes at the receivers cause deformation in the piezoelectric crystals, generating electronically recordable voltage signals.

Defining the average density as a function of space helps to have inhomogeneous media in small-amplitude modelling [86].

After substituting the new parameters (7.2) in (7.1), and some manipulations [86], the mass and momentum conservation laws result:

$$\partial_t \rho_1(t,\vec{r}) + \nabla \cdot (\rho(\vec{r})\ \vec{u}(t,\vec{r})) = 0, \tag{7.3a}$$

$$\rho(\vec{r})\ \partial_t \vec{u}(t,\vec{r}) + \nabla \mathbb{p}(t,\vec{r}) = 0. \tag{7.3b}$$

Equation (7.3a) needs to be modified by omitting ρ_1 before using this set of equations. We introduce an auxiliary relation [86, 90, 87]:

$$\frac{\partial P(t,\vec{r})}{\partial \varrho(t,\vec{r})} = \frac{1}{\kappa'(\vec{r})\ \varrho(t,\vec{r})}, \tag{7.4}$$

where κ' is the compressibility parameter, which is the inverse of the average adiabatic bulk modulus of the fluid in units of pressure $(\mathrm{N/m^2})^{-1}$[86, 90, 87]. Substituting the definitions (7.2) into (7.4), we have

$$\frac{\mathbb{p}(t,\vec{r})}{\rho_1(t,\vec{r})} = \frac{1}{\kappa'(\vec{r})\ \rho(\vec{r})}, \tag{7.5}$$

or

$$\rho_1(t,\vec{r}) = \kappa'(\vec{r})\ \rho(\vec{r})\ \mathbb{p}(t,\vec{r}). \tag{7.6}$$

Substituting Equation (7.6) into (7.3a), our set of equations becomes [91]:

$$\kappa'(\vec{r})\ \partial_t \mathbb{p}(t,\vec{r}) + \nabla \cdot \vec{u}(t,\vec{r}) = 0, \tag{7.7a}$$

$$\rho(\vec{r})\ \partial_t \vec{u}(t,\vec{r}) + \nabla \mathbb{p}(t,\vec{r}) = -\nabla \mathbb{p}^{src}(t,\vec{r}), \tag{7.7b}$$

where $F^{src} = -\nabla \mathbb{p}^{src}$ is the source term which consists of the imposing force to the system.

Comparing equations (7.7a) and (7.7b) with the non-dispersive lossless electromagnetic set of equations of (2.3) (when $\sigma_s = 0$ and $\vec{\mathcal{J}}_M$=0), one can setup a duality between the two sets of EM and US equations as follows:

$$\begin{aligned}
EM &\rightleftharpoons US \\
\varepsilon &\rightleftharpoons \kappa' \\
\mu &\rightleftharpoons \rho \\
c^{em} = \frac{1}{\sqrt{\mu\varepsilon}} &\rightleftharpoons c^{us} = \frac{1}{\sqrt{\rho\kappa'}} \\
Z^{em} = \sqrt{\frac{\mu}{\varepsilon}} &\rightleftharpoons Z^{us} = \sqrt{\frac{\rho}{\kappa'}} \\
\vec{\mathcal{E}} &\rightleftharpoons \mathbb{p} \\
\vec{\mathcal{H}} &\rightleftharpoons \vec{u} \\
\vec{\mathcal{J}}_E &\rightleftharpoons \nabla \mathbb{p}^{src} \\
\pm\nabla\times &\rightleftharpoons \nabla.\ (\nabla)
\end{aligned}$$

where c^{em} and Z^{em} are the speed and impedance of electromagnetic wave in a media with constitutive parameters μ and ε. c^{us} and Z^{us} are the ultrasound speed and impedance in a media with constitutive parameters ρ and κ'.

To construct a vector of unknowns in ultrasound (similar to the EM), we introduce similar definitions for the parameters of ρ and κ'. We divide the density to two parts; the background density ρ_0, which is usually water with density $\rho_0 = 1000$ (kg/m^3), and the relative density $\rho_r(\vec{r})$ as

$$\rho(\vec{r}) = \rho_0\ \rho_r(\vec{r}). \tag{7.8}$$

The compressibility follows a similar rule

$$\kappa'(\vec{r}) = \kappa'_0\ \kappa'_r(\vec{r}) \tag{7.9}$$

where κ_0' is the background compressibility. If water is taken as the default background, the speed of ultrasound waves would be about $c_0^{us} = 1483$ m/s^2. This makes the background (water) compressibilty equal to $\kappa_0' = 4.5469 \times 10^{-10}$ (N/m^2)$^{-1}$ [92].

After applying normalization factors, similar to the EM case, the ultrasound forward solver is summarize by:

$$\boldsymbol{\mathcal{K}}^{us} \underline{v}^{us} = -\underline{s}^{us}, \tag{7.10}$$

where:

$$\boldsymbol{\mathcal{K}}^{us} = \begin{bmatrix} \kappa_r' \, \partial_{c_0^{us} t} & \nabla\cdot \\ \nabla & \rho_r \partial_{c_0^{us} t} \end{bmatrix}, \qquad \underline{v}^{us} = \begin{bmatrix} v_1 \\ \vec{v}_2 \end{bmatrix} = \begin{bmatrix} \mathbb{p} \\ z_0^{us} \vec{u} \end{bmatrix}, \qquad \underline{s}^{us} = \begin{bmatrix} 0 \\ \vec{s}_2 \end{bmatrix} = \begin{bmatrix} 0 \\ \nabla \mathbb{p}^{src} \end{bmatrix}. \tag{7.11}$$

Note that the normalization process converts derivative ∂_t to $\partial_{c_0^{us} t}$, similar in electromagnetic.

From now on, we limit the ultrasound problem to 2D in x-y plain, so that the parameters have no variation in the z-direction. Assume that the pressure is applied to the system in the z-direction (note that pressure is a scalar, but it acts perpendicular to the surface), so the non-zero velocity is in x- and y-direction in the coordinate system. We can rewrite the ultrasound forward solver matrices 7.11, as the following:

$$\boldsymbol{\mathcal{K}}^{us} = \begin{bmatrix} \kappa_r' \, \partial_{c_0^{us} t} & \partial_x & \partial_y \\ \partial_x & \rho_r \, \partial_{c_0^{us} t} & 0 \\ \partial_y & 0 & \rho_r \partial_{c_0^{us} t} \end{bmatrix}, \qquad \underline{v}^{us} = \begin{bmatrix} \mathbb{p} \\ z_0^{us} \; u_x \\ z_0^{us} \; u_y \end{bmatrix}, \qquad \underline{s}^{us} = \begin{bmatrix} 0 \\ \partial_x \mathbb{p}^{src} \\ \partial_y \mathbb{p}^{src} \end{bmatrix}. \tag{7.12}$$

Based on the analogy between the electromagnetic set of equations and the ultrasound derived equations of (7.12), the procedure for formulating an ultrasound DGM-FBTS inverse solver

[2]Note that the speed of sound in water (as in other mediums) is a function of temperature, e.g. [92] presents it as $c_0^{us} = 1405.610 + 4.59754\ \mathbb{T} - 0.0381796\ \mathbb{T}^2$, where $\mathbb{T}$ [°C] stands for temperature, in the range of 15 °C to 35 °C. In this work, we take this quantity constant and equal to 1483 m/s^2 at the temperature of 20 °C, which is a usual temperature of laboratories.

amounts to reproducing the work of the previous chapters with minor modifications. Although we do not present the procedure here for brevity, the ultrasound gradients with respect to the relative compressibility and relative density in the imaging domain are:

$$\begin{cases} \underline{\mathcal{G}}_{\kappa_r'}(\underline{p}^{us},\vec{r}) = -2\sum\limits_{m=1}^{M}\int_0^T & w_{1m}^{us}(\underline{p}^{us},t,\vec{r})\ \partial_{c_0 t}\mathbb{p}_m(\underline{p}^{us},t,\vec{r})\ dt, \\ \underline{\mathcal{G}}_{\rho_r}(\underline{p}^{us},\vec{r}) = -2\sum\limits_{m=1}^{M}\int_0^T & [w_{2m}^{us}(\underline{p}^{us},t,\vec{r})\ \partial_{c_0 t}[z_0^{us}\ u_{xm}(\underline{p}^{us},t,\vec{r})] + \dots \\ & \qquad w_{3m}^{us}(\underline{p}^{us},t,\vec{r})\ \partial_{c_0 t}[z_0^{us}\ u_{ym}(\underline{p}^{us},t,\vec{r})]]\ dt, \end{cases}$$

where the ultrasound constitutive parameters vector $\underline{p}^{us}$ and the ultrasound field adjoint vector $\underline{w}^{us}$ are:

$$\underline{p}^{us}(\vec{r}) = \begin{bmatrix} \kappa_r'(\vec{r}) \\ \rho_r(\vec{r}) \end{bmatrix}, \tag{7.13}$$

$$\underline{w}^{us}(\underline{p}^{us},t,\vec{r}) = \begin{bmatrix} \vec{w}_1^{us}(\underline{p}^{us},t,\vec{r}) \\ \vec{w}_2^{us}(\underline{p}^{us},t,\vec{r}) \end{bmatrix}. \tag{7.14}$$

7.2 DGM Discretization of Ultrasound Formulations

In this section, we use the DGM method to spatially discretize the ultrasound equations above.

7.2.1 Local DG Volumetric Matrices in Ultrasound

This section is allocated to the DGM local expansions of parameters in the ultrasound PDEs (7.10). In this section we restrict consideration to an arbitrary nth mesh element, and for simplicity superscript n is omitted throughout. Note that the theory is similar to DGM discretization in EM.

Consider testing the ultrasound PDEs (7.10) at a fixed time t by the scalar test function

$\psi(\vec{r})$, where we consider a "strong form":

$$\int_{V_n} \psi(\vec{r})\ \kappa_r'(\vec{r})\ \partial_{c_0^{us}t}\ v_1(t,\vec{r})\ \vec{dr} - \int_{V_n} \psi(\vec{r})\ \nabla\cdot\vec{v}_2(t,\vec{r})\ \vec{dr} + \ldots$$
$$\oiint_{\partial V_n} \psi(\vec{r})\ \hat{n}(\vec{r})\cdot\left(\vec{v}_2(t,\vec{r}) - \vec{v}_2^{\wedge}(t,\vec{r})\right)\vec{dr} = 0, \tag{7.15a}$$

$$\int_{V_n} \psi(\vec{r})\ \rho_r\ \partial_{c_0^{us}t}\ \vec{v}_2(t,\vec{r})\ \vec{dr} + \int_{V_n} \psi(\vec{r})\ \nabla v_1(t,\vec{r})\ \vec{dr} - \ldots$$
$$\oiint_{\partial V_n} \psi(\vec{r})\ \hat{n}(\vec{r})\left(v_1(t,\vec{r}) - v_1^{\wedge}(t,\vec{r})\right)\vec{dr} = \int_{V_n} \psi(\vec{r})\ \vec{s}_2(t,\vec{r})\ \vec{dr}. \tag{7.15b}$$

By adopting the Lagrange polynomial (4.1) as the basis and test functions, and substituting the mass and stiffness matrices, the 2D ultrasound formulations become:

$$\partial_{c_0t}[\underline{v_1(t)}] + \underline{\underline{\kappa_r'}}^{-1}\underline{\underline{\mathcal{D}}}_x\underline{v_{2x}(t)} + \underline{\underline{\kappa_r'}}^{-1}\underline{\underline{\mathcal{D}}}_y\underline{v_{2y}(t)} + \underline{\underline{\kappa_r'}}^{-1}\underline{\underline{\mathcal{M}}}^{-1}\underline{\mathcal{F}^{v1}(t)} = 0\ , \tag{7.16a}$$

$$\partial_{c_0t}[\underline{v_{2x}(t)}] + \underline{\underline{\rho_r}}^{-1}\underline{\underline{\mathcal{D}}}_x\underline{v_1(t)} + \underline{\underline{\rho_r}}^{-1}\underline{\underline{\mathcal{M}}}^{-1}\underline{\mathcal{F}_x^{v2}(t)} = -\underline{\underline{\rho_r}}^{-1}\ \underline{s_{2x}(t)}\ , \tag{7.16b}$$

$$\partial_{c_0t}[\underline{v_{2y}(t)}] + \underline{\underline{\rho_r}}^{-1}\underline{\underline{\mathcal{D}}}_y\underline{v_1(t)} + \underline{\underline{\rho_r}}^{-1}\underline{\underline{\mathcal{M}}}^{-1}\underline{\mathcal{F}_y^{v2}(t)} = -\underline{\underline{\rho_r}}^{-1}\ \underline{s_{2y}(t)}\ . \tag{7.16c}$$

The simplified version of (7.16) set of equations, which contains the local matrices are:

$$\partial_{c_0t}\ \underline{v(t)}^n = -\underline{\underline{A}}^n\ \underline{v(t)}^n - \underline{\underline{B}}^n\ \underline{\underline{\mathcal{F}^n(t)}}\ \underline{v(t)}^n - \underline{C}^n\ , \tag{7.17}$$

where $\underline{\underline{\mathcal{F}^n(t)}}$ is the sparse flux matrix with non-zero elements regarding the nth adjacent elements, and:

$$\underline{\underline{A}} = \begin{bmatrix} \underline{0} & \underline{\underline{\kappa_r'}}^{-1}\underline{\underline{\mathcal{D}}}_x & \underline{\underline{\kappa_r'}}^{-1}\underline{\underline{\mathcal{D}}}_y \\ \underline{\underline{\rho_r}}^{-1}\underline{\underline{\mathcal{D}}}_x & \underline{0} & \underline{0} \\ \underline{\underline{\rho_r}}^{-1}\underline{\underline{\mathcal{D}}}_y & \underline{0} & \underline{0} \end{bmatrix}\ , \tag{7.18}$$

$$\underline{\underline{B}} = \text{Block Diag}(\begin{bmatrix} \underline{\underline{\kappa_r'}}^{-1}\underline{\underline{\mathcal{M}}}^{-1} \\ \underline{\underline{\rho_r}}^{-1}\underline{\underline{\mathcal{M}}}^{-1} \\ \underline{\underline{\rho_r}}^{-1}\underline{\underline{\mathcal{M}}}^{-1} \end{bmatrix}) \ , \qquad \underline{C}^n = \begin{bmatrix} \underline{0} \\ \underline{\underline{\rho_r}}^{-1}\underline{s_{2x}(t)} \\ \underline{\underline{\rho_r}}^{-1}\underline{s_{2y}(t)} \end{bmatrix} , \qquad \underline{v(t)}^n = \begin{bmatrix} \underline{v_1(t)} \\ \underline{v_{2x}(t)} \\ \underline{v_{2y}(t)} \end{bmatrix} . \tag{7.19}$$

So far in this section, the local matrices for a specific element n have been generated using the Mass and Stiffness matrices and local interpolation coefficients. The resulted matrices' sizes are $3N_p$-by-1 for the field and source coefficient vectors $\underline{v(t)}^n$ and $\underline{C}^n$ and $3N_p$-by-$3N_p$ for the other matrices $\underline{\underline{A}}^n$, $\underline{\underline{B}}^n$ and $\underline{\underline{\mathcal{F}^n(t)}}$.

7.2.2 Evaluating Ultrasound Fluxes on Interfaces

The goal here is to evaluate the surface integrals of equations (7.15) by summing the contributions over each of the element faces. Following the same method used to find the flux terms in EM, a natural choice for the ultrasound flux terms in the integral (4.21) is [3]:

$$\Phi^{v1}(t,\vec{r}^{n,f}) \triangleq \frac{\alpha}{Z^-(\vec{r}^{n,f})+Z^+(\vec{r}^{n,f})} \left[v_1^+(t,\vec{r}^{n,f}) - v_1^-(t,\vec{r}^{n,f})\right] + \ldots$$
$$\frac{Z^+(\vec{r}^{n,f})}{Z^-(\vec{r}^{n,f})+Z^+(\vec{r}^{n,f})} \left[\vec{v_2}^+(t,\vec{r}^{n,f}) - \vec{v_2}^-(t,\vec{r}^{n,f})\right] \cdot \hat{n}(\vec{r}^{n,f}) \cdot \hat{n}(\vec{r}^{n,f}), \tag{7.20a}$$

$$\vec{\Phi}^{v2}(t,\vec{r}^{n,f}) \triangleq \frac{Y^+(\vec{r}^{n,f})}{Y^-(\vec{r}^{n,f})+Y^+(\vec{r}^{n,f})} \left[v_1^+(t,\vec{r}^{n,f}) - v_1^-(t,\vec{r}^{n,f})\right] \hat{n}(\vec{r}^{n,f}) - \ldots$$
$$\frac{\alpha}{Y^-(\vec{r}^{n,f})+Y^+(\vec{r}^{n,f})} \left(\left[\vec{v_2}^+(t,\vec{r}^{n,f}) - \vec{v_2}^-(t,\vec{r}^{n,f})\right] \cdot \hat{n}(\vec{r}^{n,f})\right) \hat{n}(\vec{r}^{n,f}), \tag{7.20b}$$

where $Z(\vec{r})$ is the ultrasound impedance defined by $\sqrt{\frac{\rho_0\rho_r(\vec{r})}{\kappa_0'\kappa_r'(\vec{r})}}$ at the location $\vec{r}$ and $Y(\vec{r})$ is the ultrasound admittance defined by $Y(\vec{r}) = Z(\vec{r})^{-1}$ at the location $\vec{r}$. Note that Φ^{v1} is an scalar and $\vec{\Phi}^{v2}$ is a vector here.

7.2.3 Ultrasound Absorbing Boundary Condition

The characteristics of an absorbing boundary imposes zero outgoing waves of pressure and velocity from the absorbing layer, means that the flux terms arising from $\vec{v}_1^+$ and v_2^+ are zero. Assuming zero incoming flux from the neighbouring elements leads to a simple Silver-Müller absorbing boundary condition:

$$\Phi^{v1}_{ABC}(t,\vec{r}^{n,f}) \triangleq \frac{-\alpha}{2Z^-(\vec{r}^{n,f})}\ v_1^-(t,\vec{r}^{n,f}) - \frac{1}{2}\ \vec{v_2}^-(t,\vec{r}^{n,f})\cdot\hat{n}(\vec{r}^{n,f}),$$
$$\vec{\Phi}^{v2}_{ABC}(t,\vec{r}^{n,f}) \triangleq \frac{-1}{2}\ v_1^-(t,\vec{r}^{n,f})\ \hat{n}(\vec{r}^{n,f}) + \frac{\alpha}{2Y^-(\vec{r}^{n,f})}\ \Big(\hat{n}(\vec{r}^{n,f})\cdot\vec{v_2}^-(t,\vec{r}^{n,f})\Big)\ \hat{n}(\vec{r}^{n,f}).$$

7.2.4 Constructing the Global System

So far, we focused on discretizing ultrasound's PDEs in a local volume V_n. The last step of this discretization is to collect the local equations into a sparse block of global system of equations:

$$\partial_{c_0 t}\ \underline{v(t)} = -\underline{\underline{E}}\ \underline{v(t)} - \underline{\underline{Q}}\ \underline{\underline{\mathcal{F}(t)}}\ \underline{v(t)} - \underline{R(t)}, \tag{7.22}$$

similar to the (4.26) in EM. At the end, (7.22) is a system of ODEs. We can solve this system of ODEs after temporal discretizing (Chapter 5). Having developed a forward model and expressions for the gradients, it is straightforward to combine them into an ultrasound DGM-FBTS scheme by following the steps discussed in Chapter 6.

7.3 Evaluating the Ultrasound TD-DGM Forward Solver

In this section we validate the incident/scattered pressure/velocity parameters by comparing them to their FD counterparts in frequency domain. Again, we choose the well-proven frequency domain discontinuous Galerkin forward solver formulated for ultrasound wave propagation, as

the FD counterpart[3].

This comparison is performed by calculating the harmonic pressure/velocity at the dominant frequency of the TD source signal using discrete Fourier transform (as previously discussed in 5.7). The scattered and incident pressure/velocity will be compared over the domain D, which is a 5.0 cm-sided square.

We use a simple off-center cylinder target in this section. The constitutive parameters of this target are shown in Figure 7.1. The center of this circular cylinder is at $(x,\ y) = (0.4,\ 0.0)$ cm and it's radius is 0.4 cm. Relative compressibility and density of this target are respectively 1.1 and 1.0. The background is water and the problem's absorbing boundary is a circle of 5.0 cm radius.

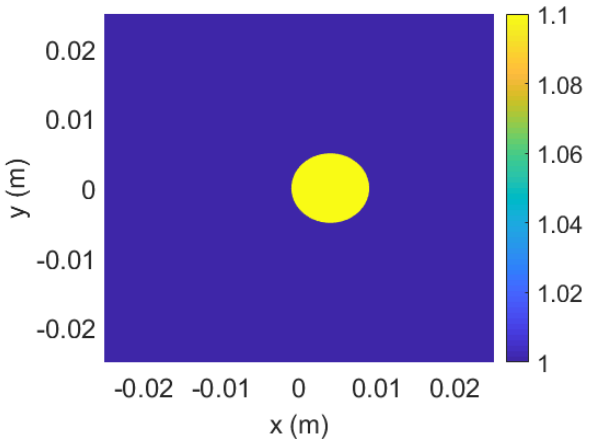

Figure 7.1: (Scenario 4) off-center cylinder's relative compressibility

We assume a transmitter located at $(x,\ y,\ z) = (3.64,\ 0,\ 0)$ cm. The same fine mesh with 1st order basis function for all of the parameters/constitutives is used for the both TD and FD solvers.

The frequency of 100 KHz is chosen for this geometry so that its wavelength in water is about 1.48 cm. For this reason, the dominant frequency of the source signal in the TD forward solver is

[3]The Ultrasound FD code was implemented by the UofM-EIL members before the start of this thesis.

chosen to be 100 KHz by selecting the τ in equation (5.4) equal to 806.815 ns. The comparisons of incident waves are shown in Figures 7.2 (amplitudes) and 7.3 (angles). Scattered wave (from the designated target) comparisons are shown in Figures 7.4 (amplitudes) and 7.5 (angles).

Note that the same procedure as in 5.7.1 is used here to extract the scattered field of the TD wave results. Note that the artifacts or the amount of errors seem to be less from EM to US, mostly because the antenna-boundary and target-boundary distances with respect to the problem's wavelength are larger in US and also likely because of the difference in the level of parameters[4]. Obviously, by putting the boundaries of an imaging problem further from the imaging domain and the antennas, receivers record less interactions of the propagating wave to the boundary.

In all of the related figures, the right column shows the results of the TD DGM while the FD results are in the left column. The first, second, and third rows show $\mathbb{p}$, u_x, and u_y. The figures demonstrate that the general shape of the TD and FD results are the same. Differences in the results are attributed to the modeling errors discussed in 5.7.

[4]For instance $\rho_0 = 1000$ kg/m^3, while its dual parameter is $\mu_0 = 4\pi 10^{-7}$ H/m.

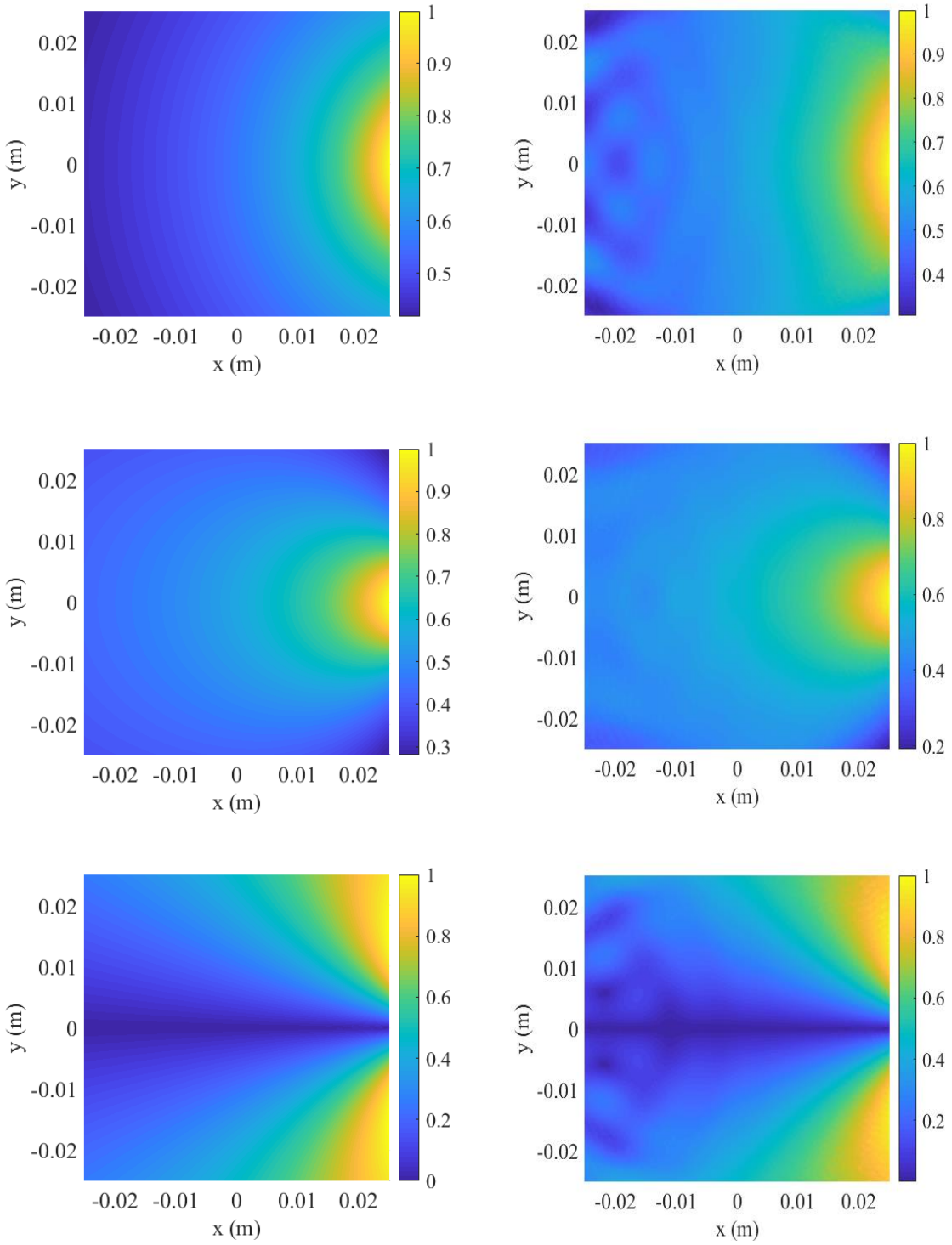

Figure 7.2: The normalized amplitude of the incident $\mathbb{p}$ (first row), u_x (second row) and u_y (third row) by the FD-DGM (left) and the TD-DGM (right) at 100 KHz.

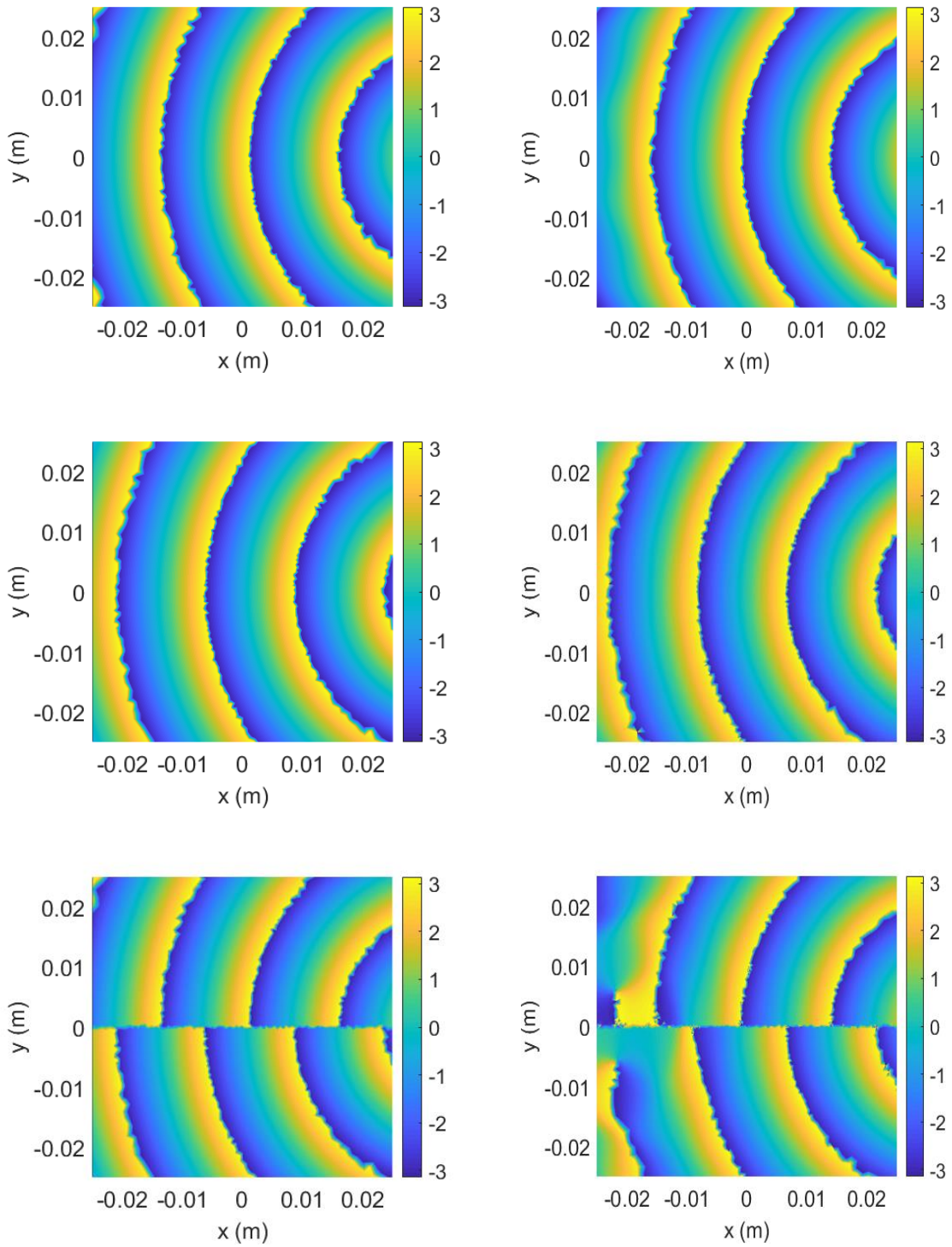

Figure 7.3: The phase of the incident $\mathbb{p}$ (first row), u_x (second row) and u_y (third row) by the FD-DGM (left) and the TD-DGM (right) at 100 KHz.

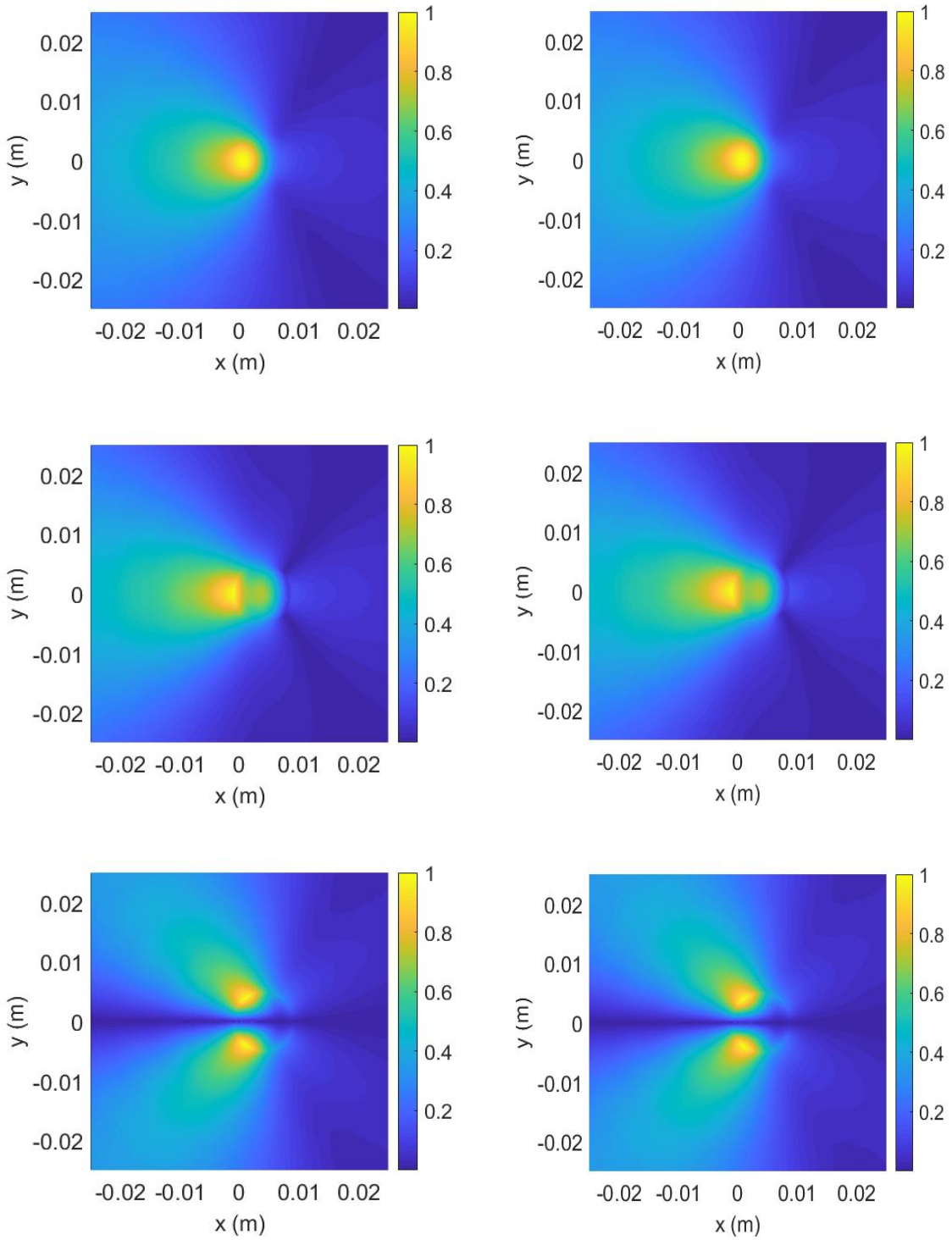

Figure 7.4: The normalized amplitude of the scattered $\mathbb{p}$ (first row), u_x (second row) and u_y (third row) by the FD-DGM (left) and the TD-DGM (right) at 100 KHz.

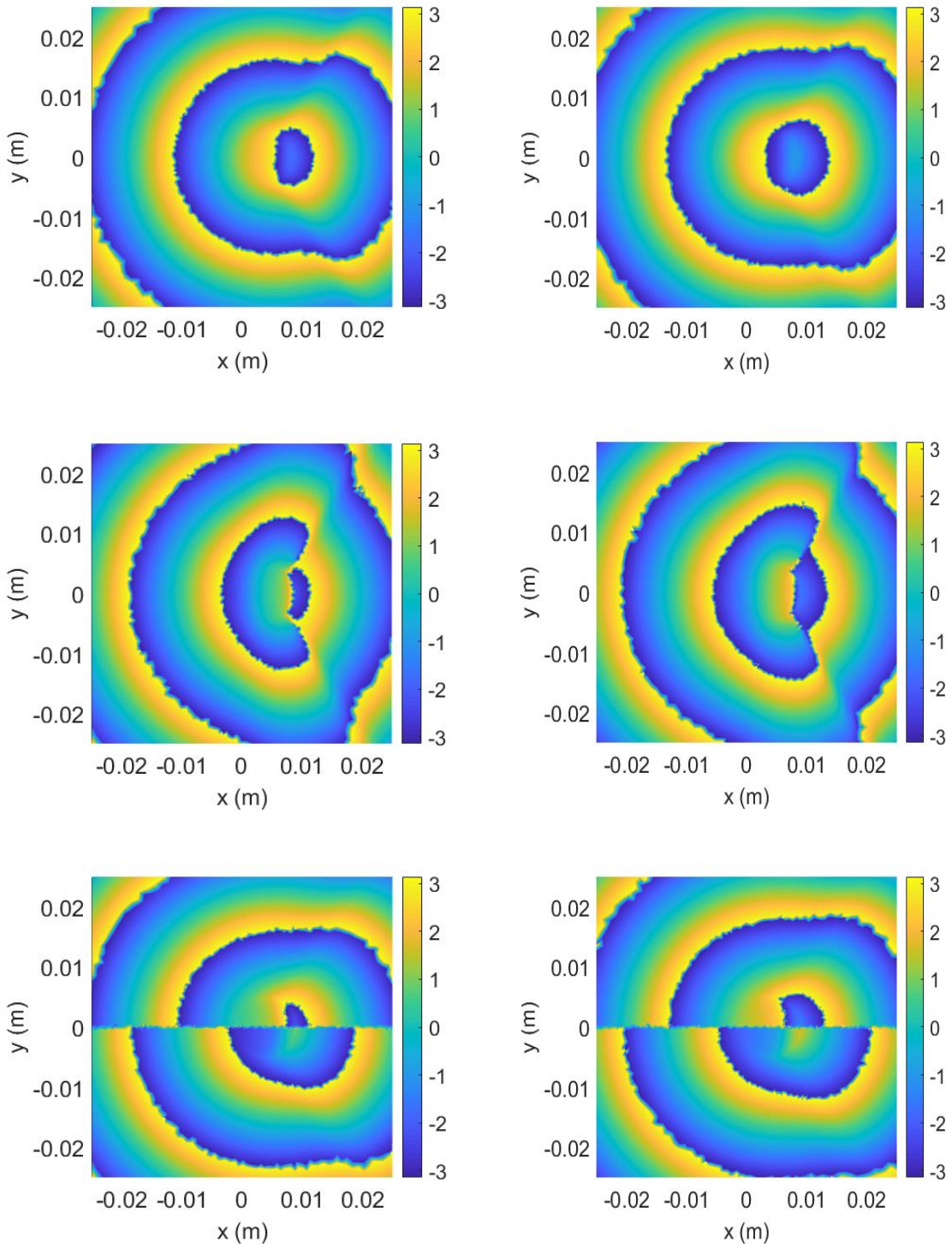

Figure 7.5: The phase of the scattered p (first row), u_x (second row) and u_y (third row) by the FD-DGM (left) and the TD-DGM (right) at 100 KHz.

Chapter 8

Results

In the previous chapters, we have developed a DGM-FBTS inversion algorithm.

This presentation started with electromagnetics and has been expanded to ultrasound waves. The modifications required to convert the solver from EM to ultrasounds was presented in Chapter 7.

The present chapter aims to evaluate the implemented TD DGM-FBTS algorithms for both EM and US. For EM problems, the focus is on experimental imaging and providing, for the first time, a side-by-side comparison of experimental TD and FD imaging, beginning with the hardware setup description and calibration process. For US problems, the results are limited to a very simple synthetic example that simply demonstrates the correctness of the formulation. A rigorous synthetic and/or experimental study of the US code is beyond the scope of this thesis.

Two DGM-based frequency-domain algorithms, which UofM-EIL members previously developed, are employed in this chapter to help us compare TD and FD imaging capabilities. Algorithms used for the frequency-domain microwave imaging are the popular Contrast Source Inversion (CSI) method discretized by DGM: DGM-CSI [93], and the Gauss-Newton Inversion method (GNI), which can be shown to be equivalent to the Distorted Born Iterative Method,

again discretized by DGM: DGM-GNI [52].

Some of the results in this chapter, which compare the TD and FD algorithms, are regenerated from [1], a published paper as a contribution of this thesis.

8.1 Hardware Setup

The hardware generating this work's experimental data is an air-filled Plexiglas cylindrical chamber with an inner diameter of 44 cm.

This chamber was originally designed to have twenty-four transducers, and was one of several different systems developed by the University of Manitoba's Electromagnetic Imaging Lab (EIL). In this work, just sixteen transducers are installed inside this chamber, to highlight the benefit of fewer transmitter requirements in TD imaging as a specific interest. The TD data (here) contains a wide-band range of frequencies, and we can benefit from fewer transmitters compared to FD, as each antenna collects a lot more data (information about the target(s)) for TD [1].

A picture of the system is shown in Figure 8.1. The inner edge of the installed Vivaldi antennas make a 12 cm radius circle. The other 20 cm of the remaining space houses the antenna body (7 cm each) and the SMA connectors. So, the imaging domain has a maximum permissible diameter of 24 cm. The Vivaldi antennas used in this work, are double-layered with nominal operating range of about 1 GHz to 10 GHz. This chamber is connected to a broadband VNA and a switch, via these antennas.

For calibration purposes, we need a known target established at a known position. To this end, a metallic cylinder of 46 cm height and 8.89 cm outer diameter is serving as the calibration object (CO) during this work.

Note that we positioned the CO and antennas setup by hand so that their locations are approximate; The CO is assumed to be at the center during the simulations. This imposes an extra measurement error on the data collected by this device.

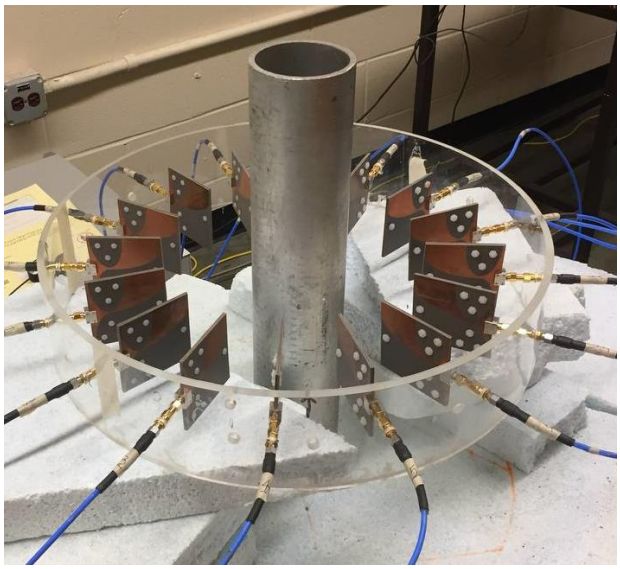

Figure 8.1: The imaging system's hardware, possessed by the UofM-EIL, with 16 Vivaldi antennas during collecting data from a metallic cylinder calibration object (CO).

Also, during system modeling, a corresponding Absorbing Boundary Condition (ABC) is implemented at the chamber's inner radius.

The VNA was set to collect 1601 frequencies from 10 MHz to 12 GHz which are subsequently converted to a time-domain signal for the time-domain imaging algorithm for all of the experimental targets. Recall that the Vivaldi antennas' nominal operating frequency starts from 1 GHz to 10 GHz. Although choosing a wider range of frequency for the measurements in this work may not add any information, it does not add more noise to the measured data after calibration either. One of the measurement frequencies, based on the problem size, is picked for the frequency-domain imaging algorithms. The dominant frequency of the source's time-signal is also chosen based on the problem sizes.

All of the experiments in this work are approximated as a 2D TM configuration. Because of this reason, the Vivaldi antennas are installed vertically, and the targets are restricted to be cylinders elongated in the vertical z-direction.

In all of the experiments, data were collected using 15 antennas, and monostatic measurements was removed from the data for imaging purposes. Therefore, for the TD and FD algorithms, we have 15 measurements per transmitter.

8.2 The Simulation Setup

It is required to discuss how we model the synthetic sources or the transducers during this work's experiments. As previously mentioned, two-dimensional transverse magnetic imaging problems are concerned in this thesis. Here, we model all of the sources, either the synthetic or the Vivaldi antennas, as ideal line sources (actually point sources in 2D). These sources are modelled with a time-varying amplitude, i.e., the mth transmitter is defined by the z-directed current density:

$$\mathcal{J}_{z,m}(t,\vec{r}) = \mathcal{I}_{z,m}(t)\delta(\vec{x}-\vec{x}_m),$$

located at the transmitter location $\vec{x}_m$. The time function $\mathcal{I}_{z,m}(t)$ dictates the spectral content of the source and has a broadband spectrum, shown by the formulation (8.1), illustrated in Figure 8.2 for all examples (synthetic and experimental).

$$\mathcal{I}_{z,m}(t) = (\frac{t}{\tau})^3(4-\frac{t}{\tau})e^{-\frac{t}{\tau}}. \tag{8.1}$$

According to previous EIL work in FD MWI, the Vivaldi antennas, used in this work, propagate from the tip at lower frequencies and the nearer to the feed at higher frequencies. Although we tried some different locations for the simulated source points, the best result are obtained at 18.75 cm radius for the frequencies used in this work for all of the FD and TD schemes, unless it is mentioned otherwise. We found this radius (18.75 cm) as a part of calibration process, which is fully described in Section 8.4.1.

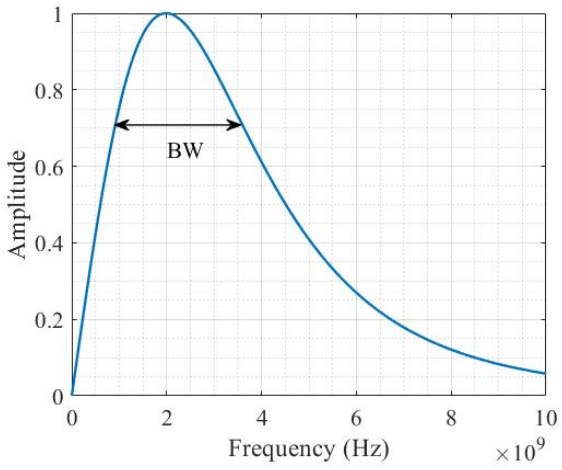

Figure 8.2: Frequency response of the time-domain source signal $\mathcal{I}_{z,m}(t)$ at (8.1). [The image is reproduced from [1] with permission.]

8.3 Imaging Targets

This section is allocated to describe the synthetic and experimental imaging targets used to test the DGM-FBTS algorithm.

Note that all of the targets studied in this work are generally non-metallic (except the CO). This means that the static conductivity of these targets is negligible. As we mentioned in the definition of dispersive media, the loss in these (dielectric) targets is due to the dispersivity, which is traceable by the Debye or other similar models.

At the time of writing this thesis, the only available frequency-domain codes (DGM-CSI and DGM-GNI) are implemented for the non-dispersive media. In these codes, the permittivity's imaginary part presents all loss types as a single quantity. Therefore, we define an equivalent conductivity to capture the dispersive targets' dispersivity and reconstruct it by the non-dispersive FD and TD codes to have a fair comparison.

To this end, the dispersive targets are reconstructed twice by the TD code; once as a dispersive target with the optical and static permittivities as the two unknowns, and once again as a non-dispersive target with equivalent permittivity and equivalent conductivity as unknown

parameters.

The relationship between the dispersive permittivities and the equivalent parameters of permittivity and conductivity is extracted in the following. After rewriting the effective relative permittivity of Equation (2.10), we have

$$\varepsilon_{r,eff}(\omega,\vec{r}) = \left[\varepsilon_{\infty}(\vec{r}) + \frac{\Delta\varepsilon_r(\vec{r})}{1+\omega^2\ \tau_r^2(\vec{r})}\right] - j\left[\frac{\Delta\varepsilon_r(\vec{r})\ \omega\ \tau_r(\vec{r})}{1+\omega^2\ \tau_r^2(\vec{r})}\right].$$

By equating the real and imaginary parts of the result by $\varepsilon_{eq,r}$ and $-\frac{\sigma_{eq,s}}{\omega\ \varepsilon_0}$, which are the real and imaginary parts of a non-dispersive lossy target in FD, the equivalent relative permittivity and (static) conductivity would be

$$\sigma_{eq,s} = \frac{\Delta\varepsilon_r(\vec{r})\ \omega^2\ \tau_r(\vec{r})\ \varepsilon_0}{1+\omega^2\ \tau_r^2(\vec{r})}, \tag{8.2a}$$

$$\varepsilon_{eq,r} = \varepsilon_{\infty}(\vec{r}) + \frac{\Delta\varepsilon_r(\vec{r})}{1+\omega^2\ \tau_r^2(\vec{r})}. \tag{8.2b}$$

Therefore, by knowing the dispersive parameters, we could find the loss in the frequency domain, which is the imaginary part of the relative permittivity in FD.

Synthetic Target 1: The Lossy/Lossless BoxTarget

The lossy BoxTarget is introduced and used for the first time in Section 5.7.1. The constitutive parameters are shown in Figure 5.4 and described in that section. We do not repeat this information, here again, to avoid redundancy.

The lossless BoxTarget has all of the features of the lossy BoxTarget except that the conductivity is set to zero.

The transducers for this target, either with or without loss, are located on a circle of 25 cm radius (note that this is different from the 18.75 cm radius used for the experimental examples), and the source waveform is shown in Figure 8.2.

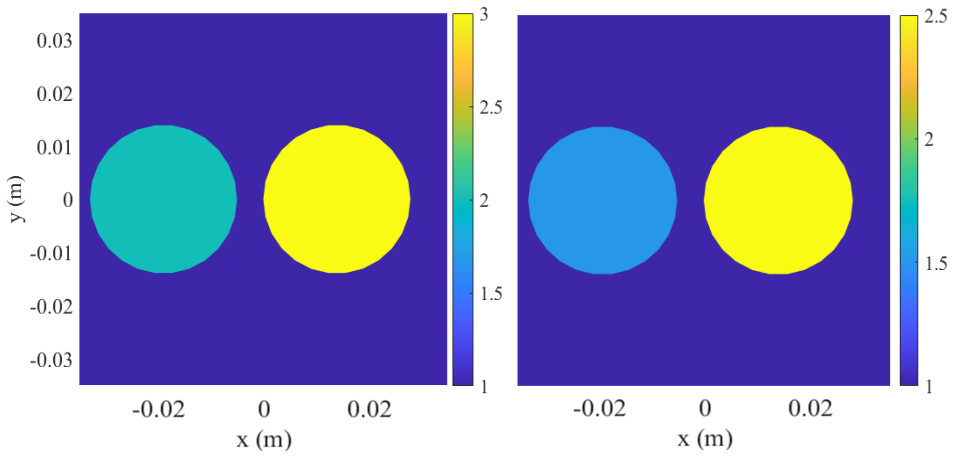

Figure 8.3: The Dispersive Cylinders Properties. Left: (relative) static permittivity, Right: (relative) optical permittivity.

Synthetic Target 2: The Dispersive Cylinders

This target contains of two cylinders with centers located at $(x,\ y,\ z) = (-0.019,\ 0,\ 0)$ m and $(x,\ y,\ z) = (0.014,\ 0,\ 0)$ m. The constitutive parameters of this target are shown in Figure 8.3. The optical permittivity and the static permittivity of cylinders are $\varepsilon_\infty = (1.5,\ 2.5)$ and $\varepsilon_s = (2,\ 3)$, respectively from left to right. The problem's absorbing boundary is a circle of 0.066 m radius and the imaging domain's diameter is 0.035 m.

To reconstruct this target's image, 4 transmitters and 8 receivers are used, so that in each round of measurement 1 transmitter and 7 receivers are used. These antennas are located on a circle of the radius 0.055 cm, with the source signal shown in Figure 5.2. The imaging time interval of $[0,\ T = 3.3$ ns$]$ is selected here.

Synthetic Target 3: The Ultrasound Off-Center Cylinder

The only ultrasound target presented in this thesis is an off-center cylinder.

This 0.5 cm radius cylinder is centered at $(x,\ y,\ z) = (0.4,\ 0,\ 0)$ cm. The background is water and the constitutive parameters of this target relative to water are $\kappa_r' = 2.0$ and $\rho_r = 1.0$. The relative compressibility of this target is shown in Figure 8.4.

We have 4 transmitters and 8 receivers in this problem, so that in each round of measurement 1 transmitter and 7 receivers (we neglect the monostatic measurement) are working. The transmitter (and receivers) are located equally spaced on a 3.64 cm radius circle. The imaging domain and the total domain Ω are circles with respective 1.2 and 5.0 cm radius.

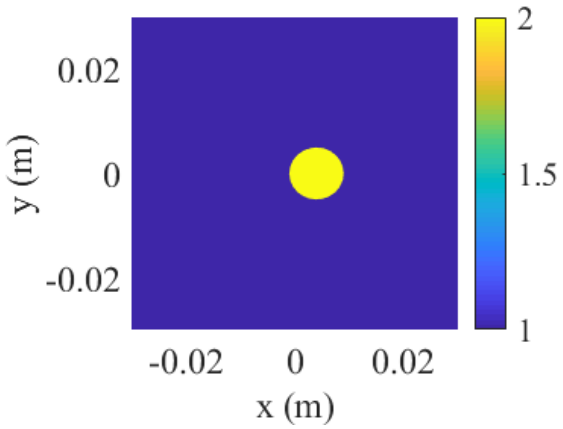

Figure 8.4: The relative compressibility κ_r' of the ultrasound Off-Center cylinder target.

Experimental Target 1: The Lossless TwoCylinder Target

The first EM experimental target consists of two lossless cylinders, that we refer to it as the lossless TwoCylinder target. This target is shown in Figure 8.5.

The cylinders' diameters are 3.8 cm and 5.08 cm, with the respective height of 29.9 cm and 65 cm. Both of the cylinders are nylon with a relative permittivity of about 2.7 (at 2 GHz) [94]. Note that we do not have the exact amounts of these nylon's dielectric parameters, but we expect that they may have different permittivities as they are different colors.

Experimental Target 2: The Lossless E-Phantom Target

The most complicated free-space experimental target in the UofM-EI lab is the lossless E-phantom target. This target is shown in the Figure 8.6.

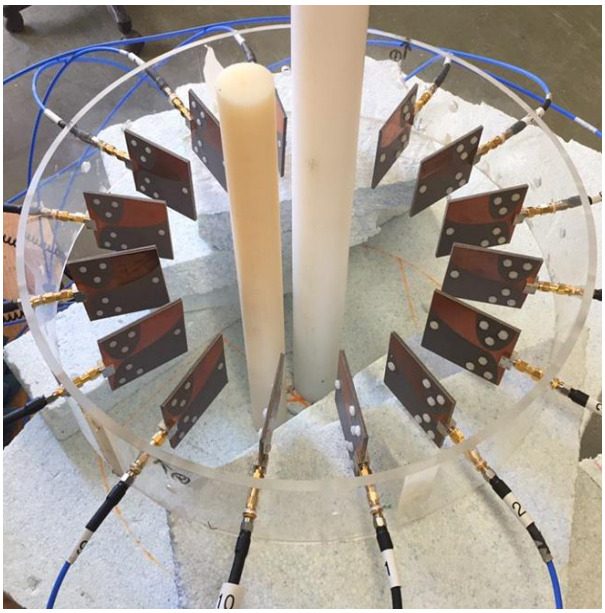

Figure 8.5: The lossless TwoCylinder target. [The image is reproduced from [1] with permission.]

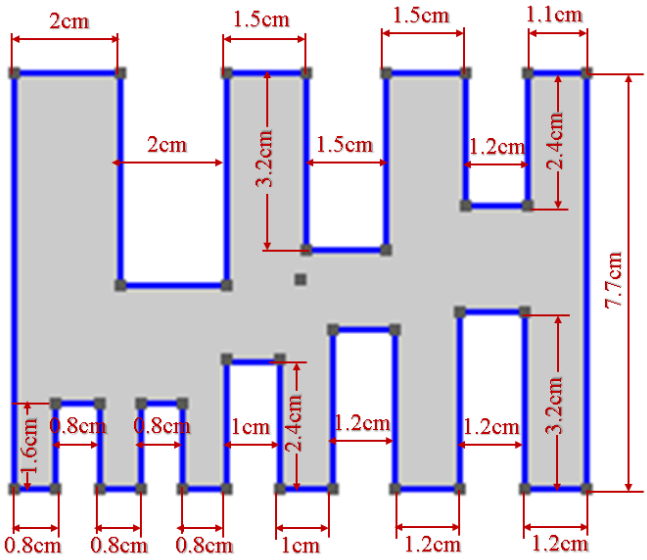

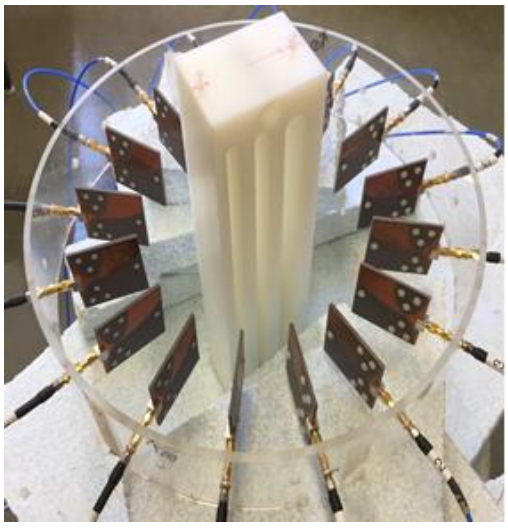

Figure 8.6: Left: The lossless E-phantom target's cross section, Right: The lossless E-phantom target image, inside the imaging system. [The image is reproduced from [1] with permission.]

This E-phantom target has been featured in a number of EIL publications, as both a synthetic and experimental target [95, 1]. The E-phantom is made of ultra-high molecular weight polyethylene with a relative permittivity of about 2.5 [95].

Experimental Target 3: The Lossy WoodTarget

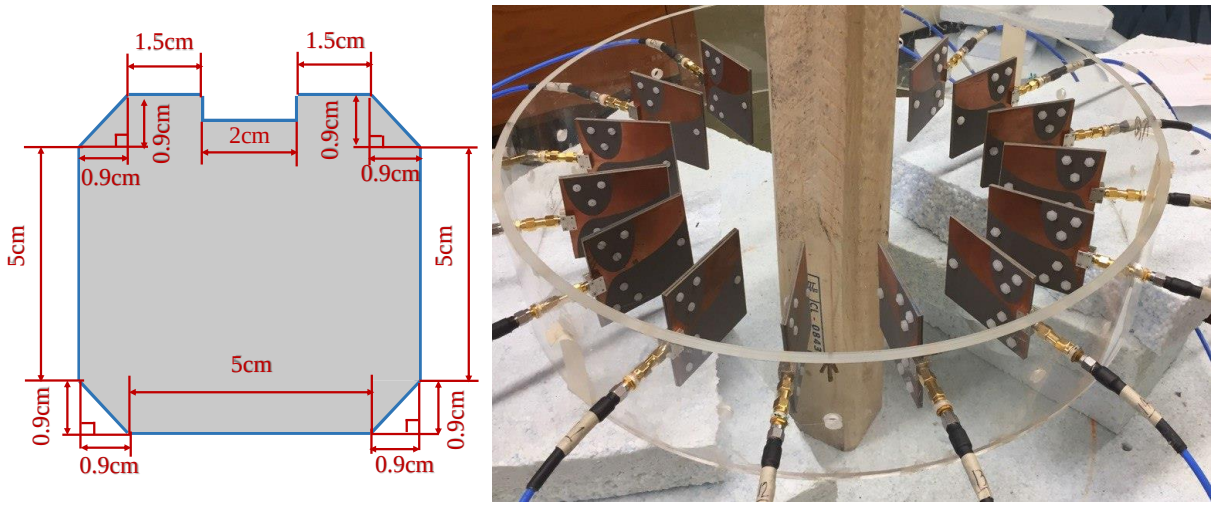

Figure 8.7: Left: The lossy Wood target's cross section, Right: The lossy Wood target image, inside the imaging system. [The image is reproduced from [1] with permission.]

The first lossy experimental target is the lossy WoodTarget. This cylindrical wooden target has about 110 cm length, whose cross-sectional shape and dimensions are shown in Figure 8.7.

The dielectric properties of woods change drastically based on their tree type, moisture level, and frequency. The WoodTarget is treated spruce[1] wood. The humidity of the air at the time (late September, 2020) and location (Winnipeg, MB, Canada) of WoodTarget measurement was about 65%, and according to [96], the spruce wood moisture level is about 11.7% to 12.8%. As a result, we estimate $\varepsilon' = 2.5$ and $\varepsilon'' = 0.3$ ($\sigma = 0.035$) at 2 GHz [96, 97, 98].

Note that no device[2] was available at the time of the MWI measurement to measure/validate

[1]Softwood trees like spruce usually remain evergreen and their wood is not very dense. The woods obtained from hardwood trees, which lose their leaves annually, are denser.

[2]The dielectric Probe Kit 85070, used to measure the average dielectric parameters of the Salted-Butter target, can not be used here, as it is not appropriate for solid materials like woods.

the (estimated) dielectric parameters for this solid target. Also, the estimated parameters here are valid as far as the target's moisture is from the humidity of the air. We do not guarantee that the target was not exposed directly to water before coming to our lab.

Experimental Target 4: The Salted-Butter Target

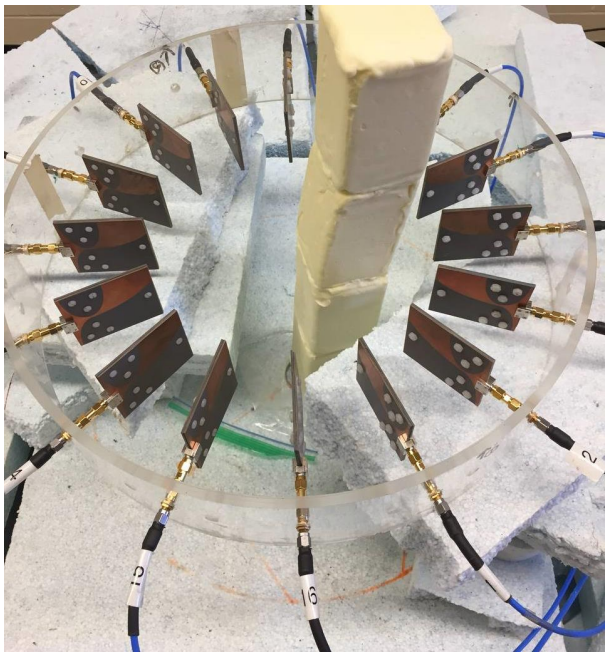

Figure 8.8: The lossy Salted-Butter target image, inside the imaging system.

A target of salted butter is another lossy target used in this work. This target has higher loss than the WoodTarget, making it a more challenging target to reconstruct with the dispersive code.

Four whole blocks of salted butter, one pound each with the dimensions of about 6.3×6.5×11.6 cm are used to build this target. After stacking the butter, as shown in Figure 8.8, the resulted height is about 46.4 cm.

The Salted-Butter target has an effective complex relative permittivity of about $\varepsilon_{eff,r}(\omega) = 5 - j0.74$ at $f = 2$ GHz, which is equivalent to $\varepsilon_{eq,r} = 5$ and $\sigma_{eq,s} = 0.082$ S/m at this frequency.

This parameter has been measured by a Dielectric Probe Kit 85070, made by Keysight Technologies. According to this measurement, the dispersive permittivities are about $\varepsilon_\infty = 1.8$ and $\varepsilon_s = 5.13$. Figure 8.9 shows the equivalent relative permittivity and static conductivity measured by the probe in a frequency range of 0.5 GHz to 8.5 GHz.

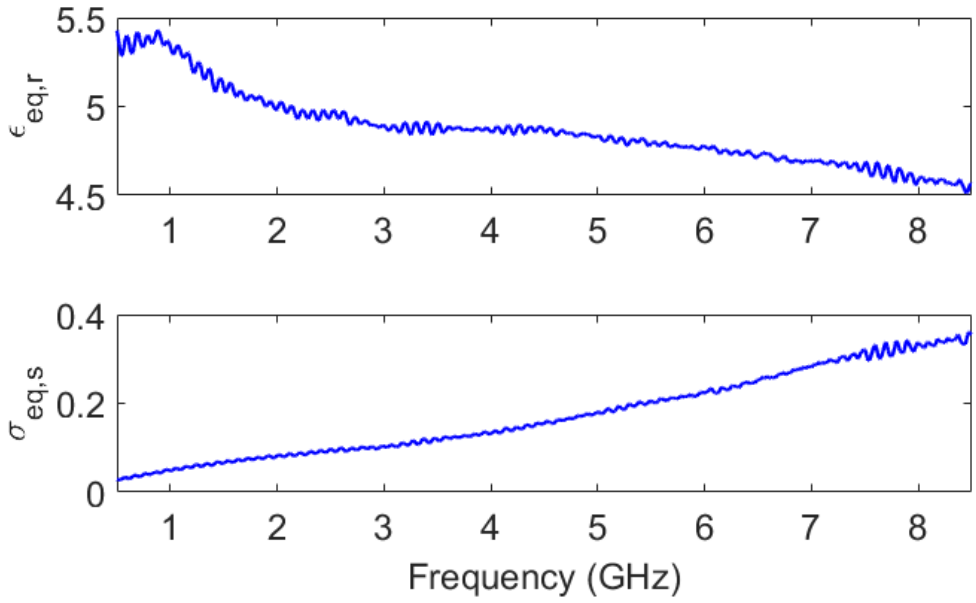

Figure 8.9: Salted-Butter constitutive parameters, measured by the dielectric probe; (top) relative permittivity, and (bottom) conductivity.

Experimental Targets 5 & 6: The High-Constitutive Tree-Trunk-1 & Tree-Trunk-2 Targets

We use two tree trunks at two different states; wet and dry. Figure 8.10 shows the tree trunks. Tree-Trunk-1 is the smaller tree trunk with 10.5 cm average diameter and 73 cm height. Tree-Trunk-2 is the larger tree trunk with 11.7 cm average diameter and 98 cm height. The height of the vivaldi antennas is approximately 1/2 and 1/3 of the respective target heights for Tree-Trunk-1 and Tree-Trunk-2.

Wet state: These two tree trunks were collected from a forest in early April when they

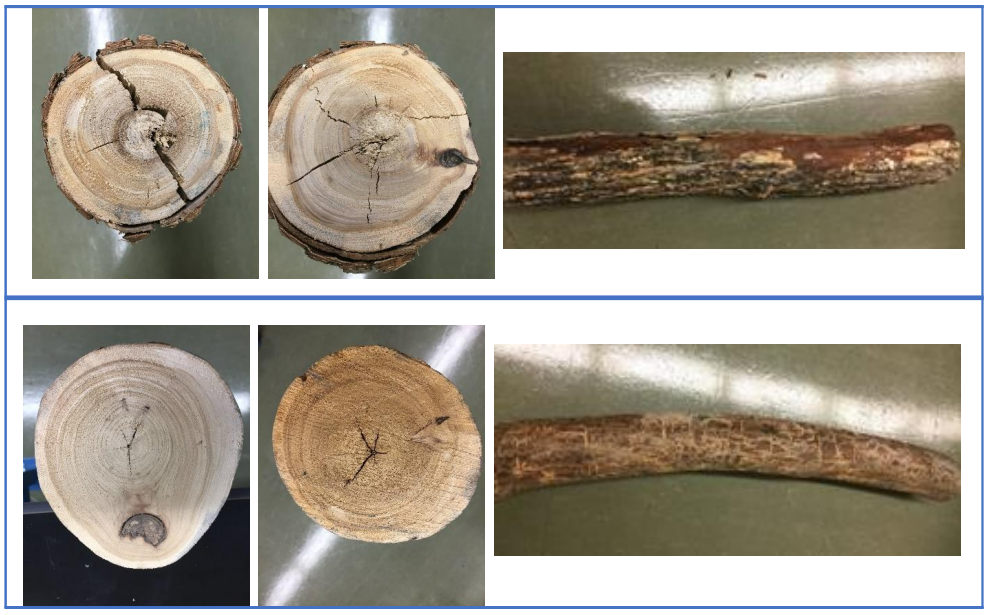

Figure 8.10: The lossy Tree-Trunk-1 (top) and Tree-Trunk-2 (bottom) targets.

were cut and left on the ground, covered thoroughly by snow. In this thoroughly wet state, their constitutive parameters are high, and they serve as two high-contrast targets when the imaging background is air.

Dry(er) state: We do a second round of measurements of the same tree trunks, after keeping them indoor for about three months. Although the targets in this state are still high-contrast targets (compared to air background), we expect that the imaging process reveals smaller constitutive parameters than before, as they are dryer.

8.4 Calibration

The experimental imaging chamber is made of an air-filled Plexiglas chamber with a relative permittivity larger than 2. This chamber is attached to cables, VNA, and a switch by SMAs. However, we simulate this hardware system as a simple open-space region with absorbing boundary condition (ABC) at the chamber's inner radius using line sources. The calibration process alleviates this modeling/measurement error between the simulated and physical systems. The

VNA measures S-parameters, and another cause for having a data calibration process is to convert these S-parameters to the required electrical fields adoptable by the inversion algorithms.

The FD and TD data calibration procedures adopted in this work are based on a scattered-field data calibration procedure [95, 1]. Because the VNA measures total S-parameters $S^{tot}(f)$ at frequency f, we are required to take one extra step of measuring the incident S-parameters $S^{inc}(f)$ without the presence of any target to calculate the scattered S-parameters $S^{sct}(f)$ by:

$$S^{sct}(f) = S^{tot}(f) - S^{inc}(f). \tag{8.3}$$

Therefore, after the data calibration process, either in TD or FD, the scattered fields from the unknown targets at the receiver locations are the retrieved data.

The following sections explain the FD and TD data calibration procedures after closely investigating how to model the Vivaldi antennas.

8.4.1 Source Calibration

The point from which the electromagnetic radiation spreads from an antenna is that antenna's phase center. The Vivaldi antennas used in this work are dispersive, and their phase center changes by frequency. The problem of using such antennas for a TD imaging purpose is that the modeling error of these antennas increases as we have to use just one phase center for a wide range of frequencies. This section presents a source calibration process to decrease the source modeling error due to the frequency-dependency of the Vivaldi antenna's phase center.

We mentioned earlier in Section 8.2 that we chose the radius of 18.75 cm as the point source location to simulate the Vivaldi antennas. We found this radius as a part of the calibration process using trial and error over the range of $r_{viv} = 12$ cm to $r_{viv} = 19$ cm antennas radius[3]. In

[3]The length of Vivaldi antennas are about 7 cm, starting from the radius of $r_{viv} = 12$ cm in the chamber after installation.

the following, we briefly explain the process of this radius selection.

A second metallic cylinder of 44.9 cm height and 3.9 cm outer diameter is used to do the calibration of Vivaldi antennas in the time-domain. The steps of this source calibration procedure are:

1. Picking a random r_{viv} from the range of 12 cm to 19 cm,
2. Measuring the S-parameters for the second metallic cylinder,
3. Calibrating the total electric fields as discussed in Section 8.4.3,
4. Modelling the total electric field for the second metallic cylinder,
5. Comparing the measured and modelled electric fields at different receiver locations (we have 16 receivers),
   The generated time-domain signal at the receivers shifts back and forth in time if the chosen r_{viv} is respectively larger and smaller than the right amount.
6. Increasing/decreasing the amount of r_{viv} according to the results, and repeating the procedure from step 3 until we decrease this time-shifting reasonably.

Before ending this section, we need to clarify a couple of things:
1- As mentioned before, the CO and also the second metallic cylinder used for the source calibration are positioned at the center of the imaging chamber by hand. This causes different time-shifting between the modelled and the measured (and then calibrated) electric fields at different receiver locations. This discrepancy is one of the measurement errors during the experiments. Note that as the TD DGM-FBTS is a really robust inversion technique, we did not get into more details for the source calibration for brevity and we picked a simulation radius by trial and error, without quantifying the time-shifting errors.

2- Although the radius $r_{viv} = 18.75$ is selected as the phase center for the dispersive antennas for the wide-band range of frequencies used in this work, this radius is also valid for the single-frequency FD inversion algorithms used in this thesis at the used/required frequencies. We backup this claim by having a brief comparison of the FD inversion results of an experimental lossy target, at frequencies 1 GHz, 2 GHz, 3 GHz, 4 GHz, and 5 GHz, with two radius selections in Section 8.5.4; 1- $r_{viv} = 18.75$ cm, and 2- $r_{viv} = 14.40$ cm, which is previously selected by UofM-EIL for the same hardware setup, by a different procedure in frequency-domain [95].

8.4.2 Frequency-Domain Data Calibration

In this process, the measured scattered S-parameters of the known CO and unknown object plus the field solution of a forward model with the CO target generate the calibrated scattered field of the unknown object at the receivers' location.

The scattered field calibration method compares the measured scattered S-parameters of a known CO to the field solution of a forward model with the same target [95]. Then, the relation between the modeled electric field in the direction and the related S-parameter measurement would be:

$$\vec{E}^{sct,meas}_{target,cal}(f) \cdot \vec{p} = \mathcal{S}^{sct}_{target}(f) \frac{\vec{E}^{sct,model}_{CO}(f) \cdot \vec{p}}{\mathcal{S}^{sct}_{CO}(f)} \tag{8.4}$$

where $\vec{E}^{sct,model}_{CO}(f) \cdot \vec{p}$ is the FD modeled/simulated scattered field with the target of the CO, and $\mathcal{S}^{sct}_{CO}(f)$ and $\mathcal{S}^{sct}_{target}(f)$ are the scattered S-parameters for the CO and the unknown target, all at frequency f.

Note that $\vec{p}$ here is the unit vector in the z-direction to support the TM wave.

8.4.3 Time-Domain Data Calibration

Compared to frequency-domain data calibration, the time-domain calibration scheme necessitates some additional steps. We explain these steps utilizing the lossless E-Phantom data as an example.

Herein, the collected data is the S-parameters by the VNA as a function of frequency; $\mathcal{S}^{sct}_{CO}$,

$\mathcal{S}^{sct}_{target}$. The difference is that we collect broadband measurement at frequencies $[f_1 : df' : f_2]$, by the measurement frequency-step of df'.

For instance, Figure 8.11 shows the incident, total, and scattered measured S_{91}-parameters for the CO and the E-Phantom target, shown using gain definition of $g_{91} = 20\log_{10} \mid S_{91} \mid$. Here, the underscript 91 means the parameters are regarding the 9th receiver, when the 1st transmitter is active. Also, the measurement frequencies are: [0.01 GHz : 7.5 MHz : 12.01 GHz].

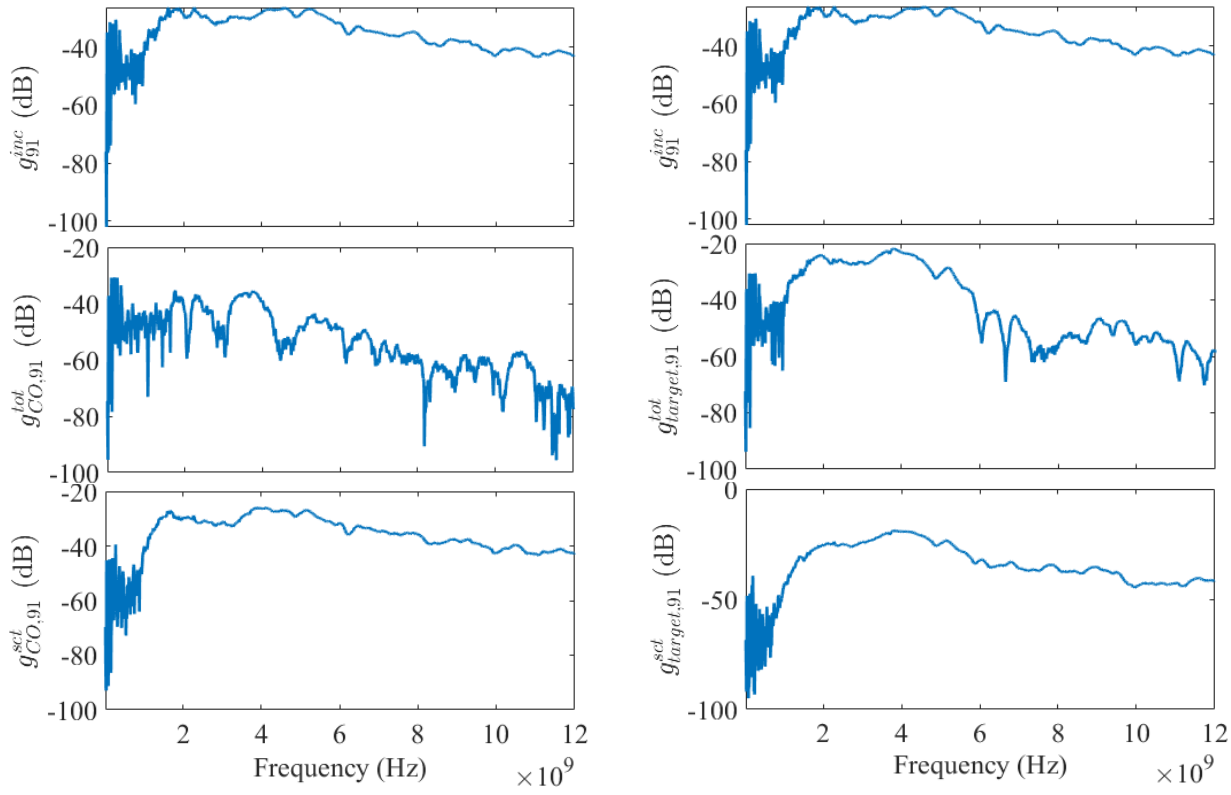

Figure 8.11: Measured incident(top), total (middle), and scattered (bottom) gains, measured for the CO and the E-Phantom target, from left to right.

The Flowchart illustrated in Figure 8.12 draws all of the required steps of the time-domain calibration procedure.

Similar to the FD calibration procedure, the first step is to generate the TD forward model's

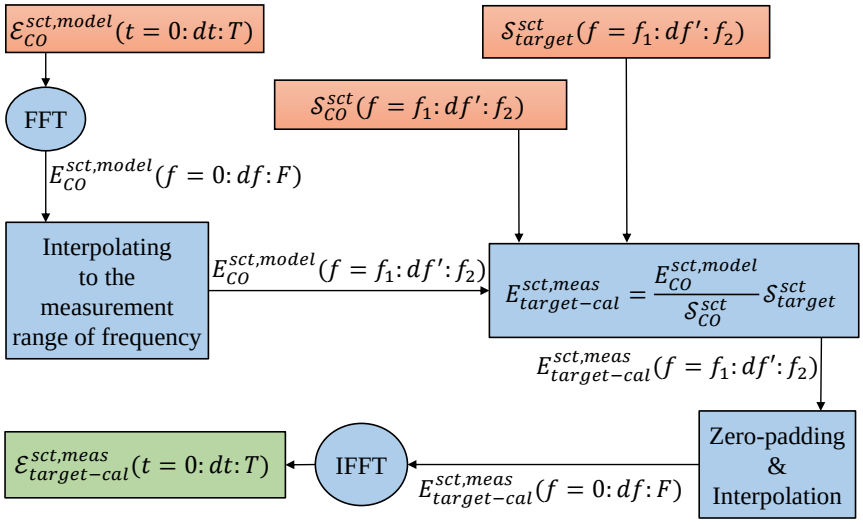

Figure 8.12: The time-domain calibration procedure to convert the VNA measured S-parameters to calibrated TD scattered electric fields applicable by the inverse imaging algorithm. [This diagram is reproduced from [1] with permission.]

field solution with the CO target by the designated time-domain forward solver. In the flowchart, $\mathcal{E}_{CO}^{sct,model} = \vec{\mathcal{E}}_{CO}^{sct,model} \cdot \vec{p}$ is the projection of the TD modeled scattered electric field of the calibration object, where $\vec{p}$ is the z-direction for the TM waves. In the E-Phantom example, the modeled incident, total, and scattered electric fields due to the calibration object are shown in Figure 8.13. Here the fields are modeled at times $[t : dt : T] = [0 : 9.5 \text{ ps} : 5.5 \text{ ns}]$.

The next step is to compute $E_{CO}^{sct,model}\ (f = f_1 : df' : f_2)$ by taking the Fourier transform of $\mathcal{E}_{CO}^{sct,model}\ (t = 0 : dt : T)$ and applying appropriate interpolation. Figure 8.14 shows this modeled signal in our example by its real and imaginary parts.

Next, Equation (8.4) produces calibrated fields in the frequency-domain $E_{target,cal}^{sct,meas}\ (f = f_1 : df' : f_2)$. Figure 8.15 shows the calibrated measured electric field, scattering from the E-Phantom target, due to 1st transmitter and 9th receiver. The last step of the TD calibration procedure is taking the Inverse Fourier Transform of the data after zero-padding and interpolation applied to the calibrated data. The interpolation is required herein, to take the data from $[f_1 : df' : f_2]$ band to the $[0 : df : F]$ frequency-band. Also, the zero-padding is required to get a smooth time-domain

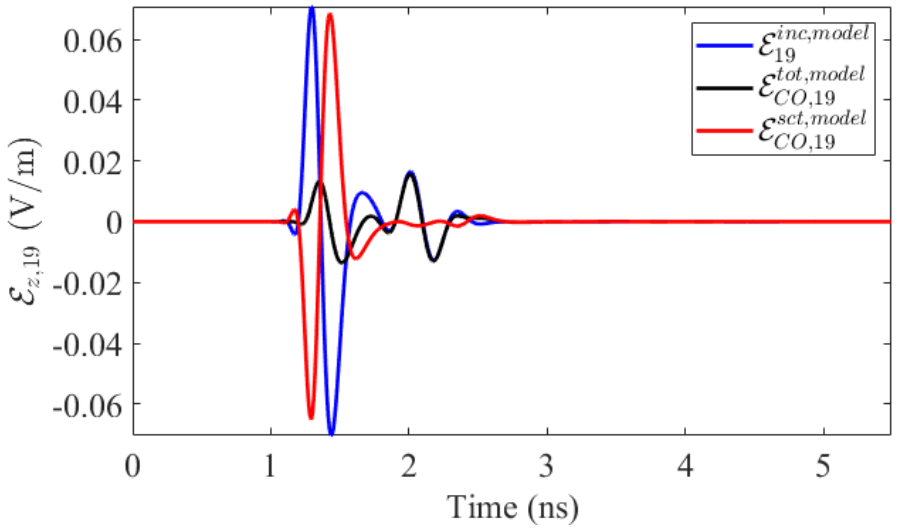

Figure 8.13: The time-domain incident, total, and scattered modeled electric field at the location of 9th receiver from the calibration object, when the 1st transmitter is on.

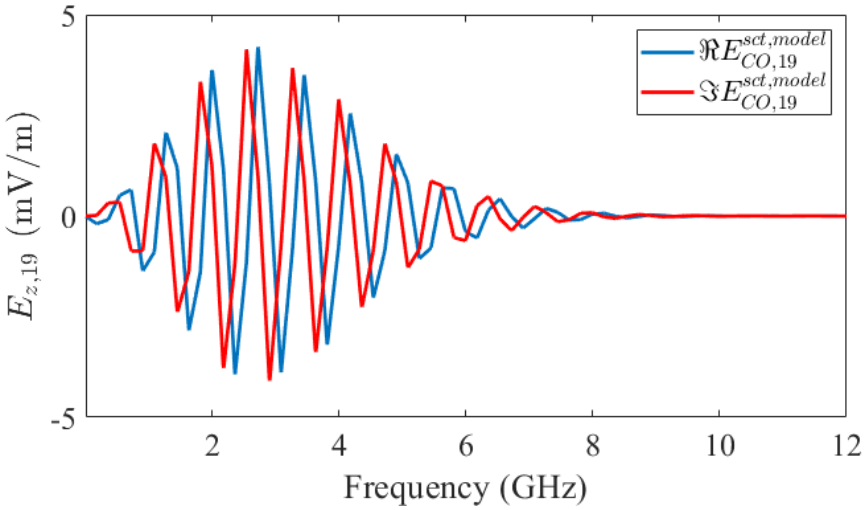

Figure 8.14: The interpolated frequency-domain scattered modeled electric field at the location of receiver 9 from the calibration object, when the 1st transmitter is on.

signal of $\mathcal{E}_{target,cal}^{sct,meas}$ $(t = 0 : dt : T)$. The time-domain calibrated field $\mathcal{E}_{target,cal}^{sct,meas}$ $(t = 0 : dt : T)$ for the E-Phantom target is shown in Figure 8.16 as example. This signal, along with other $16 \times 15 - 1$ signals retrieved from the rest of the transmitter-receiver pairs, is utilized to reconstruct the image

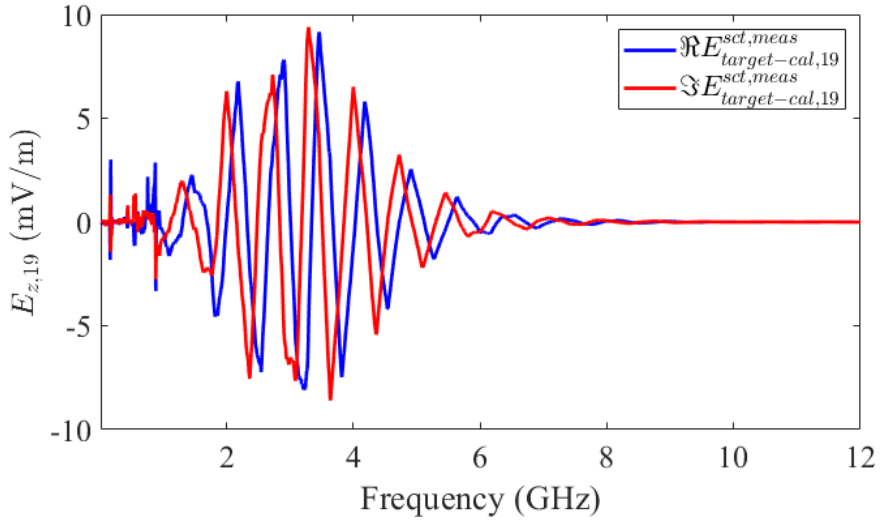

Figure 8.15: The calibrated frequency-domain scattered measured electric field at the location of receiver 9 from the E-Phantom target, when the 1st transmitter is on.

of the E-Phantom target by the inversion algorithm DGM-FBTS.

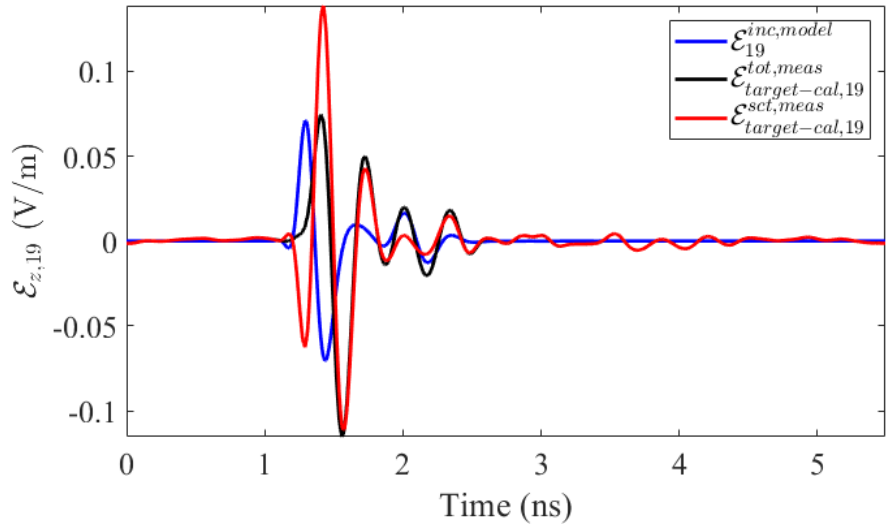

Figure 8.16: The calibrated time-domain measured electric fields at the location of receiver 9 for the E-Phantom target, when the 1st transmitter is on.

8.5 Comparing FD DGM-CSI and DGM-GNI with the non-dispersive TD DGM-FBTS

This section compares FD DGM-CSI and DGM-GNI with the non-dispersive TD DGM-FBTS, to highlight the benefits of this TD scheme over the designated single-frequency FD scheme.

8.5.1 The Lossy BoxTarget Example

We first consider the synthetic BoxTarget to see the performance of the DGM-FBTS scheme, and compare it with the performance of DGM-CSI and DGM-GNI.

The frequency-domain imaging results are taken from the results generated by the DGM-CSI and DGM-GNI methods in the range of 1 GHz to 5 GHz, to demonstrate the best single-frequency output here. The best[4] FD results for this specific target by these methods were obtained at 2 GHz ($\lambda_0 = 15$ cm). Note that at 2 GHz, $\sigma = 0.0556$ S/m corresponds to a relative imaginary permittivity of -0.5, the value adopted for frequency-domain simulations.

The time-domain inversion method adopts the source spectrum shown in Figure 8.2, which is a wide-band signal with dominant frequency and half power bandwidth of 2 GHz and 2.68 GHz, respectively.

For this synthetic example, some noise analysis for the time- and frequency-domain inversion algorithms has been done in the paper [2] by the author. Here in this report, no noise was added to the time- and frequency-domain DGM forward solvers, because the experimental examples presented shortly demonstrate the algorithms' capabilities in noisy scenarios. In all of the cases, inversion was performed on a different mesh that did not include any geometric information about the target, to avoid any inverse crime.

Two imaging scenarios were considered for this synthetic setup in order to illustrate different aspects of the TD FBTS scheme: an Absorbing Boundary Condition (ABC) and a PEC on the

[4]We did not use any quantitative metric to find the best result here. A visual comparison was deemed sufficient to qualify the results.

system.

BoxTarget with Absorbing Boundary

In this section, we place the BoxTarget within an absorbing boundary conditions and compare the results of DGM-FBTS with DGM-CSI and DGM-GNI. We end this section by comparing TD image reconstructions with 1st solution order and higher solution orders to discuss DGM discretization effects on the DGM-FBTS inversion algorithm.

The meshes which are used for BoxTarget image reconstructions, are shown in Figure 8.17. For the first comparison of FD and TD algorithms, the frequency-domain inversion mesh is coarser with the order of nodal DGM coefficients of 4 and 3 for the fields and constitutive parameters, respectively. Also, the basis order of the contrast sources in DGM-CSI is 3. This mesh is shown in Figure 8.17(a). For this comparison, the time-domain inversion mesh is finer, shown in Figure 8.17(b), and basis functions have the order of 1. As the next step, 4th solution order for fields' basis functions, with a coarser mesh (about four times coarser) than the TD 1st order mesh, is used for DGM-FBTS to study DGM benefits in TD inversion algorithm more closely. This mesh is shown in Figure 8.17(c).

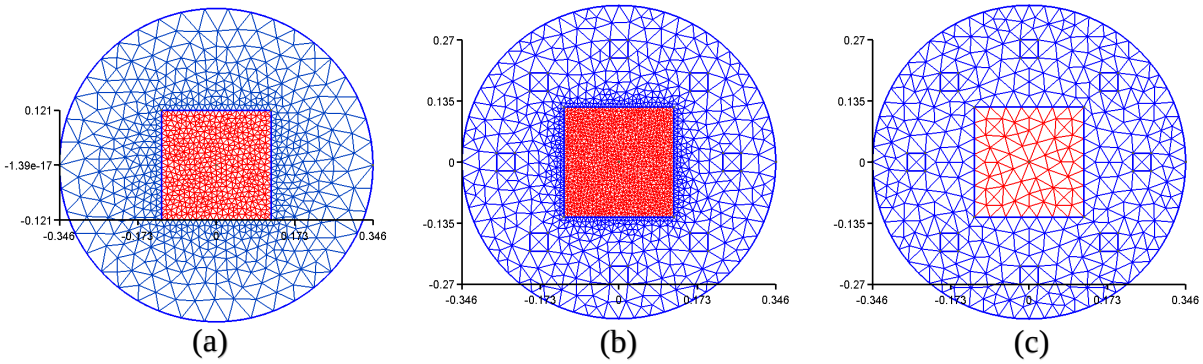

Figure 8.17: Meshes used for the BoxTarget image reconstruction by algorithms from (a) to (c): FD, TD with 1st order of basis functions, TD with higher (4th) order of basis functions.

Note, the effect of solution order for FD algorithms has previously been observed in [93] to

enable high-order solutions on coarse meshes that provide faster reconstruction times without significantly changing the resulting image.

The reconstructed images of the BoxTarget, with 8 transmitters and 15 receivers (the mono-static measurement is removed), are compared for DGM-FBTS, DGM-CSI, and DGM-GNI in Figure 8.18. In this figure, DGM-FBTS was run for 12 iterations using mesh (b) (row 1), FD DGM-CSI for 200 iterations using mesh (a) (row 2), and FD DGM-GNI for 15 (row 3) iterations using mesh (a). Comparing the results, the top-right cylinder's permittivity is under-estimated in the frequency-domain results, while the conductivity is over-estimated. The time-domain DGM-FBTS clearly results in higher resolution, and it corrects the top-right cylinder's permittivity.

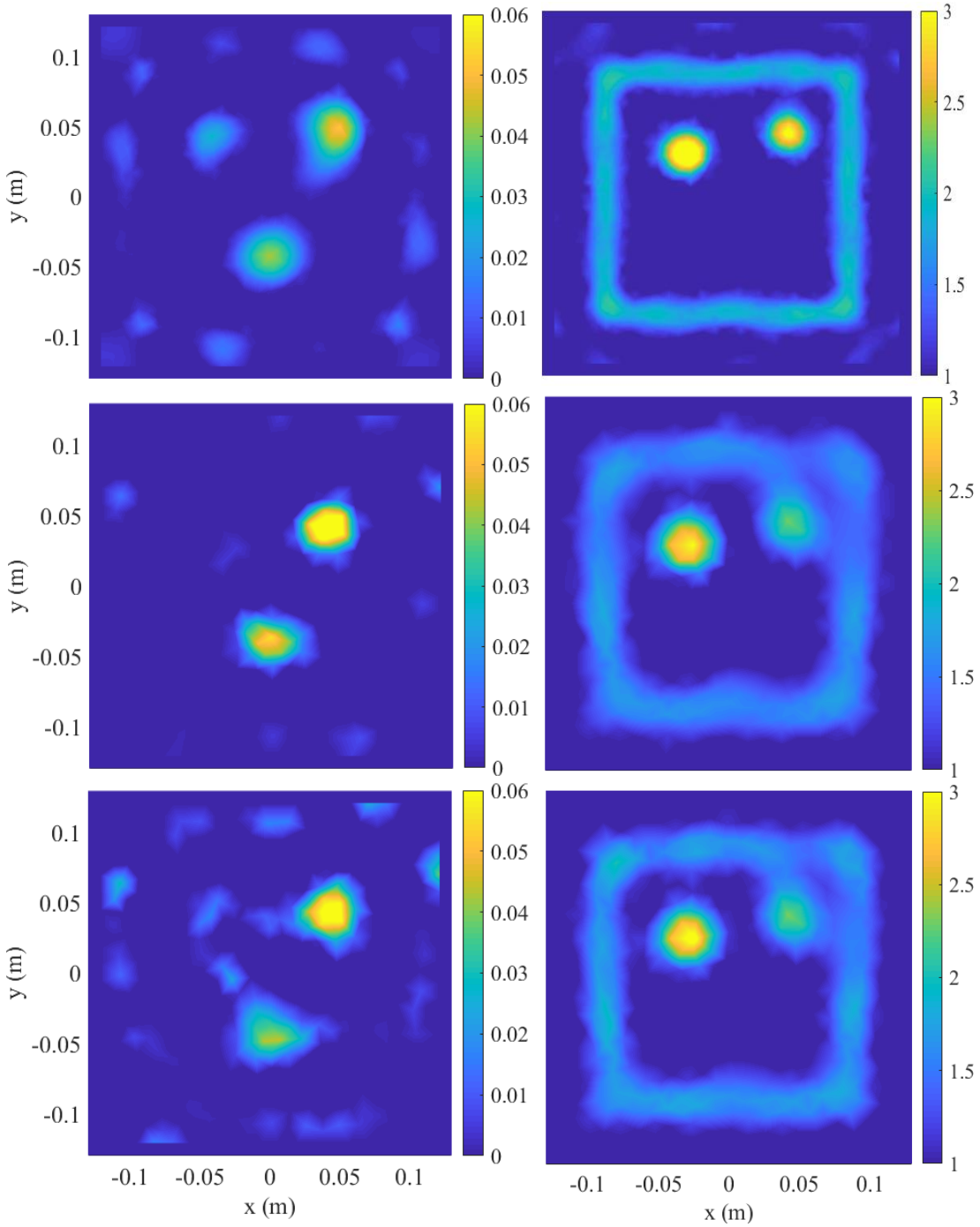

Figure 8.18: The BoxTarget reconstruction images using 8 transmitters and 16 receivers at 2 GHz, (left) conductivity and (right) permittivity. From top to bottom: DGM-FBTS using mesh (b), DGM-CSI using mesh (a), DGM-GNI using mesh (a). [The image is reproduced from [1] with permission.]

Next, we increased the number of transmitters (with the same number of receivers) in the FD simulations, to provide the FD algorithms with more information. Figure 8.19 illustrates FD DGM-CSI and DGM-GNI results after doubling the number of transmitters, when the number of iterations are the same as before. We witness that both DGM-CSI and DGM-GNI reproduce similar reconstructions after increasing the number of transmitters and consequently extending the amount of frequency-domain data did not improve the results appreciably for this target.

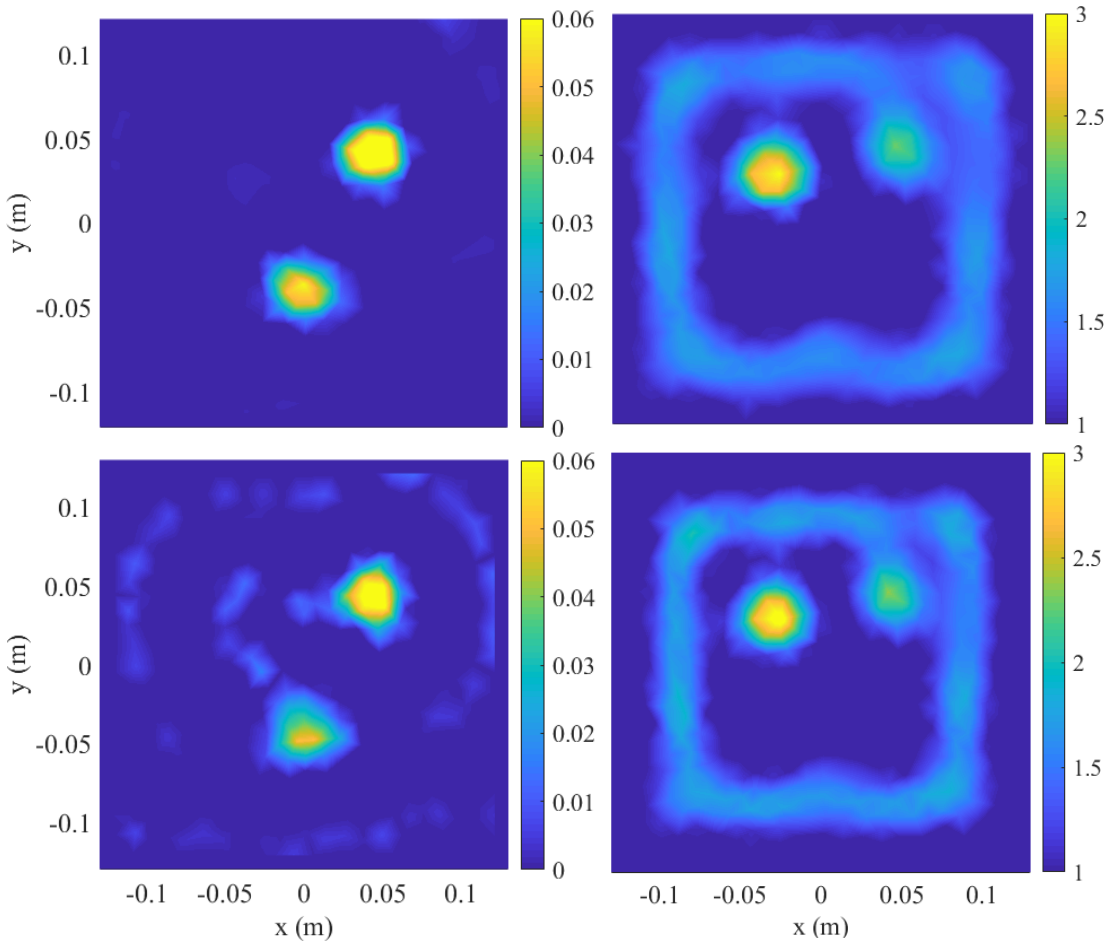

Figure 8.19: The BoxTarget reconstruction images using 16 transmitters and 16 receivers at 2 GHz using mesh (a), (left) conductivity and (right) permittivity. From top to bottom: DGM-CSI, DGM-GNI. [The image is reproduced from [1] with permission.]

Note that in all cases, the iteration counts were selected based on our experience with the

algorithms, and additional iterations did not significantly improve the results.

Evaluating imaging algorithms using synthetic targets gives us the opportunity to quantify the reconstruction error, as the true target is known. The quantitative Root Mean Square Deviation (RMSD) metric, denoted by ζ_P is given by:

$$\zeta_P = \sqrt{\frac{(\underline{P}_{true} - \underline{P})^T (\underline{P}_{true} - \underline{P})}{N_D}}, \tag{8.5}$$

where $\underline{P}_{true}$ and $\underline{P}$ are the N_D-long arrays containing the real-valued coefficients of any one of the respective true and the corresponding reconstructed constitutive functions. Table 8.1 summarizes the error in the reconstructions for the synthetic target. While DGM-CSI and DGM-GNI offer comparable results, DGM-FBTS quantitatively out-performs both in the reconstruction of the permittivity, with slightly degraded reconstruction of the conductivity.

Configuration	ζ_{ε_r}	ζ_σ
DGM-FBTS / 8Tx	0.1955	0.0064
DGM-CSI / 8Tx	0.3208	0.0056
DGM-GNI / 8Tx	0.2969	0.0060
DGM-CSI / 16Tx	0.3186	0.0051
DGM-GNI / 16Tx	0.2935	0.0054

Table 8.1: Synthetic lossy BoxTarget reconstruction RMSD error. [This table is reproduced from [1] with permission.]

The BoxTarget reconstruction cost functional by TD DGM-BFTS using mesh (b) and the 1st order of basis functions is shown in Figure 8.20. This curve is normalized to the cost functional quantity at the first iteration, when the modeled fields are the fields of the free space (the initial parameters for this reconstruction was $\varepsilon_r = 1$, and $\sigma = 0$).

In the following, we refer to the cost functional value associated with the free space modeled fields by *free space cost functional*[5], for brevity.

The effect of solution order has been previously studied for the FD DGM-CSI and DGM-

[5]Note that the *free space cost functional* quantity is different for different targets.

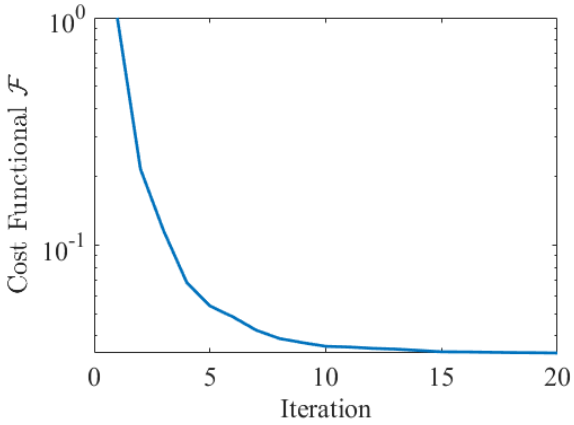

Figure 8.20: The BoxTarget reconstruction cost functional by TD DGM-BFTS using mesh (b) and the 1st order of basis functions.

GNI algorithms [93]. Here, we do a similar study for the time-domain inversion algorithm FBTS. The same BoxTarget with the same geometry setup is used for this purpose. Figure 8.21 shows the image reconstruction of this target with 8 transmitters and 15 receivers by the DGM-FBTS method. The 1st solution order (same images from Figure 8.18) results are shown at the first row of Figure 8.21. We take the mesh size in this case as the reference for the following comparison. The results regarding 4/3-th fields/constitutives solution orders and 4/4-th fields/constitutives solution orders, with about 4 times coarser imaging-domain mesh illustrated in Figure 8.17(c), are shown in this figure's second and third rows, respectively. To have a better evaluation of the execution time, we use a time average over the first 5 inverse algorithm iterations for each of these inversions. After changing the solution orders from 1/1-st fields/constitutives to 4/3-th fields/constitutives and 4/4-th fields/constitutives, time-per-iteration decreased by 19.66% and 40.78%, respectively.

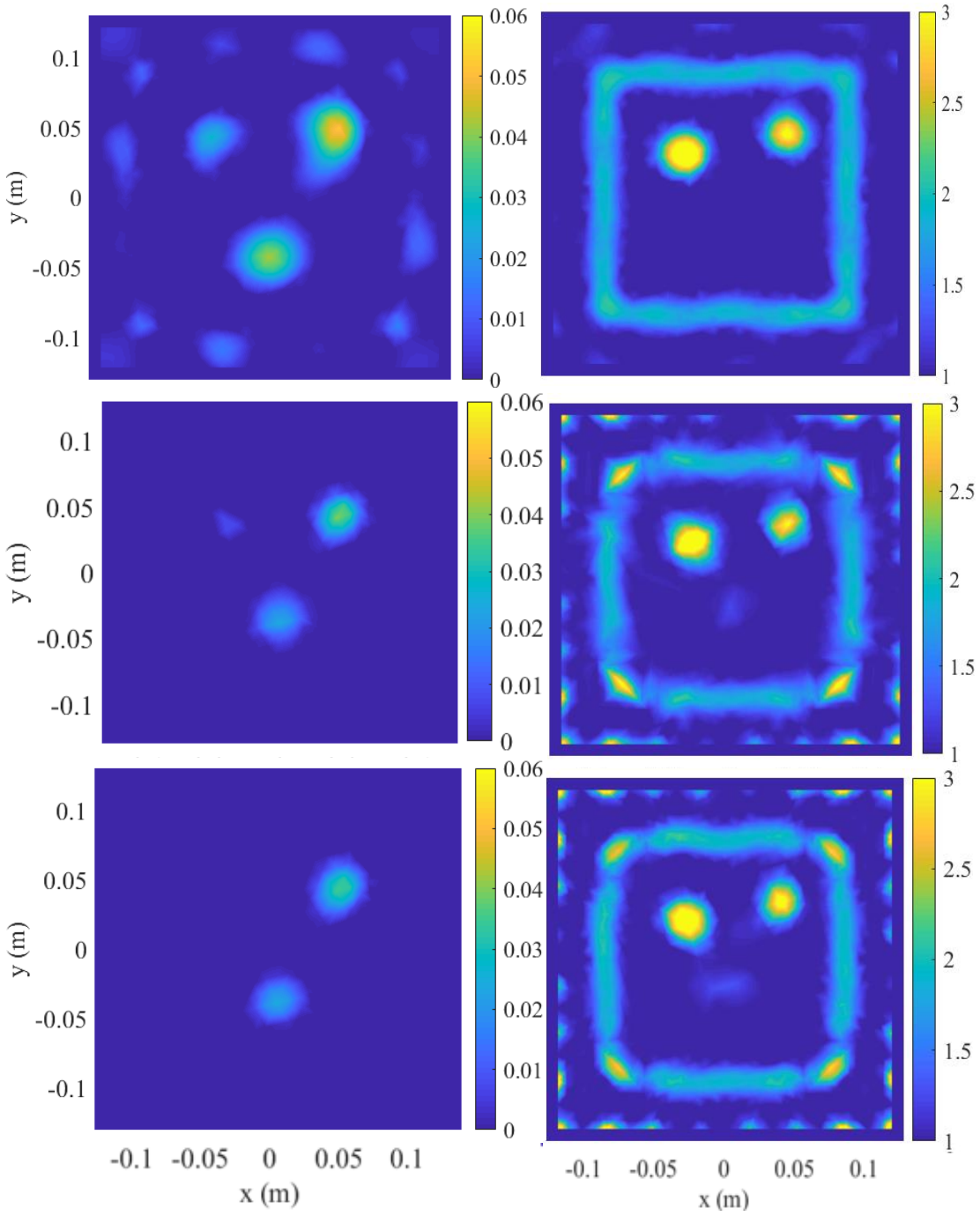

Figure 8.21: The BoxTarget reconstruction images of permittivity (right) and conductivity (left) with 8 transmitters and 15 receivers by DGM-FBTS after 12 iterations with: 1st solution order using mesh (b) (top), 4th and 3rd solution orders for respective fields and constitutives using mesh (c) (middle), and 4th solution orders for fields and constitutives both using mesh (c) (bottom).

Note that the per-iteration execution time increases when the order of basis functions of constitutives is different from the order of basis functions of fields. This slowing speed results from extra step(s) of multiplication(s) in each iteration to interpolate different quantities to their proper basis function orders. Although choosing different solution orders for fields and constitutives accompany increasing the execution time, this method adds more flexibility to the problem.

Comparing the image reconstructions in Figure 8.21, we witness a decreased effect of the shell shadow in conductivity result and an increased effect of the imaging domain shadow in the permittivity when increasing the solution order. The upper left cylinder is detected as a lossy target in the 1st order results (causing false recognition), which is fixed after increasing the field's solution order to 4.

The presence of imaging domain boundary effect at higher solution orders makes it difficult to have a fair quantitatively comparison. We know that these effects do not occur in high order FD counterparts, and can not be interpreted as false/positive alarm error in practice. Additional research is needed to find the reason and mitigate the issues at the edges of the imaging domain.

The BoxTarget reconstruction cost functional by TD DGM-BFTS using mesh (c) and the 4th order of basis functions is shown in Figure 8.22. This curve is again normalized to *free space cost functional* of this target.

BoxTarget with Perfect Electric Conductor Boundary

Although using resonant enclosures, modeled with PEC boundary conditions, is common in microwave imaging [99, 100, 101], it imposes a great challenge for frequency domain inversion algorithms as the collected data at the presence of high reflective boundaries (PEC) makes the inversion problem more difficult. In this section, we aim to show the benefit of the time domain DGM-FBTS imaging scheme over FD imaging for PEC-enclosed problems.

Within a PEC enclosure, the electromagnetic wave does not penetrate (or attenuate by) the

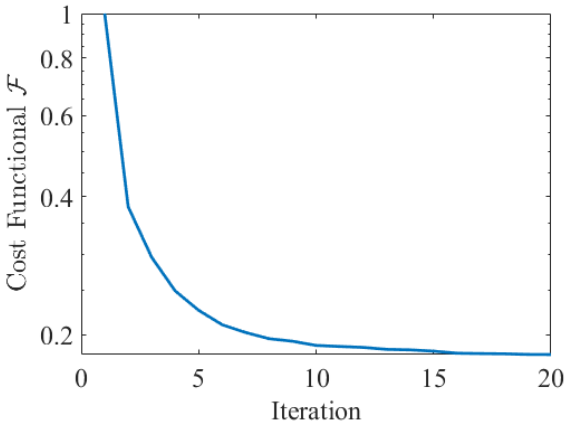

Figure 8.22: The BoxTarget reconstruction cost functional by TD DGM-BFTS using mesh (c) and the 4th order of basis functions.

chamber walls. Energy remains inside the chamber, bouncing until the wave attenuates due to loss (if loss exists). This effect makes DGM-FBTS computationally more expensive compared to an analogous case with an absorbing boundary. In order to compute meaningful DGM-FBTS gradients, we need to choose a proper final measurement time. This final measurement time has to be long enough that after windowing the measured fields by $\mathcal{W}_m(t)$ in (3.1), we do not lose meaningful data.

On the other hand, due to the mode patterns inside the PEC chamber, FD algorithms may not work at all at many frequencies, requiring us to sweep a large number of frequencies to find an acceptable result.

First we try the BoxTarget with the same settings as before except changing the boundary condition to PEC, to see the effects of PEC chamber on the TD and FD algorithms. The reconstructed images of the BoxTarget, by the time-domain DGM-FBTS solver with 8 transmitters and 15 receivers, and DGM-CSI and DGM-GNI frequency-domain solvers with 16 transmitters and 15 receivers are shown in Figure 8.23. TD DGM-FBTS was run for 12 iterations (row 1), FD DGM-CSI for 200 iterations (row 2), and FD DGM-GNI for 15 iterations (row 3). The dominant source frequency is 2 GHz and the FD results are generated at 2 GHz. The final measurement

time in DGM-FBTS remains 3 ns.

As expected, the TD results are degraded due to the more complicated wave propagation problem, however the broadband interrogation provides meaningful results. The FD results are not good at all, which is not surprising having picked a single frequency. Note that there is very little loss in this problem, so it is very difficult.

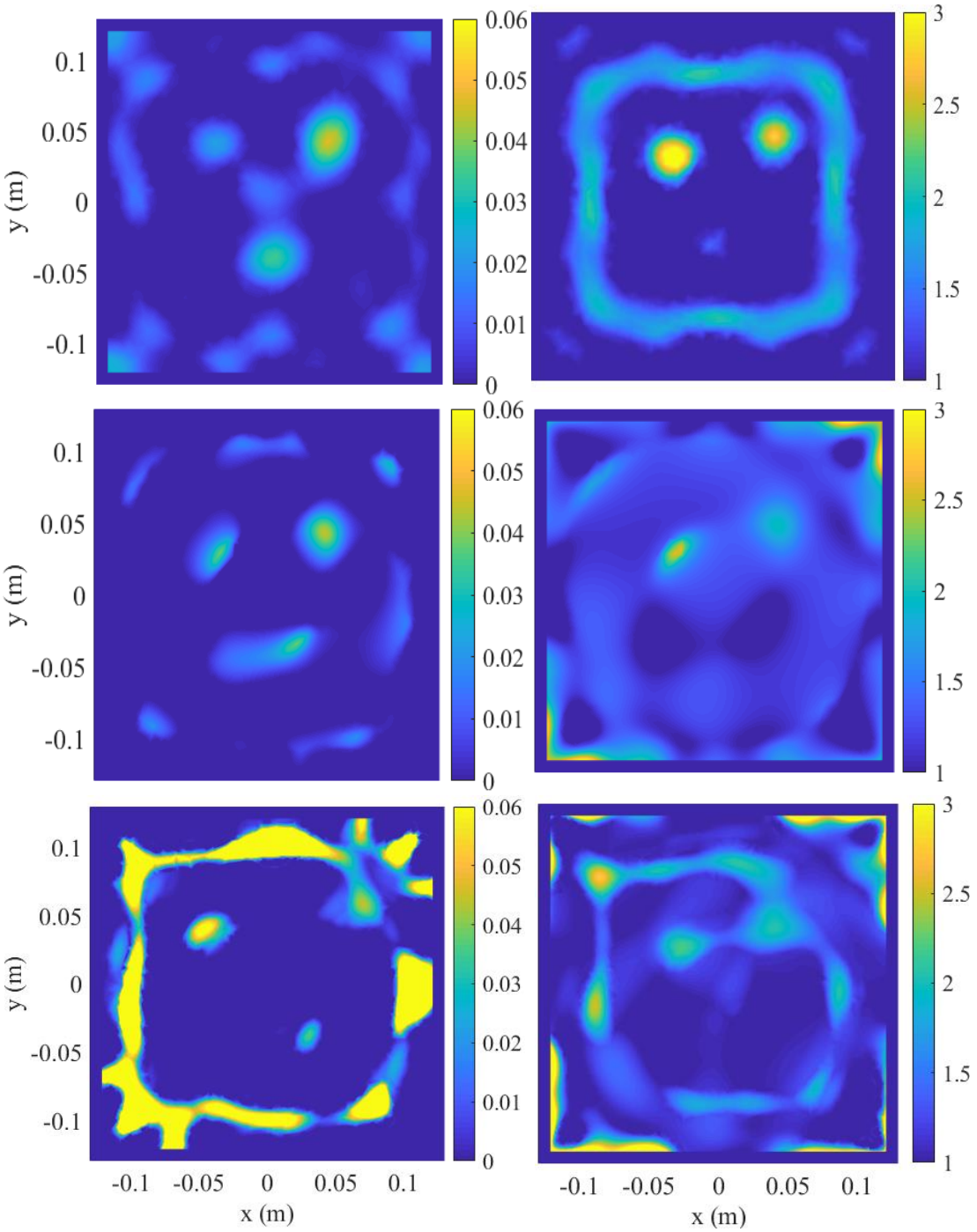

Figure 8.23: The BoxTarget reconstruction images, (left) conductivity and (right) permittivity. From top to bottom: DGM-FBTS by 8 transmitters and 16 receivers using mesh (b), DGM-CSI by 16 transmitters and 16 receivers at 2.0 GHz using mesh (a), DGM-GNI by 16 transmitters and 16 receivers at 2.0 GHz using mesh (a).

As the next experiment, we increase the final measuring time to 7 ns in DGM-FBTS. Also we sweep a frequency range from 800 MHz to 2.5 GHz with 50 MHz step size to find the best results by DGM-CSI and DGM-GNI. The reconstructed images resulting from these changes are shown in Figure 8.24. FD DGM-CSI was run for 200 iterations, FD DGM-GNI for 15 iterations, and TD DGM-FBTS for 15 iterations. FD results are shown at 2.2 GHz, one of the best imaging frequencies (We do not show the other frequency results here, for brevity). The improvements in the FD results obtained after changing the frequency by 200 MHz support the idea of the sensitivity/difficulty of these FD algorithms face for PEC boundary condition. This may be related to the fact that calibrating to a PEC cylinder at one frequency or another may lead to different modelling error.

Comparing the TD to FD results in Figure 8.24, the top-right cylinder's permittivity is under-estimated in the frequency-domain results, while the conductivity is over-estimated. The conductivity result by FD DGM-GNI is not as clear as the absorbing boundary condition case. The time-domain DGM-FBTS clearly resulted in higher resolution, and it corrects the top-right cylinder's permittivity and conductivity.

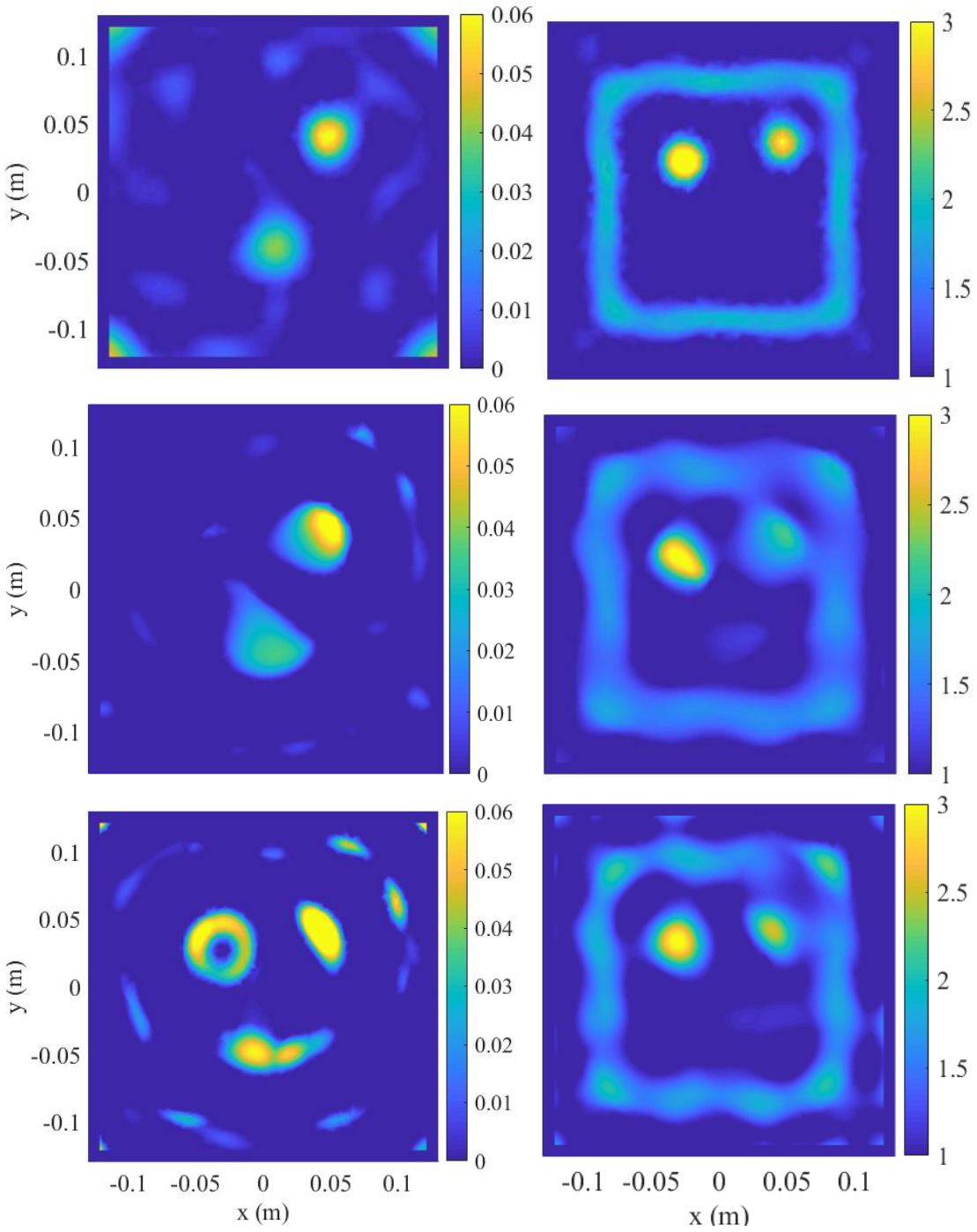

Figure 8.24: The BoxTarget reconstruction images, (left) conductivity and (right) permittivity. From top to bottom: DGM-FBTS by 8 transmitters and 16 receivers using mesh (b), DGM-CSI by 16 transmitters and 16 receivers at 2.2 GHz using mesh (a), DGM-GNI by 16 transmitters and 16 receivers at 2.2 GHz using mesh (a).

8.5.2 The Experimental Lossless TwoCylinder Example

The previous sections confirmed the resolution benefits of the time-domain DGM-FBTS imaging. The following sections focus on reconstructing the experimental targets described earlier, starting with the lossless TwoCylinder target. Moving to experimental targets, we want to demonstrate the additional advantages of time-domain imaging, e.g., the TD algorithm's robustness in the presence of noise or the ability to overcome frequency selection issues.

The reconstructed images of the TwoCylinder target are shown in Figure 8.25. The first image, at top, shows the reconstruction obtained from DGM-FBTS after 10 iterations. The second- and third-row images at the left-column show 200-iteration DGM-CSI reconstruction and 15-iteration DGM-GNI at 2.05 GHz. The second- and third-row images at the right-column show 200-iteration DGM-CSI reconstruction and 15-iteration DGM-GNI at 3.10 GHz.

Examining the results, DGM-FBTS could nicely detect the circular shapes of the targets, while neither of the two FD algorithms could do this task clearly.

Based on Figure 8.25, it lookes that our guess about different permittivities for the two cylinders was not entirely wrong, and the cylinder with the smaller diameter shows larger permittivity in all of the results. Considering this, the DGM-FBTS imaging result for this target configuration is significantly improved over both results of DGM-CSI and DGM-GNI. Even though there is no regularization added to DGM-FBTS in this thesis, this inversion method was robust enough to detect the experimental TwoCylinder target through noise- and modelling error-contaminated data. Recall that both DGM-CSI and DGM-GNI algorithms used here benefit from regularization which can help with the non-ideal data.

The cost functional (normalized to the *free space cost functional*) of DGM-FBTS is shown in Figure 8.26 to demonstrate the convergence speed of this algorithm for the TwoCylinder target reconstruction.

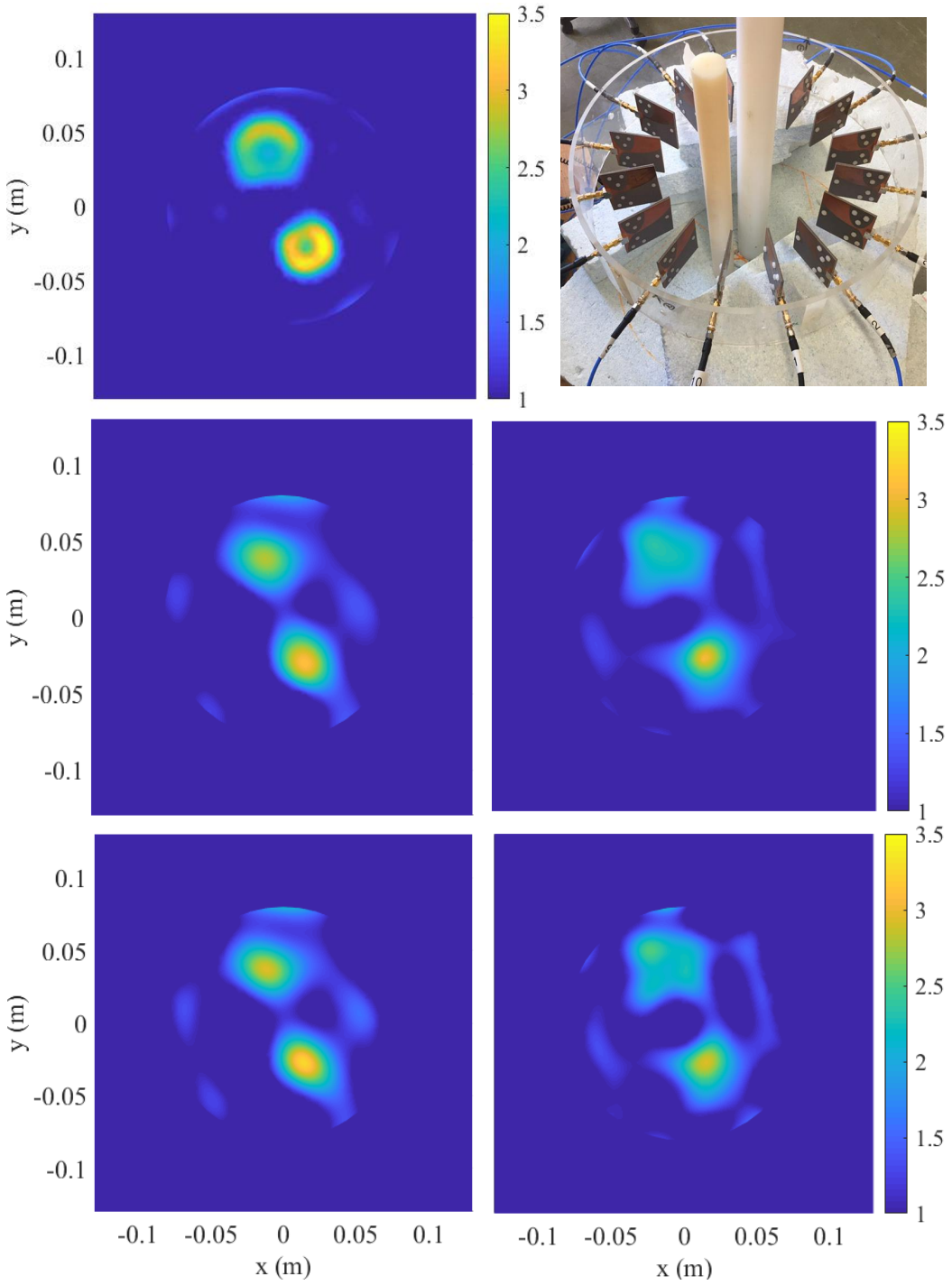

Figure 8.25: Reconstructed relative permittivity for the experimental TwoCylinder target. From top-to-bottom: DGM-FBTS (left), DGM-CSI and DGM-GNI. From left-to-right: at 2.05 GHz, and 3.10 GHz. Top-right photo: the TwoCylinder target inside the imaging chamber. [The image is reproduced from [1] with permission.]

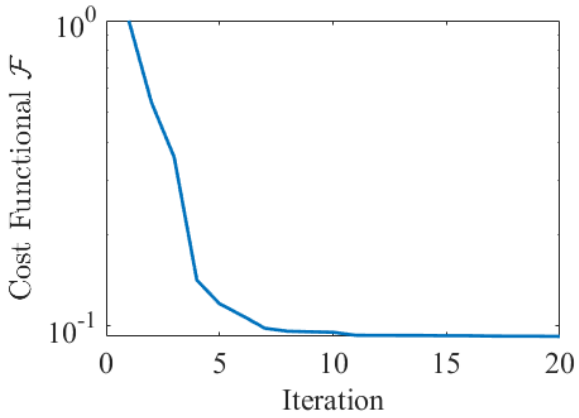

Figure 8.26: The cost functional of image reconstruction of experimental TwoCylinder target by DGM-BFTS.

8.5.3 The Experimental Lossless E-Phantom Example

The reconstructed images of the E-Phantom target are shown in Figure 8.27. The first image, on top, shows the reconstruction obtained from DGM-FBTS after 11 iterations. The second- and third-row images at the left-column show 200-iteration DGM-CSI reconstruction and 15-iteration DGM-GNI at 2.05 GHz. The second- and third-row images at the right-column show 200-iteration DGM-CSI reconstruction and 15-iteration DGM-GNI at 3.10 GHz.

Examining the results in Figure 8.27, DGM-FBTS had a significant improvement over the two FD algorithms in reconstructing this target. The data collected at a single frequency was not enough to reconstruct the image of this complicated target (by DGM-CSI and DGM-GNI).

The cost functional (normalized to the *free space cost functional*) of DGM-FBTS is shown in Figure 8.28 to demonstrate the convergence speed of this algorithm for the Experimental E-Phantom target reconstruction.

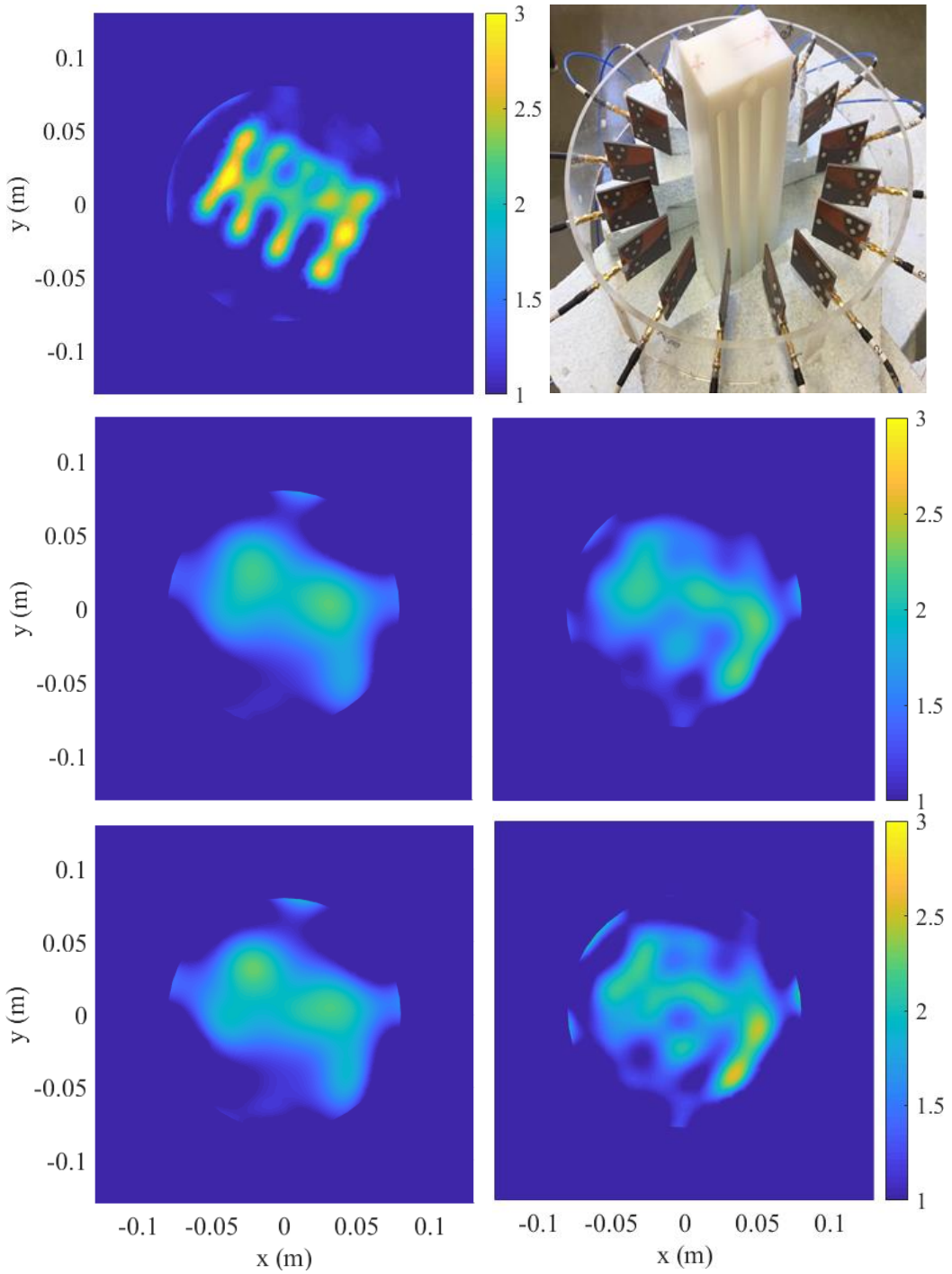

Figure 8.27: Reconstructed relative permittivity for the experimental E-phantom target. From top-to-bottom: DGM-FBTS (left), DGM-CSI and DGM-GNI. From left-to-right: at 2.05 GHz, and 3.10 GHz. Top-right photo: the E-phantom target inside the imaging chamber. [The image is reproduced from [1] with permission.]

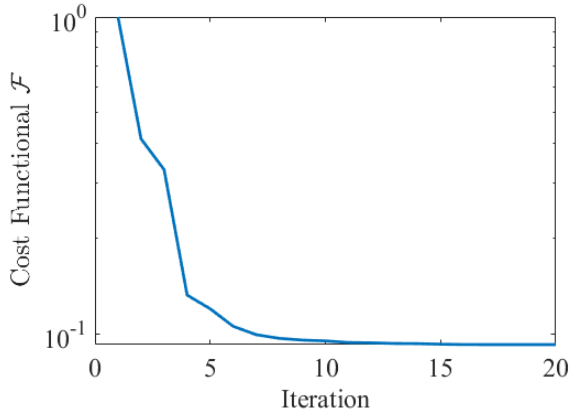

Figure 8.28: The cost functional of image reconstruction of experimental E-Phantom target by DGM-BFTS.

8.5.4 The Experimental Lossy WoodTarget Example

So far we have evaluated the non-dispersive TD DGM-FBTS code with one synthetic lossy target and experimental lossless targets. This section aims to take this evaluation further with a lossy experimental target; the Lossy WoodTarget.

Although the WoodTarget is a dielectric with dispersive loss, this section uses the equivalent (static) conductivity and permittivity of this target as unknowns instead of the dispersive parameters (optical and static permittivity), for two reasons: to have a better understanding of the non-dispersive TD code's performance for the lossy targets, and, to have a comparison of the two non-dispersive and dispersive versions of TD DGM-FBTS (the dispersive code result is in Section 8.6.2).

As the DGM-GNI result for this target is similar to DGM-CSI, here we present only the DGM-CSI frequency-domain algorithm. The first row of Figure 8.29 shows the DGM-FBTS results after 12 iterations. The DGM-CSI reconstructions after 200 iterations at 3.10 GHz and 4.00 GHz are also shown in the last two rows of this figure.

It looks that the FD algorithm struggles to maintain consistency across frequencies for this

target and the DGM-FBTS result is an obvious improvement over the DGM-CSI results.

In the experimental examples, and based on the Vivaldi antennas' features [86], the FD single-frequency algorithms are sensitive to the simulated/modeled location of the sources. In these cases, the modeled location of the sources should be chosen carefully based on the frequency. This sensitivity is less pronounced in time-domain algorithms because of dealing with a wide range of frequencies in the TD scenario. In the following, we do an experiment by changing the modeled transceivers' radius from the default quantity of 18.75 cm to 14.40 cm, with the hope of improving the FD results. We picked radius 14.40 cm because it has been used before by the UofM-EIL in the past and resulted in reasonable outputs [95]. The related results of DGM-CSI, when the transceivers' radius is modeled at 14.4 cm, are shown in Figure 8.30. In this figure, we have reconstructions after 200 iterations at 3.10 GHz, 4.00 GHz, and 5.00 GHz in rows 1-3. The results show no improvement but some overshooting for the conductivity.

Again, the FD algorithm struggles to maintain consistency across frequencies, after changing the location of the modelled sources. Indeed, image reconstruction of (equivalent) conductivity by frequency-domain inversion schemes is a significant challenge in microwave imaging. Different strategies, including balancing of the real and imaginary part [102], material property dependencies [103], and mixture models [104], proposed in the recent literature, show some improvement. In addition to these techniques, treating the dielectric targets as lossy dispersive targets instead of lossy conductive materials is a potential remedy which is investigated in the next section.

To finish this section, the DGM-FBTS cost functional (normalized to the *free space cost functional*) for image reconstruction of the experimental lossy WoodTarget is shown in Figure 8.31 to demonstrate the convergence speed of this non-dispersive algorithm for the first lossy experimental target.

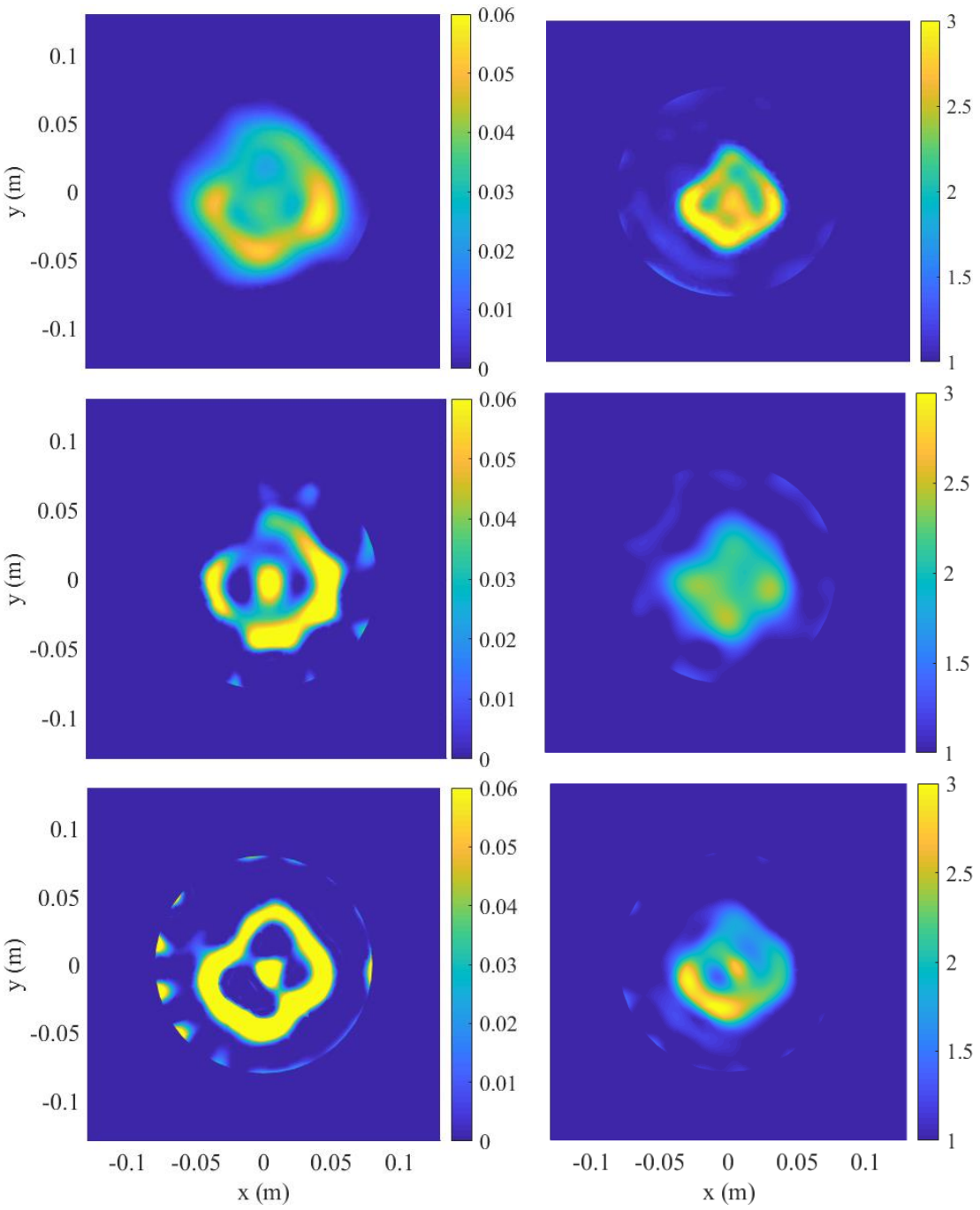

Figure 8.29: The WoodTarget reconstructed (left) conductivity and (right) relative permittivity. From top to bottom: DGM-FBTS, DGM-CSI at 3.10 GHz, DGM-CSI at 4.00 GHz. [The image is reproduced from [1] with permission.]

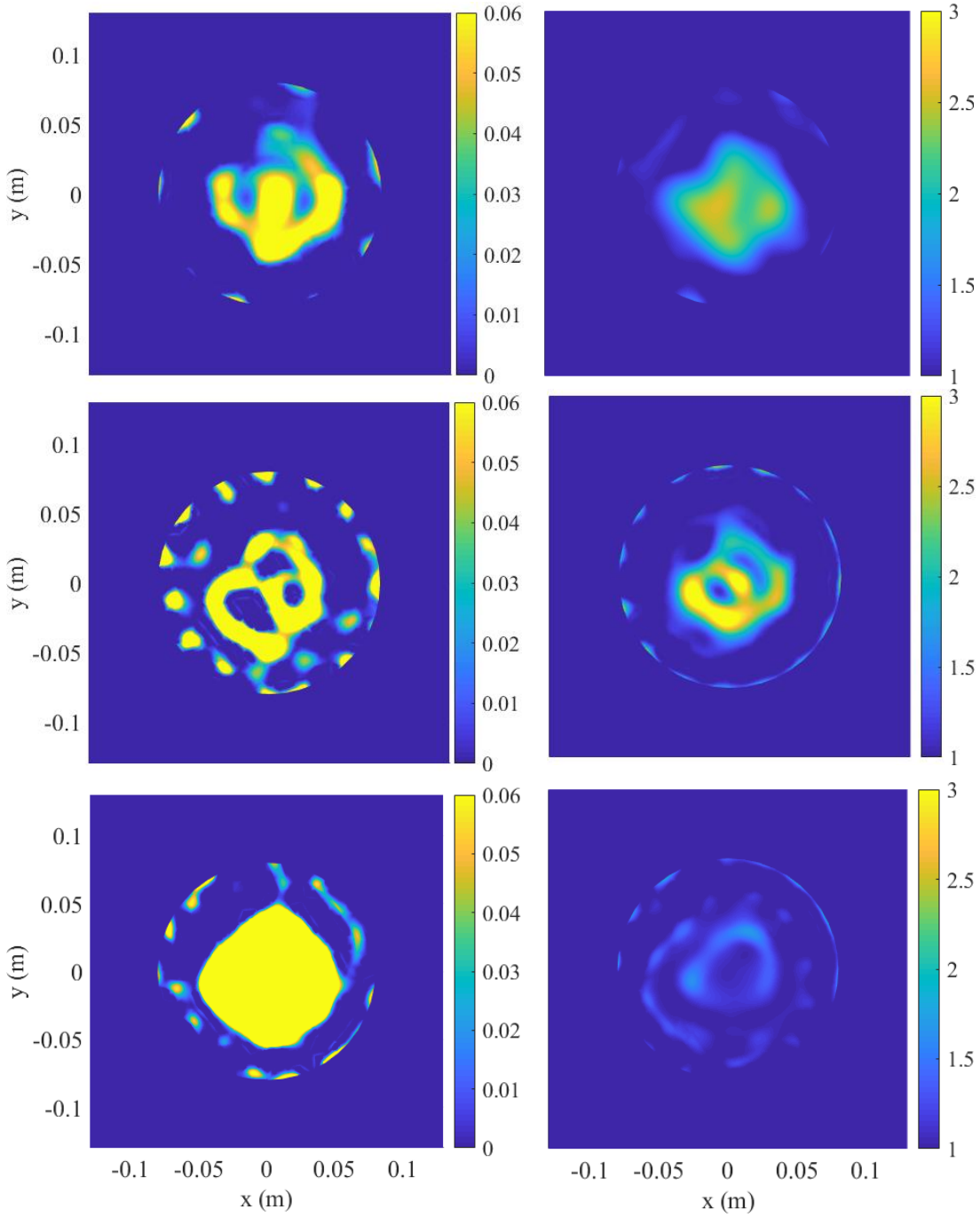

Figure 8.30: The WoodTarget reconstructed (left) conductivity and (right) relative permittivity, when the transceivers' radius is changed to 14.4 cm (from 18.75 cm). From top to bottom: DGM-CSI at 3.10 GHz, DGM-CSI at 4.00 GHz, DGM-CSI at 5.00 GHz.

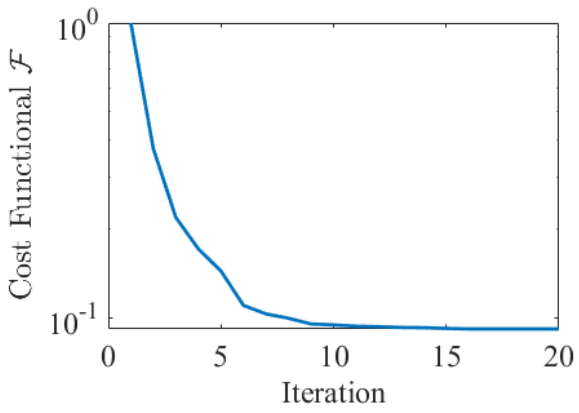

Figure 8.31: The cost functional of image reconstruction of the experimental lossy WoodTarget by the non-dispersive DGM-BFTS code.

8.6 Dispersive TD DGM-FBTS Evaluation

In this section we perform microwave imaging on simple dispersive synthetic target and lossy experimental targets using the dispersive DGM-FBTS inversion algorithm.

Here, we assume that the target's loss is entirely dispersive, i.e., we assume there is no conductive loss. As discussed in Section 2.3, we assume a relaxation time equal to 17.5 ps, leaving two unknown Debye parameters: the optical permittivity ε_∞ and static permittivity ε_s.

For the experimental targets, representing the constitutive parameters by the equivalent quantities described in (8.2) is convenient for the purpose of comparison. Therefore, besides the static and optical permittivities, we also illustrate the equivalent permittivity and conductivity calculated by (8.2) for each experimental target. As these equivalent parameters are frequency dependant, we show the parameters at 2 GHz as it is the dominant frequency of the time-domain source used to interrogate the experimental targets.

8.6.1 The Synthetic Dispersive Cylinders Example

As the first dispersive target, we study a simple synthetic target in this section. This target, called dispersive cylinders, is introduced in Section 8.3.

The true parameters of relative static (left) and optical (right) permittivities for this target are shown in the first row Figure 8.32.

The image reconstruction of this target by the dispersive DGM-FBTS after 15 iterations, with $\varepsilon_\infty = 1$ and $\varepsilon_s = 1$ initial values, is shown in bottom row Figure 8.32. The left image is the static, and the right image is the optical permittivity.

Although there are just 4 transmitters used for reconstructing this dispersive target, the result properly shows the constitutive parameters, location and boundaries of these two cylinders.

8.6.2 The Experimental Dispersive WoodTarget Example

As the first experimental dispersive target, we image the WoodTarget described in Section 8.5.4. Note that this target is genuinely a dispersive material, but we previously assumed it as a lossy non-dispersive target in Section 8.5.4. We now compare the dispersive reconstruction capabilities of DGM-FBTS to those previous results.

The image reconstruction of the WoodTarget by the dispersive DGM-FBTS after 8 iterations, with $\varepsilon_\infty = 1$ and ε_s=2 initial values[6], is shown in Figure 8.33. The top images are the static permittivity ε_s and optical permittivity ε_∞, from left to right. Also, the equivalent permittivity and conductivity of this target are shown in the left middle and right middle, respectively.

The reconstructed image of this target by the non-dispersive DGM-FBTS code are repeated in Figure 8.33 from the previous section, for a better comparison. The permittivity and conductivity of this target are shown in the left bottom and right bottom, respectively.

Comparing the equivalent constitutive parameters with the same parameters produced by

[6]Recal that $\varepsilon_s > \varepsilon_\infty$ is the requirement of dispersive media

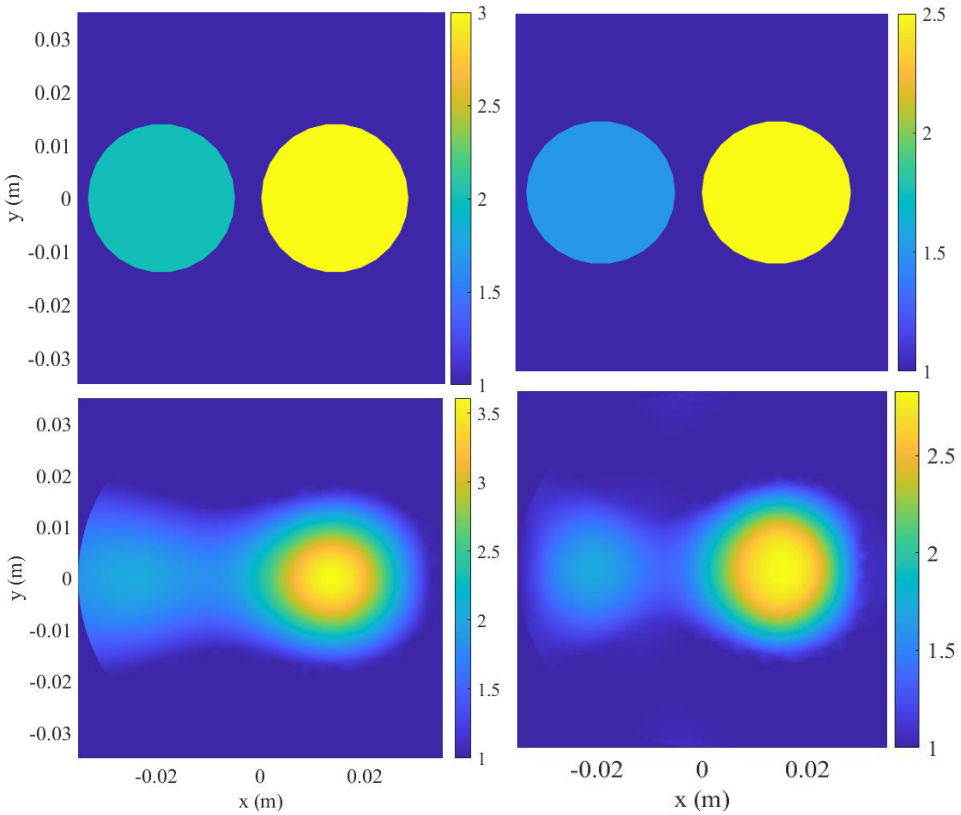

Figure 8.32: The image reconstruction results of the syntheticdispersive cylinders by dispersive DGM-FBTS with $\varepsilon_\infty = 1$ and $\varepsilon_s = 1$ initial values after 15 iterations.
True target: Top left: static permittivity, top right: optical permittivity.
Dispersive code results: Top left: static permittivity, Bottom right: optical permittivity.

the non-dispersive DGM-FBTS algorithm after 12 iterations in Figure 8.29, demonstrates that the dispersive algorithm converged faster (by 33%) and revealed more accurate shape of the WoodTarget. The shadowy parts in the conductivity (and permittivity) image resulted from the non-dispersive code disappeared in the image generated by the dispersive DGM-FBTS. This supports the idea of having a more robust inversion algorithm by counting the dispersivity of materials [41].

All of the image reconstructions of this target so far show some inconsistency at the bottom boundary. This inconsistency can be interpreted due to the higher percentage of humidity.

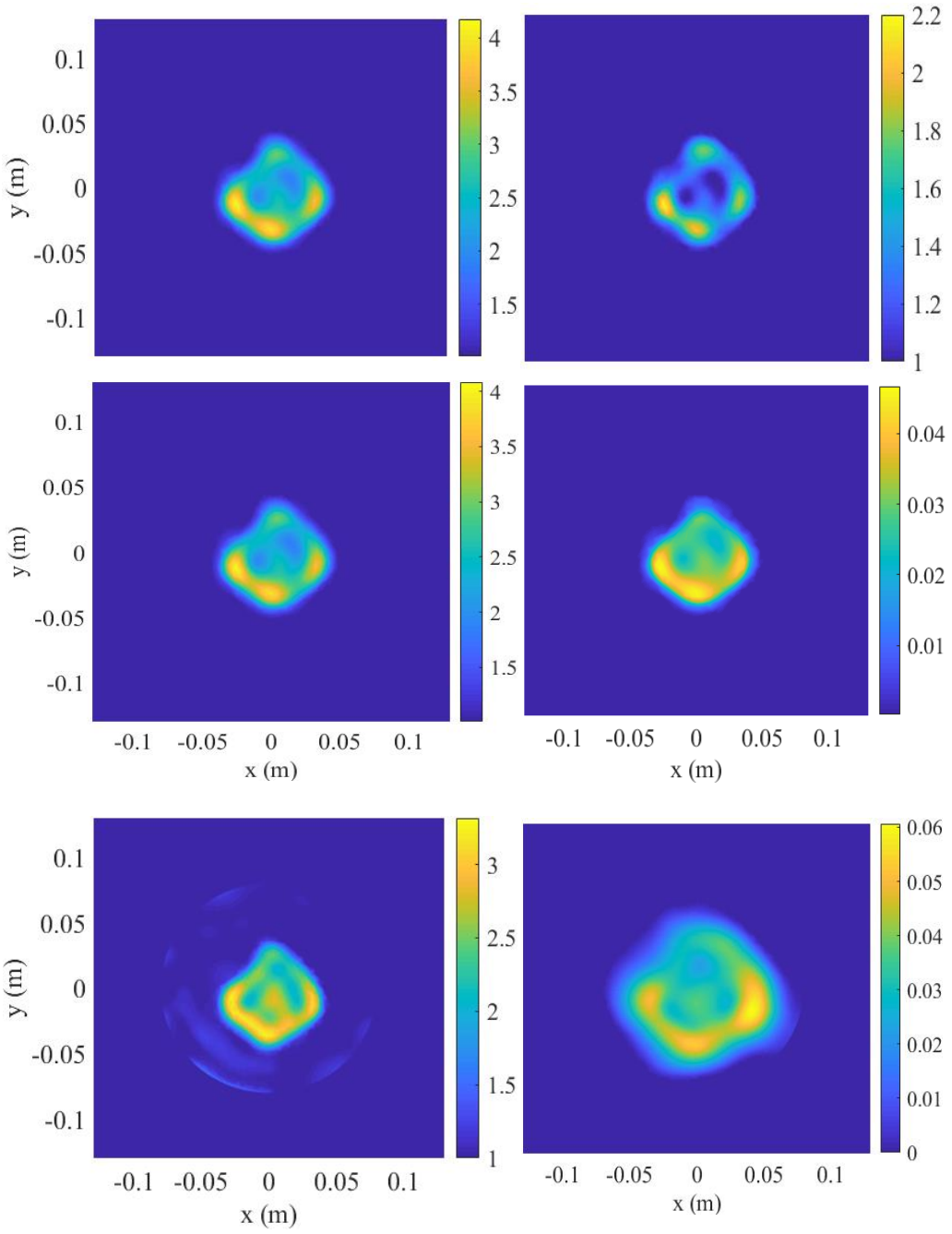

Figure 8.33: Comparing the image reconstruction results of the experimental WoodTarget by dispersive DGM-FBTS with $\varepsilon_\infty = 1$ and ε_s=2 initial values after 8 iterations and non-dispersive DGM-FBTS with free space initial values after 12 iterations.
Dispersive code results: Top left: static permittivity, top right: optical permittivity, middle left: equivalent permittivity at 2 GHz, middle right: equivalent conductivity at 2 GHz.
Non-dispersive code results from Figure 8.29: Bottom left: permittivity, bottom right: conductivity.

Also, the dispersive DGM-FBTS cost functional, normalized to the *free space cost functional*, is shown in Figure 8.34. Here, the cost functional at iteration 8 is 0.14326, which is slightly larger than the cost functional at iteration 12 from the non-dispersive code in Figure 8.31, which is 0.0934. Although the dispersive code is still minimizing the cost functional after iteration 8, e.g., the cost functional is about 0.14033 at iteration 15, the resulted images at iteration 8 have the consistency of the target geometry and they seem quite converged.

Note that the Cost functional curve in Figure 8.34 initiates from 1.1814, because the initial values in this case are not free space parameters anymore.

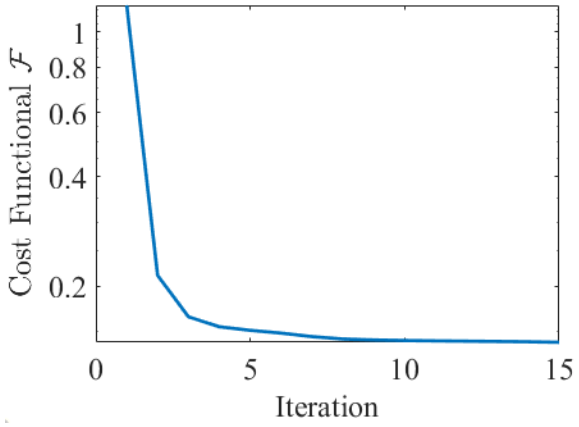

Figure 8.34: The cost functional of image reconstruction of the experimental lossy WoodTarget by the dispersive DGM-BFTS code.

8.6.3 The Experimental Dispersive Salted-Butter Example

In this section, we move on to the Salted-Butter target. This target has higher constitutive parameters which makes it a relatively high contrast target when the background is free space.

Figure 8.35 shows the reconstructed image of this target by the dispersive DGM-FBTS after just 3 iterations, when $\varepsilon_s = 3.0$ is the initial static permittivity of the imaging domain. The top images are the static permittivity ε_s and optical permittivity ε_∞, from left to right. Also, the equivalent permittivity and equivalent conductivity of this target are shown respectively in the

left bottom and right bottom of Figure 8.35.

Interestingly, the dispersive DGM-FBTS has generated an almost united image (especially about the conductivity) of this target, which can be considered a great improvement. Also the constitutive parameter quantities show some agreement with the measured numbers by the dielectric probe: $\varepsilon_\infty = 1.8$ and $\varepsilon_s = 5.13$ (Section 8.3).

The DGM-FBTS cost functional for image reconstruction of the dispersive Salted-Butter target is shown in Figure 8.36 to demonstrate the convergence speed of the dispersive algorithm for this target.

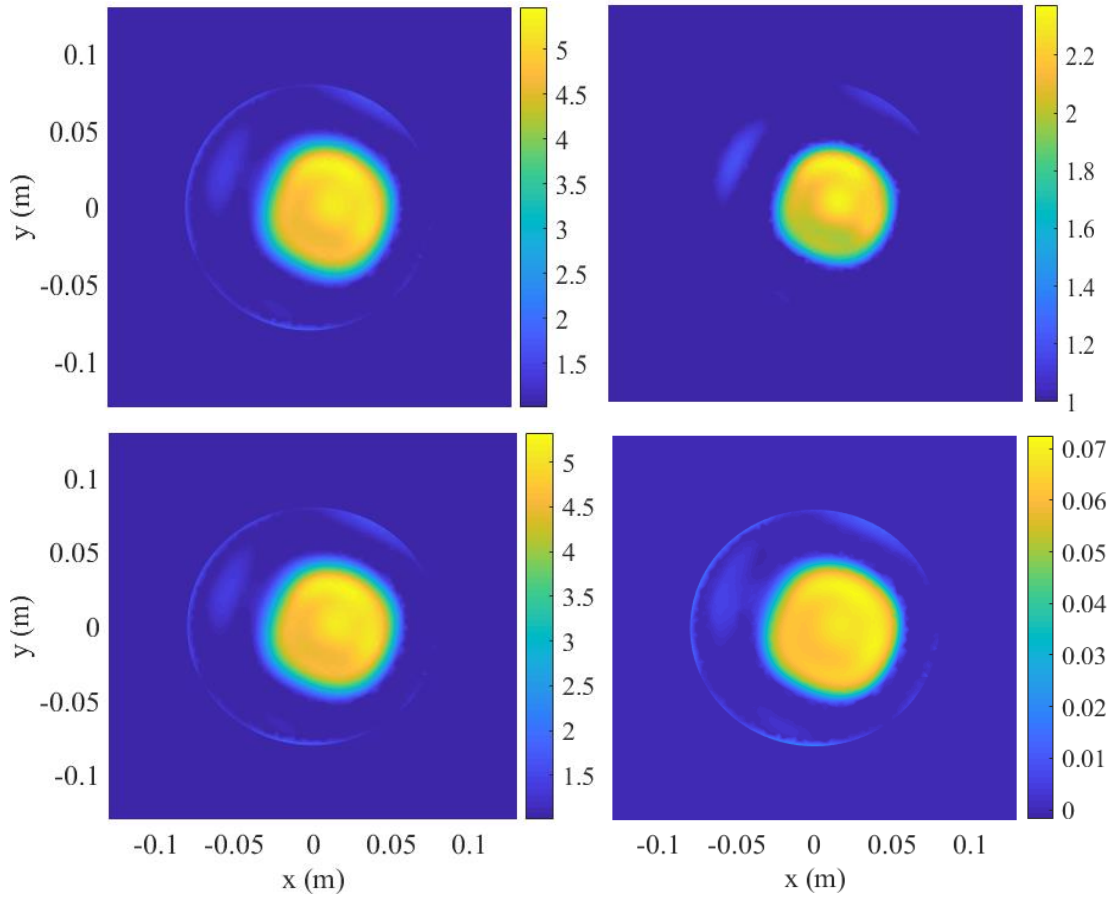

Figure 8.35: The dispersive Salted-Butter target reconstructed image by dispersive DGM-FBTS after 3 iterations. Top left: static permittivity, top right: optical permittivity, bottom left: equivalent permittivity at 2 GHz, bottom right: equivalent conductivity at 2 GHz.

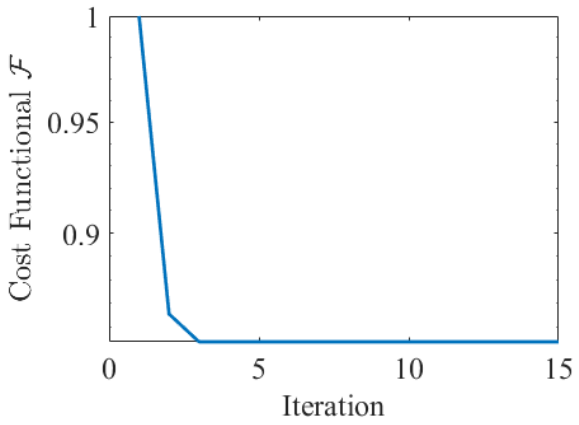

Figure 8.36: The cost functional of image reconstruction of the experimental dispersive Salted-Butter target by the dispersive DGM-BFTS code.

8.6.4 The Experimental Dispersive Tree-Trunk-1 & Tree-Trunk-2 Examples

To show the capability of the dispersive DGM-FBTS algorithm with high contrast targets, we test it with Tree-Trunk-1 & Tree-Trunk-2 when they are in their wet state, as described in Section 8.3. Next, we do imaging of these logs when they are dryer, confirming the idea of decreasing loss with decreasing moisture content. Note that although we tried to keep imaging at the same approximate height of trunks, some variation may have occurred when changed from wet state to dry state. Also the orientation of targets from "wet state" to their "dry state" has been changed as these experiments were run months apart.

Wet State:

Figure 8.37 shows the Tree-Trunk-1 image reconstruction by dispersive DGM-FBTS after 6 iterations. When dealing with high contrast targets, good initial values have to be selected for inversion algorithms. Here, we took $\varepsilon_\infty = 1$ and $\varepsilon_s = 5$ as initial values of the imaging domain. The top left image shows ε_s and the top right shows ε_∞ reconstructed for this target. The equiv-

alent permittivity and conductivity[7] of this target are shown in the left bottom and right bottom, respectively.

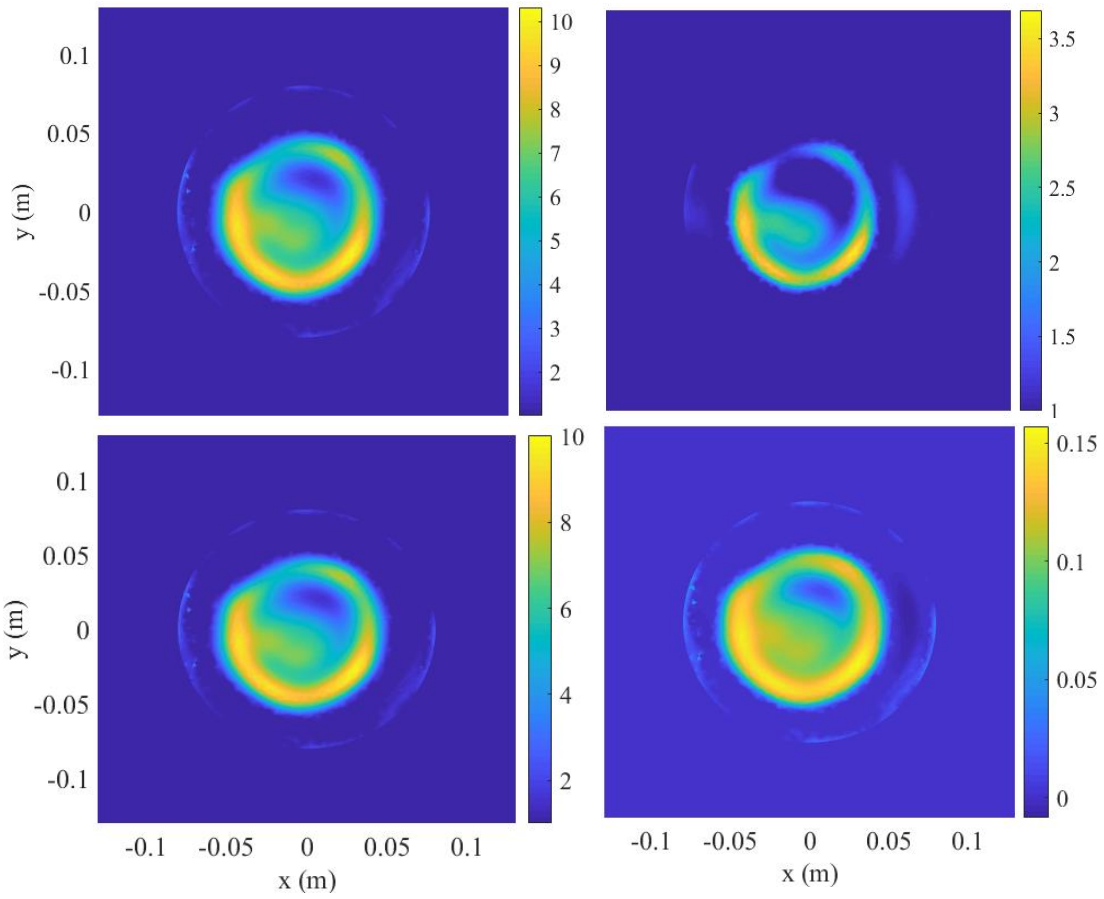

Figure 8.37: The dispersive Tree-Trunk-1 target reconstructed image by dispersive DGM-FBTS after 6 iterations, with $\varepsilon_\infty = 1$ and $\varepsilon_s = 5$ initial values. Top left: static permittivity, top right: optical permittivity, bottom left: equivalent permittivity at 2 GHz, bottom right: equivalent conductivity at 2 GHz.

Figure 8.38 shows the Tree-Trunk-2 image reconstruction by dispersive DGM-FBTS after 5 iterations. The initial constitutive parameters of the imaging domain for this reconstruction are $\varepsilon_\infty = 2$ and $\varepsilon_s = 10$. The top images are the static permittivity ε_s and optical permittivity ε_∞, from left to right. Also, the equivalent permittivity and conductivity of this target are shown in

[7]See Section 8.3 for the equivalent permittivity and conductivity definitions.

the bottom-left and bottom-right part of the figure respectively.

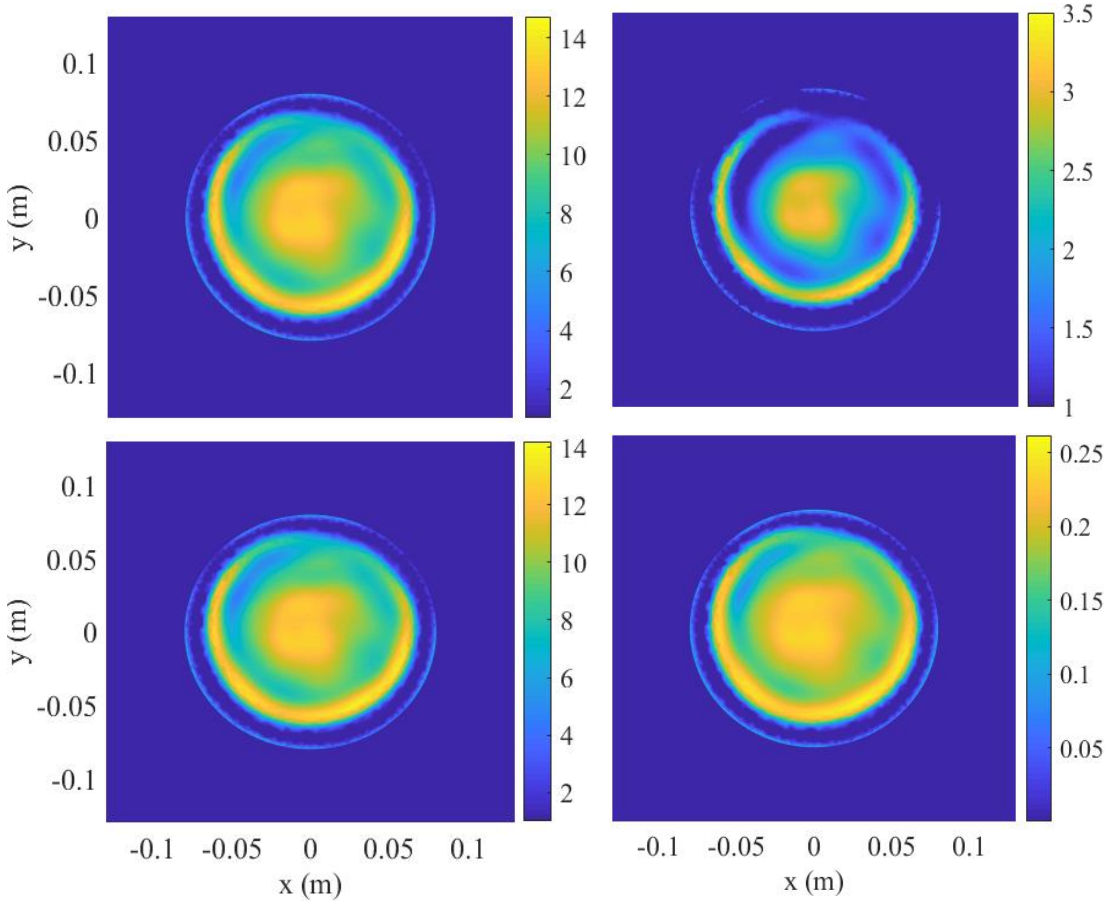

Figure 8.38: The dispersive Tree-Trunk-2 target reconstructed image by dispersive DGM-FBTS after 5 iterations, with $\varepsilon_\infty = 2$ and $\varepsilon_s = 10$ initial values. Top left: static permittivity, top right: optical permittivity, bottom left: equivalent permittivity at 2 GHz, bottom right: equivalent conductivity at 2 GHz.

The DGM-FBTS cost functional for the Tree-Trunk-1 and Tree-Trunk-2 are shown in Figure 8.39, from left to right.

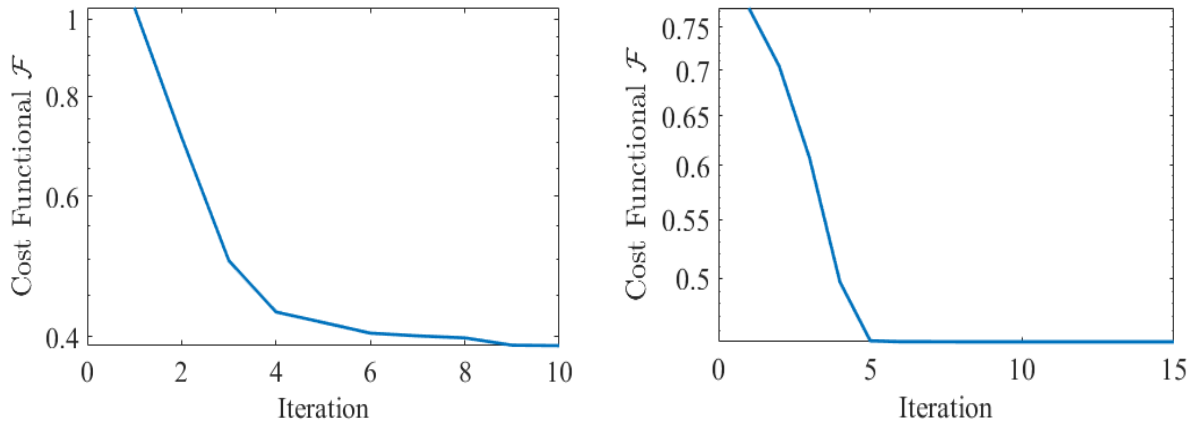

Figure 8.39: The cost functional of image reconstruction of the experimental Tree-Trunk-1 (left), and Tree-Trunk-2, both in wet state, by DGM-BFTS.

Dry State:

Figure 8.40 shows the Tree-Trunk-1 image reconstruction by dispersive DGM-FBTS after 3 iterations, after the target had been drying indoors for about 3 months. Here, we used $\varepsilon_\infty = 1$ and $\varepsilon_s = 3$ as initial values for the constitutive parameters everywhere within the imaging domain.

Similarly, Figure 8.41 shows the drier Tree-Trunk-2 image reconstruction by dispersive DGM-FBTS after 5 iterations. The initial constitutive parameters of the imaging domain for this reconstruction is $\varepsilon_\infty = 2$ and $\varepsilon_s = 10$. The top images are the static permittivity ε_s and optical permittivity ε_∞, from left to right. Also, the equivalent permittivity and conductivity of this target are shown in the left bottom and right bottom, respectively.

Comparing the Tree-Trunk-1 results at two wet and dry state, Figures 8.37 and 8.40, and the Tree-Trunk-2 results at two wet and dry state, Figures 8.38 and 8.41, confirms the idea of increasing loss and permittivity when the objects are wet. Although we were unable to accurately measure these solid dielectrics using our probe kit, the results are quite reasonable based on how wet the wood was originally, and that the targets' radiuses are accurately reconstructed.

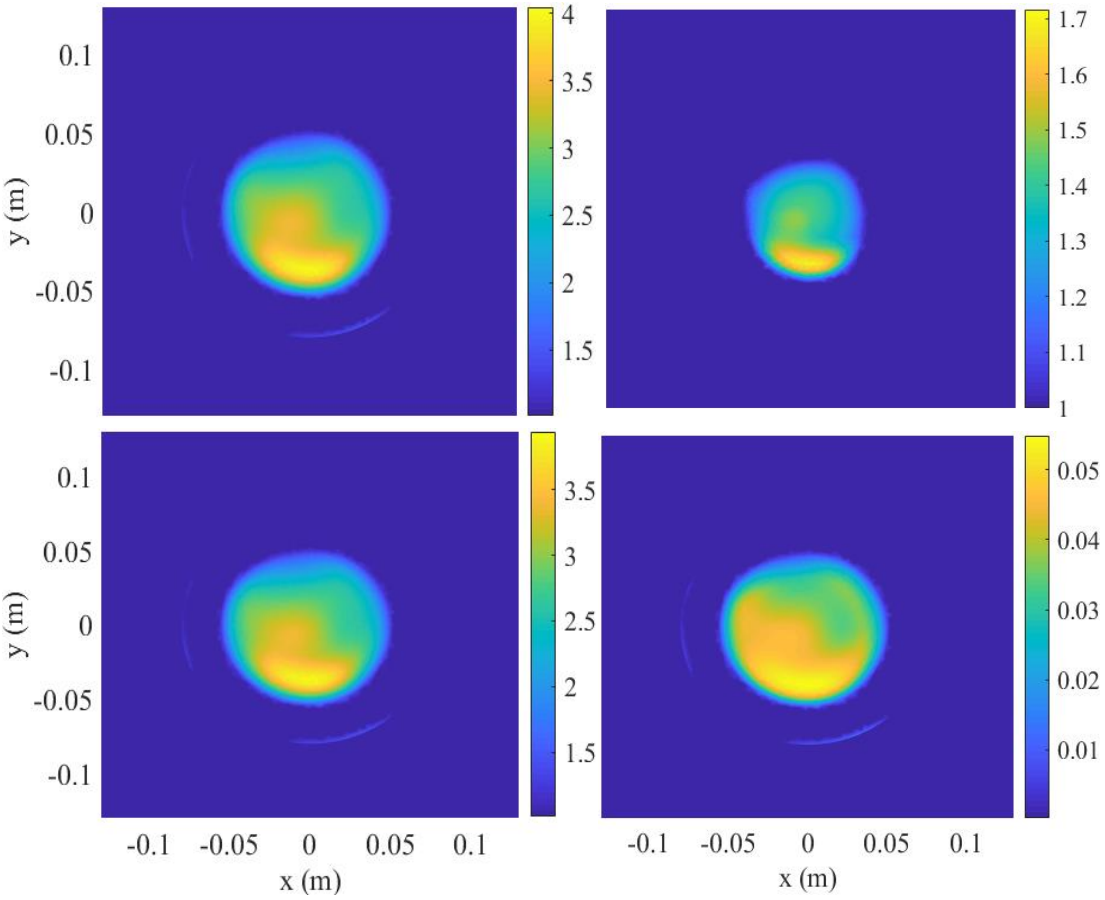

Figure 8.40: The dispersive dry Tree-Trunk-1 target reconstructed image by dispersive DGM-FBTS after 3 iterations, with $\varepsilon_\infty = 1$ and $\varepsilon_s = 3$ initial values. Top left: static permittivity, top right: optical permittivity, bottom left: equivalent permittivity at 2 GHz, bottom right: equivalent conductivity at 2 GHz.

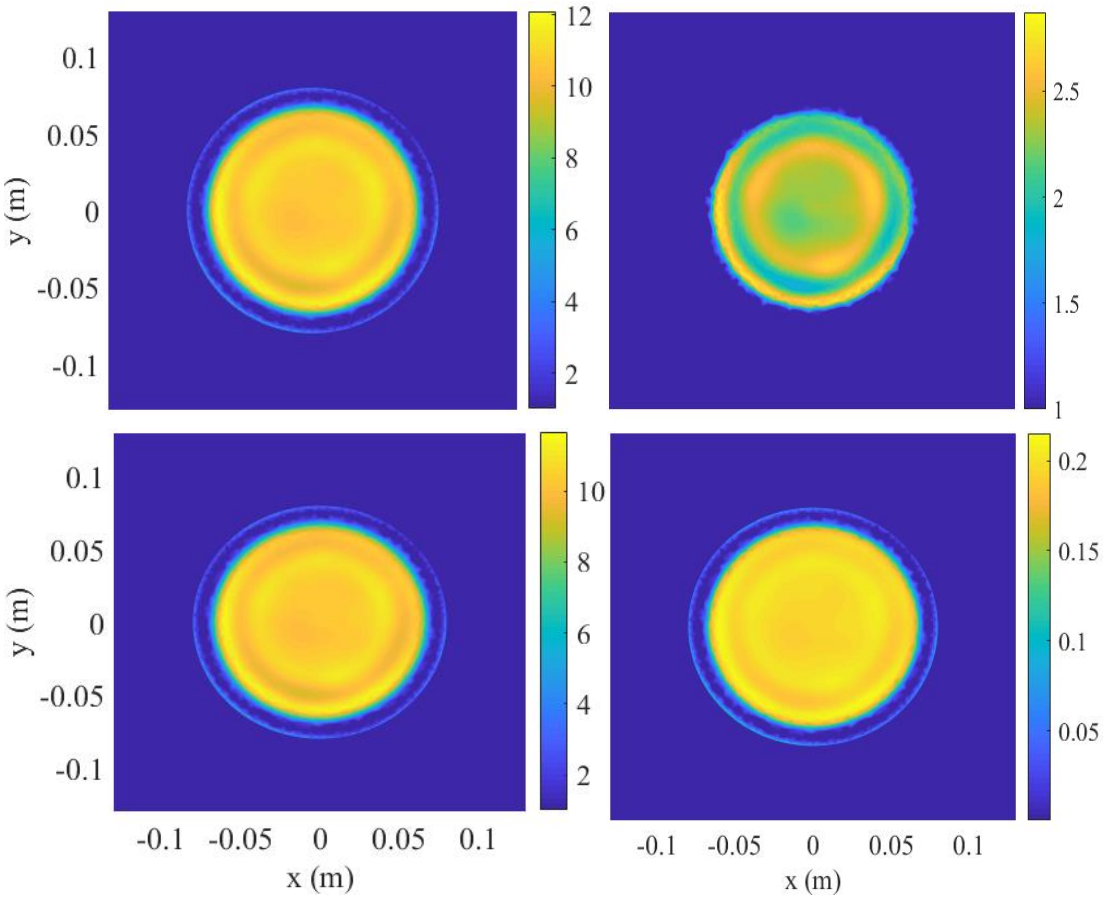

Figure 8.41: The dispersive dry Tree-Trunk-2 target reconstructed image by dispersive DGM-FBTS after 5 iterations, with $\varepsilon_\infty = 2$ and $\varepsilon_s = 10$ initial values. Top left: static permittivity, top right: optical permittivity, bottom left: equivalent permittivity at 2 GHz, bottom right: equivalent conductivity at 2 GHz.

The DGM-FBTS cost functional for the Tree-Trunk-1 and Tree-Trunk-2 are shown in Figure 8.42, from left to right.

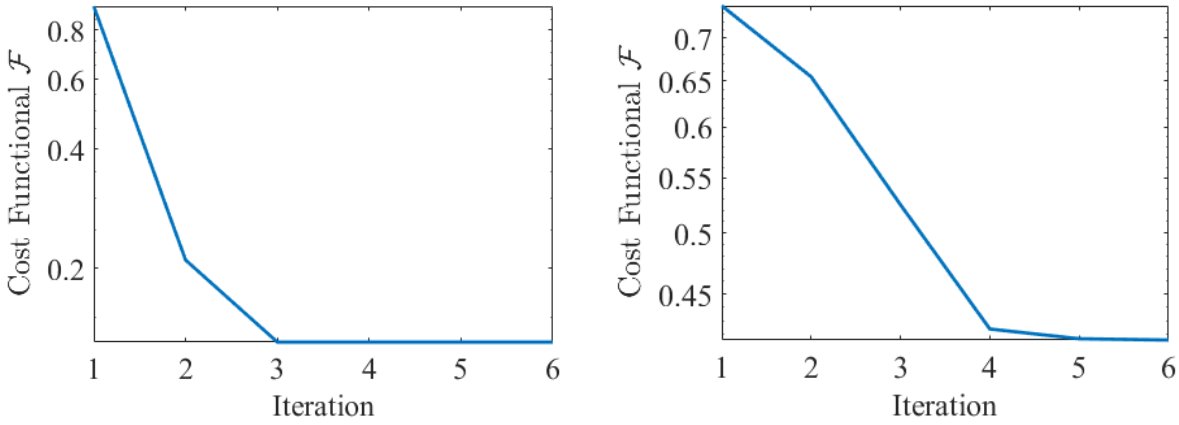

Figure 8.42: The cost functional of image reconstruction of the experimental Tree-Trunk-1 (left), and Tree-Trunk-2, both in dry(er) state, by DGM-BFTS.

8.7 TD Ultrasound DGM-FBTS Evaluation

The evaluation of TD ultrasound DGM-FBTS in this thesis is quite limited and is simply to provide preliminary validation of the ultrasound DGM-FBTS algorithm. In this section we briefly evaluate this inversion algorithm by reconstructing the image of a simple target; the synthetic Off-Center cylinder target.

The same source signal (5.4) with $\tau = 806.815$ ns (dominant frequency 100 KHz) was used for this problem.

Figure 8.43 shows the true (left) and the reconstructed (right) relative compressibility image of this target. The compressibility image reconstruction is resulted by US DGM-FBTS, by free space initial values and after 6 iterations. The location, shape, and the amplitude of this target are reconstructed by this algorithm nicely, as we expect. Note that the only unknown in this image reconstruction is the relative compressibility. Also, the DGM-FBTS cost functional for this target and the Root Mean Square Deviation (RMSD) (Equation 8.5) of the reconstructed

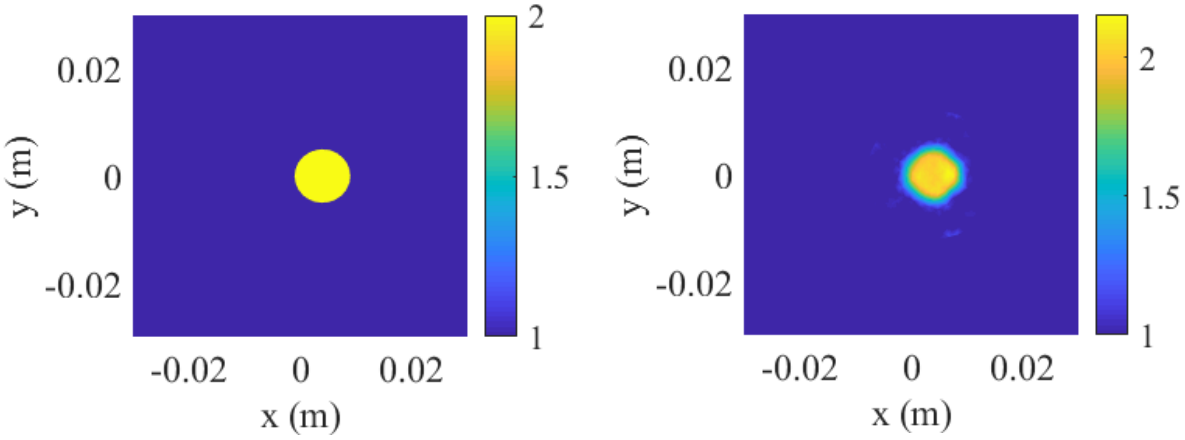

Figure 8.43: The true (left), and reconstructed relative compressibility of the synthetic Off-Center cylinder target by US DGM-FBTS.

compressibility in the imaging domain are shown from left to right in Figure 8.44, to demonstrate the convergence speed of this algorithm for this target.

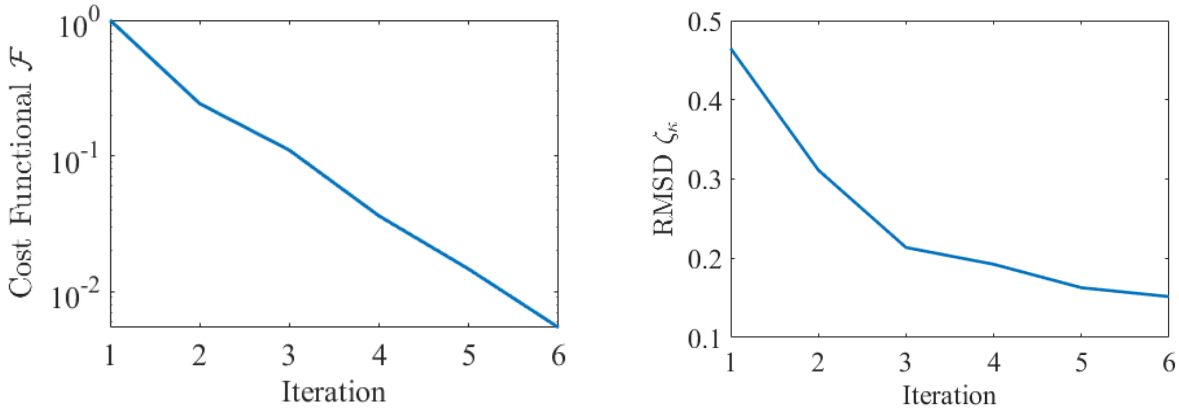

Figure 8.44: The cost functional (left) and the imaging domain reconstructed RMSD (right) of the US image reconstruction of the synthetic Off-Center cylinder target by DGM-BFTS.

8.8 Computational Time

A potential drawback of time-domain microwave imaging is its computational cost. There are many possible techniques to alleviate expense, for example: optimally choosing time parame-

ters, employing an efficient time-marching method, applying a coarse enough spacial mesh while using higher-order DGM expansions, benefiting from a fast and efficient local minimum function, or code parallelization as an additional step of algorithm implementation. Some of these remedies depend on the application/geometries of the imaging problem. This section explains these speed-up techniques for general DGM-FBTS imaging, followed by examples from the thesis.

Choosing the right final measurement time has a significant role in the image resolution and the computational cost of the inversion algorithm. If this parameter is too small, the wave scattering from the target[8] does not reach all of the receivers, and the image reconstructed by the inversion algorithm may be degraded. A straightforward technique to find the optimum final measurement time is to run a synthetic forward solver with our transmitter/receiver setup and the whole imaging domain as the target with the maximum expected constitutive parameters. The final measurement time can then be selected by monitoring the received signals at the receiver antennas.

The next parameters determining the computational cost of a TD imaging scheme are the time-step and the employed time-marching technique. Chapter 5 presented details of some implicit and explicit time-marching methods. We discussed that increasing time-step parameter too much in explicit methods makes the forward solver diverge and in implicit methods makes the received time-signal erroneous by improperly capturing, or entirely missing, high-frequency components. Table 5.2 gives a numerical evaluation of some of the time-marching methods tested in this thesis. This table shows that a properly chosen time-step could easily speed up the inversion algorithm and decrease the computational cost by about 65.88% (e.g., by increasing $dt = 2$ ps in LSERK to $dt = 30$ ps in TR-BDF2).

[8] only the meaningfully large-amplitude scattered fields

Employing higher-order expansions in discontinuous Galerkin method, the DGM-FBTS inversion method can perform faster than having 1st order basis function. While using a higher order expansion, we can use a coarser mesh for the inversion solver. In Section 8.5.1, we showed that by increasing the solution order from 1 to 4, we could decrease the computational time of the inversion algorithm by about 40.78%.

Before getting into implementation details of the GSS-SPI minimum seeker algorithm in Chapter 6, we discussed the requirements of an efficient minimum seeker algorithm; the guarantee of convergence and a reasonable convergence speed. Recall that in this thesis, we chose the serial GSS-SPI iteration algorithm because it meets these requirements.

Although GSS-SPI is a pretty efficient algorithm, it can still be improved/modified, or replaced to speed up the inversion process. For instance, according to [83], there exist parallel algorithms, possibly faster than the serial GSS-SPI. As the accuracy/performance of these algorithms compared to GSS-SPI in DGM-FBTS is unknown, a separate study in this area remains a great option to improve the DGM-FBTS computational cost.

8.8.1 A rigorous comparison of the computational time of DGM-FBTS and DGM-CSI or DGM-GNI

We now present a rigorous comparison of the computational time of DGM-FBTS and DGM-CSI or DGM-GNI.

Recall that all three algorithms are implemented as Matlab-based codes. The DGM-GNI and DGM-CSI algorithms adopt a hybridizable DGM formulation to reduce the computational time compared to the standard DGM implementations [93]. Further, the DGM-FBTS implementation is still in the research phase, neither heavily optimized nor supporting a time-domain variant of the hybridizable DGM formulation. All computations have been run on Intel Xeon processors.

As a representative example, consider the BoxTarget with absorbing boundary whose results are presented in Section 8.5.1. The DGM-FBTS algorithm takes approximately 4 minutes per iteration (averaged over 12 iterations), resulting in the image shown in Figure 8.18 after about 50 minutes. However, this execution time decreases by 8 times, if we use non-transducer antennas. The single-frequency DGM-GNI takes about 50 seconds per iteration, resulting in the image shown in Figure 8.19 after about 14 minutes, and the single-frequency DGM-CSI takes about 4 seconds per iteration, resulting in the image shown in Figure 8.19 after about 12 minutes. However, to obtain reasonable imaging results, it was necessary to perform inversions at 1, 2, 3, 4, and 5 GHz[9]. This additional cost will vary greatly depending on the imaging problem. So while the time-domain solver may take 5-10 times longer, the robustness of the algorithm and improved resolution has significant benefits. In the next chapter we seek to combine FD and TD imaging in beneficial ways.

Although the DGM-FBTS computational cost is more extensive than single-frequency DGM-CSI and DGM-GNI, the quality of the reconstructed image compensates for this cost difference. We suspect that in 3-D problems, the DGM-FBTS inversion scheme can outperform any multi-frequency inversion due to the increased computational expense of solving 3-D frequency domain problems.

[9]Note that this is not a multi-frequency imaging like frequency hopping or simultaneously imaging techniques. A multi-frequency DGM-CSI inversion, using four frequencies 1, 2, 3 and 4 GHz, takes about 10 seconds per iteration, or roughly 30 minutes for 200 iterations [1].

Chapter 9

Quantitative TD-FD and FD-TD Hybrid Methods

Improving the performance of MWI algorithms has been a major subject since the very beginning of MWI history, mostly because of the nonlinearity and illposedness of the MW inverse problem. Using Prior Information (PI) has been a great subject for this purpose, as high-quality prior information can greatly reduce the non-linearity of the imaging problem.

Dual-mode image reconstruction using prior information, for instance using ultrasound or MRI results as PI, is a pervasive way of improving the reconstructed image in microwave imaging [105, 106, 107, 108]. However, obtaining prior information from another modality introduces challenges to the imaging process. PI image adjustments from one mode to another or increasing the time of data acquisitions due to doing different types of measurements in different modes with the same fixed-position target are some of these challenges. If we are able to limit prior information in MWI to that obtained from the MWI system itself, we alleviate the need to register the two images created from data collected from two different systems.

In this chapter, we present the novel implementation of quantitative single-mode hybrid time- and frequency-domain algorithms. Synthetic and experimental comparisons of these methods with

stand-alone DGM-FBTS, DGM-CSI, and DGM-GNI schemes demonstrates the benefits of the hybrid formulations.

Note that in this chapter, similar to the previous chapter, the provided FD algorithms results are qualitatively the best images obtained from the available data, i.e., the frequency is chosen to obtain good FD images. Also, no noise is added to the synthetic data.

Also, the execution times presented here are due to running Matlab codes with the controlled maximum number of 4 computational threads, on an Intel Xeon processor.

Some of the results in this chapter are regenerated from [2], a published paper as a contribution of this thesis.

9.1 TD-FD Hybrid Method

Monochromatic FD algorithms benefit from accurate PI. For instance, we showed in the previous chapter that switching to more complicated targets like the E-phantom, single frequency DGM-CSI and DGM-GNI did not generate good results without prior information.

This section uses an early-iteration time-domain image produced by DGM-FBTS, as prior information for the two single-frequency FD algorithms, DGM-CSI and DGM-GNI, to enhance the image quality of the FD inversion results. A rule of thumb chooses the number of iterations for the TD algorithm, and the first experiments show that the early-iteration TD results are good enough to offer improved FD images.

In this thesis, we refer to this approach as the TD-FD hybrid algorithm. The goal of this hybridization is to generate a final response more efficient/accurate than the FD approaches (DGM-CSI and DGM-GNI) without the use of dual-mode prior information while mostly preserving the speed of the FD algorithms.

In the following, we begin by applying the proposed TD-FD hybrid to the synthetic lossy

BoxTarget, and then explore two experimental targets: the TwoCylinder and E-phantom targets.

9.1.1 BoxTarget Reconstruction by TD-FD Hybrid

In this section we consider reconstructing the BoxTarget constitutives by the hybrid TD-FD.

The configurations of TD and FD solvers for the BoxTarget are the same as in the previous chapter used to generate the results in Figure 8.18, with 8 transmitters and 16 receivers.

Figure 9.1 shows TD-FD hybrid performance for the synthetic BoxTarget, when the TD algorithm is DGM-FBTS and the FD algorithm is DGM-CSI. The prior information generated by DGM-FBTS, after 4 iterations, is illustrated in row 1. The reconstructed images from DGM-CSI with (row 2) and without (row 3) the PI are generated after 200 iterations at 2 GHz.

Figure 9.2 shows TD-FD hybrid performance for the synthetic BoxTarget, when the TD algorithm is DGM-FBTS and the FD algorithm is DGM-GNI. The prior information generated by DGM-FBTS, after 4 iterations, is illustrated in row 1. The reconstructed images from DGM-GNI with (row 2) and without (row 3) the PI are generated after 15 iterations at 2 GHz.

Note that DGM-FBTS at the 4th iteration can generate a crisper image of the permittivity than DGM-CSI and DGM-GNI alone. Recall that DGM-FBTS converges after about 12 iterations for this target (Section 8.5.1).

Table 9.1 gives the execution time breakdown of reconstructing the lossy BoxTarget by the stand-alone DGM-FBTS, DGM-CSI, DGM-GNI and also the hybrids of TD-FD in minutes (m) and seconds (s). The TD-FD hybrids with respective DGM-CSI and DGM-GNI algorithms are about 42.8% and 40.5% faster than the stand-alone DGM-FBTS.

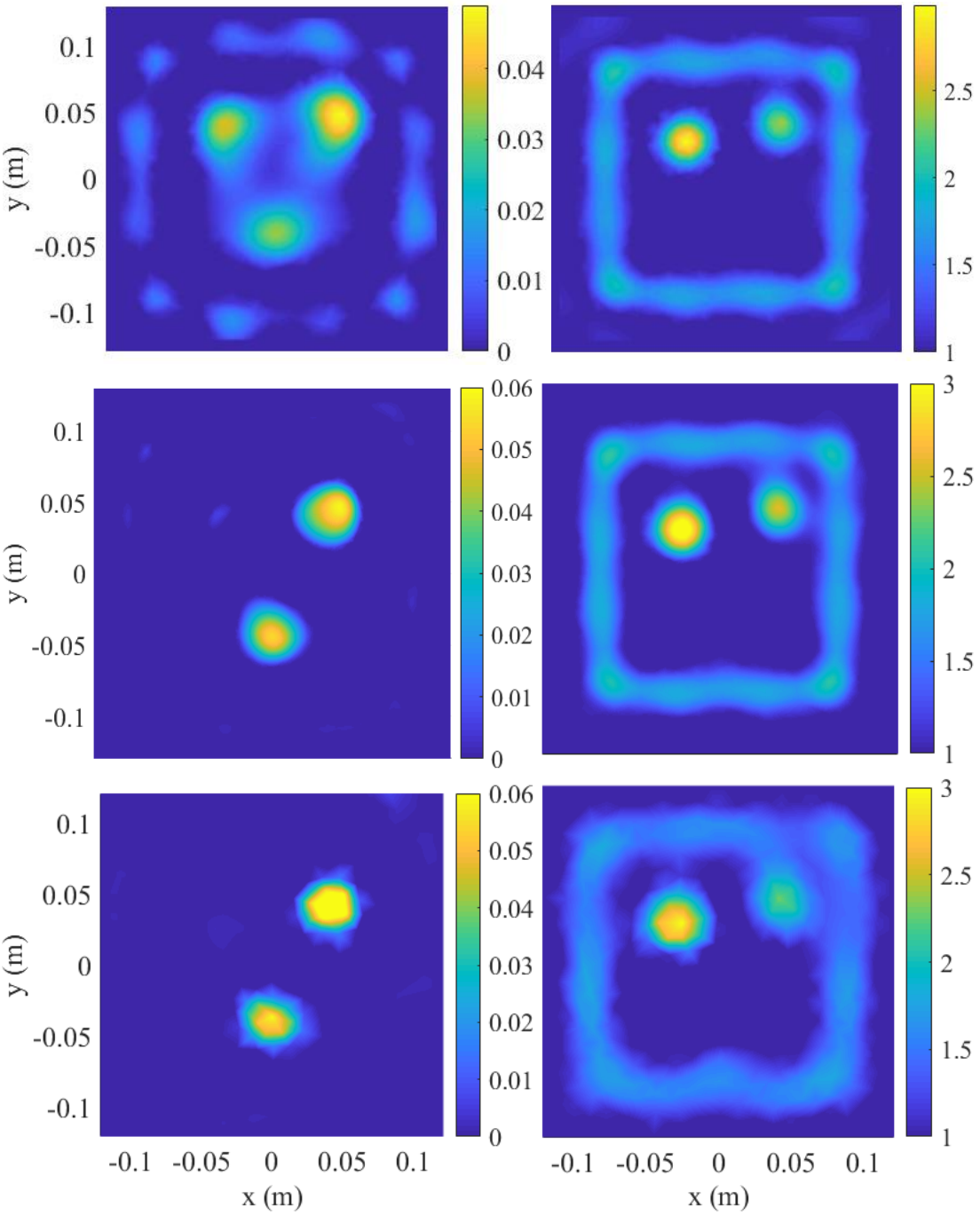

Figure 9.1: TD-FD hybrid performance for the synthetic BoxTarget by TD DGM-FBTS and FD DGM-CSI. Reconstructed relative permittivity (right) and conductivity (left) by DGM-FBTS after 4 iterations as PI (column 1), hybrid TD-FD (FD with PI) (column 2), and stand-alone FD (column 3). [The image is reproduced from [2] with permission.]

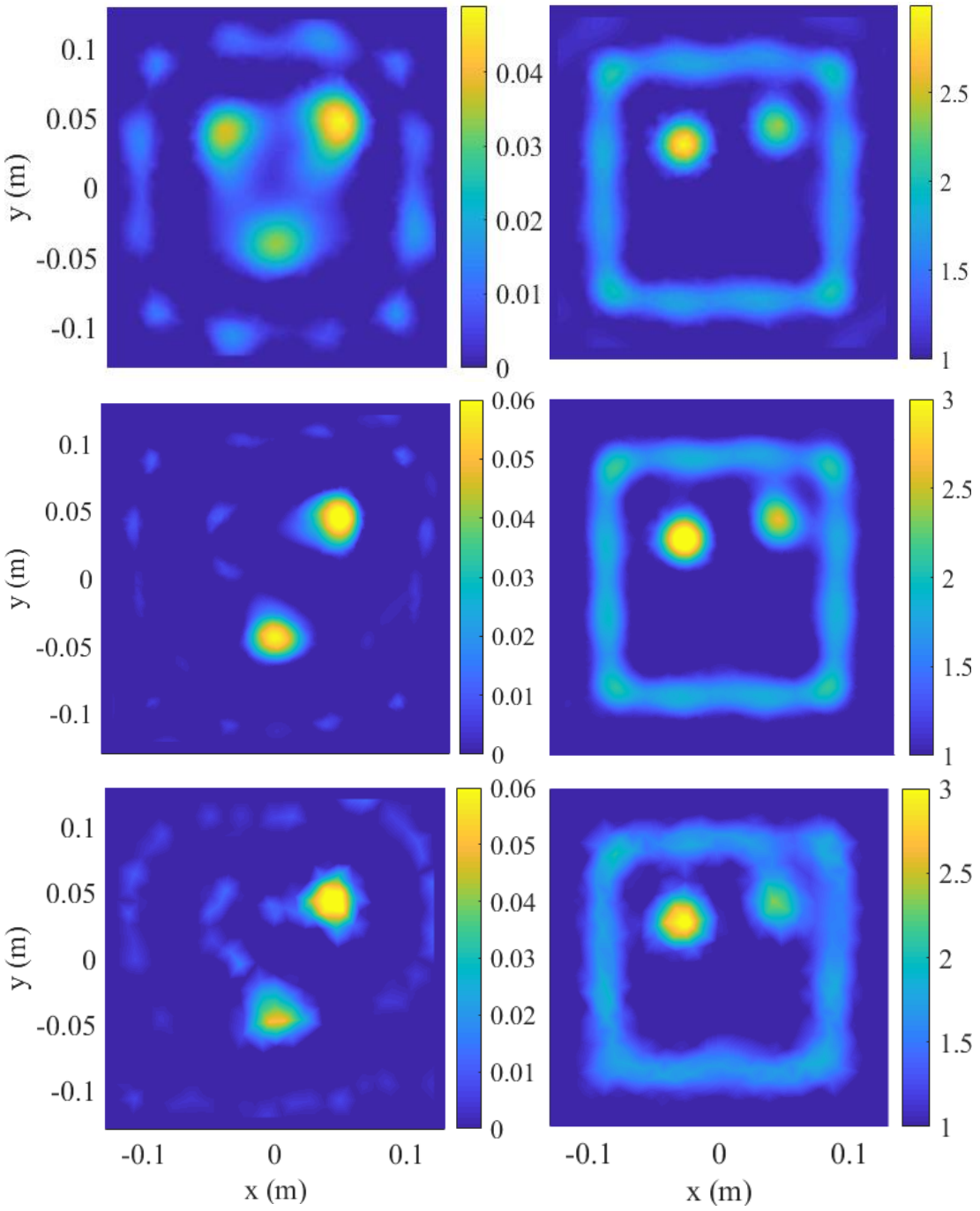

Figure 9.2: TD-FD hybrid performance for the synthetic BoxTarget by TD DGM-FBTS and FD DGM-GNI. Reconstructed relative permittivity (right) and conductivity (left) by DGM-FBTS after 4 iterations as PI (column 1), hybrid TD-FD (FD with PI) (column 2), and stand-alone FD (column 3). [The image is reproduced from [2] with permission.]

	TD algorithm iterations	FD algorithm iterations	TD execution time	FD execution time	Total execution time
FBTS	12	0	247 s × 12	0	49 m & 24 s
CSI	0	200	0	3.54 s × 200	11 m & 48 s
GNI	0	15	0	51.72 s × 15	12 m & 55.8 s
FBTS-CSI	4	200	247 s × 4	3.54 s × 200	28 m & 16 s
FBTS-GNI	4	15	247 s × 4	51.72 s × 15	29 m & 23.8 s

Table 9.1: Lossy BoxTarget reconstruction computational cost evaluation of the TD-FD hybrids

From the figures we can see a clear benefit of the proposed TD-FD hybrid formulation. The final FD images retain high-resolution features from the initial time-domain iterations, and serve to clean up the imaginary part of the target using significantly faster FD iterations.

9.1.2 TwoCylinder target Reconstruction using a TD-FD Hybrid

In this section we continue assessing the TD-FD hybrid approach by applying it to the TwoCylinder experimental targets.

The first row of Figure 9.3 shows the prior information used for this target. This PI is the result of DGM-FBTS after 2 iterations.

The images reconstructed by the stand-alone DGM-CSI and DGM-GNI methods at 3.10 GHz for the TwoCylinder target are illustrated in the right column, rows 2 and 3, of Figure 9.3. These images are generated after 200 iterations of DGM-CSI and 15 iterations of DGM-GNI.

The second row of the left column in Figures 9.3 shows the hybrid TD-FD results using DGM-CSI after 70 iterations at frequency at 3.10 GHz. The third row of the left column in Figures 9.3 shows the hybrid TD-FD results using DGM-GNI after 4 iterations at frequency at 3.10 GHz.

Table 9.2 gives the execution time breakdown of reconstructing the TwoCylinder target by the stand-alone DGM-FBTS, DGM-CSI, DGM-GNI and also the hybrids of TD-FD. The TD-FD

hybrids with respective DGM-CSI and DGM-GNI algorithms are about 75.6% and 77.1% faster than the stand-alone DGM-FBTS.

Although the TwoCylinder target is not a complicated target, employing early iteration TD images as PI to FD inversion algorithms improves the final image accuracy of the target, compared to the stand-alone FD algorithms.

	TD algorithm iterations	FD algorithm iterations	TD execution time	FD execution time	Total execution time
FBTS	10	0	461.39 s × 10	0	76 m & 53.90 s
CSI	0	200	0	2.93 s × 200	9 m & 46 s
GNI	0	15	0	33.74 s × 1156	8 m & 26 s
FBTS-CSI	2	70	461.39 s × 2	2.93 s × 70	18 m & 47.90 s
FBTS-GNI	2	4	461.39 s × 2	33.74 s × 4	17 m & 37.70 s

Table 9.2: TwoCylinder target reconstruction computational cost evaluation of the TD-FD hybrids

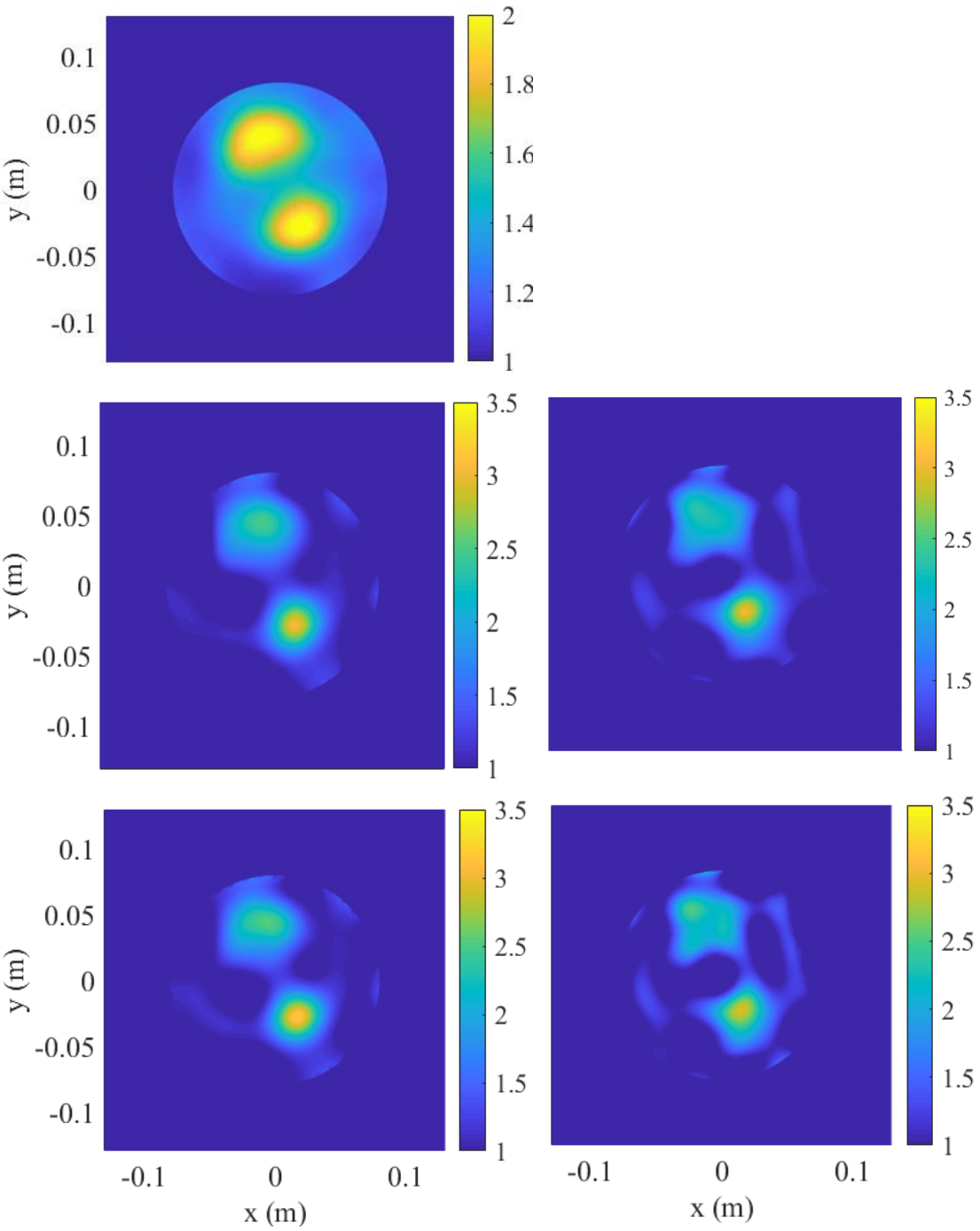

Figure 9.3: TD-FD hybrid performance for the experimental TwoCylinder target. Reconstructed relative permittivity by DGM-FBTS after 2 iterations as PI (row 1), DGM-CSI (row 2), and DGM-GNI (row3). left: TD-FD hybrid, right: stand-alone FD (without PI). [The image is reproduced from [2] with permission.]

9.1.3 E-phantom target Reconstruction by TD-FD Hybrid

As the final assessment of the TD-FD hybrid approach, we consider the E-phantom experimental target.

The first row of Figure 9.4 shows the prior information used for this target. This PI is the result of DGM-FBTS after 2 iterations.

The images reconstructed by the stand-alone DGM-CSI and DGM-GNI methods at 3.10 GHz for the E-phantom target are illustrated in the right column, rows 2 and 3, of Figure 9.4. These images are generated after 200 iterations of DGM-CSI and 15 iterations of DGM-GNI.

The second row of the left column in Figure 9.4 shows the hybrid TD-FD results using DGM-CSI after 200 iterations at frequency at 5.05 GHz. The third row of the left column in Figures 9.4 shows the hybrid TD-FD results using DGM-GNI after 15 iterations at frequency at 5.05 GHz.

Table 9.3 gives the execution time breakdown of reconstructing the E-phantom target by the stand-alone DGM-FBTS, DGM-CSI, DGM-GNI and also the hybrids of TD-FD. The TD-FD hybrids with respective DGM-CSI and DGM-GNI algorithms are about 69.3% and 70.2% faster than the stand-alone DGM-FBTS for this target.

Employing the prior information generated by the robust TD scheme for the FD inversion modalities could result in significantly more accurate images of this target compared to the stand-alone FD algorithms. The E-phantom is a complicated target, and interestingly, an early iteration of the quantitative TD algorithm helps the monochromatic FD inversion methods to detect this target quite correctly.

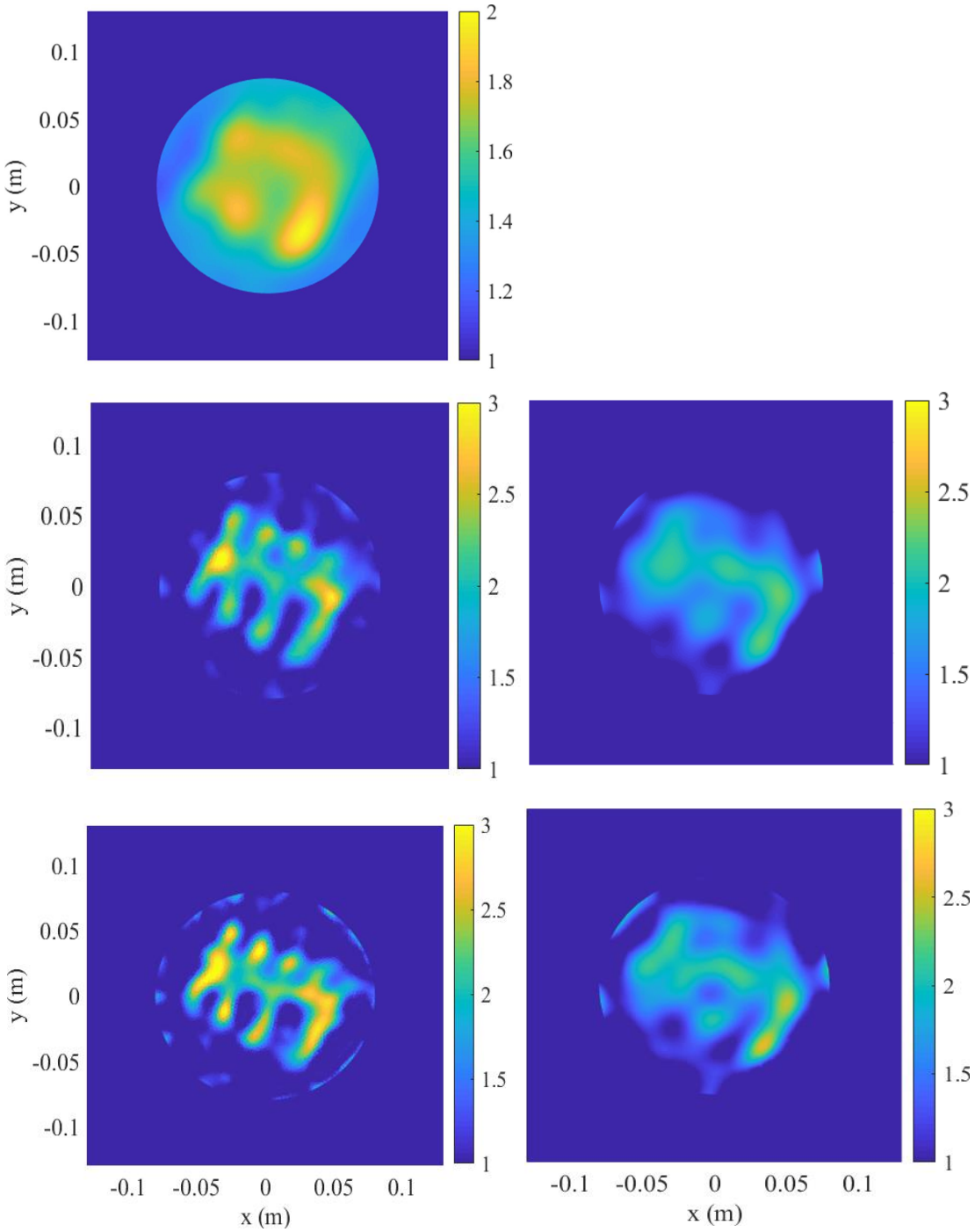

Figure 9.4: TD-FD hybrid performance for the experimental E-phantom target. Reconstructed relative permittivity by DGM-FBTS after 2 iterations as PI (row 1), DGM-CSI (row 2), and DGM-GNI (row3). left: TD-FD hybrid (with PI), right: stand-alone FD (without PI). [The image is reproduced from [2] with permission.]

	TD algorithm iterations	FD algorithm iterations	TD execution time	FD execution time	Total execution time
FBTS	11	0	461.39 s × 11	0	84 m & 35.29 s
CSI	0	200	0	3.18 s × 200	10 m & 36 s
GNI	0	15	0	39.42 s × 15	9 m & 51.3 s
FBTS-CSI	2	200	461.39 s × 2	3.18 s × 200	25 m & 58.78 s
FBTS-GNI	2	15	461.39 s × 2	39.42 s × 15	25 m & 13.30 s

Table 9.3: E-phantom target reconstruction computational cost evaluation of the TD-FD hybrids

Analyzing all of the results from the TD-FD hybrid approach, We can claim that this combination is considerably beneficial. Monochromatic FD algorithms struggle in the absence of a strong/robust initialization due to a lack of information in measured data, leading the FD algorithm to local minimums at the start of the inversion. On the other hand, a robust TD algorithm like DGM-FBTS can provide an accurate initial estimate, especially for more complicated targets. Considering that only a couple of TD imaging iterations have been shown to be enough to provide proper PI for this hybrid approach, we do not add much computational cost to the problem, especially compared to other strategies like frequency hopping or simultaneous inversions in FD. Comparing the speed of the standalone TD algorithm with the TD-FD hybrid, the TD-FD hybrid showed an average of 62.56% speed improvement for the targets in this section, while the quality of the reconstructed images is almost the same.

9.2 FD-TD Hybrid Method

Although TD algorithms may be slower per-iteration than a single-frequency FD algorithm, they can converge quickly and generally converge to higher-resolution images than their single-frequency counterparts.

Having a low-resolution frequency-domain image as prior information for subsequent time-domain inversion is the subject of this section. We refer to this hybrid approach as FD-TD hybridization. The general idea is to retain the high-resolution capabilities of time-domain iter-

ations, but to require fewer time-domain iterations than without prior information. So the idea of FD-TD hybridization is very valuable, as it helps to have high accuracy results similar to the standard quantitative TD imaging, only faster.

In the following, we begin by applying the proposed FD-TD hybrid to the synthetic BoxTarget, and then explore two experimental targets: the TwoCylinder and E-phantom targets.

9.2.1 BoxTarget Reconstruction by FD-TD Hybrid

We start the FD-TD hybrid evaluation by reconstructing the synthetic lossless BoxTarget constitutive parameters using the hybrid TD-FD imaging algorithm.

The configurations of TD and FD solvers for the BoxTarget are the same as in the TD-FD setup.

Figure 9.5 shows FD-TD hybrid performance for the synthetic BoxTarget. The prior information generated by DGM-CSI (column 1, row 1) and DGM-GNI (column 1, row 2), at 2 GHz after 200 and 15 iterations, respectively, are illustrated in this figure. The reconstructed images from DGM-FBTS with DGM-CSI PI (column 2, row 1) and DGM-GNI PI (column 2, row 2) are generated after 4 iterations. At the bottom row the stand-alone DGM-FBTS reconstruction, after 9 iterations, is shown for comparative purposes.

Although some minor undershoot is visible in the top-right cylinder image, the hybrid reconstruction results are comparable in terms of quality to those produced by the stand-alone TD algorithm. Here, we have met the goal of reducing TD execution time while retaining its accuracy: the FD-TD hybrid approach requires 66% fewer TD iterations for this target. Table 9.4 gives the execution time breakdown of stand-alone DGM-FBTS , DGM-CSI, DGM-GNI and also the hybrids of FD-TD in minutes (m) and seconds (s). The FD-TD hybrids with respective DGM-CSI and DGM-GNI algorithms are about 23.7% and 20.66% faster than the stand-alone DGM-FBTS.

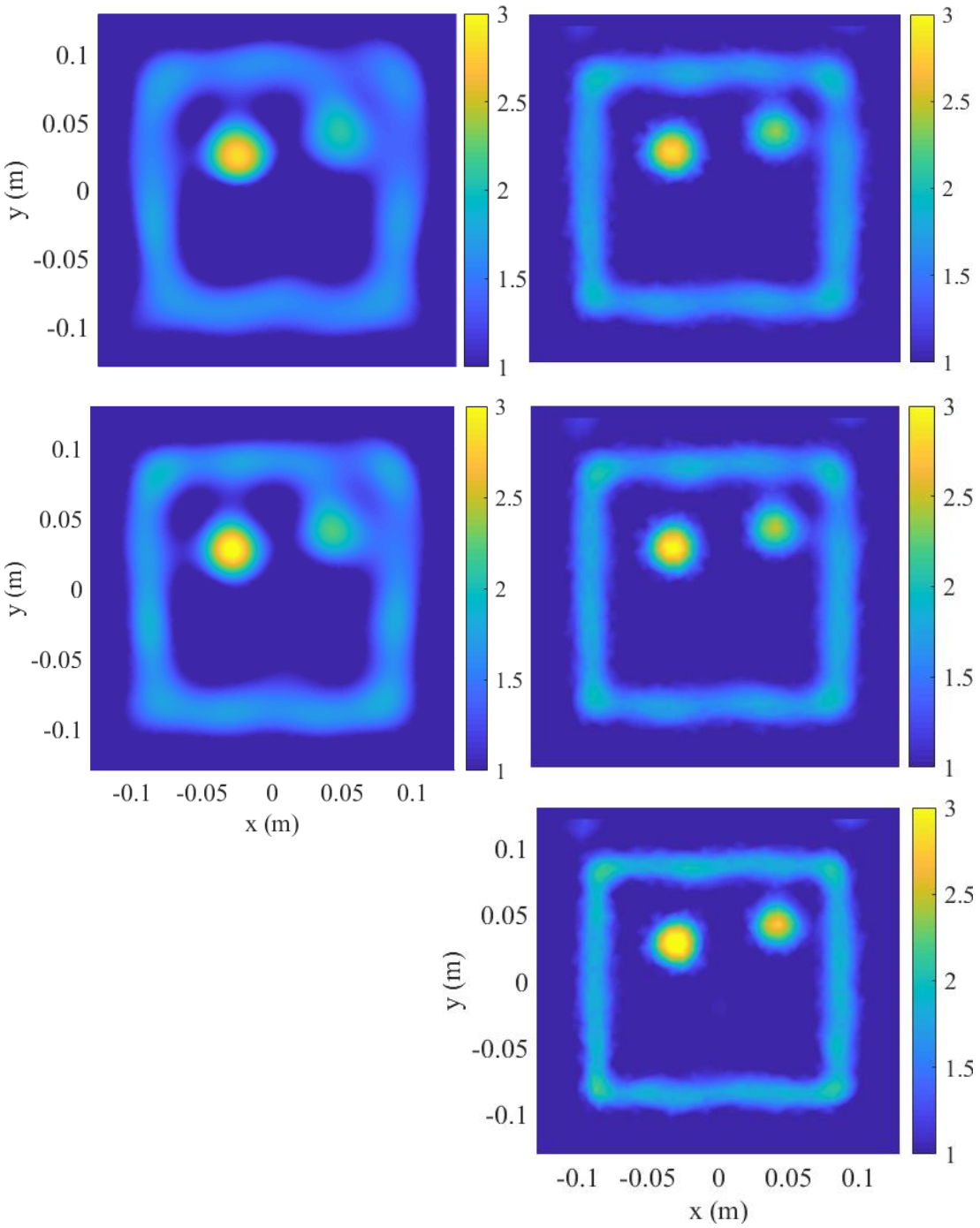

Figure 9.5: FD-TD hybrid performance for the synthetic BoxTarget by FD DGM-CSI and TD DGM-FBTS. Column 1: PI generated by DGM-CSI (row 1) and DGM-GNI (row 2), Column 2: DGM-FBTS results by using DGM-CSI PI (row 1), DGM-GNI PI (row 2), and no PI (row 3). [The image is reproduced from [2] with permission.]

	TD algorithm iterations	FD algorithm iterations	TD execution time	FD execution time	Total execution time
FBTS	9	0	247 s × 9	0	37 m & 3 s
CSI	0	200	0	3.54 s × 200	11 m & 48 s
GNI	0	15	0	51.72 s × 15	12 m & 56 s
CSI-FBTS	4	200	247 s × 4	3.54 s × 200	28 m & 16 s
GNI-FBTS	4	15	247 s × 4	51.72 s × 15	29 m & 24 s

Table 9.4: Lossless BoxTarget reconstruction computational cost evaluation of the FD-TD hybrids

9.2.2 TwoCylinder Target Reconstruction by FD-TD Hybrid

Moving on to experimental problems, in this section we continue assessing the FD-TD hybrid approach by applying it to the TwoCylinder experimental target.

Figure 9.6 shows FD-TD hybrid performance for the experimental TwoCylinder target. The prior information generated by DGM-CSI at 3.10 GHz (column 1, row 1) and DGM-GNI at 2.05 GHz (column 1, row 2), after 200 and 15 iterations, respectively, are illustrated in this figure. We picked different frequencies for the FD algorithms, to challenge the hybrid scheme with different PIs having different accuracies.

The reconstructed images from DGM-FBTS with DGM-CSI PI (column 2, row 1) and DGM-GNI PI (column 2, row 2) are generated after 6 iterations. At the bottom row the stand-alone DGM-FBTS reconstruction, after 10 iterations, is provided for reference.

Table 9.5 gives the execution time breakdown of stand-alone DGM-FBTS , DGM-CSI, DGM-GNI and also the hybrids of FD-TD. The FD-TD hybrids with respective DGM-CSI and DGM-GNI algorithms are about 27.30% and 29.03% faster than the stand-alone DGM-FBTS.

While the final results are comparable, the FD-TD hybrid approach requires 40% fewer expensive TD iterations, again demonstrating the benefit of the hybrid approach.

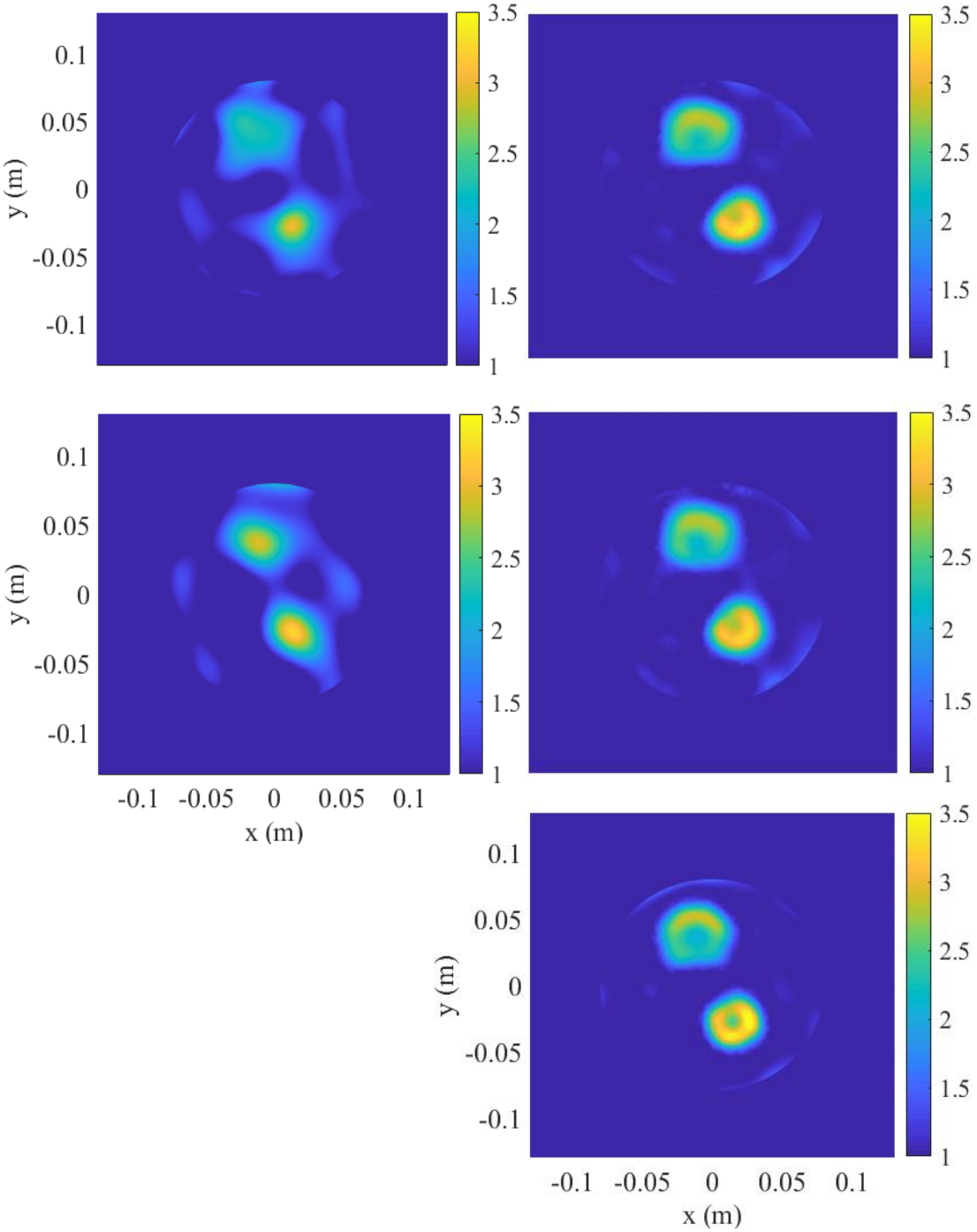

Figure 9.6: FD-TD hybrid performance for the experimental TwoCylinder target by FD DGM-CSI and TD DGM-FBTS. Column 1: PI generated by DGM-CSI (row 1) and DGM-GNI (row 2), Column 2: DGM-FBTS results by using DGM-CSI PI (row 1), DGM-GNI PI (row 2), and no PI (row 3). [The image is reproduced from [2] with permission.]

	TD algorithm iterations	FD algorithm iterations	TD execution time	FD execution time	Total execution time
FBTS	10	0	461.39 s × 10	0	76 m & 53.90 s
CSI	0	200	0	2.93 s × 200	9 m & 46 s
GNI	0	15	0	33.74 s × 15	8 m & 26 s
CSI-FBTS	6	200	461.39 s × 6	2.93 s × 200	55 m & 54.34 s
GNI-FBTS	6	15	461.39 s × 6	33.74 s × 15	54 m & 34.44 s

Table 9.5: TwoCylinder target image reconstruction computational cost evaluation of the FD-TD hybrids

9.2.3 E-phantom Target Reconstruction by FD-TD Hybrid

As the final assessment of the FD-TD hybrid approach, we consider the E-phantom experimental target.

Figure 9.7 shows FD-TD hybrid performance for the experimental E-phantom target. The prior information generated by DGM-CSI at 2.05 GHz (column 1, row 1) and DGM-GNI at 3.10 GHz (column 1, row 2), after 200 and 15 iterations, respectively, are illustrated in this figure. We again picked different frequencies for the FD algorithms due to the same reason as before.

The reconstructed images from DGM-FBTS with DGM-CSI PI (column 2, row 1) and DGM-GNI PI (column 2, row 2) are generated after 7 iterations. At the bottom row the stand-alone DGM-FBTS reconstruction, after 11 iterations, is provided for reference. Table 9.6 gives the execution time breakdown of stand-alone DGM-FBTS , DGM-CSI, DGM-GNI and also the hybrids of FD-TD. The FD-TD hybrids with respective DGM-CSI and DGM-GNI algorithms are about 23.83% and 24.71% faster than the stand-alone DGM-FBTS.

Similar to the TwoCylinder target, the hybrid results caused a decrease of 36% of expensive TD iterations for the E-phantom. So again, the hybrid results support the motivation of using prior information for the TD algorithm.

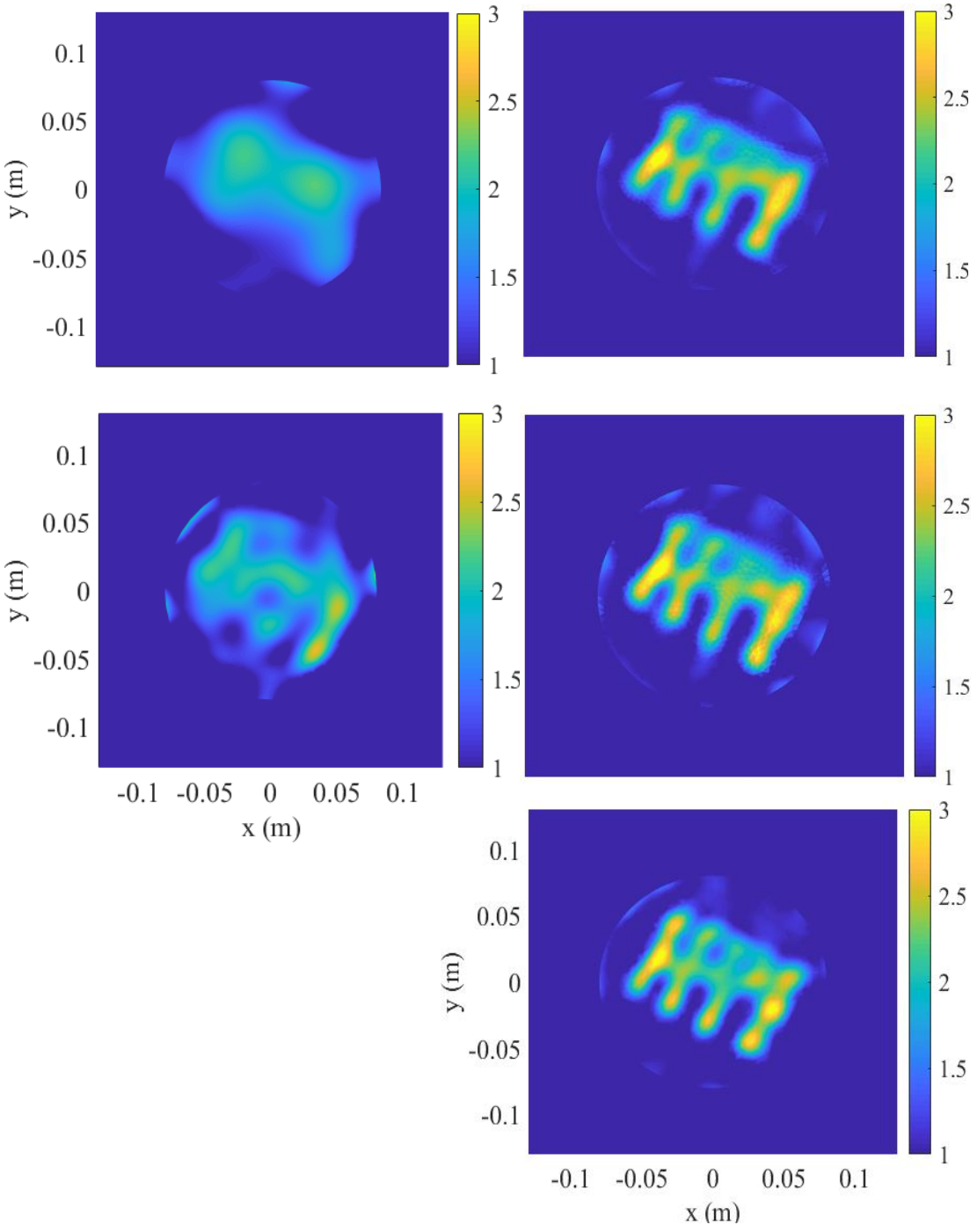

Figure 9.7: FD-TD hybrid performance for the experimental E-phantom target by FD DGM-CSI and TD DGM-FBTS. Column 1: PI generated by DGM-CSI (row 1) and DGM-GNI (row 2), Column 2: DGM-FBTS results by using DGM-CSI PI (row 1), DGM-GNI PI (row 2), and no PI (row 3). [The image is reproduced from [2] with permission.]

	TD algorithm iterations	FD algorithm iterations	TD execution time	FD execution time	Total execution time
FBTS	11	0	461.39 s × 11	0	84 m & 35.29 s
CSI	0	200	0	3.18 s × 200	10 m & 36 s
GNI	0	15	0	39.42 s × 15	9 m & 51.30 s
CSI-FBTS	7	200	461.39 s × 7	3.18 s × 200	64 m & 25.73 s
GNI-FBTS	7	15	461.39 s × 7	39.42 s × 15	63 m & 41.03 s

Table 9.6: E-phantom target image reconstruction computational cost evaluation of the FD-TD hybrids

Applying the FD-TD hybrid with three different scenarios, confirms the benefits of the proposed approach. In all cases we could generate more accurate reconstructions than the stand-alone FD results, comparable to the stand-alone TD results. The hybrid approach is significantly (24.87% in average) faster, lowering the number of TD algorithm required iterations with the application of FD prior information.

9.3 TD-FD Hybrid versus FD-TD Hybrid

Here in this section, we weigh the advantages of the TD-FD and FD-TD hybrids based on the presented results for the BoxTarget, TwoCylinder, and E-phantom targets.

Although the execution time reduction reports show that the TD-FD hybrid is computationally less expensive, FD-TD seems to be more accurate. This higher accuracy is more obvious for the simpler target; the TwoCylinder target. On the other hand, as it is more difficult to generate quality prior information by single-frequency imaging FD schemes, TD-FD hybrid technique is preferred for more complicated targets, e.g., the E-Phantom.

Further, a limitation of the present study about these two hybrids is that the number of iterations for each of the algorithms is chosen based on the experience and requires a more rigorous study of when to optimally transition from one modality to another in a hybrid technique.

The writer believes that such a study could reveal a better perspective of the trade-off between accuracy and computational cost.

Chapter 10

Conclusions and Future Work

This dissertation introduced a novel Microwave imaging technique in the time-domain by combining the discontinuous Galerkin method time-domain spatial discretization technique and the time-domain forward-backward time-stepping inversion scheme. The development and implementation of this time-domain DGM-FBTS imaging technique were presented in detail, followed by an evaluation of the time-domain DGM forward solver and the time-domain inversion algorithm DGM-FBTS.

The time-domain DGM forward solver was the time-domain version of a pre-existing frequency-domain DGM forward solver able to model arbitrary imaging chambers and high-order solution representations, either the electric and/or magnetic fields, or the constitutive parameters.

The three-dimensional time-domain electromagnetic and ultrasound wave-field imaging was formulated and the two-dimensional transverse magnetic problem were solved by the DGM-FBTS imaging technique. The method was utilized to reconstruct the electromagnetic and ultrasound constitutive parameters of a variety of targets. Both electromagnetic and ultrasound formulations were validated; ultrasound results were limited to a single test case providing a preliminary validation of the formulation.

Validation extended to a number of experimental targets to evaluate the electromagnetic

version of DGM-FBTS. A calibration procedure was developed to the S-parameters collected from a 16 Vivaldi-antenna system using a VNA. The developed DGM-FBTS algorithm was extensively compared to two frequency-domain algorithms; such a comparison has not, to the best of my knowledge, been previously performed. This comparison shows the robustness and high accuracy of TD DGM-FBTS compared to these single-frequency FD schemes.

Further comparisons can be conducted between this TD technique and multiple-frequency FD schemes to investigate the TD scheme better.

Also, one simple synthetic target is used for the ultrasound TD DGM-FBTS inversion technique evaluation. This dissertation was mostly focused on the electromagnetic version of the TD imaging, and we did not get further to experimental ultrasound evaluations. This thesis provides a foundation for quantitative ultrasound imaging using TD DGM-FBTS, and future studies and applications to experimental scenarios are warranted.

Due to its highly accurate and robust responses in either electromagnetic and ultrasound, the method of TD DGM-FBTS can/should be applied to more practical biomedical data (as the next step toward applying TD DGM-FBTS for breast cancer detection). This requires investigating an appropriate time-domain pulse generator with a suitable excitation and duration time. Also, some investigation about proper transmitters/receivers in the presence of a matching medium[1], while having very high contrast targets like body tissues, is future work.

Finally, we introduced a couple of new hybrid combinations of quantitative time- and frequency-domain schemes by TD DGM-FBTS and single-frequency FD DGM-CSI and DGM-GNI. The experimental results of these hybrids show that the TD-FD hybrids' accuracy and the FD-TD hybrids' computational costs are improved compared to the FD and TD algorithms, respectively.

As an extension of this dissertation, it will be helpful to find a stopping criterion for the TD DGM-FBTS inverse algorithm. Furthermore, implementing the three-dimensional code and

[1]To have better penetration into targets in the electromagnetic area, they usually use matching mediums. By having a matching medium as the background medium, the contrast between the biomedical target and the background decreases, causing better wave penetration into the target and so higher resolution images.

experimenting with it is undoubtedly one of the forthcoming works of this dissertation.

References

[1] F. M. Saraskanroud and I. Jeffrey, "A comparison of time-domain and frequency-domain microwave imaging of experimental targets," *IEEE Transactions on Computational Imaging*, vol. 7, pp. 611–623, 2021.

[2] F. M. Saraskanroud and I. Jeffrey, "Hybrid approaches in microwave imaging using quantitative time-and frequency-domain algorithms," *IEEE Transactions on Computational Imaging*, 2022.

[3] J. S. Hesthaven and T. Warburton, *Nodal discontinuous Galerkin methods: algorithms, analysis, and applications*. Springer Science & Business Media, 2007.

[4] M. Kreslavsky, N. Bondarenko, J. Head, A. Basilevsky, and M. Ivanov, "Venus'surface layer: A neglected class of venus exploration targets." *Program and Abstract Volume*, p. 38, 1781.

[5] S. Vakalis and J. A. Nanzer, "Microwave imaging using noise signals," *IEEE Transactions on Microwave Theory and Techniques*, vol. 66, no. 12, pp. 5842–5851, 2018.

[6] M. Costin, O. Baltag, C. ŞTEFĂNESCU, and C. Costin, "Medical image processing useful tool in cancer diagnosis," in *7th WSEAS International Conference on Applied Compter Science (ACS'07)*. Citeseer, 1790, pp. 288–293.

[7] P. M. Meaney, M. W. Fanning, D. Li, S. P. Poplack, and K. D. Paulsen, "A clinical prototype for active microwave imaging of the breast," *IEEE Transactions on Microwave Theory and Techniques*, vol. 48, no. 11, pp. 1841–1853, 2000.

[8] K. M. Yemelyanov, N. Engheta, A. Hoorfar, and J. A. McVay, "Adaptive polarization contrast techniques for through-wall microwave imaging applications," *IEEE Transactions on Geoscience and Remote Sensing*, vol. 47, no. 5, pp. 1362–1374, 2009.

[9] F. Aryanfar and K. Sarabandi, "Through wall imaging at microwave frequencies using space-time focusing," in *IEEE Antennas and Propagation Society Symposium, 2004.*, vol. 3. IEEE, 2004, pp. 3063–3066.

[10] L. Wang, R. Simpkin, and A. Al-Jumaily, "Holographic microwave imaging for medical applications," *Journal of Biomedical Science and Engineering*, vol. 2013, 2013.

[11] N. Joachimowicz, B. Duchêne, C. Conessa, and O. Meyer, "Reference phantoms for microwave imaging," in *2017 11th European Conference on Antennas and Propagation (EUCAP)*. IEEE, 2017, pp. 2719–2722.

[12] M. Bassi, M. Caruso, M. S. Khan, A. Bevilacqua, A.-D. Capobianco, and A. Neviani, "An integrated microwave imaging radar with planar antennas for breast cancer detection," *IEEE Transactions on microwave theory and techniques*, vol. 61, no. 5, pp. 2108–2118, 2013.

[13] J.-C. Bolomey, "Recent european developments in active microwave imaging for industrial, scientific, and medical applications," *IEEE Transactions on microwave theory and techniques*, vol. 37, no. 12, pp. 2109–2117, 1989.

[14] R. Zoughi, *Microwave non-destructive testing and evaluation principles*. Springer Science & Business Media, 2000, vol. 4.

[15] B. D. Steinberg, "Microwave imaging of aircraft," *Proceedings of the IEEE*, vol. 76, no. 12, pp. 1578–1592, 1988.

[16] D. Ireland, K. Bialkowski, and A. Abbosh, "Microwave imaging for brain stroke detection using born iterative method," *IET Microwaves, Antennas & Propagation*, vol. 7, no. 11, pp. 909–915, 2013.

[17] P.-H. Tournier, M. Bonazzoli, V. Dolean, F. Rapetti, F. Hecht, F. Nataf, I. Aliferis, I. El Kanfoud, C. Migliaccio, M. De Buhan *et al.*, "Numerical modeling and high-speed parallel computing: New perspectives on tomographic microwave imaging for brain stroke detection and monitoring." *IEEE Antennas and Propagation Magazine*, vol. 59, no. 5, pp. 98–110, 2017.

[18] S. Mustafa, B. Mohammed, and A. Abbosh, "Novel preprocessing techniques for accurate microwave imaging of human brain," *IEEE Antennas and Wireless Propagation Letters*, vol. 12, pp. 460–463, 2013.

[19] B. Mohammed, A. Abbosh, and D. Ireland, "Stroke detection based on variations in reflection coefficients of wideband antennas," in *Proceedings of the 2012 IEEE International Symposium on Antennas and Propagation*. IEEE, 2012, pp. 1–2.

[20] L. Guo and A. M. Abbosh, "Optimization-based confocal microwave imaging in medical applications," *IEEE Transactions on Antennas and Propagation*, vol. 63, no. 8, pp. 3531–3539, 2015.

[21] E. C. Fear, X. Li, S. C. Hagness, and M. A. Stuchly, "Confocal microwave imaging for breast cancer detection: Localization of tumors in three dimensions," *IEEE Transactions on biomedical engineering*, vol. 49, no. 8, pp. 812–822, 2002.

[22] T. M. Grzegorczyk, P. M. Meaney, P. A. Kaufman, K. D. Paulsen *et al.*, "Fast 3-d tomographic microwave imaging for breast cancer detection," *IEEE transactions on medical imaging*, vol. 31, no. 8, pp. 1584–1592, 2012.

[23] Y. Xie, B. Guo, L. Xu, J. Li, and P. Stoica, "Multistatic adaptive microwave imaging for early breast cancer detection," *IEEE Transactions on Biomedical Engineering*, vol. 53, no. 8, pp. 1647–1657, 2006.

[24] W. C. Chew and Y.-M. Wang, "Reconstruction of two-dimensional permittivity distribution using the distorted born iterative method," *IEEE transactions on medical imaging*, vol. 9, no. 2, pp. 218–225, 1990.

[25] S. Caorsi, G. L. Gragnani, and M. Pastorino, "Two-dimensional microwave imaging by a numerical inverse scattering solution," *IEEE Transactions on Microwave Theory and Techniques*, vol. 38, no. 8, pp. 981–980, 1990.

[26] R. Kleinman and P. Van den Berg, "A modified gradient method for two-dimensional problems in tomography," *Journal of Computational and Applied Mathematics*, vol. 42, no. 1, pp. 17–35, 1992.

[27] A. Franchois and C. Pichot, "Microwave imaging-complex permittivity reconstruction with a levenberg-marquardt method," *IEEE Transactions on Antennas and Propagation*, vol. 45, no. 2, pp. 203–215, 1997.

[28] P. M. Meaney, K. D. Paulsen, and T. P. Ryan, "Two-dimensional hybrid element image reconstruction for tm illumination," *IEEE transactions on antennas and propagation*, vol. 43, no. 3, pp. 239–247, 1995.

[29] I. T. Rekanos and T. D. Tsiboukis, "An iterative numerical method for inverse scattering problems," *Radio Science*, vol. 34, no. 6, pp. 1401–1412, 1999.

[30] I. Rekanos, "Time-domain inverse scattering using lagrange multipliers: An iterative fdtd-based optimization technique," *Journal of Electromagnetic Waves and Applications*, vol. 17, no. 2, pp. 271–289, 2003.

[31] T. Tanaka, T. Takenaka, and S. He, "An fdtd approach to the time-domain inverse scattering problem for an inhomogeneous cylindrical object," *Microwave and Optical Technology Letters*, vol. 20, no. 1, pp. 72–77, 1999.

[32] M. Pastorino, "Stochastic optimization methods applied to microwave imaging: A review," *IEEE Transactions on Antennas and Propagation*, vol. 55, no. 3, pp. 538–548, 2007.

[33] ——, *Microwave imaging*. John Wiley & Sons, 2010, vol. 208.

[34] M. Gustafsson and S. He, "A wave-splitting based optimization approach to multi-dimensional time-domain electromagnetic inverse problems," *Mathematics and computers in simulation*, vol. 50, no. 5-6, pp. 541–551, 1999.

[35] A. Fhager, P. Hashemzadeh, and M. Persson, "Reconstruction quality and spectral content of an electromagnetic time-domain inversion algorithm," *IEEE Transactions on Biomedical Engineering*, vol. 53, no. 8, pp. 1594–1604, 2006.

[36] C. Kaye, I. Jeffrey, and J. LoVetri, "Improvement of multi-frequency microwave breast imaging through frequency cycling and tissue-dependent mapping," *IEEE Transactions on Antennas and Propagation*, vol. 67, no. 11, pp. 7087–7096, 2019.

[37] P. I. U. T. D. Data, "Nonlinear two-dimensional velocity profile inversion using time domain data," *IEEE Transactions on Geoscience and Remote Sensing*, vol. 30, no. 1, p. 147, 1992.

[38] W. H. Weedon, "Broadband microwave inverse scattering: Theory and experiment," Ph.D. dissertation, University of Illinois at Urbana-Champaign, 1994.

[39] S. He, S. Ström, and V. H. Weston, *Time domain wave-splittings and inverse problems*. Oxford University Press on Demand, 1998, no. 44.

[40] T. G. Papadopoulos and I. T. Rekanos, "Estimation of the parameters of 2d debye dispersive media using a time-domain inverse scattering technique," in *2011 XXXth URSI General Assembly and Scientific Symposium*. IEEE, 2011, pp. 1–4.

[41] H. Sato and S. Kidera, "Noise-robust microwave breast imaging applied to multi-frequency contrast source inversion," *IEEE Journal of Electromagnetics, RF and Microwaves in Medicine and Biology*, vol. 5, no. 2, pp. 187–193, 2020.

[42] J. D. Shea, P. Kosmas, S. C. Hagness, and B. D. Van Veen, "Three-dimensional microwave imaging of realistic numerical breast phantoms via a multiple-frequency inverse scattering technique," *Medical physics*, vol. 37, no. 8, pp. 4210–4226, 2010.

[43] N. Geddert, L. Sparling, J. LoVetri, and I. Jeffrey, "Frequency-weighting for multi-frequency electromagnetic source contrast inversion," in *2018 International Workshop on Computing, Electromagnetics, and Machine Intelligence (CEMi)*. IEEE, 2018, pp. 15–16.

[44] W. C. Chew and J. Lin, "A frequency-hopping approach for microwave imaging of large inhomogeneous bodies," *IEEE Microwave and Guided Wave Letters*, vol. 5, no. 12, pp. 439–441, 1995.

[45] V. Thomas, C. Gopakumar, A. Lonappan, G. Bindu, V. Hamsakutty, and K. Mathew, "Microwave imaging of two-dimensional dielectric cylinders with a multiscaled frequency hopping approach," *Microwave and Optical Technology Letters*, vol. 43, no. 4, pp. 353–355, 2004.

[46] T. Tanaka, N. Kuroki, and T. Takenaka, "Filtered forward-backward time-stepping method applied to reconstruction of dielectric cylinders," *Journal of electromagnetic waves and applications*, vol. 17, no. 2, pp. 253–270, 2003.

[47] J. J. McCombe and N. K. Nikolova, "Snr assessment of microwave imaging systems," in *2014 IEEE Antennas and Propagation Society International Symposium (APSURSI)*. IEEE, 2014, pp. 149–150.

[48] W. Shao, A. Edalati, T. R. McCollough, and W. J. McCollough, "A time-domain measurement system for uwb microwave imaging," *IEEE Transactions on Microwave Theory and Techniques*, vol. 66, no. 5, pp. 2265–2275, 2018.

[49] D. Shumakov, A. Beaverstone, J. McCombe, and N. Nikolova, "Quadrupole illumination for improving the signal to noise ratio in microwave imaging," in *2016 10th European Conference on Antennas and Propagation (EuCAP)*. IEEE, 2016, pp. 1–4.

[50] S. Kwon, S. Son, and K. Lee, "Experimental demonstration of in-place calibration for time domain microwave imaging system," *Radio Science*, vol. 53, no. 4, pp. 429–439, 2018.

[51] I. Jeffrey, N. Geddert, K. Brown, and J. LoVetri, "The time-harmonic discontinuous galerkin method as a robust forward solver for microwave imaging applications," *Progress In Electromagnetics Research*, vol. 154, pp. 1–21, 2015.

[52] K. Brown, "Implementation of parallel 3-d dgm-csi and dgm-gni for electromagnetic imaging applications," 2019.

[53] S. J. Orfanidis, "Electromagnetic waves and antennas," 2002.

[54] S. Lanteri and C. Scheid, "Convergence of a discontinuous galerkin scheme for the mixed time-domain maxwell's equations in dispersive media," *IMA Journal of Numerical Analysis*, vol. 33, no. 2, pp. 432–459, 2013.

[55] G. Kristensson, S. Rikte, and A. H. Sihvola, *Mixing formulas in time domain*. Citeseer, 1997.

[56] C. A. Balanis, *Advanced engineering electromagnetics*. John Wiley & Sons, 2012.

[57] M. D. Bui, S. S. Stuchly, and G. I. Costache, "Propagation of transients in dispersive dielectric media," *IEEE transactions on microwave theory and techniques*, vol. 39, no. 7, pp. 1165–1172, 1991.

[58] M. Han, R. W. Dutton, and S. Fan, "Model dispersive media in finite-difference time-domain method with complex-conjugate pole-residue pairs," *IEEE microwave and wireless components letters*, vol. 16, no. 3, pp. 119–121, 2006.

[59] D. W. Winters, J. D. Shea, P. Kosmas, B. D. Van Veen, and S. C. Hagness, "Three-dimensional microwave breast imaging: Dispersive dielectric properties estimation using patient-specific basis functions," *IEEE Transactions on Medical Imaging*, vol. 28, no. 7, pp. 969–981, 2009.

[60] M. Okoniewski, M. Mrozowski, and M. Stuchly, "Simple treatment of multi-term dispersion in fdtd," *IEEE Microwave and Guided Wave Letters*, vol. 7, no. 5, pp. 121–123, 1997.

[61] T. Lu, P. Zhang, and W. Cai, "Discontinuous galerkin methods for dispersive and lossy maxwell's equations and pml boundary conditions," *Journal of Computational Physics*, vol. 200, no. 2, pp. 549–580, 2004.

[62] R. Siushansian and J. LoVetri, "An efficient higher order numerical convolution for modelling nth-order lorentz dispersion," in *IEEE Antennas and Propagation Society International Symposium. 1995 Digest*, vol. 1. IEEE, 1995, pp. 632–635.

[63] S.-C. Kong, J. J. Simpson, and V. Backman, "Ade-fdtd scattered-field formulation for dispersive materials," *IEEE Microwave and Wireless Components Letters*, vol. 18, no. 1, pp. 4–6, 2008.

[64] D. F. Kelley and R. J. Luebbers, "Piecewise linear recursive convolution for dispersive media using fdtd," *IEEE Transactions on Antennas and Propagation*, vol. 44, no. 6, pp. 792–797, 1996.

[65] M. Lazebnik, M. Okoniewski, J. H. Booske, and S. C. Hagness, "Highly accurate debye models for normal and malignant breast tissue dielectric properties at microwave frequencies," *IEEE microwave and wireless components letters*, vol. 17, no. 12, pp. 822–824, 2007.

[66] J. Li, Y. Huang, and Y. Lin, "Developing finite element methods for maxwell's equations in a cole–cole dispersive medium," *SIAM Journal on Scientific Computing*, vol. 33, no. 6, pp. 3153–3174, 2011.

[67] D. M. Pozar, *Microwave engineering*. John wiley & sons, 2011.

[68] V. Hutson, J. Pym, and M. Cloud, *Applications of functional analysis and operator theory*. Elsevier, 2005.

[69] M. Asefi, I. Jeffrey, J. LoVetri, C. Gilmore, P. Card, and J. Paliwal, "Grain bin monitoring via electromagnetic imaging," *Computers and Electronics in Agriculture*, vol. 119, pp. 133–141, 2015.

[70] I. Higueras and T. Roldán, "Construction of additive semi-implicit runge–kutta methods with low-storage requirements," *Journal of Scientific Computing*, vol. 67, no. 3, pp. 1019–1042, 2016.

[71] N. I. C. Jawias, F. Ismail, M. Suleiman, and A. Jaafar, "Fourth order four-stage diagonally implicit runge-kutta method for linear ordinary differential equations," *Malaysian Journal of Mathematical Sciences*, vol. 4, no. 1, pp. 95–105, 2010.

[72] L. M. Skvortsov, "Efficient implementation of second-order implicit runge-kutta methods," *Mathematical Models and Computer Simulations*, vol. 5, no. 6, pp. 565–574, 2013.

[73] D. Cavaglieri and T. Bewley, "Low-storage implicit/explicit runge–kutta schemes for the simulation of stiff high-dimensional ode systems," *Journal of Computational Physics*, vol. 286, pp. 172–193, 2015.

[74] B. S. Attili, K. Furati, and M. I. Syam, "An efficient implicit runge–kutta method for second order systems," *Applied Mathematics and Computation*, vol. 178, no. 2, pp. 229–238, 2006.

[75] J. Williamson, "Low-storage runge-kutta schemes," *Journal of Computational Physics*, vol. 35, no. 1, pp. 48–56, 1980.

[76] P. DeVries and J. Hasbun, *A First Course in Computational Physics*. Jones & Bartlett Learning, 2011.

[77] E. Hairer, G. Wanner, and S. P. Nørsett, "Runge-kutta and extrapolation methods," *Solving Ordinary Differential Equations I: Nonstiff Problems*, pp. 129–353, 1993.

[78] Y. Saad, *Iterative methods for sparse linear systems*. SIAM, 2003.

[79] C. Geuzaine and J.-F. Remacle, "Gmsh: A 3-d finite element mesh generator with built-in pre-and post-processing facilities," *International journal for numerical methods in engineering*, vol. 79, no. 11, pp. 1309–1331, 2009.

[80] R. F. Harrington, *Time-harmonic electromagnetic fields*. McGraw-Hill, 1961.

[81] R. Fletcher and C. M. Reeves, "Function minimization by conjugate gradients," *The computer journal*, vol. 7, no. 2, pp. 149–154, 1964.

[82] B. T. Polyak, "The conjugate gradient method in extremal problems," *USSR Computational Mathematics and Mathematical Physics*, vol. 9, no. 4, pp. 94–112, 1969.

[83] R. P. Brent, *Algorithms for minimization without derivatives*. Courier Corporation, 2013.

[84] C. Gilmore, A. Zakaria, S. Pistorius, and J. LoVetri, "Microwave imaging of human forearms: Pilot study and image enhancement," *International journal of biomedical imaging*, vol. 2013, 2013.

[85] C. Kaye, I. Jeffrey, and J. LoVetri, "Novel stopping criteria for optimization-based microwave breast imaging algorithms," *Journal of Imaging*, vol. 5, no. 5, p. 55, 2019.

[86] G. P. Faucher, "Calibration of an ultrasound tomography system for medical imaging with 2d contrast-source inversion," 2013.

[87] P. Mojabi, "Ultrasound tomography: An inverse scattering approach," 2014.

[88] A. Arnau *et al.*, *Piezoelectric transducers and applications*. Springer, 2004, vol. 2004.

[89] C. Kumaragamage and P. Oramasionwu, "Design of an ultrasound tomography system for breast cancer imaging," *University of Manitoba, Tech. Rep*, 2010.

[90] D. H. Staelin, A. W. Morgenthaler, and J. A. Kong, *Electromagnetic waves*. Pearson Education India, 1994.

[91] P. M. Morse, K. U. Ingard, and R. Beyer, "Theoretical acoustics," *Journal of Applied Mechanics*, vol. 36, no. 2, p. 382, 1969.

[92] J. Lubbers and R. Graaff, "A simple and accurate formula for the sound velocity in water," *Ultrasound in medicine & biology*, vol. 24, no. 7, pp. 1065–1068, 1998.

[93] K. G. Brown, N. Geddert, M. Asefi, J. LoVetri, and I. Jeffrey, "Hybridizable discontinuous galerkin method contrast source inversion of 2-d and 3-d dielectric and magnetic targets," *IEEE Transactions on Microwave Theory and Techniques*, vol. 67, no. 5, pp. 1766–1777, 2019.

[94] R. L. Cravey, P. I. Tiemsin, K. Bussell, and K. L. Dudley, "Dielectric property measurements in the electromagnetic properties measurement laboratory," 1995.

[95] M. Ostadrahimi, P. Mojabi, C. Gilmore, A. Zakaria, S. Noghanian, S. Pistorius, and J. LoVetri, "Analysis of incident field modeling and incident/scattered field calibration techniques in microwave tomography," *IEEE Antennas and Wireless Propagation Letters*, vol. 10, pp. 900–903, 2011.

[96] E. Peyskens, M. De Pourcq, M. Stevens, and J. Schalck, "Dielectric properties of softwood species at microwave frequencies," *Wood Science and Technology*, vol. 18, no. 4, pp. 267–280, 1984.

[97] S. Razafindratsima, Z. M. Sbartaï, and F. Demontoux, "Permittivity measurement of wood material over a wide range of moisture content," *Wood Science and Technology*, vol. 51, no. 6, pp. 1421–1431, 2017.

[98] T. C. Mai, S. Razafindratsima, Z. M. Sbartaï, F. Demontoux, and F. Bos, "Non-destructive evaluation of moisture content of wood material at gpr frequency," *Construction and Building Materials*, vol. 77, pp. 213–217, 2015.

[99] M. Asefi, A. Zakaria, and J. LoVetri, "Microwave imaging using normal electric-field components inside metallic resonant chambers," *IEEE Transactions on Microwave Theory and Techniques*, vol. 65, no. 3, pp. 923–933, 2016.

[100] A. Zakaria, C. Gilmore, and J. LoVetri, "Finite-element contrast source inversion method for microwave imaging," *Inverse Problems*, vol. 26, no. 11, p. 115010, 2010.

[101] A. Fedeli, M. Pastorino, A. Randazzo, and G. L. Gragnani, "Analysis of a nonlinear technique for microwave imaging of targets inside conducting cylinders," *Electronics*, vol. 10, no. 5, p. 594, 2021.

[102] P. Mojabi and J. LoVetri, "A prescaled multiplicative regularized gauss-newton inversion," *IEEE Transactions on Antennas and Propagation*, vol. 59, no. 8, pp. 2954–2963, 2011.

[103] M. Hughson, J. LoVetri, and I. Jeffrey, "Microwave breast imaging incorporating material property dependencies," in *2019 IEEE MTT-S International Microwave Symposium (IMS)*. IEEE, 2019, pp. 1450–1453.

[104] R. Obermeier and J. A. Martinez-Lorenzo, "Compressive sensing unmixing algorithm for breast cancer detection," *IET Microwaves, Antennas & Propagation*, vol. 12, no. 4, pp. 533–541, 2018.

[105] N. Abdollahi, D. Kurrant, P. Mojabi, M. Omer, E. Fear, and J. LoVetri, "Incorporation of ultrasonic prior information for improving quantitative microwave imaging of breast," *IEEE Journal on Multiscale and Multiphysics Computational Techniques*, vol. 4, pp. 98–110, 2019.

[106] A. H. Golnabi, P. M. Meaney, and K. D. Paulsen, "3d microwave tomography of the breast using prior anatomical information," *Medical physics*, vol. 43, no. 4, pp. 1933–1944, 2016.

[107] M. T. Bevacqua, G. G. Bellizzi, T. Isernia, and L. Crocco, "A method for effective permittivity and conductivity mapping of biological scenarios via segmented contrast source inversion," *Progress In Electromagnetics Research*, vol. 164, pp. 1–15, 2019.

[108] L. M. Neira, B. D. Van Veen, and S. C. Hagness, "High-resolution microwave breast imaging using a 3-d inverse scattering algorithm with a variable-strength spatial prior constraint," *IEEE Transactions on Antennas and Propagation*, vol. 65, no. 11, pp. 6002–6014, 2017.

Appendix A

Adjoint Operator $\tilde{\mathcal{K}}^*$

This appendix goes into the details of mathematically calculating the adjoint operator of $\tilde{\mathcal{K}}$; $\tilde{\mathcal{K}}^*$. The field adjoint vector $\underline{w}$ is an operator that converts the modeled constitutive parameters at the imaging domain to the field adjoint quantities of $\underline{w}$. This process is done by the adjoint operator of $\tilde{\mathcal{K}}^*$.

Here, we start with the inner product definition between the operator $\tilde{\mathcal{K}}$ and $\tilde{\mathcal{K}}^*$, which was introduced by equation (3.25)

$$\langle \tilde{\mathcal{K}}^*(g),\ f\rangle = \langle g,\ \tilde{\mathcal{K}}(f)\rangle \tag{A.1}$$

, when

$$\begin{cases} f = \underline{v}(t,\vec{r}) \\ g = \underline{\underline{w}}(t,\vec{r}). \end{cases} \tag{A.2}$$

So

$$\langle \tilde{\mathcal{K}}^*(\underline{w}(t,\vec{r})),\ \underline{v}(t,\vec{r})\rangle = \langle \underline{w}(t,\vec{r}),\ \tilde{\mathcal{K}}(\underline{v}(t,\vec{r}))\rangle. \tag{A.3}$$

First we expand the right hand side of the equation (A.3) and try to find a definition for the

adjoint operator $\tilde{\boldsymbol{\mathcal{K}}}^*$ using the left hand side of (A.3).

$$\int_0^T \iiint_\infty (\underline{w}(t,\vec{r}))^t \; \tilde{\boldsymbol{\mathcal{K}}}(\underline{v}(t,\vec{r})) \; dVdt = \cdots$$

$$\int_0^T \iiint_\infty \begin{bmatrix} \vec{w}_1(t,\vec{r}) \\ \vec{w}_2(t,\vec{r}) \\ \vec{w}_3(t,\vec{r}) \end{bmatrix}^t \left(\begin{bmatrix} \varepsilon_\infty(\vec{r})\partial_{c_0 t} + \eta_0\alpha(\vec{r}) & -\nabla\times & -\eta_0\beta(\vec{r}) \\ \nabla\times & \mu_r(\vec{r})\partial_{c_0 t} & \emptyset \\ -\eta_0\beta(\vec{r}) & \emptyset & \Delta\varepsilon_r(\vec{r})\partial_{c_0 t} + \eta_0\beta(\vec{r}) \end{bmatrix} \begin{bmatrix} \vec{v}_1(t,\vec{r}) \\ \vec{v}_2(t,\vec{r}) \\ \vec{v}_3(t,\vec{r}) \end{bmatrix} \right) dVdt \cdots$$

$$= I1 + I2 + I3 \tag{A.4}$$

The integrals of $I1$ and $I2$ and $I3$ in the equation (A.4) are

$$I1 = \int_0^T \iiint_\infty \vec{w}_1(t,\vec{r})\varepsilon_\infty(\vec{r})\partial_{c_0 t}\vec{v}_1(t,\vec{r}) + \vec{w}_2(t,\vec{r})\mu_r(\vec{r})\partial_{c_0 t}\vec{v}_2(t,\vec{r}) + \cdots$$
$$\vec{w}_3(t,\vec{r})\Delta\varepsilon_r(\vec{r})\partial_{c_0 t}\vec{v}_3(t,\vec{r}) \; dVdt. \tag{A.5}$$

$$I2 = \int_0^T \iiint_\infty -\vec{w}_1(t,\vec{r}) \; \nabla\times\vec{v}_2(t,\vec{r}) + \vec{w}_2(t,\vec{r}) \; \nabla\times\vec{v}_1(t,\vec{r}) \; dVdt. \tag{A.6}$$

$$I3 = \int_0^T \iiint_\infty \vec{w}_1(t,\vec{r}) \; \eta_0\alpha(\vec{r}) \; \vec{v}_1(t,\vec{r}) - \vec{w}_1(t,\vec{r}) \; \eta_0\beta(\vec{r}) \; \vec{v}_3(t,\vec{r}) - \cdots$$
$$\vec{w}_3(t,\vec{r}) \; \eta_0\beta(\vec{r}) \; \vec{v}_1(t,\vec{r}) + \vec{w}_3(t,\vec{r}) \; \eta_0\beta(\vec{r}) \; \vec{v}_3(t,\vec{r}) \; dVdt. \tag{A.7}$$

The first integral of $I1$ can be expanded using the mathematical partial integration rule, which is shown in (A.8), as is shown in (A.9).

$$\int_a^b f(t) \; \partial_t g(t) \; dt = [f(t) \; g(t)]_{t=a}^{t=b} - \int_a^b \partial_t f(t) \; g(t) \; dt \tag{A.8}$$

$$I1 = \iiint_{\infty} \left[\varepsilon_{\infty}(\vec{r})\ \vec{w}_1(t,\vec{r})\vec{v}_1(t,\vec{r}) + \mu_r(\vec{r})\ \vec{w}_2(t,\vec{r})\vec{v}_2(t,\vec{r}) + \Delta\varepsilon_r(\vec{r})\ \vec{w}_3(t,\vec{r})\vec{v}_3(t,\vec{r})\right]_{c_0t=0}^{c_0t=c_0T} dV \cdots$$
$$- \int_0^T \iiint_{\infty} \varepsilon_{\infty}(\vec{r})\ \partial_{c_0t}\vec{w}_1(t,\vec{r})\ \vec{v}_1(t,\vec{r}) + \mu_r(\vec{r})\ \partial_{c_0t}\vec{w}_2(t,\vec{r})\ \vec{v}_2(t,\vec{r})\ + \cdots$$
$$\Delta\varepsilon_r(\vec{r})\ \partial_{c_0t}\vec{w}_3(t,\vec{r})\ \vec{v}_3(t,\vec{r})\ dVdt \tag{A.9}$$

By imposing some reasonable initial conditions to the problem, we can easily omit the first integral in the (A.9). These conditions are zero fields $\underline{\vec{v}}$ at time $t = 0$ and zero field adjoints $\underline{\vec{w}}$ at time $t = T$.

$$\underline{\vec{v}}\ (t = 0,\ \vec{r}) = \emptyset \tag{A.10a}$$

$$\underline{\vec{w}}\ (t = T,\ \vec{r}) = \emptyset \tag{A.10b}$$

So, using the (A.10), the $I1$ integral becomes

$$I1 = -\int_0^T \iiint_{\infty} \vec{v}_1(t,\vec{r})\ \varepsilon_{\infty}(\vec{r})\ \partial_{c_0t}\vec{w}_1(t,\vec{r}) + \vec{v}_2(t,\vec{r})\ \mu_r(\vec{r})\ \partial_{c_0t}\vec{w}_2(t,\vec{r})\ + \cdots$$
$$\vec{v}_3(t,\vec{r})\ \Delta\varepsilon_r(\vec{r})\ \partial_{c_0t}\vec{w}_3(t,\vec{r})\ dVdt. \tag{A.11}$$

cross product rule

$$\nabla \cdot (\vec{A} \times \vec{B}) = \vec{B}\ \nabla \times \vec{A} - \vec{A}\ \nabla \times \vec{B}, \tag{A.12}$$

where $\vec{A}$ and $\vec{B}$ are two arbitrary vectors and the $\nabla.$ is the divergence symbol.

According to the cross product rule of (A.12), we can rewrite the integral $I2$ in (A.6) as

$$I2 = I21 \ + \ I22, \tag{A.13}$$

$$I21 = \int_0^T \iiint_\infty \ -\nabla \cdot (\vec{v}_2(t,\vec{r}) \times \vec{w}_1(t,\vec{r})) + \nabla \cdot (\vec{v}_1(t,\vec{r}) \times \vec{w}_2(t,\vec{r}))\ dVdt, \tag{A.14}$$

$$I22 = \int_0^T \iiint_\infty \ -\vec{v}_2(t,\vec{r})\ \nabla \times \vec{w}_1(t,\vec{r}) + \vec{v}_1(t,\vec{r})\ \nabla \times \vec{w}_2(t,\vec{r})\ dVdt. \tag{A.15}$$

divergence theorem

The divergence theorem relates the divergence of a field in an enclosed volume $\mathbf{V}$ by a surface to the flux of the field through the closed surface $\mathbf{S}(\mathbf{V})$. The mathematical form of this rule is presented in (A.16). In this equation $\hat{n}$ represents the unit vector perpendicular to the surface $\mathbf{S}(\mathbf{V})$.

$$\iiint_{\mathbf{V}} (\nabla \cdot \vec{A})\ dV = \oiint_{\mathbf{S}(\mathbf{V})} (\vec{A}\ \hat{n})dS \tag{A.16}$$

According to the divergence theorem, the integral $I21$ can be rewritten as (A.17).

$$I21 = \int_0^T \oiint_{\mathbf{S}(\infty)} \ -(\vec{v}_2(t,\vec{r}) \times \vec{w}_1(t,\vec{r}) + \vec{v}_1(t,\vec{r}) \times \vec{w}_2(t,\vec{r}))\ \hat{n}\ dSdt. \tag{A.17}$$

It is obvious that the flux related to the designated fields in the equation (A.17) coming out of the surface $\mathbf{S}(\infty)$ is zero. So

$$I21 = 0, \tag{A.18}$$

and

$$I2 = \int_0^T \iiint_\infty -\vec{v}_2(t,\vec{r})\ \nabla \times \vec{w}_1(t,\vec{r}) + \vec{v}_1(t,\vec{r})\ \nabla \times \vec{w}_2(t,\vec{r})\ dVdt. \tag{A.19}$$

And the $I3$ is the same as

$$\begin{aligned} I3 = \int_0^T \iiint_\infty & \vec{v}_1(t,\vec{r})\ \eta_0\alpha(\vec{r})\ \vec{w}_1(t,\vec{r}) - \vec{v}_1(t,\vec{r})\ \eta_0\beta(\vec{r})\ \vec{w}_3(t,\vec{r}) - \cdots \\ & \vec{v}_3(t,\vec{r})\ \eta_0\beta(\vec{r})\ \vec{w}_1(t,\vec{r}) + \vec{v}_3(t,\vec{r})\ \eta_0\beta(\vec{r})\ \vec{w}_3(t,\vec{r})\ dVdt. \end{aligned} \tag{A.20}$$

Now we can rewrite the equation (A.4) by expressing the integrals of $I1$, $I2$ and $I3$ in their matrix form:

$$I1 = \int_0^T \iiint_\infty \begin{bmatrix} \vec{v}_1(t,\vec{r}) \\ \vec{v}_2(t,\vec{r}) \\ \vec{v}_3(t,\vec{r}) \end{bmatrix}^t \left(\begin{bmatrix} -\varepsilon_\infty(\vec{r})\partial_{c_0 t} & \emptyset & \emptyset \\ \emptyset & -\mu_r(\vec{r})\partial_{c_0 t} & \emptyset \\ \emptyset & \emptyset & -\Delta\varepsilon_r(\vec{r})\partial_{c_0 t} \end{bmatrix} \begin{bmatrix} \vec{w}_1(t,\vec{r}) \\ \vec{w}_2(t,\vec{r}) \\ \vec{w}_3(t,\vec{r}) \end{bmatrix} \right) dVdt, \tag{A.21}$$

$$I2 = \int_0^T \iiint_\infty \begin{bmatrix} \vec{v}_1(t,\vec{r}) \\ \vec{v}_2(t,\vec{r}) \\ \vec{v}_3(t,\vec{r}) \end{bmatrix}^t \left(\begin{bmatrix} \emptyset & \nabla\times & \emptyset \\ -\nabla\times & \emptyset & \emptyset \\ \emptyset & \emptyset & \emptyset \end{bmatrix} \begin{bmatrix} \vec{w}_1(t,\vec{r}) \\ \vec{w}_2(t,\vec{r}) \\ \vec{w}_3(t,\vec{r}) \end{bmatrix} \right) dVdt, \tag{A.22}$$

$$I3 = \int_0^T \iiint_\infty \begin{bmatrix} \vec{v}_1(t,\vec{r}) \\ \vec{v}_2(t,\vec{r}) \\ \vec{v}_3(t,\vec{r}) \end{bmatrix}^t \left(\begin{bmatrix} \eta_0\alpha(\vec{r}) & \emptyset & -\eta_0\beta(\vec{r}) \\ \emptyset & \emptyset & \emptyset \\ -\eta_0\beta(\vec{r}) & \emptyset & \eta_0\beta(\vec{r}) \end{bmatrix} \begin{bmatrix} \vec{w}_1(t,\vec{r}) \\ \vec{w}_2(t,\vec{r}) \\ \vec{w}_3(t,\vec{r}) \end{bmatrix} \right) dVdt. \tag{A.23}$$

So

$$\int_0^T \iiint_\infty (\underline{w}(t,\vec{r}))^t \ \tilde{\boldsymbol{\mathcal{K}}}(\underline{v}(t,\vec{r}))\ dVdt = \ I1 + I2 + I3 = \cdots$$

$$\int_0^T \iiint_\infty \begin{bmatrix} \vec{v}_1(t,\vec{r}) \\ \vec{v}_2(t,\vec{r}) \\ \vec{v}_3(t,\vec{r}) \end{bmatrix}^t \left(\begin{bmatrix} -\varepsilon_\infty(\vec{r})\partial_{c_0 t} + \eta_0\alpha(\vec{r}) & \nabla\times & -\eta_0\beta(\vec{r}) \\ -\nabla\times & -\mu_r(\vec{r})\partial_{c_0 t} & \emptyset \\ -\eta_0\beta(\vec{r}) & \emptyset & -\Delta\varepsilon_r(\vec{r})\partial_{c_0 t} + \eta_0\beta(\vec{r}) \end{bmatrix} \begin{bmatrix} \vec{w}_1(t,\vec{r}) \\ \vec{w}_2(t,\vec{r}) \\ \vec{w}_3(t,\vec{r}) \end{bmatrix} \right) dVdt. \tag{A.24}$$

by expanding the inner products of both sides of the relation (A.3) in (A.25)

$$\int_0^T \iiint_\infty (\underline{w}(t,\vec{r}))^t \ \tilde{\boldsymbol{\mathcal{K}}}(\underline{v}(t,\vec{r}))\ dVdt = \int_0^T \iiint_\infty (\underline{v}(t,\vec{r}))^t \ \tilde{\boldsymbol{\mathcal{K}}}^*(\underline{w}(t,\vec{r}))\ dVdt, \tag{A.25}$$

and comparing it with the results in (A.24), we can extract the adjoint operator $\tilde{\boldsymbol{\mathcal{K}}}^*$ as

$$\tilde{\boldsymbol{\mathcal{K}}}^* = \begin{bmatrix} -\varepsilon_\infty(\vec{r})\partial_{c_0 t} + \eta_0\alpha(\vec{r}) & \nabla\times & -\eta_0\beta(\vec{r}) \\ -\nabla\times & -\mu_r(\vec{r})\partial_{c_0 t} & \emptyset \\ -\eta_0\beta(\vec{r}) & \emptyset & -\Delta\varepsilon_r(\vec{r})\partial_{c_0 t} + \eta_0\beta(\vec{r}) \end{bmatrix}. \tag{A.26}$$

Appendix B

Unimodality and δ-Unimodality

A function f is called unimodal on the interval $[a,\ b]$ iff, for some unique point $\alpha \in [a,\ b]$, f is strictly monotonically decreasing on $[a,\ \alpha)$ and strictly monotonically increasing on $[\alpha,\ b]$ or f is strictly monotonically decreasing on $[a,\ \alpha]$ and strictly monotonically increasing on $(\alpha,\ b]$.

A function f is called δ-unimodal on the interval $[a,\ b]$ iff, for some amount of $\alpha \in [a,\ b]$, f is δ-$\downarrow$ on $[a,\ \alpha)$ and δ-$\uparrow$ on $[\alpha,\ b]$.

If the function f is δ-unimodal on $[a,\ b]$, there exists a unique interval of $[\alpha_1,\ \alpha_2] \subseteq [a,\ b]$ such that the α points with the mentioned property are precisely the interval $[\alpha_1,\ \alpha_2]$'s points where $\alpha_2 \leqslant \alpha_1 + \delta$.